

ALMA MATER STUDIORUM
UNIVERSITÀ DI BOLOGNA

Dipartimento di Fisica e Astronomia

DOTTORATO DI RICERCA IN
ASTROFISICA

Ciclo XXXIII

Tesi di Dottorato

**THE IMPACT OF AGN ACTIVITY ON THE
HOST-GALAXY ISM**

Presentata da:
Francesco Salvestrini

Supervisore:
Prof. Cristian Vignali

Coordinatore di Dottorato:
Prof. Francesco Rosario
Ferraro

Co-supervisore:
Dr. Carlotta Gruppioni
Prof. Francesca Pozzi

Esame finale anno 2021

Settore Concorsuale: 02/C1 – Astronomia, Astrofisica, Fisica della Terra e dei Pianeti
Settore Scientifico Disciplinare: FIS/05 – Astronomia e Astrofisica

Abstract

In this Thesis I investigate how, and to which extent, Active Galactic Nuclei (AGN) activity affects the properties of the host-galaxy interstellar medium (ISM). AGN are thought to regulate the host star formation (SF) by injecting large amount of energy in the circumnuclear region, either suppressing or enhancing the formation of new stars. To understand the interplay between AGN and SF multi-wavelength approach is needed, which allows us to trace the different gas components, as well as to identify the relative contributions of nuclear and SF activity to the galaxy global budget. Local Seyfert galaxies are the perfect laboratories to study whether and on which scales the emission from the AGN affects the properties of the host-galaxy ISM. Well suited candidates for this study are the Seyfert galaxies from the 12 μm galaxy sample (12MGS; Rush et al. 1993), a representative and unbiased collection of AGN in the local Universe, which benefits from an extensive observational coverage, from X-rays to radio frequencies.

In this context, I consider the sample of local Seyfert galaxies by Gruppioni et al. [2016], which are drawn from the 12MGS and benefit from a detailed spectral energy distribution decomposition (SED) as reference sample for our study. I adopt a two-fold strategy: on the one hand, by exploiting observation in the X-ray band, I characterise the AGN activity to unveil its intrinsic power; on the other hand, using interferometric and single-dish observations, I investigate the properties of the molecular gas, the key ingredient to form new stars, and potentially involved in the supermassive black hole (SMBH) accretion.

In the first part of the Thesis, I focus on the X-ray properties (e.g., intrinsic luminosity, level of obscuration) of 32 out of the 36 Seyfert 2 galaxies studied by Gruppioni et al. [2016], with available X-ray observations. Our goal is to use the 12MGS Type 2 AGN as a reference sample at low redshift, e.g. to study the column density distribution with limited bias. I present the result of a systematic analysis of the X-ray properties of the Seyfert 2 galaxies in our sample. To investigate the characteristics of the torus in different bands, i.e. the dusty compact structure which is responsible for the AGN obscuration, I compare the level of obscuration estimated from the X-ray spectral analysis, with the one derived from the strength of the 9.7 μm silicate feature in the mid-IR. I find that the column density of the obscuring material measured from the X-ray analysis, correlates with the strength of the silicate features as measured in the mid-IR.

In the second part of the thesis, I determine the molecular gas properties of 33 out of the 36 Seyfert 2 galaxies from Gruppioni et al. [2016] by using single-dish observations tracing the CO emission line, the more commonly adopted tracer of the cold molecular gas component. I derive the molecular gas masses and the relative depletion times for our sample of AGN. By comparing our results with a control sample of inactive galaxies, I infer if the nuclear activity affects the molecular gas reservoir in its host. I also assess the influence of AGN on the emission of mid-IR features, in particular on the emission from the polycyclic aromatic hydrocarbon (PAH) molecules, which are widely used as SF tracers. The sample of local Seyfert 2 galaxies shows depletion times similar to that in the control sample of star-forming galaxies (SFGs). Furthermore, the luminosity of the PAH features in galaxies hosting an AGN are relatively fainter than in SFGs. In the end, 29 out of the 36 Seyfert 2 galaxies from Gruppioni et al. [2016] benefit from the complementary analysis of both the AGN (the first section) and the properties of the host-galaxy ISM (the second section), resulting in one of the first statistically large samples of local AGN with such an extensive characterisation.

Finally, I apply our multi-wavelength strategy on a test case galaxy, NGC 7213, drawn from the same parent sample [Gruppioni et al., 2016], which came out to be of particular interest because of the kinematical modelling on ALMA data, which reveals the presence of two molecular outflow, likely driven by stellar activities. I complement the analysis with a detailed X-ray spectral analysis to determine the AGN accretion power, and the measurement of the molecular gas mass with single-dish CO spectroscopy. In the end, I provide a complete and coherent characterisation of NGC 7213 in terms of both its nuclear activity (confirming its low-luminosity AGN nature) and the properties of the molecular gas content.

Contents

| | | |
|----------|--|-----------|
| 1 | Scientific Context | 1 |
| 1.1 | Active Galactic Nuclei | 3 |
| 1.1.1 | AGN emission in the IR | 6 |
| 1.1.2 | AGN emission in the X-rays | 8 |
| 1.2 | Interstellar medium | 14 |
| 1.2.1 | Neutral medium | 14 |
| 1.2.1.1 | From atomic to molecular phase | 15 |
| 1.2.2 | Molecular gas | 15 |
| 1.2.2.1 | Molecular gas diagnostics | 16 |
| 1.2.2.2 | Molecular gas kinematics | 19 |
| 1.2.2.3 | Molecular gas mass | 20 |
| 1.2.3 | Ionised gas | 23 |
| 1.2.4 | Interstellar dust | 24 |
| 1.3 | Thesis aims | 26 |
| 2 | Unveiling the intrinsic power in local Seyfert 2 galaxies | 29 |
| 2.1 | The sample | 33 |
| 2.1.1 | X-ray data | 34 |
| 2.1.2 | X-ray data reduction | 35 |
| 2.1.2.1 | <i>NuSTAR</i> data reduction | 35 |
| 2.1.2.2 | <i>XMM-Newton</i> data reduction | 37 |
| 2.1.2.3 | <i>Chandra</i> data reduction | 37 |
| 2.1.2.4 | <i>Swift-XRT</i> data reduction | 37 |
| 2.1.3 | Spectral Fitting Procedure | 38 |
| 2.1.3.1 | Phenomenological models | 39 |
| 2.1.3.2 | MyTorus | 41 |
| 2.1.4 | Decomposed SED | 45 |
| 2.1.5 | Mid-IR features | 47 |
| 2.2 | Results and discussion | 48 |
| 2.2.1 | X-ray properties | 48 |
| 2.2.2 | Mid-IR and X-ray properties | 51 |
| 2.3 | Conclusions | 56 |

| | | |
|----------|--|------------|
| 3 | The effect of AGN activity on the host depletion time | 57 |
| 3.1 | The sample | 59 |
| 3.2 | Data | 59 |
| 3.2.1 | Single-dish observations in the sub-mm/mm band | 59 |
| 3.2.1.1 | APEX data reduction | 59 |
| 3.2.1.2 | Literature single-dish data | 65 |
| 3.2.1.3 | Aperture correction for the CO flux | 65 |
| 3.2.1.4 | The molecular gas content | 66 |
| 3.2.2 | Decomposed SED | 71 |
| 3.2.3 | Mid-IR features | 71 |
| 3.3 | Control sample | 72 |
| 3.4 | Results and discussion | 74 |
| 3.4.1 | $L_{IR}-L'_{CO(1-0)}$ relation | 76 |
| 3.4.2 | Molecular gas mass scaling relations | 77 |
| 3.4.3 | Molecular gas depletion times | 80 |
| 3.4.4 | PAH as tracer of the molecular gas | 80 |
| 3.5 | Conclusions | 84 |
| 4 | A test case: NGC 7213 | 87 |
| 4.1 | NGC 7213 | 88 |
| 4.2 | Multi-waveband data | 89 |
| 4.2.1 | X-ray data | 89 |
| 4.2.1.1 | X-ray data reduction | 90 |
| 4.2.1.2 | X-ray data analysis | 90 |
| 4.2.2 | ALMA data | 93 |
| 4.2.2.1 | The continuum emission | 94 |
| 4.2.2.2 | The CO(2-1) emission line | 94 |
| 4.2.3 | APEX data | 97 |
| 4.2.4 | SED decomposition | 97 |
| 4.3 | Interpreting the CO and continuum mm emission | 99 |
| 4.3.1 | The point-like continuum | 99 |
| 4.3.2 | Molecular gas kinematics | 100 |
| 4.3.3 | Complex structures in the CO emission | 102 |
| 4.3.4 | The molecular gas mass | 105 |
| 4.4 | Discussion and conclusions | 108 |
| 5 | Conclusions and future perspectives | 111 |

Appendices

| | |
|--------------------------------------|------------|
| A X-ray spectra | 119 |
| A.1 Phenomenological model | 119 |
| A.2 MyTorus model | 124 |
| Bibliography | 129 |

1

Scientific Context

The formation and evolution of galaxies is tightly related to the growth of the super massive black hole (SMBH; $M_{BH} \sim 10^6 - 10^{10} M_{\odot}$) that resides at their centre. Observatively, both BH growth and SF history peak at $z \sim 2$ (e.g., Madau and Dickinson 2014), meaning that the bulk of BH growth and SF took place between $z \sim 1 - 3$ (see Fig. 1.1; e.g., Shankar et al. 2009; Delvecchio et al. 2014; Madau and Dickinson 2014; Aird et al. 2015 and reference therein). This suggests a co-evolution of the two processes, driven by a mechanism that self-regulates the SF activity in the galaxy and the growth of the BH. Active galactic nuclei (AGN) are thought to play a major role in regulating the SF, providing feedback from the SMBH to its host galaxy and the interstellar medium (ISM; e.g., Harrison 2017; Maiolino et al. 2017; Harrison et al. 2020). Three modes of AGN feedback have been observed: “negative” feedback, when AGN suppress the star formation rate (SFR) by removing and heating the ISM, thus preventing it from cooling and forming new stars; “negative” feedback, if the AGN enhances the SF through the compression of molecular clouds (i.e. positive feedback; see Harrison 2017; Cresci and Maiolino 2018 and references therein); “preventive” (or “delayed”) feedback, where the luminous AGN is not visible anymore (or is becoming fainter) while its impact on the host galaxy remains visible. It is worth recalling that the same process which suppress the SF in the host-galaxy may also be responsible for the AGN starvation, i.e. the suppression of the feeding process onto the nucleus once the surrounding accreting material is removed by the AGN feedback (e.g., Trussler et al. 2020 are reference therein).

A wide range of analytical models and simulations support the interconnection between accretion and SF processes, predicting that stellar winds and supernovae may enhance the BH mass accretion by injecting turbulence into the gas disc (e.g., Wada

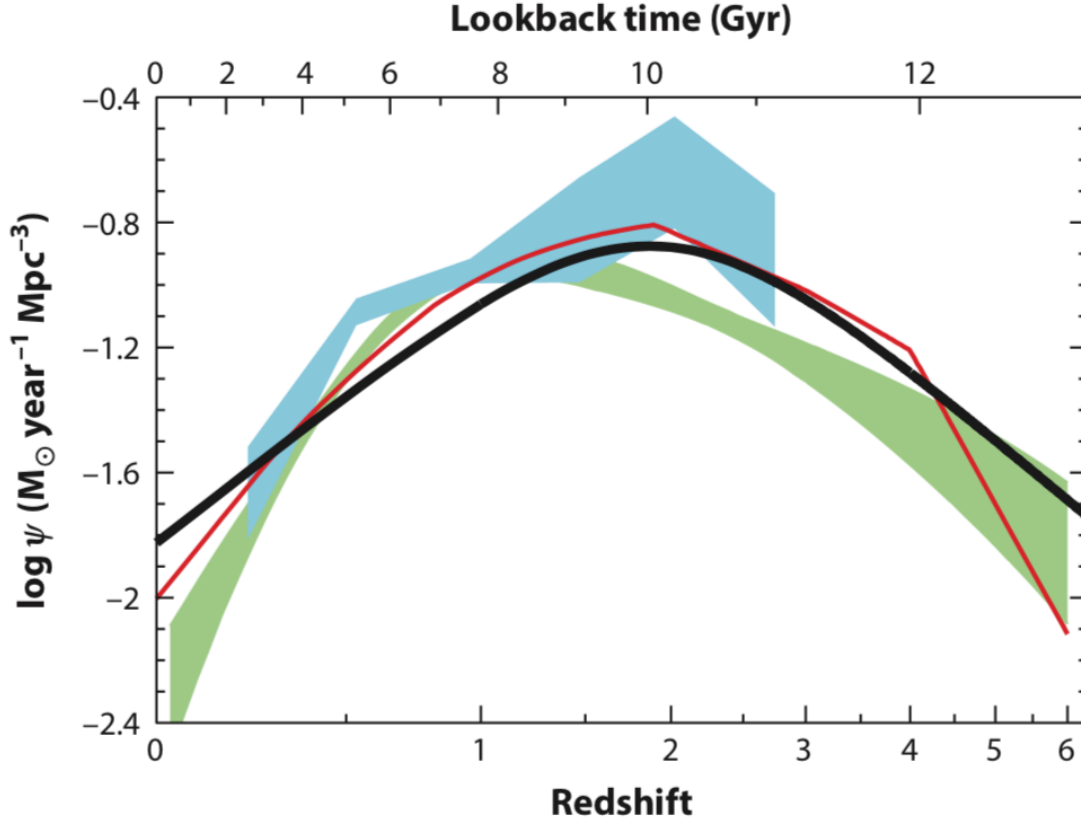


Figure 1.1: Comparison between the best-fit SF history (thick black solid curve) and the massive BH accretion history from X-ray (red curve from Shankar et al. [2009]; light green shading from Aird et al. [2010]) and infrared (light blue shading from Delvecchio et al. [2014]) data. The shading represents the $\pm 1\sigma$ uncertainty range on the total bolometric luminosity density. The radiative efficiency has been set to $\epsilon = 0.1$. The comoving rates of BH accretion have been scaled up by a factor of 3300 to facilitate visual comparison to the SF history. This figure is taken from Madau and Dickinson [2014].

and Norman 2002; Schartmann et al. 2009; Hobbs et al. 2011). Numerous studies have shown young stellar populations residing often in the central regions of nearby AGN (e.g., Storchi-Bergmann et al. 2001; Storchi-Bergmann et al. 2005; Fernandes et al. 2004), suggesting that AGN activity and ongoing SF coexist. In this context, the study of the properties and distribution of the molecular gas is crucial to understand the interplay between the two processes, as it is the fuel of SF and possibly of AGN accretion. Indeed, the molecular gas has been traced down to sub-kpc scales, co-spatially to the dusty dense core usually called “torus” (e.g., García-Burillo et al. 2014). The dense structure of molecular gas and dust could be both the outer region of the BH fuel supply disk and, in its colder part, a stellar nursery (e.g., Alexander and Hickox 2012).

As it will be discussed in the follow sections, only through a multi-wavelength approach is possible to properly characterise all the actors involved in the co-evolution play. In

particular, by combining observations in the millimetre, infrared and X-ray bands (less contaminated by the extinction effects with respect to e.g. UV/optical bands), it is possible to unveil the intrinsic power of the central AGN and investigate its influence on the surrounding ISM.

To this goal, local active galaxies are the perfect laboratories, given the extensive multi-wavelength data coverage already available, and their proximity, which allows us to spatially resolve the very central region, where the accretion onto the SMBH takes place. This Chapter aims at providing a brief introduction to the properties of local AGN, to their emission in the different bands, and to the role of the dusty torus. A summary of the ISM composition follows, which then focuses on the role played by the molecular gas component, in the context of the interplay between SF and AGN.

1.1 Active Galactic Nuclei

SMBH are thought to reside at the center of almost every massive galaxy [Kormendy and Ho, 2013], although only a fraction of them can be considered as “active” [Padovani et al., 2011]. Indeed, a galactic nucleus is considered active when this central engine can be revealed through some type of emission that cannot be attributed to the stellar activity within the host galaxy. AGN activity shows itself in many flavours (e.g., nuclear UV, optical, and X-ray emission, jets) and with different level of impact on the source energetic output (see Padovani et al. 2017 for an extensive review). The bolometric luminosity of the AGN (L_{bol}^{AGN} ; i.e., the total luminosity integrated over all wavelengths, once the emission from the stellar activity has been properly removed from the energy budget) is proportional to the rate at which the accretion process takes place:

$$L_{bol}^{AGN} = \epsilon c^2 \dot{M} \quad (1.1)$$

where ϵ is the mass-energy conversion factor (theoretically between 0.06 and 0.43, depending on the BH spin; e.g., Alexander and Hickox 2012) and c is the speed of light. A wide range of bolometric luminosities have been observed in active galaxies ($10^{40} < L_{bol}^{AGN} < 10^{48}$ erg s⁻¹; e.g., Alexander and Hickox 2012), with the quasars, populating the brightest end ($L_{bol}^{AGN} > 10^{45}$ erg s⁻¹), being able to totally overcome the emission from the host galaxy. Besides their extreme luminosity, which allows us to discover a growing number of new quasars at the highest redshift ($z > 7$; e.g., Mortlock et al. 2011; Bañados et al. 2018; Yang et al. 2020), AGN emit over the whole electromagnetic spectrum (see Fig. 1.2). This means that AGN have been discovered in all spectral bands, using different methods to identify these sources, providing different windows on AGN physics at the various wavelength regimes. The peak of the intrinsic

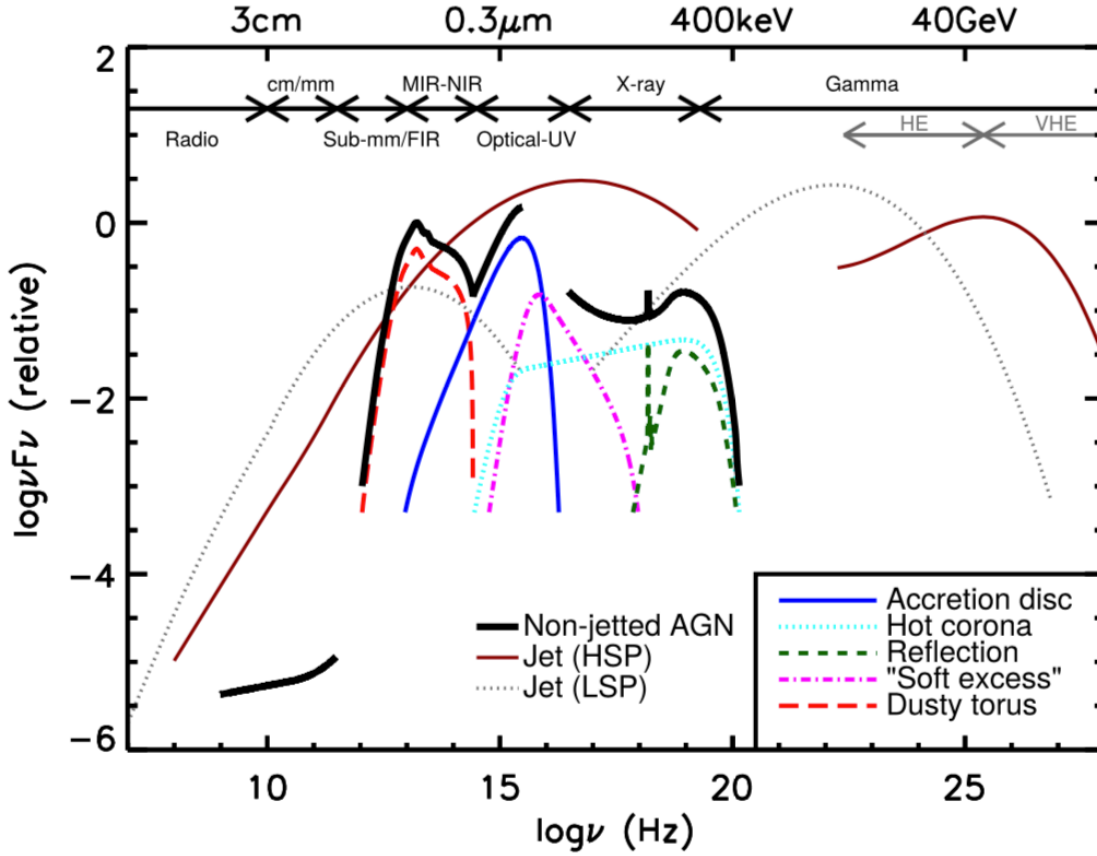


Figure 1.2: A schematic representation of an AGN spectral energy distribution (SED), loosely based on the observed SEDs of non-jetted quasars (e.g. Elvis et al. 1994; Richards et al. 2006). The black solid curve represents the total emission and the various coloured curves (shifted down for clarity) represent the individual components. The intrinsic shape of the SED in the mm-far infrared (far-IR) regime is uncertain; however, it is widely believed to have a minimal contribution (to an overall galaxy SED) compared to star formation (SF), except in the most intrinsically luminous quasars and powerful jetted AGN. The primary emission from the AGN accretion disk peaks in the UV region. The jet SED is also shown for a high synchrotron peaked blazar (HSP, based on the SED of Mrk 421, brown solid line) and a low synchrotron peaked blazar (LSP, based on the SED of 3C 454.3, dotted line). Credits: Harrison [2014].

emission from the AGN is in the optical/ultraviolet (UV) band, where the continuum emission arises from the accretion disk; the same continuum emission can be also absorbed and reprocessed by dust surrounding the nuclear region, and thus re-emitted in the IR (as described later in Section 1.1.1); furthermore, the UV photons from the accretion disk gain energy through inverse-Compton effect by the hot ($T \sim 10^{8-9}$ K) electron gas which constitutes the (putative) corona (see Section 1.1.2), thus producing the observed X-ray emission. Finally, γ -ray and (high flux density) radio objects, on the other hand, preferentially select AGN emitting strong non-thermal (jet [or associated lobe] related) radiation.

The multi-wavelength emission arising from AGN results in a proliferation classes and

types, which tend to classify the sources on the basis of their single-band properties [Padovani et al., 2017], rather than on a multi-band point of view. However, most of these seemingly different classes are due to changes in only a small number of parameters, namely orientation with respect the line-of-sight (see Fig. 1.3; e.g. Antonucci 1993; Urry and Padovani 1995; Netzer 2015), accretion rate (e.g. Heckman and Best 2014), the presence (or absence) of strong jets (e.g. Padovani et al. 2016), and possibly the host galaxy properties and the environment. For instance, the “type 1/type 2” classification strongly depends on the orientation along the line-of-sight. In type 2 sources (i.e. AGN with UV/optical spectra dimmed by obscuration and characterised only by narrow emission lines) our line-of-sight towards the nucleus is thought to be relatively close to the equatorial direction along which the torus obscuration becomes effective. Conversely, type 1 objects are believed to be rather face-on, allowing us to directly observe the primary emission from the accretion the AGN as well as to detect the broad component of optical emission lines, arising from the broad-line region (BLR).

The observation of the AGN emission in different wave-bands becomes a necessity in presence of heavy obscuration, when the UV/optical emission of the central engine and the broad line emission (e.g. Antonucci 1993; Netzer 2015) are largely suppressed by dust. The obscuration here essentially refers to the radiative absorption of UV/optical photons by dust grains in the torus, but a galactic-scale contribution to extinction cannot be ruled out, with significant evidences both in local low-luminosity AGN (LLAGN; Prieto et al. 2014) and high-redshift quasars ($z \sim 5$; Gilli et al. 2015). Furthermore, evidences for variable and/or clumpy obscuration have been observed in many objects (e.g., Risaliti et al. 2007; MacLeod et al. 2016), suggesting that the obscuring torus may consist of non-static clumped material surrounding the nucleus. Thanks to the pc-scale spatial resolution offered by ALMA, the emission from different tracers of the molecular gas has been observed from very compact region, co-spatial with the IR emission associated with the dusty torus (e.g., Combes et al. 2013; García-Burillo et al. 2014). The evidence that these structures (i.e., the dusty torus and molecular clumps) are on similar scales suggests that the dense gaseous and dusty structure is potentially the outer regions of the torus, while the inner boundary of the dust distribution are expected to be set by the sublimation temperature of the dust ($T \sim 1000-1800$ K, depending on the relative concentration of graphite and silicate), with the sublimation radius depending on the AGN luminosity $r_{sub} \propto L^{1/2}$ (e.g., Suganuma et al. 2006; Kishimoto et al. 2011; Hönig 2019). Nonetheless, it is not yet fully understood if, and how, the AGN accretion power can influence the physical extent of the torus (e.g., Sazonov et al. 2015; Lawrence and Elvis 2010). Therefore, in the case of obscuration, we cannot rely on the primary optical/UV emission (which can be totally suppressed by the dusty material along the

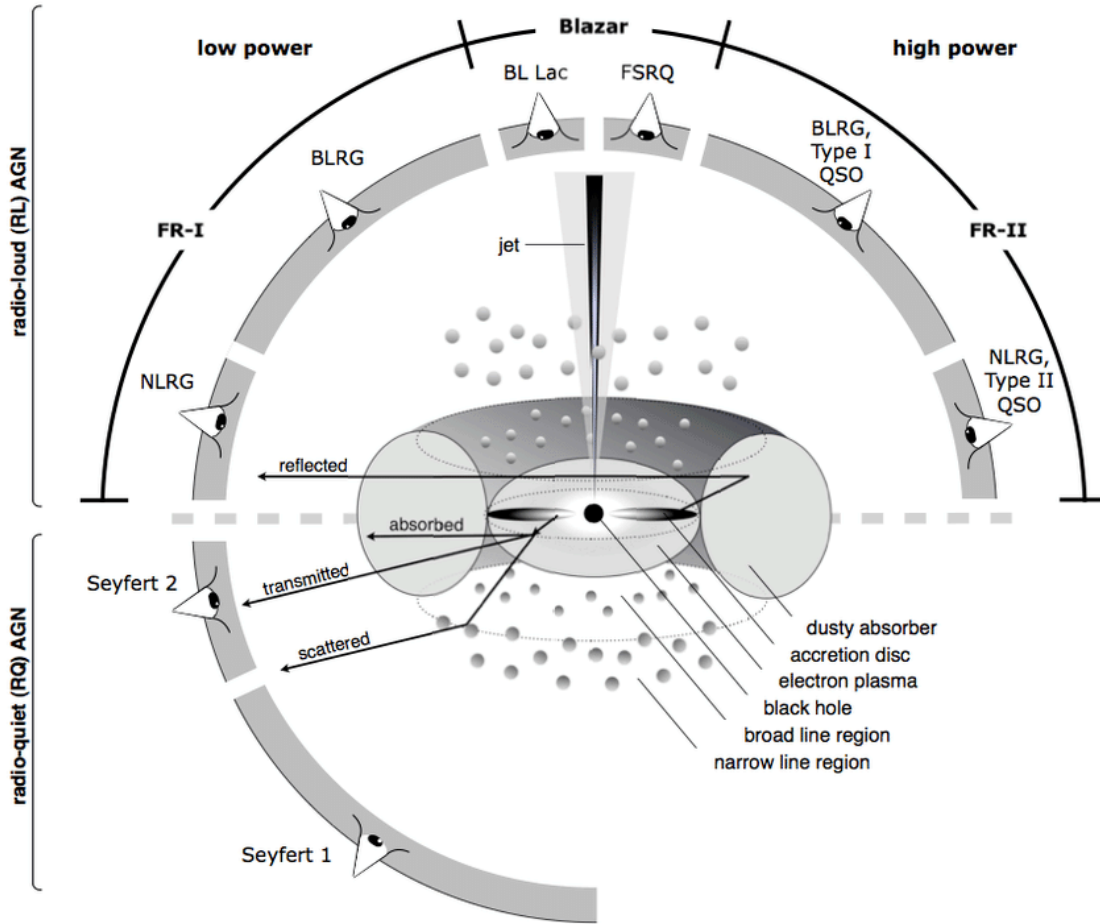


Figure 1.3: The standard AGN unification scheme. Depending on the orientation, an observer will see different emitting regions and thus, an intrinsically same objects would appear to him as a different type of AGN. Image credit: Beckmann and Shrader [2012].

line-of-sight) from the accretion disk to characterise the intrinsic power of the AGN, but rather on the emission at wavelength which are less affected by the extinction: namely IR and X-rays bands.

1.1.1 AGN emission in the IR

In luminous AGN ($L_{bol}^{AGN} > 10^{44}$ erg s $^{-1}$) the intrinsic mid-infrared (mid-IR) part of the spectrum is dominated by thermal radiation ($T \sim 200 - 800$ K) from the compact dusty torus [Ichikawa et al., 2017]. In particular, the rest-frame mid-IR flux (in particular, at 6 and 12 μ m) commonly considered as a good indicator of the intrinsic AGN continuum emission in both obscured and unobscured AGN. Indeed, both type 1 and type 2 objects emit a similar fraction of their bolometric AGN luminosity in the mid-IR, which suggest that the emission in the mid-IR regime is poorly affected by anisotropy issue (e.g.,

Spinoglio and Malkan 1989; Horst et al. 2008; Gandhi et al. 2009; Asmus et al. 2011; Hönig et al. 2011; Ramos Almeida et al. 2011; Asmus et al. 2014; Asmus et al. 2015). Unfortunately, in the case of low-luminosity AGN ($L_{bol}^{AGN} < 10^{44}$ erg s $^{-1}$) or strong starburst activity ($SFR > 100 M_{\odot} \text{ yr}^{-1}$) in the host galaxy, the mid-IR suffers contamination from the SF. Hence, by studying the mid-IR regime of the inner part of galaxies, we investigate both the SF and AGN activities, as well as on the amount of obscuration (e.g. Imanishi and Maloney 2003; Sturm et al. 2005; Imanishi et al. 2007; Hernán-Caballero and Hatziminaoglou 2011). Several components can be identify, namely the thermal dust continuum associated with SF, several spectral features from polycyclic aromatic hydrocarbon (PAH) molecules, and a plethora of line features arising from molecular, atomic, and ionic species (e.g., Spoon et al. 2007; Gallimore et al. 2010a; Tommasin et al. 2010; Gruppioni et al. 2016). Furthermore, the 9.7 μm silicate feature is characteristic of the mid-IR regime, and can appear in emission or absorption, providing insight into the geometry of the dust surrounding the central source (i.e., AGN or SF; e.g., Siebenmorgen et al. 2005; Shi et al. 2006) To properly disentangle the different contributions, the

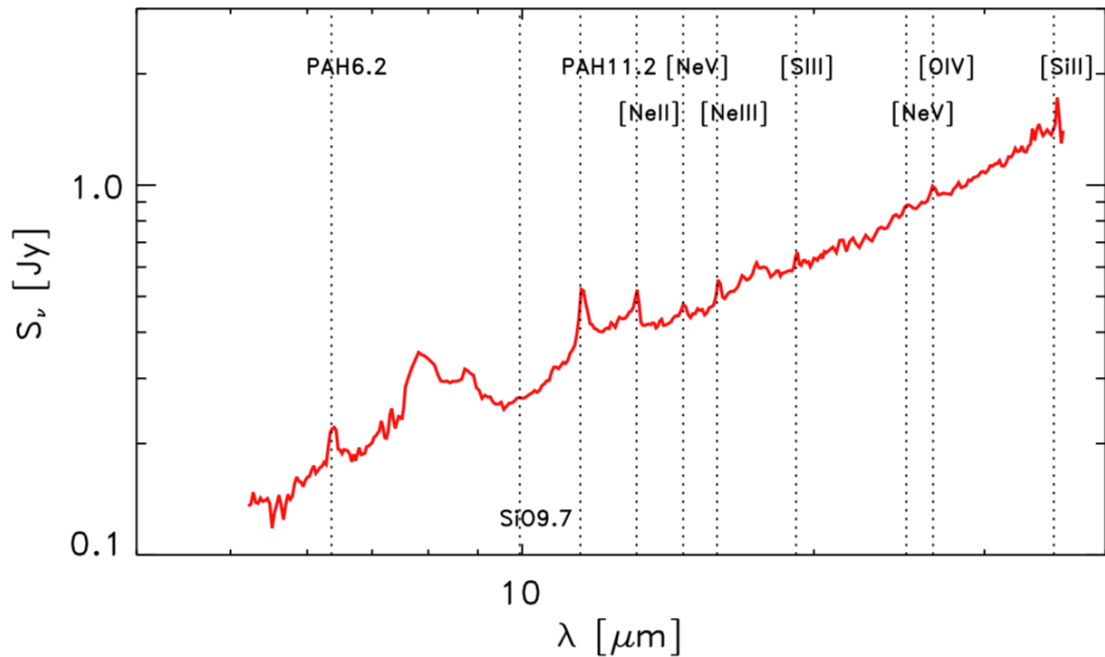


Figure 1.4: Spitzer IRS spectrum of a local Seyfert galaxy (NGC 5995). Wavelengths have been shifted to the galaxy rest frame. Several spectral features (e.g., PAH and silicate) and emission lines are indicated. Credits: Gruppioni et al. [2016].

advent of the *Spitzer* telescope¹, with its Infrared Spectrograph (IRS), revolutionized

¹The *Spitzer* Space Telescope consistd of a 0.85-meter diameter telescope and three cryogenically-cooled science instruments, able to perform imaging and spectroscopy in the 3-180 μm wavelength range. It was launched on August 25th, 2003. The instrumentation onboard, which was originally built to last for

our knowledge on the starburst and AGN phenomena and their connection, providing us a plethora of diagnostics crucial to disentangle the AGN-vs-SF activity in the nuclear regions. An example of a *Spitzer*-IRS spectrum for a local Seyfert 2 galaxy is presented in Fig. 1.4: several features can be identified, namely PAH features, widely used as a proxy of SF (e.g., Tran et al. 2001; Lutz et al. 2004; Alonso-Herrero et al. 2012; Ichikawa et al. 2014; Symeonidis et al. 2016); emission lines from ionised species, used for AGN-vs-SF diagnostics diagram (e.g., Tommasin et al. 2010; Gruppioni et al. 2016); the $9.7 \mu\text{m}$ silicate feature (which can account for a contribution from the host galaxy, depending on the inclination with respect to the line-of-sight; e.g., Goulding and Alexander 2009). By combining decomposition methods to mid-IR spectra and to broadband IR SEDs (e.g., Hatziminaoglou et al. 2008; da Cunha et al. 2008; Lyu et al. 2017; Shimizu et al. 2017) we can put constraints on the spectral emission of the AGN and the starburst (SB) component (e.g., Hernán-Caballero and Hatziminaoglou 2011; Gruppioni et al. 2016). To conclude, despite the precise estimation of AGN thermal activity is not straightforward in the case of low-luminosity AGN, several methods have been developed to derive the AGN output in the mid-IR regime, making the mid-IR band crucial to characterise the nuclear activity in the case of heavy extinction.

1.1.2 AGN emission in the X-rays

The X-ray emission (particularly at high X-ray energies, i.e. $E > 10 \text{ keV}$) is distinctive mark between AGN and non-AGN systems. What makes the study of the X-ray emission crucial to understand the physics of an AGN are the following reasons: (1) X-ray emission is directly associated with the accretion process onto the SMBH; (2) it appears to be (near) universal, even at the highest redshift ($z \sim 6 - 7$; e.g., Vignali et al. 2001; Vignali et al. 2005; Shemmer et al. 2006; Nanni et al. 2017; Shemmer et al. 2017; Salvestrini et al. 2019; Vito et al. 2020); (3) X-rays are able to penetrate through large column densities of gas and dust, letting us to probe the intrinsic emission even in the case of heavy extinction (see Fig. 1.5); (4) X-ray emission from host-galaxy processes are typically weaker when compared that due to the AGN [Brandt and Alexander, 2015]. The X-ray emission accounts for a fraction that ranges from few percent up to $\sim 10\%$ of the whole electromagnetic emission of an AGN (see Fig. 1.2; e.g., Lusso et al. 2012;

a minimum of 2.5 years but it lasted in the cold phase for over 5.5 years, consists of three main instruments: *i*) the InfraRed Array Camera (IRAC); *ii*) the InfraRed Spectrograph (IRS); *iii*) the Multiband Imaging Photometer for Spitzer (MIPS). IRAC was an IR camera (256×256 pixels) sensitive in four bands in the near and mid-IR (at $3.6, 5.8, 4.5$ e $8.0 \mu\text{m}$). IRS was a spectrograph providing moderate ($R \sim 600$) and low ($R \sim 60-130$) resolution spectral capabilities from 5.2 to $38 \mu\text{m}$. MIPS provided imaging and photometry in three broad spectral bands, centered nominally at $24, 70,$ and $160 \mu\text{m}$, and low-resolution ($R \sim 20$) spectroscopy between 55 and $95 \mu\text{m}$.

Duras et al. 2020). The primary process is thought to be inverse Compton scattering of the optical/UV accretion-disk photons to X-ray energies via the accretion-disk “corona”, which is generally depicted as an electron “atmosphere” above the inner accretion disk. The spatial distribution and the geometry of the corona are widely debated (e.g., Chartas et al. 2016; Chartas et al. 2017), however the observed variability on short timescales suggests that the hot corona resides in the innermost region of the AGN (within few tens of R_s^2 ; see Kara et al. 2013; Wilkins et al. 2014; Chartas et al. 2016).

The causal relation between the intrinsic X-ray emission from the “corona” and the optical/UV accretion-disk emission has been widely investigated (parameterised by the X-ray-to-optical luminosity ratio, α_{OX} ; e.g. Avni and Tananbaum 1986; Steffen et al. 2006; Lusso et al. 2010; Lusso and Risaliti 2016) for almost all systems, demonstrating that this relationship and, hence the X-ray emission from AGN, are universal (e.g., Salvestrini et al. 2019; Vito et al. 2020).

The spectrum is a power-law resulting from the superposition of many scattering orders of the intrinsic black body:

$$F_E = E^{-\Gamma_X} \quad (1.2)$$

where Γ_X is the photon index; it shows a high energy cut-off at $E \sim 100 - 300$ keV (e.g., Lanzuisi et al. 2019 and reference therein), corresponding to the temperature at which electrons and photons are thermalized. In addition, the inner regions of the accretion disk can contribute with a thermal emission at the lowest X-ray energies ($E < 2$ keV; e.g. Sobolewska et al. 2004), which is likely due to a warm Comptonization of the primary continuum emission (e.g., Ursini et al. 2016; Petrucci et al. 2018; Petrucci et al. 2020).

The X-ray emission is then modified due to the interaction with matter in the nuclear region (e.g. reflection, scattering, and photo-electric absorption of photons from the accretion disk and/or the obscuring AGN torus). The relative strength of these components can vary quite significantly from source to source, mostly due to differences in the geometry and inclination angle of the torus to the line-of-sight, leading to a broad range of X-ray spectral shapes. A baseline model for the X-ray spectrum of an AGN where the primary emission interacts with the surrounding material is presented in Fig. 1.6.

The prominent components arising from the interaction of the primary emission with surrounding medium are:

- soft excess: its origin its not fully understood [Done et al., 2002]. It is supposed to be emitted either by a hot diffuse gas or by the warm Comptonization of the primary continuum emission component in the inner accretion disk mentioned above (e.g., Petrucci et al. 2020 and reference therein).

²The Schwarzschild radius for a mass M is defined as $R_s = \frac{2GM}{c^2}$, where G is the Universal Gravitational constant.

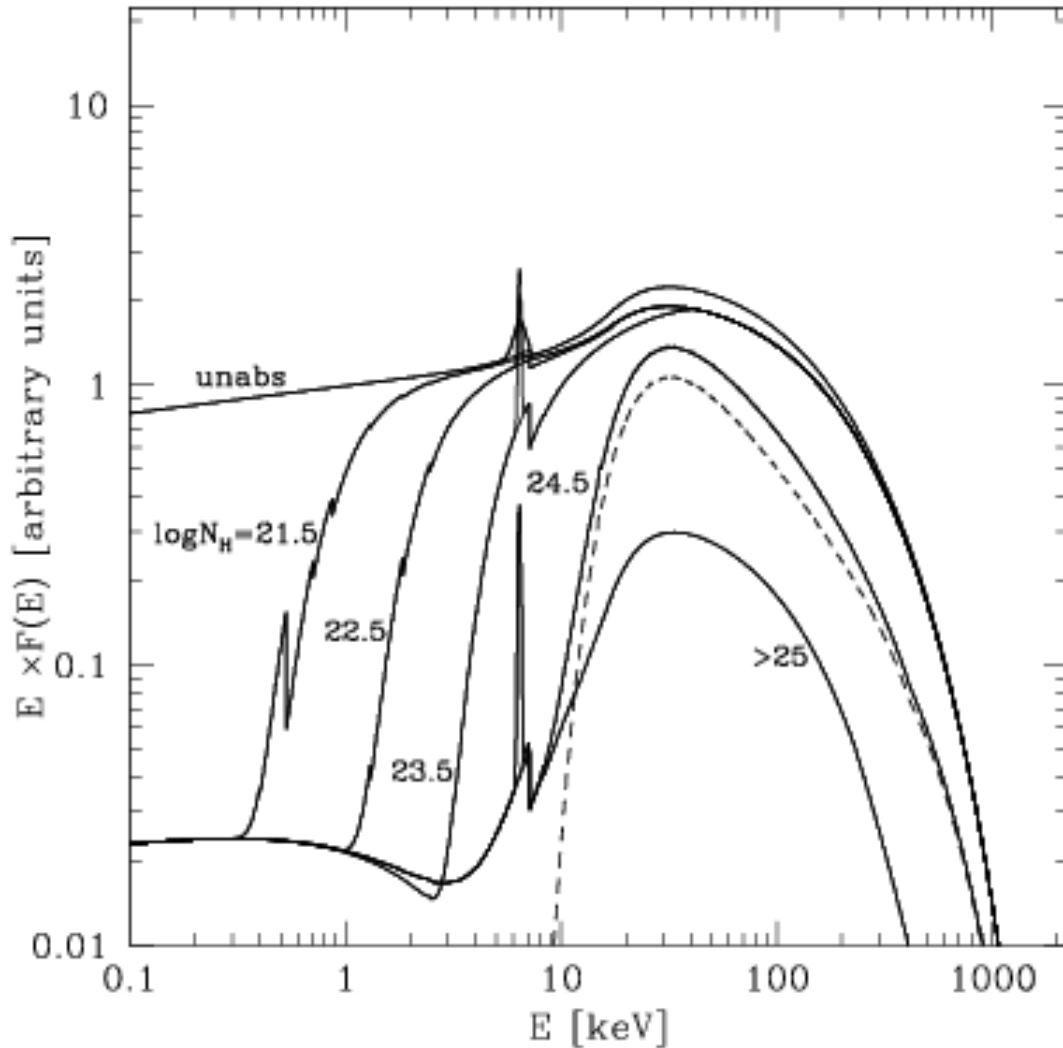


Figure 1.5: AGN X-ray spectra with different column densities assumed in the model. Solid lines from top to bottom: $N_H = 20 \text{ cm}^{-2}$ (i.e. unabsorbed AGN), $\log(N_H) = 21.5, 22.5, 23.5, 24.5, > 25$. A primary powerlaw with $\Gamma_X = 1.9$ and cut off energy $E_c = 200 \text{ keV}$ is assumed. A 3% soft scattered component is also added in the obscured AGN spectra. The spectrum of mildly Compton-thick AGN ($\log(N_H) = 24.5$) is obtained by summing a transmission component (dashed line) to the same reflection continuum used to model the spectrum of heavily ($\log(N_H) > 25$) Compton-thick AGN. In each spectrum a 6.4 keV iron emission line is also included. This image is adapted from Gilli et al. [2006].

- Warm absorber: soft X-rays are absorbed by warm ionised gas (having column density $N_H \sim \text{afew} 10^{21} \text{ cm}^{-2}$). This component is present in $\sim 50\%$ of the sources [Piconcelli et al., 2004]. In some cases the absorption lines are blueshifted with respect to the optical emission lines, indicating that the absorbing gas is part of a “wind” outflowing from an accretion disk, with velocities up to $\sim 1000 \text{ km/s}$;

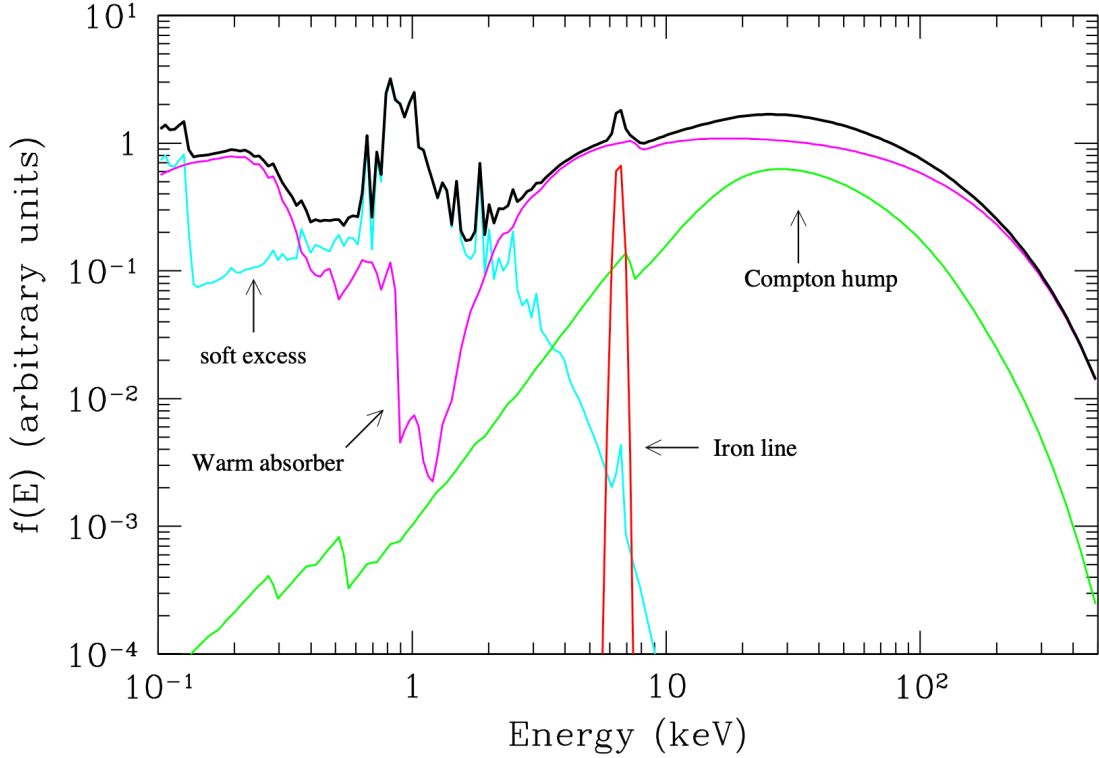


Figure 1.6: Average total spectrum (thick black line) and main components (thin grey lines) in the X-ray spectrum of a Type I AGN. The main primary continuum component is a power law with an high energy cut-off at $E \sim 100\text{--}300$ keV, absorbed at soft energies by warm gas with $N_H \sim 10^{21} - 10^{23} \text{ cm}^{-2}$. A cold reflection component is also shown. The most relevant narrow feature is the iron $K\alpha$ emission line at 6.4 keV. Finally, a “soft excess” is shown, due to thermal emission of a Compton thin plasma with temperature $kT \sim 0.1 - 1$ keV. This figure is taken from Risaliti and Elvis [2004].

- Reflection hump: a fraction of the X-ray primary emission can be Compton scattered by the circumnuclear gas (if the gas column density is sufficient, e.g. $N_H > 10^{24} \text{ cm}^{-2}$), peaking at $E \sim 30$ keV.
- Iron (Fe) fluorescence emission lines: the more prominent Fe feature is the $K\alpha$ 6.4 keV, produced by neutral or lowly ionized iron through fluorescence [Fabian et al., 2000] in the accretion disk, the BLR and/or the dusty torus. If the Fe $K\alpha$ is emitted in the innermost layers of the accretion disk, it will be affected by relativistic effects due to the presence of the black hole, in addition to the classic Doppler effect given by the disk rotation [Fabian et al., 2000]. The sum of classic and relativistic transverse Doppler effect results in a red-shifted double-peaked broadened line profile. The Fe $K\beta$ at 7.06 keV is usually observed with a fixed intensity-ratio with respect the $K\alpha$ ($\sim 1:8$ vs. $K\alpha$). Moreover, the Fe XXV/XXVI emission (at

rest-frame 6.637 and 6.966 keV, respectively) have been widely observed and interpreted as the ionized signature of a hot, optically thin plasma.

- Scattered component: a few % of the primary emission can be reflected by hot electrons filling the cone of the torus, producing a scattered power-law with a slope similar to the primary emission [Brightman et al., 2014].

In the case of obscured (type 2) AGN, heavy obscuration from the dusty torus, parametrised with the hydrogen column density (N_H), may significantly suppress the primary emission as seen along the line-of-sight (see Fig. 1.5). The so-called ‘‘Compton-thick’’ regime ($N_H > 1.5 \times 10^{24} \text{ cm}^{-2}$) is the furthest case, where the primary X-ray emission at energies below 10 keV can be almost entirely absorbed. Then, to unveil the intrinsic power of a deeply obscured AGN we need to account on observations at the highest X-ray energies, as those provided by the Nuclear Spectroscopic Telescope Array (*NuSTAR*; Harrison et al. 2013), which represent a well suited tool for this kind of investigation, with its in the . The exploitation of the focusing power by *NuSTAR* over a wide energy band (nominally $\sim 3\text{--}79$ keV) allows us to modelling the spectral shape of the AGN emission in the X-rays. Then, combining *NuSTAR* with the higher spectral resolution from the telescope sensitive at energies below 10 keV (e.g., *Chandra*, *XMM-Newton*, *Suzaku*), we are able to put constraints on the level of obscuration, which is more effective at $E < 10\text{keV}$. This has led to a spread of complex models which attempt to coherently reproduce all the components of the X-ray spectrum. The continuous distribution of obscuring material is modelled into a toroidal shape (see Fig. 1.7), with various opening angles (θ_{tor}), inclination with respect the line-of-sigh, and, in particular, within a wide range of extinction ($\log(N_H) \sim 22\text{--}25$). New models (e.g., MyTorus, Murphy and Yaqoob 2009; borus02, Baloković et al. 2018), which are usually referred to as ‘‘physical’’ models to differentiate them from the so-called ‘‘phenomenological’’ ones, and have been widely used in the recent years (e.g., Marchesi et al. 2017; Marchesi et al. 2018; Kammoun et al. 2019). While ‘‘phenomenological’’ models aim at reproducing separately the different spectral components (e.g., the primary power-law, the reflection hump, the emission lines), ‘‘physical’’ ones provide a more complete and physical modelling of the obscuring material which goes under the name of torus. Good agreement have been found when comparing the modelling of the AGN spectral shape and the level of obscuration obtained with different ‘‘phenomenological’’ and ‘‘physical’’ models (e.g., Liu and Li 2015). A growing number of models appear in recent years, proposing for the dusty torus a structure more dynamic than that originally postulated in the unified AGN model; for instance, replacing the smooth distribution of obscuring material with a potential clumpy structure [Buchner et al., 2019]. Indeed, signatures of clumpy structure of the torus have been

observed over the years, both in the X-ray and at longer wavelengths (e.g., Hickox and Alexander 2018 and references therein). For instance, heavily obscured Seyfert galaxies in the local Universe show complex spectra, which require the presence of torus regions with different densities of the obscuring material to reproduce all the spectral components (i.e., transmitted and reflected; e.g., Marchesi et al. 2019).

Recently, the results of the simultaneously fit of X-ray and mid-IR torus models were presented in single-object studies (e.g., Esparza-Arredondo et al. 2019), with the goal of achieving a coherent reprocessing of the primary AGN emission from the torus and the surrounding material. This is supported by the tight correlation that exists between the unresolved mid-IR core and the absorption-corrected X-ray luminosities of nearby AGN, even in the presence of extreme Compton-thick objects ($N_H > 1.5 \times 10^{24}$; e.g., Lutz et al. 2004). By systematically applying the combined analysis in the X-rays and the mid-IR band to large sample of galaxies, we will be able to understand the properties and distribution of obscuring matter, across different bands.

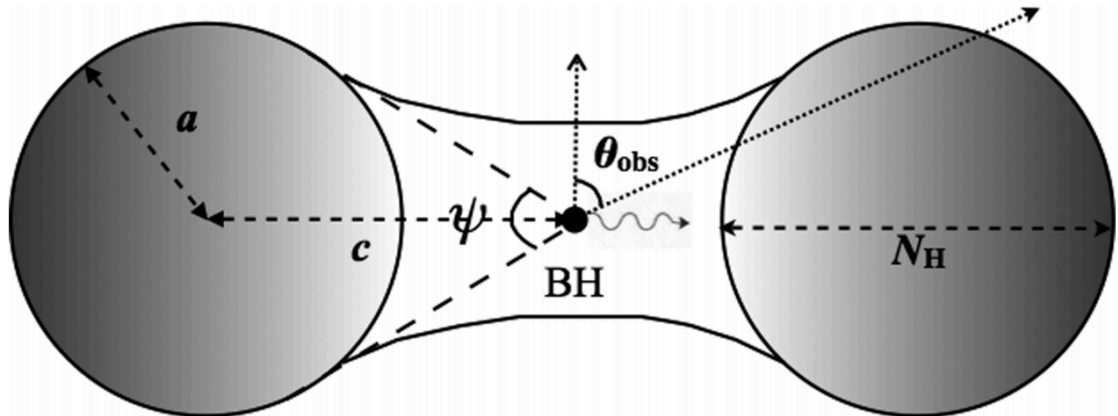


Figure 1.7: Assumed model geometry of the torus in the MyTorus code. The half-opening angle is given by $(\pi - \psi)/2$ and the inclination angle of the observer’s line-of-sight with the symmetry axis of the torus is given by θ_{obs} . MyTorus does not allow to vary the torus opening angle. The equatorial column density, N_H , of the torus is defined by the diameter of the tube of the “doughnut”. Credits: Murphy and Yaqoob [2009]

To conclude, since the X-ray emission in AGN is directly associated with the accretion process, its study is crucial to understand the physics of AGN, especially in the case of heavy obscuration, down to few gravitational radii. This allows us to probe the innermost region of AGN, where accretion takes place, which is difficult to reach with observations at longer wavelengths.

1.2 Interstellar medium

ISM has been recognised to be distributed in diverse, but well-defined phases according to the chemical state of hydrogen³ (i.e. ionised, neutral or molecular), that distinguish themselves for different temperatures, densities and ionisation states. Here, the term “phases” is used to denote components that may exist in thermal pressure equilibrium [Hollenbach and Tielens, 1999]. The interplay between the different phases is complex, and is driven by the balance of radiative cooling with heating through the transfer of kinetic energy to atoms, molecules and ions, mainly due to radiation from stars and AGN, cosmic-rays, X-rays photons and shocks.

1.2.1 Neutral medium

Most of the mass of the ISM is in neutral or “non-ionised” regions, either neutral atomic (HI) medium or gravitationally bound molecular (H₂) clouds (optically thick⁴, where star formation occurs), although they are responsible for the filling of only $\sim 1 - 2\%$ of the total volume of the ISM (Klessen and Glover 2016 and references therein). Two phases of the neutral atomic hydrogen have been distinguished in the diffuse medium: (a) the warm $T \sim 8 \times 10^3$ K neutral medium (WNM), and (b) the cool $T \sim 100$ K neutral medium (CNM) [Tacconi et al., 2020]. Most of the CNM is in discrete clumps known as HI clouds, with typical properties that varies broadly, namely number densities in the range from 10 to 100 cm⁻³, representative cloud temperature of 50-80 K, and diameters range from 1 to 100 pc. The WNM and CNM can coexist for a narrow range of thermal pressures (which depend on several parameters, e.g. heating rates, the gas-phase metallicities and

³Hydrogen (H) and helium (He) are the more abundant atomic species ($\sim 70\%$ and $\sim 28\%$ of the total mass, respectively), while all other elements, referred to as metals (Z), account for the remaining $\sim 2\%$ [Maiolino and Mannucci, 2019]. The primordial nucleosynthesis is thought to be responsible for the origin of the primordial hydrogen, deuterium, the majority of helium and a small fraction of lithium (e.g. Cyburt et al. 2016), while most of the heavy elements produced by stellar nucleosynthesis or by the explosive events (e.g., supernovae) related to the late stages of stellar evolution (e.g. Maiolino and Mannucci 2019).

⁴A medium is said to be *optically thick* if on average a photon cannot pass through the medium without absorption. If the optical depth is defined as $\tau = \ln(\frac{\phi_i}{\phi_t})$, where ϕ_i and ϕ_t are the radiant flux incident onto and transmitted by the material, an optically thick medium has $\tau_{CO} = 1$.

dust abundances), with an envelop of WNM embedding the CNM condensations (e.g., Warren et al. 2012; Stanimirović et al. 2014; Tacconi et al. 2020).

1.2.1.1 From atomic to molecular phase

In dense, optically thick clouds, the atomic-to-molecular (HI-to-H₂) transition can occur, with the balance between H₂ formation on the surfaces of dust grains and H₂ destruction by far-UV photodissociation. In photo-dissociation regions (PDRs, see Hollenbach and Tielens 1999 for a review), the far-UV ($6 \text{ eV} < h\nu < 13.6 \text{ eV}$) radiation from strong stellar sources (e.g. massive O, B stars) is responsible for the ionisation of H and other atomic species (e.g. carbon, C) with ionization potentials below 13.6 eV. As shown in Fig. 1.8, PDRs are the regions defined on the one side by an ionisation front and on the other by their surface, where the hydrogen is 50% atomic and 50% molecular [Hollenbach and Tielens, 1999]. Completely analogous to photo-dissociation regions, X-ray dissociation regions (XDRs) can be defined as predominantly neutral gas in which X-rays (for instance, from an AGN) dominate the chemistry and/or the heating (e.g., Maloney et al. 1996).

1.2.2 Molecular gas

Giant molecular clouds (GMCs) are the massive ($M \sim 10^4 - 10^{6.5} M_{\odot}$), dense ($n_{H_2} \sim 10^2 - 10^5 \text{ cm}^{-3}$) and cold ($T \sim 10\text{-}40 \text{ K}$) regions where the most of the molecular gas reside (e.g., McKee and Ostriker 2007; Kennicutt and Evans 2012). Molecular hydrogen, H₂, is the most common molecule in galaxies, and its mass dominates over the other molecular species. Given the lack of a permanent dipole moment, the lowest roto-vibrational transitions of molecular hydrogen are forbidden and have high-excitation requirements ($T_{ex} > 500 \text{ K}$ above the ground, significantly higher than the typical kinetic temperatures in GMCs, $T_{kin} \sim 15 - 100 \text{ K}$). The first accessible rotational transitions for the H₂ are those with $\Delta J = 2$ (i.e. $J + 2 \rightarrow J$, where J is the rotational quantum number), which corresponds to emission lines in the near-/mid-IR regime (e.g. $J = 2\text{-}0$, $\lambda = 28.22\mu\text{m}$; $J = 3\text{-}1$, $\lambda = 17.04\mu\text{m}$; ... $J = 10\text{-}8$, $\lambda = 5.05\mu\text{m}$). However, this traces only gas strongly heated by intense irradiation or shock waves, which is not the case for most of the H₂ in galaxies. For this reason we need to rely on different diagnostics to trace the molecular phase in its entirety, including the cold component, which is responsible for the formation of new stars.

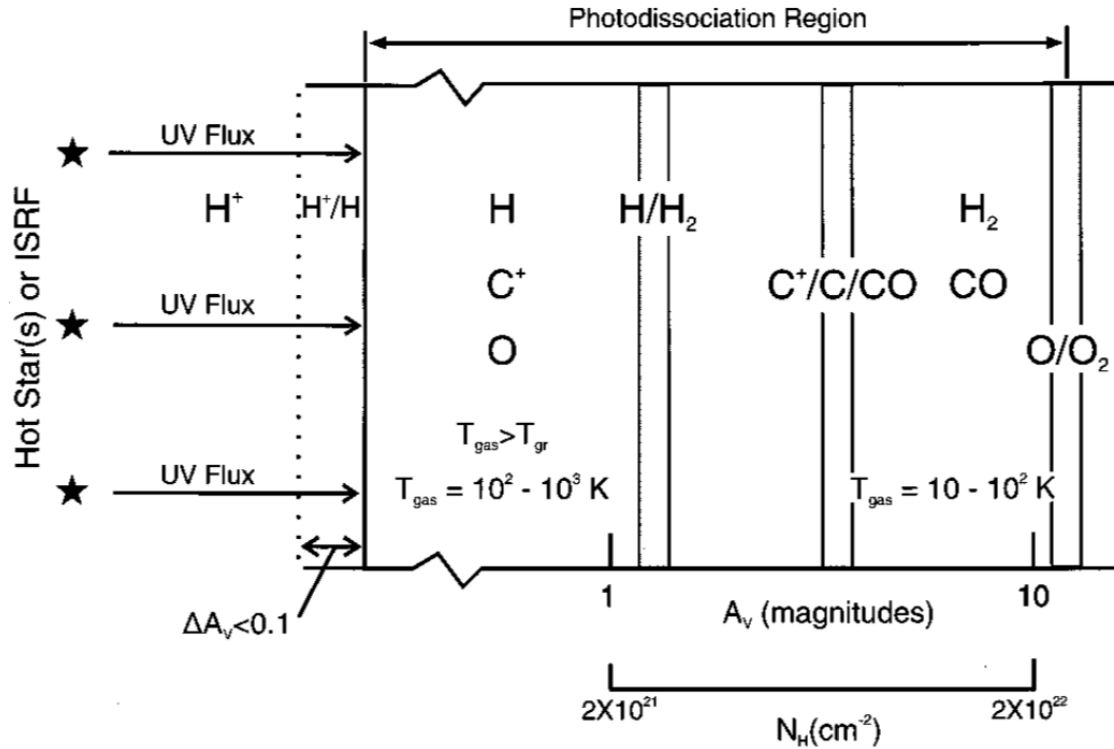


Figure 1.8: A schematic diagram of a photo-dissociation region. The PDR is illuminated from the left and extends from the predominantly atomic surface region to the point where O_2 is not appreciably photo-dissociated (with total extinction $A_V \sim 10$). Hence the PDR includes gas whose hydrogen is mainly H_2 and whose carbon is mostly CO . Large columns of warm O , C , C^+ , and CO , and vibrationally excited H_2 are produced in the PDR. Credits: Hollenbach and Tielens [1999].

1.2.2.1 Molecular gas diagnostics

A plethora of molecular rotational lines have been used to study the physical conditions of the molecular phase of the ISM (e.g., García-Burillo et al. 2014; Aalto et al. 2015; Liu et al. 2015). In particular, the carbon monoxide (^{12}CO), the second most abundant molecule after H_2 in the Universe, is the most used tracer (e.g., Young and Scoville 1991; McKee and Ostriker 2007; Carilli and Walter 2013). The low critical densities ($n \sim 10^3 \text{ cm}^{-3}$ for $J:1 \rightarrow 0$, rising up to $n \sim 10^6 \text{ cm}^{-3}$ for $J:13 \rightarrow 12$) for the lower rotational transitions make them perfect tracers of the cold diffuse component ($T \sim 10 - 20 \text{ K}$), given their low-excitation potentials. In particular, the $CO(1-0)$ results the most sensitive to the total gas reservoir; this transition occurs ($\lambda \sim 2.6 \text{ mm}$ or $\nu \sim 115.3 \text{ GHz}$) in the sub-millimetre/millimetre band, which is characterised by high atmospheric transmission. Thus, in the past thirty years, several surveys have been aimed at mapping the molecular gas in the nearby Universe, by exploiting ground-based telescopes (both single dish antennas and interferometers) to measure the emission from low- J CO transitions (e.g., Young and Scoville 1991; Young et al. 1995; Maiolino et al. 1997; Albrecht et al. 2007).

Then, the Herschel satellite extended the CO detections to high transitions levels also in the local Universe, using both the PACS (covering the 50-210 μm band) and SPIRE/FTS (sensitive to the 194-318 and 294-671 μm bands) spectrometers (e.g., van der Werf et al. 2010; Pereira-Santaella et al. 2013; Mashian et al. 2015; Rosenberg et al. 2015)

At higher-J ($J_{\text{upp}} \gtrsim 6$, i.e. $\lambda \lesssim 0.4$ mm or $\nu \gtrsim 691$ GHz), CO transitions are better suited to trace the warmer gas, where the collisional excitation (especially with H_2 ; Narayanan and Krumholz 2014) is favoured. With increasing J, higher densities are required to favour collisions. This means that these transitions are preferred to trace warmer and denser

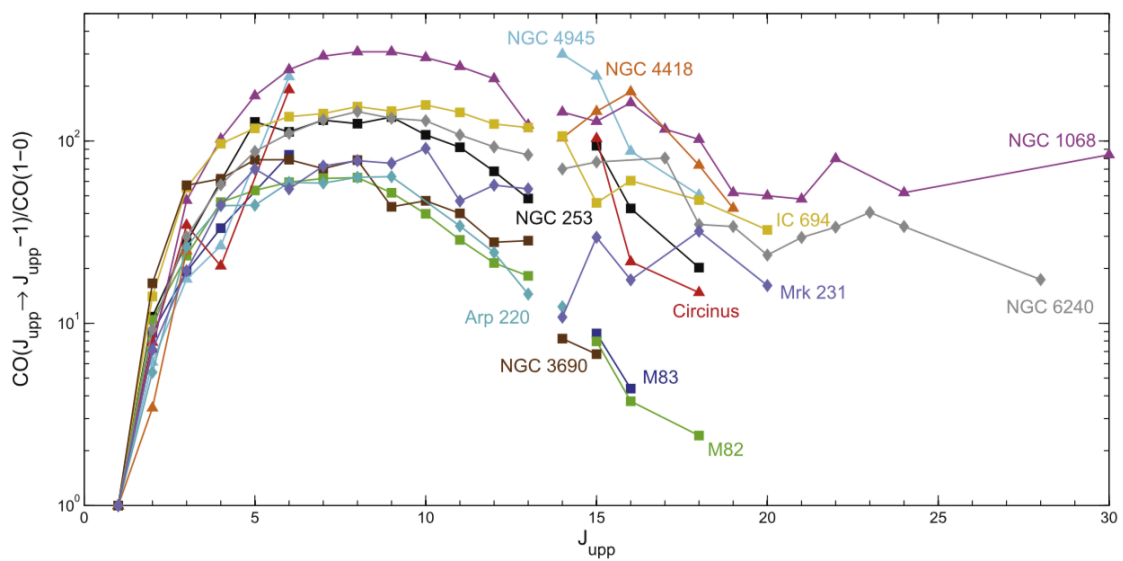


Figure 1.9: CO SLEDs for local galaxies. Starbursts, Seyfert galaxies, and (U)LIRGs are denoted with squares, triangles, and diamonds, respectively. Aperture-corrected fluxes have been normalized with respect to the CO(1-0) flux measurement. This figure is adapted from Mashian et al. [2015].

molecular gas in the center of galaxies. Several studies have been aimed at inferring the driving excitation mechanism for the molecular gas (SF, AGN, shocks) through the modelling of the CO spectral line energy distribution (CO-SLED) in nearby galaxies (see Fig. 1.9; e.g., Pereira-Santaella et al. 2014; Mashian et al. 2015; Rosenberg et al. 2015; Pozzi et al. 2017; Mingozzi et al. 2018), by exploiting the plethora of theoretical models (e.g., Usero et al. 2004; Meijerink and Spaans 2005; Meijerink et al. 2007; Proga et al. 2014; Vallini et al. 2019). SF on its own is unlikely to provide the intense radiation field to excite the ISM at such high Js, hence the presence of shocks or higher-energy photons (X-rays from XDR; e.g., Krolik and Kallman 1983; Lepp and Dalgarno 1996; Maloney et al. 1996) is required. For instance, looking at in Fig. 1.10, it is clear that the contribution from the AGN (in terms of XDR, which requires estimates of the X-ray emission from the nucleus to be modelled) is necessary to reproduce the shape of the

CO-SLED at the the highest J (i.e., $J_{up} \gtrsim 5$, corresponding to $\nu \gtrsim 576.3$ GHz), where the SF (PDR) does not provide enough energies (e.g., Pozzi et al. 2017; Mingozzi et al. 2018). Thus, modelling the CO-SLED, in particular including the high- J regime, allow us to constrain the relative impact of the AGN-vs-SF on the molecular component.

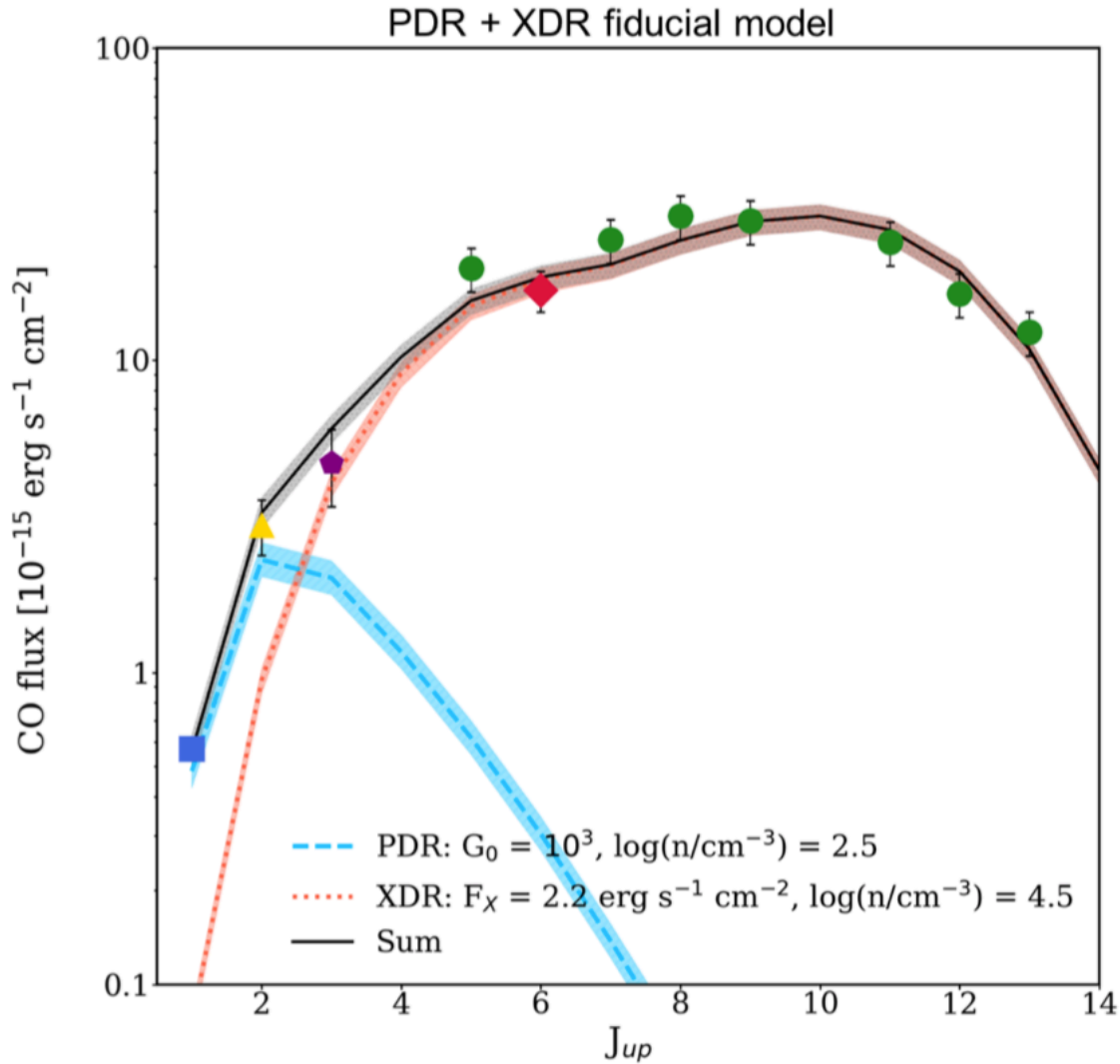


Figure 1.10: Fiducial model (PDR+XDR), overplotted to the observed data for NGC 0034, a local Seyfert 2 galaxy. The light-blue dashed line and the red dotted line represent the low-density PDR and the high-density XDR, respectively. The black solid line indicates the sum of the two components and the shaded areas indicate the $\pm 1\sigma$ uncertainty range on the normalisation of each component. The synergy with X-ray observations is necessary to model the high-energy radiation field (XDR), as likely produced by the AGN. This figure is adapted from Mingozzi et al. [2018].

Moreover, lines ratios of high-density tracers such HCN and HCO $^+$ have been used to infer the relative contribution from XDR, PDR and shocks in nearby galaxies, by exploiting the spatial resolution provided by interferometric facilities, resolving the

nuclear region down to the size of the giant molecular clouds (~ 50 pc), hence directly probing the region where the contribution from the AGN is dominant (e.g., Imanishi et al. 2016; Aalto et al. 2017; Imanishi et al. 2018; Imanishi et al. 2019).

Finally, many more tracers of the molecular gas have been used over the years, with various physical properties (e.g., the critical density) that make them suitable to trace the different physical states of the gas. For instance, in several studies SiO and HNC have been identified as good tracers for shock-heated material (e.g., Aalto 2015; Miyamoto et al. 2017; Imanishi et al. 2018), which can contribute also to the high-J end of the CO-SLED (e.g., Popping et al. 2016; Godard et al. 2019).

1.2.2.2 Molecular gas kinematics

In the last few years, the advent of the Atacama Large Millimeter Array (ALMA), as well as the NOthern Extended Millimeter Array (NOEMA, i.e. the newly implemented version of the Plateau de Bure Interferometer, PdBI) represented a breakthrough for the submillimetre/millimetre investigation of the ISM. In particular, these facilities allowed us to trace a plethora of molecular gas diagnostics both in the local Universe (e.g., Aalto et al. 2015; Sliwa et al. 2017; Henkel et al. 2018; Imanishi et al. 2018), and in high-redshift galaxies (where also atomic species can be observed; e.g., Carilli and Walter 2013; Combes 2018). Moreover, the sensitivity and the even more important high spatial resolution of the new interferometric facilities (up to $0.015''$ with the more extended configurations; e.g., Imanishi et al. 2020 and Klitsch et al. 2019 for an example at low and high redshift, respectively) supplied crucial information on the modelling of the physical conditions of the molecular gas at the spatial scales of the GMC (30-50 pc).

By exploiting such resolving power, in the recent years several studies have been dedicated to understanding the feeding and feedback processes that regulate the interaction between the central accreting SMBH and the host galaxy, both in the local Universe (e.g., Combes et al. 2013; Aalto et al. 2012; Morganti et al. 2015; Fluetsch et al. 2019), and at higher redshift ($z \sim 1 - 3$; Ciccone et al. 2014; Talia et al. 2018). In this context, a key role is played by the molecular gas, the major component of the ISM in the nuclear region of galaxies, where it acts as gas reservoir for both the SF and, potentially, the accretion material for the central SMBH. Hence, by resolving the molecular gas kinematics down to the sub-kpc scale, we may reveal the role of this ISM components in the central region of active galaxies, as done in some recent studies (e.g., Combes et al. 2013; Sabatini et al. 2018).

Furthermore, AGN are thought to be regulating the star formation in their hosts via the process known as feedback, which comprises the different interactions that transfer energy

and matter from the central SMBH to the interstellar medium (ISM; Cresci and Maiolino 2018 and references therein)). AGN feedback has been observed classified in two main categories, “radiative” mode and “kinetic” mode. In the former case, the radiation from the AGN can heat and expel most of the gas in the ISM, to eventually quench further star formation episodes; in the latter mode relativistic jets are launched by the central engine, delivering their kinetic energy as they collide with the ISM (e.g., Harrison 2017; Morganti 2017). By combining the molecular gas maps, obtained with ALMA, with multi-wavelength images tracing the ionised components of the ISM, associated with shocked material, we are able to identify the signature of potential multi-phase outflows (e.g., Cicone et al. 2018; Fluetsch et al. 2019; Fernández-Ontiveros et al. 2020) For instance, in Fig. 1.11 a multi-phase outflow of a local Seyfert galaxy (ESO 420-G13) is presented (see relevant caption for details). In this particular case, on the basis of its structure, energy and momentum balance, the molecular outflow was interpreted by the authors as a jet-driven wind powered by mechanical energy input from the AGN. Thus, ESO 420-G13 resulted on of the first local objects in which the presence of a previously unknown AGN-powered jet is revealed through its interaction with the ISM, proving the role of the investigation of the molecular gas properties with interferometric facilities. Furthermore, the high spatial resolution provided by ALMA allowed to put constrain on the molecular envelope surrounding the nuclear region in nearby objects (e.g., García-Burillo et al. 2014). For instance, this cold molecular structure was found to be co-spatial to the dense dust core, the so-called “torus”, traced by the sub-millimeter continuum emission, in a local Seyfert galaxy (NGC 1068), thus proving for the first time the dusty molecular composition for the “torus” (see Fig. 1.12 and relevant caption for details).

1.2.2.3 Molecular gas mass

Observations of GMCs in the Milky Way and nearby galaxies have established that the integrated flux of ^{12}CO millimeter rotational lines can be used to infer molecular gas masses ([Young and Scoville, 1991]; Bolatto et al. 2013), although the CO molecule makes up only a small fraction of the entire gas mass.

Low-J rotational lines (1-0, 2-1, 3-2) are almost always optically thick (i. e. a photon is absorbed and reradiated many times before reaching the surface) then its brightness temperature depends on the temperature of the optically thick surface ($\tau_{\text{CO}} = 1$; e.g., Dickman et al. 1986; Solomon et al. 1987; Bolatto et al. 2013), not the column density of the gas. In a virialised body, as in the case of a molecular cloud, the mass and the velocity dispersion are directly related. So, in the case of an emitting gas, the information about the mass of the body are then conveyed through the width of the line (the CO, for the molecular gas), which reflects the velocity dispersion. Therefore, the low-J CO emission

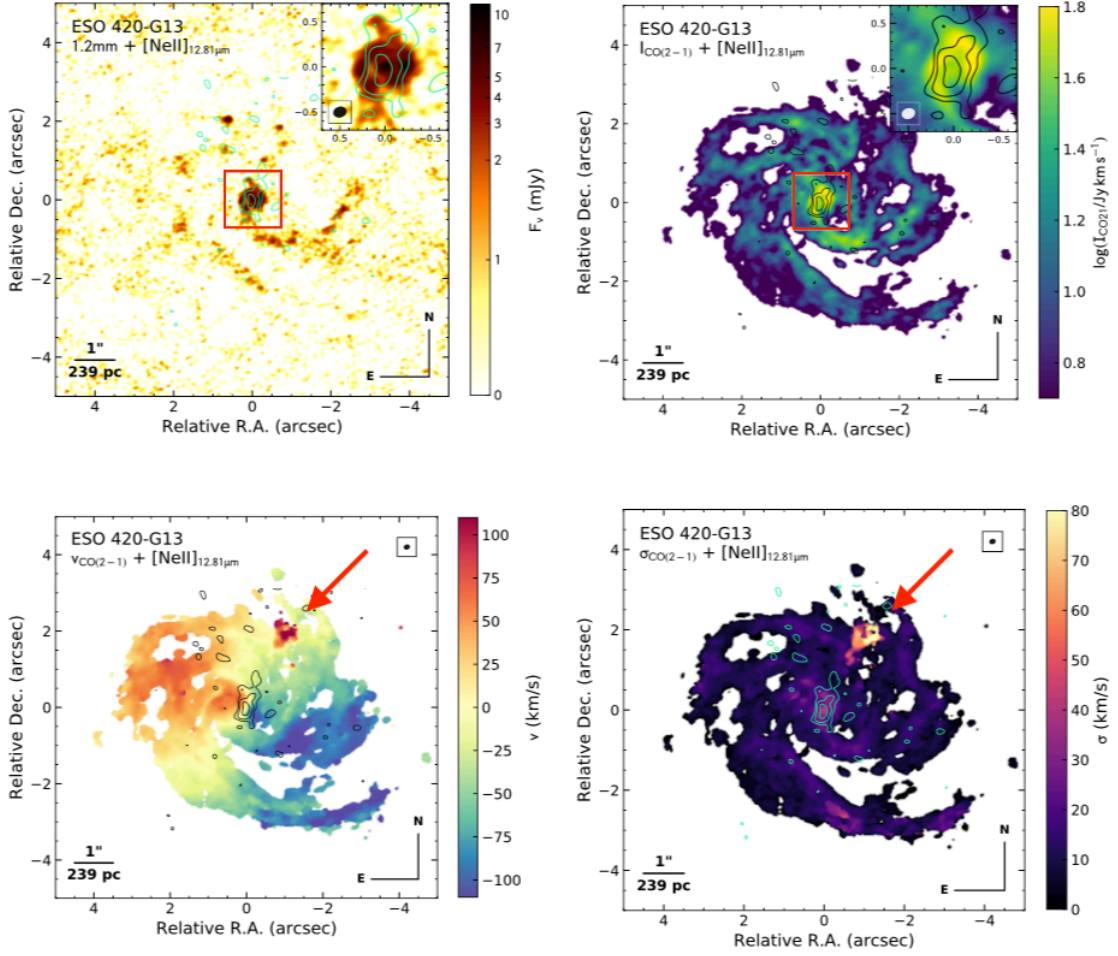


Figure 1.11: ALMA maps for the 1.2 mm continuum (upper left), CO(2-1) intensity (upper right), CO(2-1) average velocity (lower left), and CO(2-1) average velocity dispersion (lower right) maps for the Seyfert 2 galaxy ESO 420-G13. The zoomed insets in the upper left and right panels correspond to the red square regions indicated in the corresponding maps. Contours in all panels correspond to the [Ne II]12.8 μ m line emission from VLT/VISIR (starting from $3\times r_{\text{ms}}$ with a spacing of $\times 10^{N/4}$). Assuming trailing spiral arms implies that the South-East extreme of the kinematic minor axis is the nearest point to us. The synthesised beam size is shown in the inset panels and in the upper-right corner of the lower maps. A red arrow points to the position of the multi-phase outflows in the bottom row panels (velocity and velocity dispersion map, respectively), with the molecular wind being detected rather far from the AGN (at a projected distance of ~ 340 pc), with the warmer ionised gas component traced by the [Ne II] at 12.8 μ m emission at closer distances down to the nucleus. This figure is adapted from Fernández-Ontiveros et al. [2020].

line are useful to trace the total H₂ contained in a molecular cloud, as well as in any gravitationally bound ensemble of clouds, such as an entire galaxy.

The molecular gas mass is thereby proportional to the overall CO emission, which can be expressed in terms of line luminosity (L'_{CO} ; Carilli and Walter 2013):

$$L'_{\text{line}} = 3.25 \times 10^7 \times S_{\text{line}} \Delta v \frac{D_L^2}{(1+z)v_{\text{rest}}^2}, \quad (1.3)$$

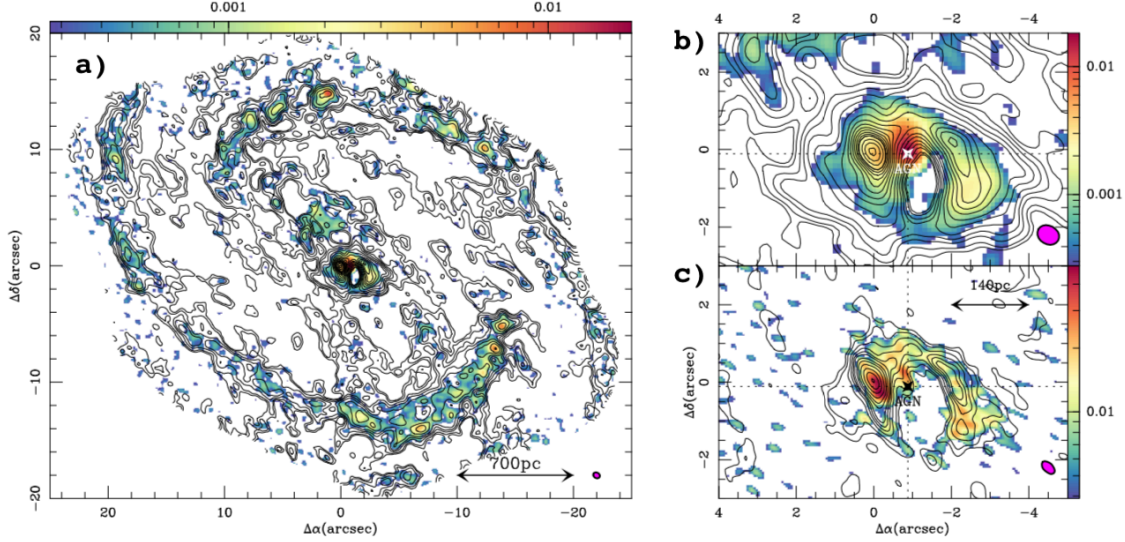


Figure 1.12: NGC 1068, a local Seyfert galaxy observed with ALMA: a) Overlay of the CO(3-2) intensity contours on the dust continuum emission at 349 GHz (color scale in Jy beam^{-1} units as indicated). The map is shown in color scale with contour levels 5σ , 10σ , 20σ , 30σ , 45σ , 70σ , 100σ to 500σ in steps of 50σ , and 600σ to 800σ in steps of 100σ , where $1\sigma = 0.22 \text{ Jy km s}^{-1} \text{ beam}^{-1}$. b) Same as a) but zooming in on the circumnuclear disk region. c) Overlay of the CO(6-5) intensity contours (levels are: 5σ , 10σ , 20σ , 30σ , 40σ , 70σ , 90σ , 120σ to 240σ in steps of 40σ , where $1\sigma = 2 \text{ Jy km s}^{-1} \text{ beam}^{-1}$) on the dust continuum emission at 689 GHz (color scale in Jy beam^{-1} units as indicated). The filled ellipses at the bottom right corners represent the CO beam sizes. Dust continuum and molecular line emission (CO 6-5 and 3-2) were detected in the proximity of the AGN (right panels), as expected from a molecular dusty compact structure surrounding the nucleus, i.e. the torus. Using CLUMPY models and the combination of ALMA observations with near-/mid-IR data, the properties of the putative torus were constrained. The resulting outer torus radius is $R_o = 20^{+6}_{-10} \text{ pc}$ with a mass $M_{\text{torus}} = (2.1 \pm 1.2) \times 10^5 M_{\odot}$. This figure has been adapted from García-Burillo et al. [2014].

where $S_{\text{line}}\Delta\nu$ is the flux of the emission line in Jy km s^{-1} , D_L is the luminosity distance in Mpc, ν_{rest} the rest-frame frequency of the line in GHz.

Then, the molecular gas mass (M_{mol}) is:

$$M_{\text{mol}} = \alpha_{\text{CO}} \times L'_{\text{CO}} \quad (1.4)$$

where α_{CO} is the CO-to- H_2 conversion factor (e.g., Solomon and Vanden Bout 2005; Bolatto et al. 2013).

As shown in Fig. 1.13, α_{CO} varies with many parameters, primarily with the metallicity

(Z), but also with the compactness (for a complete review, see Bolatto et al. 2013). However, at a given metallicity, α_{CO} can vary up to a factor ~ 4 between Milky-Way like objects and ULIRGs ($\alpha_{CO} = 4.3$ and $0.8 M_{\odot} \text{ pc}^{-2} (\text{K km s}^{-1})^{-1}$, respectively). Several studies investigated the dependence of the α_{CO} factor from the environmental properties (e.g., Downes and Solomon 1998; Papadopoulos et al. 2012), suggesting that the CO-to- H_2 conversion factor may depend on GMC-scale physical condition of the ISM, rather than on galaxy integrated properties. In general, the value of α_{CO} is likely a function of local ISM conditions, including pressure, gas dynamics, and metallicity, and remains an active area of research for nearby galaxies (Ostriker and Shetty 2011; Narayanan et al. 2012; Papadopoulos et al. 2012; Sandstrom et al. 2013). Anyway, assuming a single α_{CO} value for sample of objects with similar properties is good trade-off to obtain baseline estimates of the molecular gas content in galaxies.

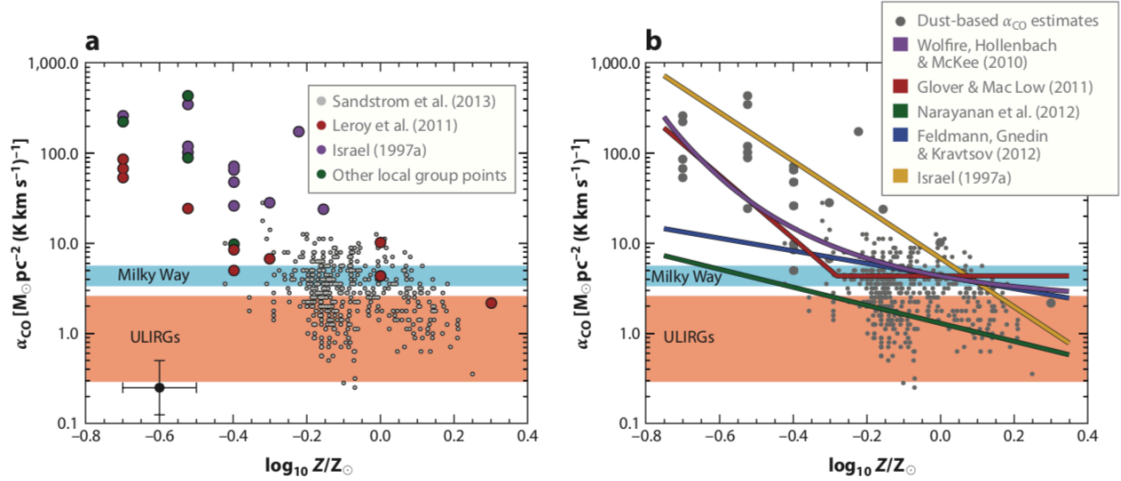


Figure 1.13: CO-to- H_2 conversion factor, estimated from dust-based approaches, as a function of gas-phase abundance. (a) Color points show estimates for very nearby galaxies [from Israel 1997; Madden et al. 1997, based on [CII]; Leroy et al. 2007; Leroy et al. 2011; Gratier et al. 2010; Roman-Duval et al. 2010; Bolatto et al. 2011; Smith et al. 2012]. Gray points show high-quality solutions from analysis of 22 nearby disk galaxies by Sandstrom et al. [2013], with typical uncertainties illustrated by the error bars near the bottom left corner. Note that significant systematic uncertainty is associated with the x-axis. The color bands illustrate our recommended ranges in α_{CO} for the Milky Way and ULIRGs. (b) Colored lines indicate predictions for X_{CO} as a function of metallicity from the references indicated, normalized to $X_{CO,20} = 2$ at solar metallicity where necessary. Dust-based determinations find a sharp increase in X_{CO} with decreasing metallicity below $Z \sim 1/3 - 1/2Z_{\odot}$. This figure is adapted from Bolatto et al. [2013].

1.2.3 Ionised gas

The majority of the volume of the ISM is occupied by the ionised gas, although it accounts for only 25% of the total mass. Ionised gas is usually found in two distinct

states, the hot ionised medium (HIM) and the warm ionised medium (WIM). The former, HIM, is usually located in large collisionally ionised bubbles, which are generated by powerful stellar winds of supernovae explosion, emitting soft X-ray photons (McKee and Ostriker 1977; Hollenbach and Tielens 1999). It is characterised by relatively low density ($n \sim 3 \times 10^{-3} \text{ cm}^{-3}$) and high temperatures ($T \sim 10^6 \text{ K}$). The WIM is composed by radiatively ionised hydrogen with temperatures around $T \sim 10^4 \text{ K}$ [Klessen and Glover, 2016]. Part of this gas is produced within the so-called HII regions, which are located in the surroundings of massive O and B stars, characterised by a surface temperature around $T \sim 2 - 5 \times 10^5 \text{ K}$, irradiating UV photons with energy $h\nu > 13.6 \text{ eV}$, hence able to ionise neutral hydrogen [Stahler and Palla, 2005].

1.2.4 Interstellar dust

Besides the gaseous phases (i.e., ionic, atomic and molecular), ISM includes also a solid-grain phase. This is generically called interstellar dust, made by micron-sized grains of graphite and silicate, and it accounts for only about $\sim 1\%$ of the total ISM mass [Klessen and Glover, 2016]. Dust plays a key role in many physical processes involving the gaseous ISM phases. For instance, dust is necessary to the formation of the H_2 molecules (with the bond between the two H atoms taking place on the dust grain surface; Draine 2010). Furthermore, it is responsible for large part of the absorption of the optical/UV emission that originates in regions of intense SF and from AGN, which is re-emitted in the IR band (i.e., the so-called “dust reddening”; Draine 2003).

Interstellar dust is distinguished in “cold” diffuse phase and in a “warm” one. The cold diffuse component is primarily made of larger grains of size $\gtrsim 250\text{\AA}$ in thermal equilibrium in a temperature range of $15 < T < 25 \text{ K}$; it is responsible for the absorption of the optical/near-IR emission, which is then re-emitted at $\lambda > 60 \mu\text{m}$. The warm phase consists of smaller grains of size $< 250\text{\AA}$, and is responsible for the reprocessing of the UV emission into mid-IR emission $\lambda < 60 \mu\text{m}$; the emission of the 3.3-11.3 μm PAH features is also accounted to the smallest grains of size $\lesssim 15\text{\AA}$ of the warmer component (see Galliano et al. 2018 for a recent review).

The global dust emission in nearby galaxies covers the entire IR band (1-1000 μm) and is usually described by a modified black body, which accounts for the contribution of the different dust phases, as presented in Fig. 1.14.

The parameters that are generally used to characterise the dust content in galaxies are the temperature and the mass. By modelling the broad band SED in the mid-IR and far-IR

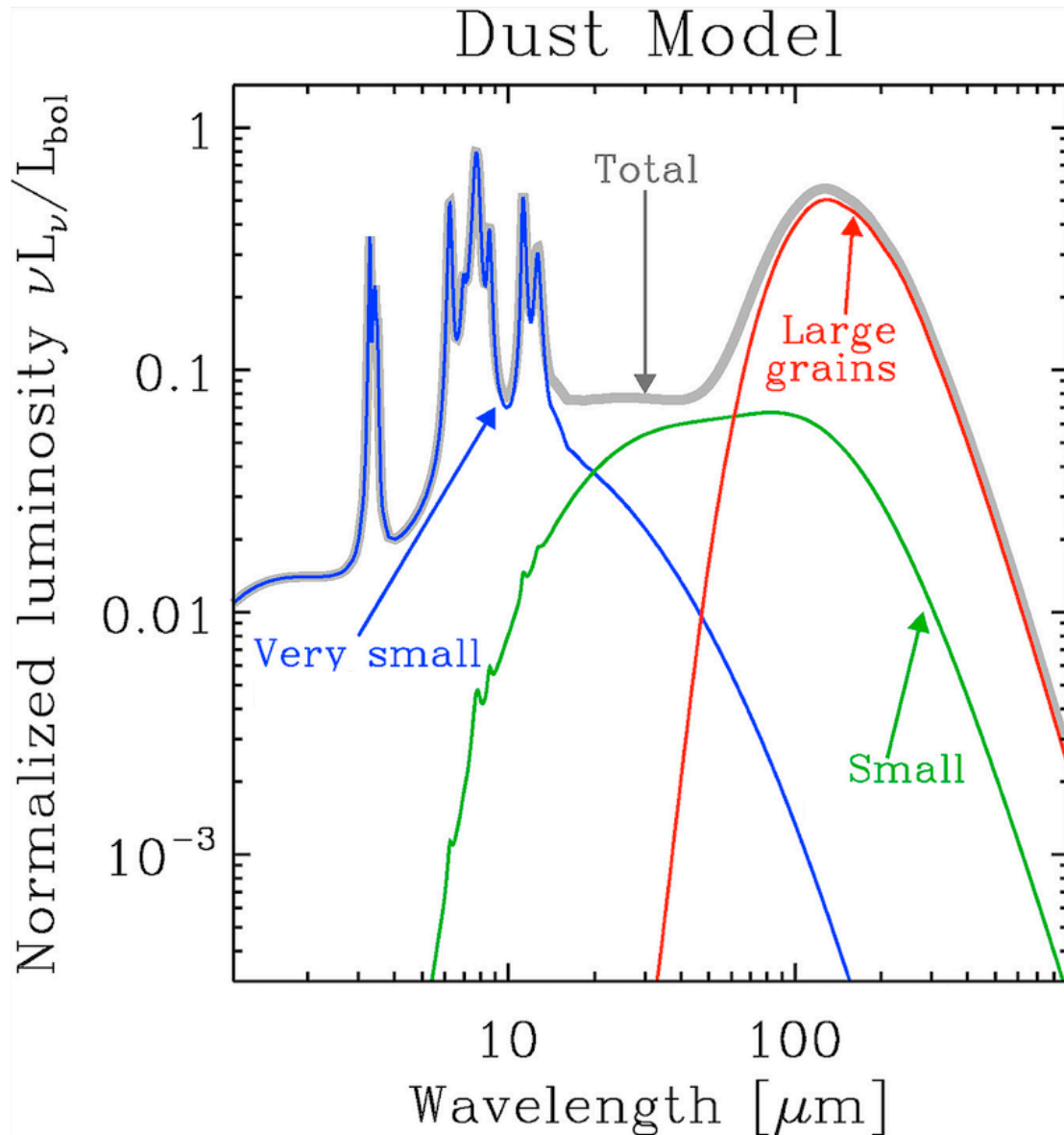


Figure 1.14: Dust SED modeling from Jones et al. [2017], heated by the interstellar radiation field. The different grains with different size are responsible for the different part of the total SED (grey thick line): the largest grain (red line) for the far-IR bump, the small grains (green line) for the mid-IR emission, while the smallest grains (blue line) for the near-/mid-IR continuum emission, as well as for the PAH features. This figure is adapted from Galliano [2017].

we can measure the typical dust temperature for the single (or multiple) component(s)⁵. Moreover, the accurate measurement of the dust mass can be derived by the luminosity in the Rayleigh-Jeans (RJ) regime (with photon energies that are much smaller than thermal energies, $h\nu \ll kT$) where the dust emission is optically thin and the observed flux

⁵This is the so-called “luminosity-weighted temperature”, depending on the IR emission of the dust, by definition. Alternatively, a “mass-weighted temperature” can be measured, depending on the global amount of dust in a galaxy, as well as the relative contribution of the different (i.e., warm and cold) dust components to the total mass (e.g., Liang et al. 2019).

density is proportional to the mass of dust [Scoville et al., 2016].

1.3 Thesis aims

The aim of this work is to assess, if any, the effect of AGN activity on the properties of the host-galaxy ISM in the local Universe. In particular, by combining the complementary information from observation at different wavelengths, I study whether, and on which scales, the emission from the AGN affects the properties of the molecular gas component of the ISM.

In this Chapter, I discuss several approaches that can be adopted to investigate the signature of accreting SMBHs within galaxies. Different physical processes and ISM phases can be traced at different wavelengths, namely the BH accretion in the X-rays (see Section 1.1), the emission from the dust in the IR (see Section 1.2.4), and the molecular gas component in the (sub-)millimetre band (see Section 1.2). Thus, it is straightforward that a multi-wavelength strategy is essential for a comprehensive picture of the interplay between BH accretion and the host-galaxy SF activity. Local Seyfert galaxies are the perfect laboratories to study the impact of AGN on the host galaxy, allowing us to develop a methodology which can then be applied to AGN at higher redshift. Very good candidates “composite” objects (i.e., where SF and AGN accretion co-exist) are the Seyfert galaxies from the extended 12 micron galaxy sample (12MGS) selected by Rush et al. [1993]. Active galaxies are thought to emit about one fifth of their bolometric luminosity at 12 μm [Spinoglio and Malkan, 1989], irrespectively of their optical/UV classification, which is intrinsically biased towards type 1 (broad-line, i.e. unobscured; see Section 1.1) nuclei. The rest-frame 12 μm flux has been considered as a reliable proxy of the intrinsic AGN continuum emission⁶ [Gandhi et al., 2009], corresponding to the central wavelength regime where the dust-reprocessed emission from the torus peaks. This made the 12MGS an unbiased (or relatively biased) sample of AGN. Then, the entire 12MGS, in particular the AGN sample included in it, has been the target of extensive studies at all wavelengths over the past 20 years, both photometric and spectroscopic, from the X-rays to radio frequencies.

In this thesis I exploit the multi-wavelength coverage of the 12MGS. I adopt a two fold-approach: i) I characterise the AGN, focusing on the Type 2 objects, in terms of level of obscuration and intrinsic power; ii) I study the properties of the molecular gas,

⁶It is worth remembering that some authors noted minor selection biases between mid-IR selected sample of AGN and radio (e.g., Buchanan et al. 2006; Hönig et al. 2011) or X-ray (e.g., Gandhi et al. 2009; Asmus et al. 2014) selected samples.

which is directly involved in the SF activity, and, potentially, in the accretion process, using both resolved and galaxy-integrated observations.

The first step, developed in Chapter 2, is the characterisation of the X-ray properties of a sample of local Seyfert 2 (i.e., obscured) galaxies, drawn from the 12MGS. In particular, I present the results of the X-ray spectral analysis, exploiting the broad energy band ($\sim 0.5 - 30$ keV), obtained with the combination of *NuSTAR* data with observations at energies $E < 10$ keV. I describe the X-ray properties (e.g., X-ray luminosity, spectral slope, level of obscuration) of the sample of 32 out of the 36 Seyfert 2 galaxies from Gruppioni et al. [2016], with available X-ray data. Moreover, I compare the extinction level in the mid-IR bands (where the emission from the dusty torus peaks), with the obscuration in the X-rays, to possibly understand the features of the obscuring torus.

To complement our study on the X-ray properties of the Seyfert 2 galaxies, I measure the molecular gas content of 33 out of the 36 objects from Gruppioni et al. [2016]. In Chapter 3 I present the measurements of the molecular gas mass (M_{mol}), derived from new and archival single-dish CO spectroscopy. To assess the effect of AGN activity on the host molecular gas reservoir, I compare the molecular gas content, and the resulting depletion time $t_{depl} = M_{mol}/SFR$ of our sample with a control sample of normal SF galaxies (SFGs). Furthermore, I investigate the effect of the nuclear activity on the PAH emission, a widely used tracer of ongoing SF.

The results presented in the first two Chapters provide an extensive characterisation of both the AGN (Chapter 2) and the properties of the host-galaxy ISM (Chapter 3) for 29 out of the 36 Seyfert 2 galaxies from Gruppioni et al. [2016], which then result in one of the first statistically large samples of local AGN with such a detailed and comprehensive study.

In Chapter 4, I select one of the AGN from the 12MGC to test our multi-wavelength approach. I combine the characterisation of the AGN (obtained through the X-ray spectral analysis), with a spatially resolved study of the host-galaxy molecular gas, obtained with an ALMA archival observation (see Section 4.2.2). I present the modelling of the molecular gas kinematics.

Finally, in Chapter 5 I summarise the results and draw the conclusions of the work presented, providing a coherent interpretation of the effect of AGN on the properties of host-galaxy ISM, and outlining future developments.

2

Unveiling the intrinsic power in local Seyfert 2 galaxies

This Chapter is mainly based on “Unveiling the intrinsic power in local Seyfert 2 galaxies”, F. Salvestrini, et al., in prep.

In this Chapter we present a systematic study of the X-ray properties of a sample of local Seyfert 2 galaxies drawn from G16, to determine the intrinsic power (i.e., corrected for potential obscuration) of their central engine. As shown in Sect. 1.1.2, revealing the emission from an AGN can be challenging, in particular in the case of heavy obscuration or relatively weak nuclear emission. To this purpose, we need high sensitivity and the largest band available to probe the X-ray emission up to the highest energy regime, i.e. $\gtrsim 10$ keV, where the obscuration is less effective. The Nuclear Spectroscopic Telescope Array (*NuSTAR*¹; Harrison et al. 2013) is the perfect tool for this kind of investigation, with its unparalleled focusing power at energies above 10 keV. By combining *NuSTAR*

¹The *NuSTAR* mission has deployed the first orbiting telescopes to focus light in the high energy X-ray (nominally 3-79 keV). It was launched by NASA on March 21, 2012 and it is equipped with a deployable arm, at which end are placed two focusing optics with a 10.15 m focal length. Focal plane host two detector units, each one comprised of four Cadmium-Zinc-Telluride (CdZnTe) detector. The on-board instrumentation provide a spectral Resolution (FWHM) of 400 eV at 10 keV, and 900 eV at 68 keV. The field of view (FoV) is $\sim 10'$ at 10 keV with and angular resolution of $18''$ (FWHM).

with 0.3-10 keV energy band observation, we are able to model also the complex spectra of heavily obscured AGN. From the broad-band X-ray spectral analysis, we place constraints on the level of obscuration and determine the intrinsic luminosity.

Furthermore, in Section 1.1 we emphasise the importance of combining X-rays and mid-IR information to unveil the intrinsic power of the AGN, as well as to constrain the level of obscuration. Here we compare the obscuration in the X-rays and in the mid-IR, where we account on the results of the SED modelling from a previous work from our collaboration (G16) and the analysis of *Spitzer*/IRS spectra by Hernán-Caballero and Hatziminaoglou [2011]. This Chapter is structured as follows: in Sect. 2.1 we present the sample and the data included in the analysis, the results are presented in 2.2, while the conclusion are summarised in 2.3. Throughout the Chapter, distance-dependent quantities are calculated for a standard flat Λ CDM cosmology with the matter density parameter $\Omega_M = 0.30$, the dark energy density parameter $\Omega_\Lambda = 0.70$, and the Hubble constant $H_0 = 70 \text{ km s}^{-1} \text{ Mpc}^{-1}$ [Komatsu et al., 2009]. Errors are given at 68 per cent confidence level.

| Name | RA | DEC | z | SFR [$M_{\odot} \text{ yr}^{-1}$] | $\log(M_{*}/M_{\odot})$ | $\log(L_{IR}^{tot}/L_{\odot})$ | $\log(L_{IR}/L_{\odot})$ | f_{AGN} | $\log(L_{bol}^{IR}/L_{\odot})$ | |
|-----------------|--------------|---------------|--------|-------------------------------------|-------------------------|--------------------------------|--------------------------|-----------|--------------------------------|---|
| CGCG381-051 | 23h48m41.29s | +02d14m21.01s | 0.0307 | 13.26±0.07 | 10.43±0.05 | 11.12±0.01 | 11.12±0.01 | 0.01±0.42 | 9.48±0.27 | ★ |
| ESO033-G002 | 04h55m59.59s | -75d32m26.99s | 0.0181 | 2.86±0.02 | 10.6±0.1 | 10.58±0.01 | 10.46±0.01 | 0.61±0.02 | 10.76±0.01 | ★ |
| IC5063 | 20h52m1.99s | -57d4m9.01s | 0.0113 | 5.28±0.63 | 10.69±0.08 | 10.84±0.03 | 10.72±0.12 | 0.46±0.05 | 11.27±0.3 | ★ |
| IRASF01475-0740 | 01h50m2.69s | -07d25m48.0s | 0.0177 | 3.49±0.42 | 9.05±0.1 | 10.59±0.03 | 10.54±0.12 | 0.25±0.6 | 9.97±0.05 | ★ |
| IRASF04385-0828 | 04h40m54.91s | -08d22m22.01s | 0.0151 | 3.36±0.28 | 10.27±0.1 | 10.83±0.03 | 10.53±0.08 | 0.71±0.03 | 11.25±0.02 | ◇ |
| IRASF05189-2524 | 05h21m01.36s | -25d21m45.4s | 0.0426 | 155.3±18.64 | 10.55±0.07 | 12.21±0.03 | 12.19±0.12 | 0.12±0.04 | 11.8±0.03 | ★ |
| IRASF15480-0344 | 15h50m41.50s | -03d53m17.99s | 0.0303 | 10.16±1.34 | 10.75±0.1 | 11.11±0.12 | 11.01±0.13 | 0.52±0.1 | 11.51±0.3 | ★ |
| MCG-03-34-064 | 13h22m24.38s | -16d43m43.0s | 0.0165 | 5.65±0.56 | 10.65±0.1 | 11.06±0.03 | 10.75±0.1 | 0.72±0.07 | 11.48±0.15 | ★ |
| MCG-03-58-007 | 22h49m36.91s | -19d16m23.99s | 0.0315 | 20.15±0.88 | 10.95±0.07 | 11.37±0.04 | 11.3±0.04 | 0.48±0.07 | 11.6±0.02 | ★ |
| MCG+00-29-023 | 11h21m12.20s | -02d59m3.01s | 0.0249 | 18.71±0.55 | 10.95±0.09 | 11.31±0.03 | 11.27±0.03 | 0.34±0.13 | 11.23±0.21 | ◇ |
| MRK0273 | 13h44m42.11s | +55d53m12.65s | 0.0378 | 66.85±8.02 | 11.04±0.08 | 11.92±0.03 | 11.83±0.12 | 0.39±0.02 | 11.86±0.3 | ★ |
| MRK0463 | 13h56m2.90s | +18d22m18.98s | 0.0504 | 15.4±2.03 | 11.22±0.1 | 11.67±0.02 | 11.19±0.13 | 0.87±0.02 | 12.5±0.3 | ★ |
| MRK0897 | 21h7m45.80s | +03d52m40.01s | 0.0263 | 28.23±3.39 | 10.91±0.11 | 11.46±0.03 | 11.45±0.12 | 0.08±0.02 | 10.81±0.01 | ★ |
| NGC0034 | 00h11m06.55s | -12d06m26.33s | 0.0196 | 24.44±1.79 | 10.58±0.09 | 11.42±0.05 | 11.39±0.07 | 0.19±0.1 | 11.03±0.05 | ★ |
| NGC0262 | 00h48m47.1s | +31d57m25.1s | 0.015 | 1.35±0.19 | 10.45±0.09 | 10.53±0.04 | 10.13±0.14 | 0.79±0.03 | 11.34±0.02 | ★ |
| NGC0424 | 01h11m27.49s | -38d5m1.0s | 0.0118 | 1.26±0.05 | 10.49±0.1 | 10.56±0.01 | 10.1±0.04 | 0.8±0.03 | 11.19±0.01 | ★ |
| NGC0513 | 01h24m26.85s | +33d47m58.01s | 0.0195 | 6.64±0.44 | 10.78±0.08 | 10.83±0.07 | 10.82±0.07 | 0.08±0.3 | 10.19±0.28 | ★ |
| NGC1056 | 02h42m48.30s | +28d34m27.1s | 0.0052 | 0.66±0.01 | 9.86±0.1 | 9.82±0.01 | 9.82±0.01 | | | ★ |
| NGC1125 | 02h51m40.39s | -16d39m1.98s | 0.0109 | 2.23±0.06 | 9.52±0.09 | 10.4±0.02 | 10.35±0.02 | 0.28±0.13 | 10.26±0.08 | ★ |
| NGC1320 | 03h24m48.71s | -03d2m33.0s | 0.0089 | 0.92±0.01 | 10.43±0.11 | 10.1±0.01 | 9.96±0.01 | 0.56±0.01 | 10.58±0.06 | ★ |
| NGC2992 | 09h45m42.01s | -14d19m35.0s | 0.0077 | 3.61±0.26 | 9.19±0.08 | 10.58±0.07 | 10.56±0.07 | 0.35±0.03 | 10.13±0.06 | ★ |
| NGC3079 | 10h01m57.80s | +55d40m47.24s | 0.0037 | 3.81±0.04 | 9.76±0.09 | 10.6±0.01 | 10.58±0.01 | 0.2±0.1 | 10.03±0.25 | ★ |
| NGC4388 | 12h25m46.75s | +12d39m43.51s | 0.0084 | 3.7±0.11 | 9.31±0.08 | 10.67±0.03 | 10.57±0.03 | 0.4±0.1 | 10.74±0.2 | ★ |
| NGC4602 | 12h40m36.52s | -5d7m54.98s | 0.0085 | 2.99±0.07 | 9.42±0.1 | 10.49±0.02 | 10.48±0.02 | 0.12±0.31 | 10.12±0.11 | ◇ |
| NGC5135 | 13h25m44.06s | -29d50m01.2s | 0.0137 | 15.61±1.87 | 10.71±0.07 | 11.23±0.03 | 11.19±0.12 | 0.25±0.04 | 10.72±0.08 | ★ |
| NGC5256 | 13h38m17.50s | +48d16m37.0s | 0.0279 | 31.72±1.39 | 10.42±0.1 | 11.52±0.03 | 11.5±0.04 | 0.14±0.17 | 11.18±0.17 | ★ |
| NGC5347 | 13h53m17.83s | +33d29m26.98s | 0.0078 | 0.71±0.01 | 10.11±0.1 | 9.96±0.01 | 9.85±0.01 | 0.53±0.04 | 10.35±0.3 | ★ |
| NGC5506 | 14h13m14.81s | -03d12m27.0s | 0.0062 | 1.96±0.08 | 10.41±0.09 | 10.45±0.02 | 10.29±0.04 | 0.65±0.07 | 10.63±0.07 | ★ |
| NGC5953 | 15h34m32.30s | +15d11m42.0s | 0.0066 | 2.56±0.1 | 9.99±0.1 | 10.41±0.04 | 10.41±0.04 | 0.02±0.6 | 8.87±0.3 | ★ |
| NGC5995 | 15h48m24.91s | -13d45m28.01s | 0.0252 | 19.19±2.3 | 10.87±0.09 | 11.33±0.03 | 11.28±0.12 | 0.34±0.05 | 11.32±0.02 | ★ |
| NGC6890 | 20h18m18.11s | -44d48m23.0s | 0.0081 | 2.05±0.25 | 9.86±0.1 | 10.33±0.01 | 10.31±0.12 | 0.13±0.69 | 9.73±0.57 | ★ |
| NGC7130 | 21h48m19.52s | -34d57m04.48s | 0.0162 | 20.93±0.05 | 10.49±0.09 | 11.32±0.03 | 11.32±0.01 | | | ★ |
| NGC7496 | 23h9m47.20s | -43d25m40.01s | 0.0055 | 1.55±0.19 | 9.46±0.12 | 10.19±0.03 | 10.19±0.12 | | | ◇ |

Continued on next page

Table 2.1 – Continued from previous page

| Name | RA | DEC | z | SFR [$M_{\odot} \text{ yr}^{-1}$] | $\log(M_{*}/M_{\odot})$ | $\log(L_{IR}^{tot}/L_{\odot})$ | $\log(L_{IR}/L_{\odot})$ | f_{AGN} | $\log(L_{bol}^{IR}/L_{\odot})$ |
|--------------|--------------|---------------|--------|-------------------------------------|-------------------------|--------------------------------|--------------------------|-----------|--------------------------------|
| NGC7674 | 23h27m56.70s | +08d46m45.01s | 0.0289 | 23.58±2.83 | 11.11±0.07 | 11.53±0.03 | 11.37±0.12 | 0.58±0.6 | 11.73±0.3 |
| TOL01238-364 | 12h40m52.90s | -36d45m22.0s | 0.0109 | 5.76±0.17 | 9.66±0.1 | 10.83±0.01 | 10.76±0.03 | 0.32±0.6 | 10.6±0.3 |
| UGC05101 | 09h35m51.60s | +61d21m11.45s | 0.0394 | 55.21±6.63 | 10.92±0.11 | 11.91±0.01 | 11.74±0.12 | 0.65±0.03 | 12.04±0.13 |

Table 2.1: (1): Source name; (2): RA in units of hms; (3): DEC in units of dms; (4): Redshift; (5): SFR, in units of $M_{\odot} \text{ yr}^{-1}$; (6): Logarithm of the stellar mass, in units of M_{\odot} ; (7): Logarithm of the global 8-1000 μm IR luminosity, in units of L_{\odot} ; (8): Logarithm of the 8-1000 μm IR luminosity of the host-galaxy, in units of L_{\odot} ; (9): fraction of the 5-40 μm IR emission due to the AGN; (10): Logarithm of the bolometric luminosity of the AGN, in units of L_{\odot} , as derived from the nuclear contribution to the IR. (11) & (12): \star and \diamond mean that the source has X-ray (this Chapter) and sub-millimetre data (see Chapter 3), respectively.

2.1 The sample

Our reference sample is the collection of 76 mid-IR selected active galaxies by G16, where the authors performed a detailed SED decomposition to trace the BH accretion and determine the relative contribution of nuclear activity to the global outcome of the galaxy. We focused on the optically-classified (i.e., narrow-line) Seyfert 2 galaxies from the G16, since the SED decomposition analysis of type 2 (i.e. obscured) galaxies produces more solid determination of the host-galaxy properties (e.g., the stellar content, M_* , and the SFR), given the lower contribution in the optical-UV band from the nuclear activity, with respect to type 1 objects.

36 (out of 76) AGN in G16 were classified as Seyfert 2 galaxies (see the full list in Table 2.1), among which we only selected the objects with available X-ray observations, with the aim of assessing the intrinsic power of the BH accretion exploiting X-ray spectroscopy. To properly constrain the spectral shape and the level of obscuration we limited our analysis to the 32 targets for which *NuSTAR* observations are already available in the archive². Since *NuSTAR* instrumentation are sensitive and well calibrated only above 3 keV, we looked for the availability of combined-simultaneous observations with one of the X-ray telescopes with sensibility in the soft band, i.e. below 3 keV, namely *XMM-Newton*³, *Swift*⁴, and *Chandra*⁵ (see Table for the list of selected datasets). Details about the selected X-ray data are provided in Sect. 2.1.1.

²https://heasarc.gsfc.nasa.gov/docs/nustar/nustar_archive.html

³The *XMM-Newton* telescope was launched by ESA on December 10, 1999. It is equipped with three X-ray telescopes, which focus on the focal plane detector, the European Photon Imaging Camera (EPIC). For a complementary analysis of the spectrum, two of the three telescopes have a grating structure (the Reflection Grating Spectrometer, RGS) on their mirror module that reflects about 40 per cent of the incoming rays to a secondary focus, with its own CCD camera. A optical/UV telescope, the Optical Monitor (OM), is the third instrument on-board. The X-ray mirrors, combined with EPIC detectors, provide a spectral resolution of $E/dE \sim 20 - 50$, while the spatial resolution reaches $15''$ (FWHM).

⁴The main goal of the Swift Gamma Ray Burst Explorer (*Swift*) telescope is to monitor and reveal Gamma-ray burst events. To this goal, the spacecraft was launched by NASA on November 20, 2004. It is equipped with the X-Ray Telescope (XRT), a focusing X-ray telescope with $23.6 \times 23.6'$ FOV, and $18''$ resolution, operating in the 0.2-10 keV energy range. The Burst Alert Telescope (BAT) is a telescope with a large FoV (up to 1.4 sr) sensitive to the 15-150 keV band. It is responsible for the monitoring of gamma-ray event, which are then observed with XRT. Also a UV/optical telescope (UVOT) is present onboard.

⁵*Chandra* is an X-ray telescope, launched by NASA on July 23, 1999. The High Resolution Mirror Assembly (HRMA) focuses X-rays onto one of two instruments, ACIS or HRC. Only one detector (HRC or ACIS) is in the focal plane at any given time. Two grating spectrometers (low and high Low Energy Transmission Grating, LETG and HETG, respectively) can be placed in the optical path behind the HRMA. The Advanced CCD Imaging Spectrometer (ACIS) is an X-ray imager which reaches the $\sim 1''$ spatial resolution, with a spectra resolution of ~ 100 eV and a FoV of $\sim 16 \times 16'$. The High Resolution Camera (HRC) is a microchannel plate (MCP) instrument with two detectors, one optimised for imaging and the other for spectroscopy.

2.1.1 X-ray data

Our goal is to provide a systematic analysis of the X-ray spectral properties for the Seyfert 2 galaxies from G16 with available X-ray observations (see Table 2.2), both proprietary data (ID:06158, PI: Salvestrini) and from the archive, by adopting a uniform approach. The source of the sample are optically obscured and thus it is probable that they are characterise by X-ray obscuration as well. The X-ray spectra of obscured AGN are typically characterised by: 1) a primary emission is due to Compton-up scattering of optical/UV photons, emitted by the accretion disk, onto the hot corona of relativistic electrons and surrounding the disk itself (e.g., Zdziarski et al. 1994) The cut-off at softer energies is due to the photoelectric absorption of the obscuring material along the line-of-sight; 2) A scattered continuum component, reflected by the material surrounding the accreting SMBH; 3) Fe K-shell fluorescent emission lines (e.g., Fabian et al. 2000). Finally, 4) a soft emission ($E < 3$ keV) due to one or a combination of the following components: the high-energy tail of the SF from the host galaxy (e.g., Mineo et al. 2012b); the higher-energy component of the thermal emission; the reflection from the disk (e.g., Brightman et al. 2014); two coronae (hot and warm; e.g., Ursini et al. 2020). The relative normalisation between the components depends on the properties of the dusty torus surrounding the central SMBH. In particular, the most relevant parameters are related to the torus geometry (i.e., inclination with respect to the los, the aperture angle) and physical properties (i.e., the density profile of obscuring material). Since the absorption in the X-rays is more “efficient” at soft energies (i.e., below 10 keV), to place solid constrain on the spectral shape of the intrinsic emission, and on the level of obscuration, the largest energy band available is necessary, especially extending at energies $E > 10$ keV.

We collected archival data obtained with the X-ray Multi-Mirror Mission (*XMM-Newton*), *Chandra* and *Swift*. We adopted the following criteria: when available, we considered *XMM-Newton* observation, possibly taken simultaneously to the *NuSTAR* one; if no *XMM-Newton* observation was available, we checked for *Chandra* one. Eventually, if neither *XMM-Newton* and *Chandra* data were available, we retrieved *Swift* observations. Furthermore, if multiple *XMM-Newton* or *Chandra* observations were available, we chose the longest one. We checked in the literature for evidence of significant X-ray spectral variability (e.g., in either spectral shape or flux) for the objects in our sample with multi-epoch data, finding no significant variability effect in the large part of the sample. An exception is NGC 2992, which has been observed multiple times over the last forty years, showing its 2-10 keV flux varying up to a factor four, and spectral features changing shape (for further details see Marinucci et al. 2018).

Thirty-two out the 36 Seyfert 2 galaxies form G16 have been observed in the X-rays, out

of which 29 have *NuSTAR* data. The remaining four objects have only observations in the band at energies below 10 keV. The collection of dataset for each object are listed in Table 2.2. To the 24 objects with *NuSTAR* observations, we associated an XMM-*Newton* counterpart in 21 cases, *Chandra* for 5 objects, while the remaining 3 have a *Swift* observation. CGCG 381-051, Mrk 0897, and NGC 5953 were never targeted by a *NuSTAR* observations, hence we collected the archival XMM-*Newton* data for the former three, while for NGC 5953 we used the *Chandra* observation. Among the XX sources listed in Table 2.2, we included also NGC 1056 for which *NuSTAR*-XMM-*Newton* proprietary data have been recently obtained (ID:06158, PI: Salvestrini).

2.1.2 X-ray data reduction

We reduced all data sets included in our study by using a uniform and homogeneous approach. Data reduction was performed by using the standard guidelines suggested for each telescope, using the dedicated software. Furthermore, we checked the light curves for potential time variability, once flaring-background periods were filtered out, for each data set. We found no evidence for significant time variability.

Furthermore In the following sections, we describe the data reduction procedures adopted for each telescope set.

2.1.2.1 *NuSTAR* data reduction

We processed the data of both the *NuSTAR* Focal Plane Modules (FPMA and FPMB) using the *NuSTAR* Data Analysis Software (NuSTARDAS) v1.7.1, from the HEASOFT (v. 6.24) distribution. The event data files were calibrated running the nupipeline task using the response file from the Calibration Database (CALDB) v. 20100101. For each focal plane instrument, we extracted the source counts using 50'' circular aperture centred on the position of the source, retrieved from the NASA/IPAC Extragalactic Database (NED⁶). The 50'' extraction radius corresponds to at least the 50% of the encircled energy fraction (EEF) on the entire energy band (3-79 keV) for both FPM cameras [An et al., 2014]. For the background counts, we used the same circular extraction aperture from regions free from sources in the same frame. With the “nuproducts” script, we produced both the source and background spectra, as well as the ancillary and response matrix files. *NuSTAR* spectra were grouped with a minimum number of 30 counts per bin, to reasonably apply the standard goodness-of-fit test for Gaussian data, i.e. the χ^2 test, to evaluate the goodness of the fit.

⁶<https://ned.ipac.caltech.edu/>

Table 2.2 – X-ray datasets

| Source | Telescope | Observation ID | Observation date | Exposure |
|------------------|-------------------|----------------|------------------|----------|
| CGCG 381-051 | <i>XMM-Newton</i> | 655380201 | 2010-12-02 | 16.4 |
| ESO 033-G002 | <i>NuSTAR</i> | 60061054002 | 2014-05-04 | 23.5 |
| | <i>Swift</i> | 80345001 | 2014-05-04 | 6.9 |
| IC 5063 | <i>NuSTAR</i> | 60061302002 | 2013-07-08 | 18.4 |
| | <i>Swift</i> | 80269001 | 2013-07-08 | 7.1 |
| IRAS F01475-0740 | <i>NuSTAR</i> | 60360005002 | 2019-06-16 | 30.7 |
| | <i>XMM-Newton</i> | 0200431101 | 2004-01-21 | 11.9 |
| IRAS F05189-2524 | <i>NuSTAR</i> | 60201022002 | 2016-09-05 | 155.0 |
| | <i>XMM-Newton</i> | 0790580101 | 2016-09-06 | 99.0 |
| IRAS F15480-0344 | <i>NuSTAR</i> | 90601603002 | 2020-03-23 | 48.0 |
| | <i>XMM-Newton</i> | 600690201 | 2010-01-30 | 51.9 |
| MCG-03-34-064 | <i>NuSTAR</i> | 60101020002 | 2016-01-17 | 78.5 |
| | <i>XMM-Newton</i> | 0763220201 | 2016-01-17 | 142.5 |
| MCG-03-58-007 | <i>NuSTAR</i> | 60101027002 | 2015-12-06 | 138.0 |
| | <i>XMM-Newton</i> | 0764010101 | 2015-12-06 | 134.3 |
| Mrk 0273 | <i>NuSTAR</i> | 60002028002 | 2013-11-04 | 69.8 |
| | <i>XMM-Newton</i> | 722610201 | 2013-11-04 | 22.8 |
| Mrk 0463 | <i>NuSTAR</i> | 60061249002 | 2014-01-01 | 23.8 |
| | <i>XMM-Newton</i> | 94401201 | 2001-12-22 | 26.8 |
| Mrk 0897 | <i>XMM-Newton</i> | 655381001 | 2010-05-04 | 20.3 |
| NGC 0034 | <i>NuSTAR</i> | 60101068002 | 2015-07-31 | 21.4 |
| | <i>XMM-Newton</i> | 150480501 | 2002-12-22 | 22.1 |
| NGC 0262 | <i>NuSTAR</i> | 60160026002 | 2015-10-28 | 21.5 |
| | <i>XMM-Newton</i> | 67540201 | 2002-07-18 | 49.5 |
| NGC 0424 | <i>NuSTAR</i> | 60061007002 | 2013-01-26 | 15.5 |
| | <i>XMM-Newton</i> | 550950101 | 2008-12-07 | 127.5 |
| NGC 0513 | <i>NuSTAR</i> | 60061012002 | 2013-02-16 | 16 |
| | <i>XMM-Newton</i> | 301150401 | 2006-01-28 | 16.8 |
| NGC 1056 | <i>NuSTAR</i> | 60664006002 | 2020-07-25 | 113.2 |
| | <i>XMM-Newton</i> | 0871000101 | 2020-07-24 | 30.3 |
| NGC 1125 | <i>NuSTAR</i> | 60510001002 | 2019-06-10 | 31.7 |
| | <i>Chandra</i> | 21418 | 2018-10-24 | 55.8 |
| NGC 1320 | <i>NuSTAR</i> | 60061036004 | 2013-02-10 | 27.9 |
| | <i>XMM-Newton</i> | 405240201 | 2006-08-06 | 17.1 |
| NGC 2992 | <i>NuSTAR</i> | 60160371002 | 2015-12-02 | 20.7 |
| | <i>XMM-Newton</i> | 654910301 | 2010-05-06 | 59.4 |
| NGC 3079 | <i>NuSTAR</i> | 60061097002 | 2013-11-12 | 21.5 |
| | <i>XMM-Newton</i> | 80030001 | 2013-11-12 | 6.7 |
| NGC 4388 | <i>NuSTAR</i> | 60061228002 | 2013-12-27 | 20.7 |
| | <i>XMM-Newton</i> | 0675140101 | 2011-06-17 | 61.4 |
| NGC 5135 | <i>NuSTAR</i> | 60001153002 | 2015-01-14 | 33.3 |
| | <i>Chandra</i> | 2187 | 2001-09-04 | 29.9 |
| NGC 5256 | <i>NuSTAR</i> | 60465005002 | 2019-02-08 | 32.3 |
| | <i>XMM-Newton</i> | 55990501 | 2002-05-15 | 23.1 |
| NGC 5347 | <i>NuSTAR</i> | 60001163002 | 2015-01-16 | 47.3 |
| | <i>Chandra</i> | 4867 | 2004-06-05 | 37.4 |
| NGC 5506 | <i>NuSTAR</i> | 60061323002 | 2014-04-01 | 56.5 |
| | <i>XMM-Newton</i> | 761220101 | 2015-07-07 | 132 |
| NGC 5953 | <i>Chandra</i> | 2930 | 2002-06-11 | 10.1 |
| NGC 5995 | <i>NuSTAR</i> | 60061267002 | 2014-08-28 | 21.1 |
| | <i>Swift</i> | 80153001 | 2014-08-28 | 6.7 |
| NGC 6890 | <i>NuSTAR</i> | 60375003002 | 2018-05-25 | 34.6 |

Continued on next page

Table 2.2 – Continued from previous page

| Source | Telescope | Observation ID | Observation date | Exposure |
|-----------------|-------------------|----------------|------------------|----------|
| | <i>XMM-Newton</i> | 301151001 | 2005-09-29 | 12.8 |
| NGC 7130 | <i>NuSTAR</i> | 60261006002 | 2016-12-15 | 42.1 |
| | <i>Chandra</i> | 2188 | 2001-10-23 | 39.5 |
| NGC 7674 | <i>NuSTAR</i> | 60001151002 | 2014-09-30 | 51.9 |
| | <i>XMM-Newton</i> | 200660101 | 2004-06-02 | 10.4 |
| TOLOLO 1238-364 | <i>NuSTAR</i> | 60001164002 | 2015-01-09 | 58.7 |
| | <i>Chandra</i> | 4844 | 2004-03-07 | 9.6 |
| UGC 05101 | <i>NuSTAR</i> | 60001068002 | 2014-03-21 | 18.2 |
| | <i>XMM-Newton</i> | 85640201 | 2001-11-12 | 34.9 |

Table 2.2: (1): Source name; (2) Name of the telescope used for the observation. (3): Observation ID. (4): Observing date; (5): Total exposure time in 10^3 s.

2.1.2.2 XMM-Newton data reduction

XMM-Newton data were reduced with the Science Analysis Software (SAS) v.16.1.0, adopting a standard procedure, for both European photon imaging camera (EPIC) pn and Metal Oxide Semi-conductor (MOS) cameras. Source counts were extracted from circular regions of $15''$ centred on the source position ($\sim 90\%$ of the EEF at $E < 5$ keV for both EPIC pn and MOS cameras), while the background counts were extracted from circular aperture of $40''$ in a region surrounding the target, free from contamination from external sources. EPIC pn and MOS spectra were binned with at least 20 and 30 minimum counts per bin, respectively.

2.1.2.3 Chandra data reduction

We reprocessed *Chandra* data using the software Chandra Interactive Analysis of Observations (CIAO; Fruscione et al. 2006) v. 4.9, and the Chandra Calibration DataBase (caldb) 4.6.9, adopting standard procedures. We checked for potential pile-up: no significant evidence for pile-up was found in any of the considered *Chandra* observations. We extracted the source counts from a circular region of $2''$ ($\sim 95\%$ of the EEF for $E \sim 1.5$ keV) centred on the source position. The background counts were extracted from contiguous source-free circular region with $10''$ radius, near to the target. Each spectrum has been binned with at least 15 counts per bin.

2.1.2.4 Swift-XRT data reduction

We retrieved *Swift* spectra from the *Swift* data products generator available online⁷ [Evans et al., 2009]. Given the low-counts statistics of typical *Swift*-XRT spectra, we binned the spectra with at least 7 counts per bin.

⁷http://www.swift.ac.uk/user_objects/

2.1.3 Spectral Fitting Procedure

As discussed in Section 2.1.1, many spectral components have been observed in the X-ray emission of obscured AGN, namely the primary absorbed continuum emission, the reflection hump, the contamination from the SF-related emission in the soft band, and emission line features. To properly reproduce the X-ray spectra of AGN, a plethora of models has been developed over the years. A first approach is to combine different models, each one of these being responsible for a single, or a few, spectral components, to reproduce the entire emission. This approach is called “phenomenological”, and requires the combination of a variable number of distinct model components, which lacks in providing a complete picture of the structure and properties of the surrounding material in the nearby of the SMBH. Recently, the so-called “physical” models have been presented and widely applied to study the X-ray emission in local AGN (e.g., Marchesi et al. 2018; Kammoun et al. 2019; Marchesi et al. 2019; Zaino et al. 2020). These models assume that the intrinsic emission is self-consistently absorbed and reprocessed by the toroidal material. Due to the complexity of the parameter space, “physical” models requires the Markov chain Monte Carlo (MCMC) over the straightforward χ^2 minimization, given the large number of free parameters. In this work, we adopted a “phenomenological” approach for the entire sample, providing more solid constraints on the spectral properties also in the case of low statistics, while we performed a “physical” modelling for those objects with higher quality spectra. To this goal, we considered the MyTorus model by Murphy and Yaqoob [2009].

The spectral analysis was performed using the X-Ray Spectral Fitting Package (XSPEC) v. 12.10.0c [Arnaud, 1996]. All the considered models include a Galactic absorption component, based on the measurements by Kalberla et al. [2005]. To account for potential (minor) variability between non-simultaneous observations (e.g., *NuSTAR* and the counterpart at $E < 10$ keV), as well as different responses between cameras (e.g., FPMA and FPMB in *NuSTAR*; EPIC pn and MOS in *XMM-Newton*), we also included cross-calibration constants. For the objects with *NuSTAR* observations, we set the constant associated with the spectrum obtained with the FPMA equal to one ($C_A = 1$), leaving the remaining constants free to vary. For the three objects lacking of *NuSTAR* observations, we set the cross-calibration constant of the EPIC pn spectrum to unity ($C_{pn} = 1$), leaving the remaining free to vary. For the fitting procedure, we assumed a χ^2 statistic, and χ^2 test as standard goodness-of-fit test. The best-fit value for the spectral parameters presented in Section 2.1.3.1 and 2.1.3.2 were obtained by running Monte Carlo Markov Chain. Upper and lower errors (1 *sigma*) relative to the best-fit parameters are measured as the difference between the best fit value (50th percentile) and the 84th and 16th percentiles, respectively. In the case of NGC 2992, we fit together the longest *NuSTAR* observation with one the

latest XMM-Newton observations (0147920301; Marinucci et al. 2018), with the cross-calibration constants (C_i) included in the spectral model, accounting for the variability between the two observations. Indeed, between the two considered observations, a minor flux variation was observed (about a factor ~ 3).

2.1.3.1 Phenomenological models

Among the plethora of model components available within the XSPEC libraries, we included model dedicated to each one of the spectral components described in 2.1.1. Indeed, our baseline model is composed of:

- i)* a power-law continuum (“pow” in XSPEC) absorbed by neutral material intrinsic to the sources (“zwabs”);
- ii)* a reflection component caused by cold material close to the BH accretion disk (“pexrav”);
- iii)* a variable number of narrow Gaussian functions to model the expected neutral/ionized Fe K-shell emission lines in the interval $E \sim 6.4-7$ keV (“zgauss”);
- iv)* a scattered power-law in the soft X-rays, usually with the same slope of the primary emission, but accounting for only a few % of the primary emission;
- v)* when required to reduce the residuals at $E < 3$ keV, thermal components due to a hot plasma (“mekal”), which accounts for the diffuse emission from the host galaxy.

The adopted fitting strategy is the following: first, we model the absorbed primary continuum emission; then, depending on the presence of residuals at energies above 10 keV, we included the reflection component. Case by case, depending on the residual in the 6.4-7 keV energy band, we tested for the presence of multiple Gaussian functions. We included one components at a time, starting with the neutral Fe $K\alpha$ emission line with rest-frame energy $E = 6.4$ keV. We set the line width to 0.01 keV for the Fe $K\alpha$, and for any additional Gaussian function. Further Gaussian functions were included to account for the neutral Fe $k\beta$ at rest-frame 7.06 keV, and the ionized Fe XXV and Fe XXVI lines at rest-frame 6.7 and 6.97 keV. To determine if it was reasonable to add each new component (different from Gaussian functions), after a visual inspection of the residuals, we run a “F-test”. In case of low “F-test” probability, we include the new component. The “F-test” is not totally reliable to evaluate the statistical significance of the inclusion of Gaussian functions [Protassov et al., 2002], hence we use a visual inspection of the residuals and we evaluated if the new χ^2 was lower and the null hypothesis probability higher. Finally, if an excess was present in the residuals in the soft band ($E < 3$ keV), we

added one phenomenological thermal component to reduce the χ^2 of the best-fit model. The thermal component at energies $E \lesssim 3$ is likely due to both diffuse SF in the host galaxy, as well as X-ray binary objects (e.g, Mineo et al. 2012a; Mineo et al. 2012a), and is clearly visible in *Chandra* images of local Seyfert galaxies, thanks to the high-spatial resolution of the telescope ($<1''$; e.g., Levenson et al. 2004).

| Source | χ^2 | d.o.f. | Γ_X | $F_{2-10keV}$ | $N_H 10^{22} \text{ cm}^{-2}$ | $\log(L_{2-10keV})$ |
|------------------|----------|--------|---|--|--|---|
| CGCG 381-051 | 72.3571 | 90 | 1.9 | 0.02 ^{+0.01} _{-0.02} | 0.11 ^{+0.48} _{-0.08} | 40.7 ^{+0.15} _{-0.39} |
| ESO 033-G002 | 457.96 | 463 | 1.83 ^{+0.04} _{-0.03} | 13.3 ^{+0.4} _{-0.38} | 1.87 ^{+0.15} _{-0.4} | 42.99 ^{+0.01} _{-0.01} |
| IC 5063 | 351.27 | 326 | 1.793 ^{+0.02} _{-0.13} | 17.7 ^{+0.08} _{-1.82} | 24.5 ^{+2.4} _{-0.12} | 42.7 ^{+0.01} _{-0.04} |
| IRAS F01475-0740 | 97.2509 | 129 | 1.983 ^{+0.22} _{-0.02} | 0.62 ^{+0.14} _{-0.23} | 0.46 ^{+0.07} _{-0.05} | 41.64 ^{+0.1} _{-0.16} |
| IRAS F05189-2524 | 610.445 | 506 | 2.10 ^{+0.03} _{-0.02} | 5.83 ^{+0.15} _{-0.08} | 7.79 ^{+0.17} _{-0.16} | 43.39 ^{+0.01} _{-0.01} |
| IRAS F15480-0344 | 43.0337 | 55 | 2.274 ^{+0.026} _{-0.008} | 4.54 ^{+0.11} _{-0.10} | 320.0 ^{+4.2} _{-1.7} | 43.28 ^{+0.01} _{-0.01} |
| MCG-03-34-064 | 1242.83 | 766 | 2.14 ^{+0.03} _{-0.01} | 6.6 ^{+0.1} _{-0.1} | 23.77 ^{+0.02} _{-0.02} | 42.92 ^{+0.01} _{-0.01} |
| MCG-03-58-007 | 789.616 | 465 | 1.90 ^{+0.02} _{-0.03} | 2.49 ^{+0.04} _{-0.09} | 22.98 ^{+0.07} _{-0.07} | 42.75 ^{+0.01} _{-0.02} |
| Mrk 0273 | 167.219 | 166 | 1.95 ^{+0.15} _{-0.09} | 2.19 ^{+0.68} _{-0.39} | 63 ⁺¹³ ₋₇ | 42.86 ^{+0.14} _{-0.08} |
| Mrk 0463 | 170.177 | 123 | 1.93 ^{+0.14} _{-0.15} | 1.98 ^{+1.18} _{-1.01} | 59 ⁺³ ₋₆ | 43.08 ^{+0.26} _{-0.22} |
| Mrk 0897 | 28.9552 | 27 | 1.9 | 0.18 ^{+0.12} _{-0.12} | 22.95 ^{+9.51} _{-11.95} | 41.45 ^{+0.3} _{-0.3} |
| NGC 0034 | 81.9216 | 39 | 1.9 | 0.56 ^{+0.11} _{-0.09} | 40 ⁺¹³ ₋₁₇ | 41.69 ^{+0.08} _{-0.07} |
| NGC 0262 | 1047.32 | 1025 | 1.88 ^{+0.11} _{-0.2} | 90.2 ^{+24.6} _{-30.7} | 18.82 ^{+0.09} _{-1.8} | 43.66 ^{+0.12} _{-0.15} |
| NGC 0424 | 165 | 139 | 1.96 ^{+0.08} _{-0.09} | 6.32 ^{+1.1} ₋₁ | 58 ⁺¹⁹ ₋₃₅ | 42.29 ^{+0.04} _{-0.04} |
| NGC 0513 | 208.165 | 201 | 1.69 ^{+0.01} _{-0.01} | 5.26 ^{+0.33} _{-0.23} | 7.04 ^{+0.03} _{-0.02} | 42.66 ^{+0.03} _{-0.02} |
| NGC 1056 | 95.1894 | 132 | 1.9 | 0.03 ^{+0.01} _{-0.01} | 0.01 ^{+0.01} _{-0.01} | 39.28 ^{+0.13} _{-0.15} |
| NGC 1125 | 146.033 | 90 | 1.92 ^{+0.2} _{-0.29} | 3.27 ^{+1.93} _{-2.91} | 174 ⁺⁶⁴ ₋₃₁ | 41.94 ^{+0.26} _{-0.39} |
| NGC 1320 | 167.3 | 100 | 2.39 ^{+0.13} _{-0.63} | 6.38 ^{+2.26} _{-2.13} | 58 ⁺⁴² ₋₈ | 42.05 ^{+0.15} _{-0.15} |
| NGC 2992 | 902.92 | 902 | 1.72 ^{+0.3} _{-0.19} | 59.8 ^{+1.17} _{-20.8} | 2.7 ^{+3.6} _{-1.6} | 42.9 ^{+0.01} _{-0.15} |
| NGC 3079 | 88.7775 | 82 | 1.47 ^{+0.12} _{-0.05} | 8.8 ^{+2.3} _{-0.6} | 293 ⁺³¹ ₋₂₀ | 41.42 ^{+0.1} _{-0.03} |
| NGC 4388 | 711.244 | 649 | 1.578 ^{+0.002} _{-0.002} | 16.6 ^{+0.2} _{-0.2} | 24.41 ^{+0.02} _{-0.03} | 42.42 ^{+0.01} _{-0.01} |
| NGC 5135 | 91.5995 | 85 | 1.83 ^{+0.06} _{-0.06} | 2.07 ^{+0.98} _{-0.39} | 436.25 ⁺⁶⁰ ₋₅₇ | 41.94 ^{+0.21} _{-0.08} |
| NGC 5256 | 118.228 | 95 | 1.94 ^{+0.19} _{-0.19} | 0.06 ^{+0.04} _{-0.04} | 178 ⁺⁴² ₋₃₁ | 41 ^{+0.35} _{-0.29} |
| NGC 5347 | 90 | 68 | 1.92 ^{+0.29} _{-0.14} | 125 ^{+86.2} _{-57.4} | 463 ⁺¹⁹⁰ ₋₂₀₆ | 43.23 ^{+0.3} _{-0.2} |
| NGC 5506 | 1886.76 | 1670 | 1.96 ^{+0.15} _{-0.19} | 58.8 ^{+42.6} _{-33.1} | 4 ^{+0.08} _{-0.64} | 42.7 ^{+0.31} _{-0.24} |
| NGC 5953 | 63.4281 | 93 | 1.9 | 0.03 ^{+0.02} _{-0.02} | 0.24 ^{+0.45} _{-0.11} | 39.4 ^{+0.34} _{-0.26} |
| NGC 5995 | 520.336 | 539 | 1.9 ^{+0.23} ₋₀ | 15.4 ^{+6.34} _{-9.65} | 1.62 ^{+0.09} _{-0.16} | 43.35 ^{+0.18} _{-0.27} |
| NGC 6890 | 257.562 | 227 | 2.42 ^{+0.04} _{-0.04} | 1.36 ^{+0.21} _{-0.25} | 15.9 ^{+1.16} _{-0.04} | 41.3 ^{+0.07} _{-0.08} |
| NGC 7130 | 194.076 | 147 | 2.2 ^{+0.11} _{-0.16} | 7.18 ^{+1.83} _{-2.29} | 479 ⁺⁵⁶ ₋₉₇ | 42.63 ^{+0.11} _{-0.14} |
| NGC 7674 | 132.92 | 121 | 2.09 ^{+0.33} _{-0.31} | 0.45 ^{+0.21} _{-0.21} | 25 ⁺²⁵ ₋₁₀ | 41.93 ^{+0.21} _{-0.21} |
| TOLOLO 1238-364 | 70.9824 | 80 | 2.34 ^{+0.29} _{-0.06} | 3.99 ^{+2.23} _{-2.18} | 590 ⁺⁴⁶ ₋₁₈₃ | 42.02 ^{+0.24} _{-0.24} |
| UGC 05101 | 42.9 | 37 | 1.9 | 3.16 ^{+0.64} _{-2.24} | 171 ⁺⁴⁵ ₋₂₉ | 43.06 ^{+0.09} _{-0.31} |

Table 2.3: (1): Source name; (2) χ^2 of the best-fit model (3): Degree of freedom; (4): X-ray Spectral index. For 7 sources we assumed $\Gamma_X = 1.9$ (hence reported in the Table without errors) because we were not able to determine the spectral index from the fit; (5): Intrinsic 2-10 keV flux, in units of $10^{-12} \text{ erg s}^{-1} \text{ cm}^{-2}$; (6) Column density of the obscuring material in units of 10^{22} cm^{-2} ; (7) Logarithm of the intrinsic 2-10 keV luminosity, in units of erg s^{-1} . Quantities which are provided without errors were left fixed during the fitting procedure.

We also checked the consistency of the results from our X-ray spectral analysis with the literature: our best-fit parameters resulted consistent with the extensive literature on

these objects. In particular, we focused on the determination of the column density of the obscuring material, allowing us to infer the intrinsic luminosity ($L_{2-10\text{keV}}$, L_X hereafter). The summary of the best-fit parameters which are more relevant to the analysis we are presenting are reported in Table 2.3. Some of the best-fit spectra are presented in Fig. 2.1, while the remaining are shown in Appendix A.

2.1.3.2 MyTorus

To investigate the structure and geometry of the torus, which is responsible for the obscuration and reprocessing of the AGN primary emission in the X-rays, we used the MyTorus code by Murphy and Yaqoob [2009]. MyTorus includes three distinct and separable components. The first one accounts for the attenuation of the primary emission (usually a power-law); it contains the photo-electric absorption and Compton scattering terms which are responsible for the suppression of the emission in the soft band in heavily obscured AGN. This component is primarily parametrised with the column density of the neutral hydrogen N_H . The second MyTorus component is the scattered continuum, also known as the “reflected component”, i.e. the photons that interact with the material surrounding the SMBH and are hence reflected toward the observer. Finally, the third component models the neutral fluorescence Fe K lines, namely the Fe $K\alpha$ and $K\beta$ at 6.4 and 7.06 keV, respectively.

Each one of the three components depends on the column density of the obscuring material and the viewing angle (i.e. the angle between the observer and the torus axis), which can be fitted separately. Furthermore, the relative normalisation of the three components can be “decoupled” by adding a cross-normalisation constant in front of them free to vary. Since the physical interpretation of different inclination angles and column densities among the three components is not straightforward, our baseline model assumes inclination angles and N_H tied together, while we let the cross-calibration constants (A_S and A_L for the scattered and emission lines components, respectively) free to vary if necessary. It is worth noticing that in 9 cases, we have to fix the inclination angle. The choice of the fixed inclination angle was chosen upon the following strategy: we fixed the inclination angle at increasing value from 60° to 90° , with $\delta_\theta = 5^\circ$. We compared the best-fit χ^2 value obtained for each model, hence we selected the one with the lowest χ^2 . Depending on the spectrum of each sources, we added more Gaussian functions for the potential highly-ionised Fe lines (e.g., XXV/XXVI at rest-frame 6.637 and 6.966 keV, respectively), as well as thermal components (“mekal”), and a scattered continuum (see also Sect. 1.1.2 for further details). Moreover, to limit the degeneracy among different models, we fixed the spectral index of the primary power-law in the torus model to the one obtained with “phenomenological” models.

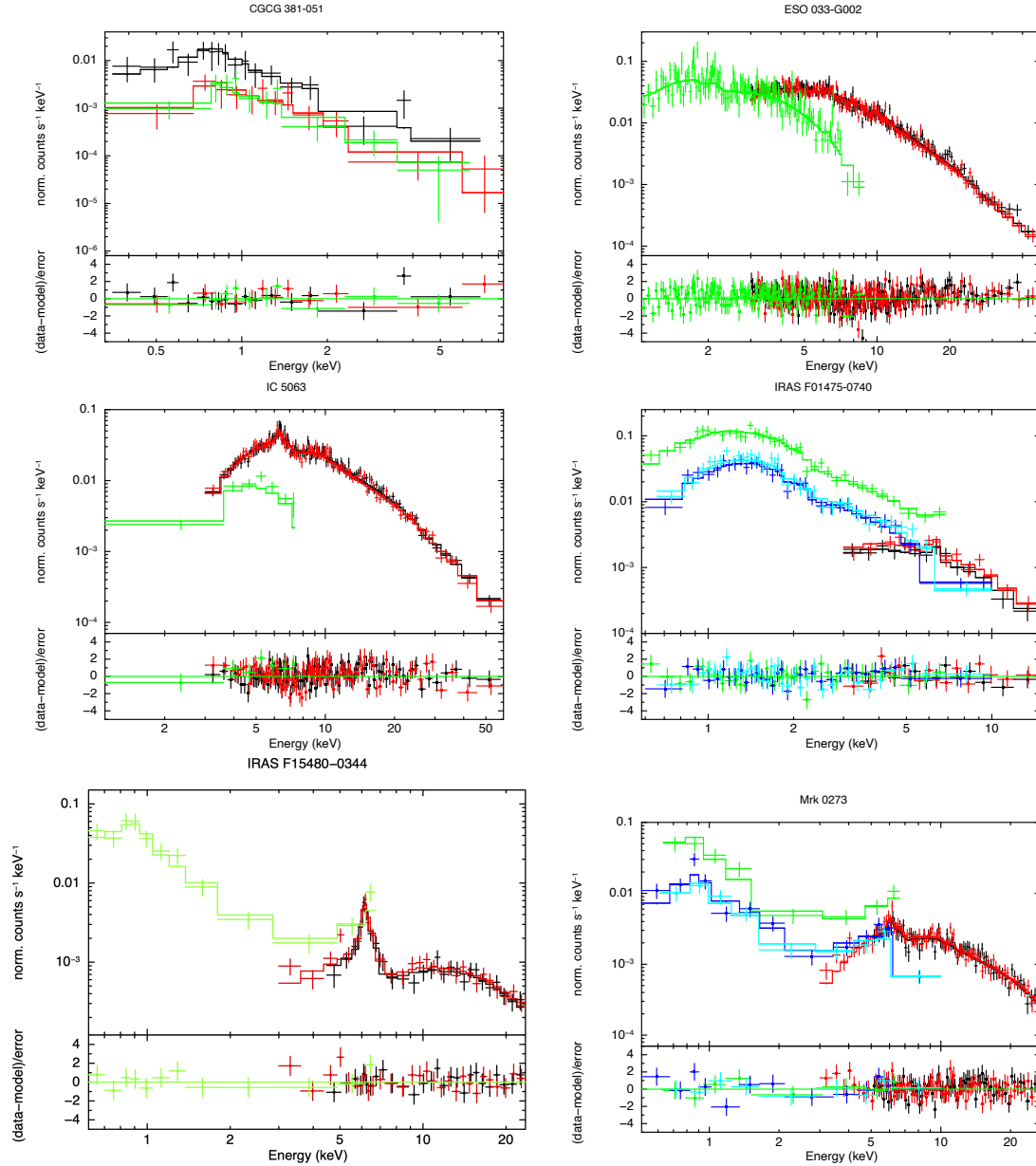


Figure 2.1: X-ray spectra of the objects in our sample, analysed using the “phenomenological” model. In the upper panel, the spectrum and best-fit model, expressed in normalised counts s^{-1} ; in the bottom panels, the residuals (data minus model) are expressed in units of σ . The dataset included in each plot are listed in Table 2.2 and are color coded depending on the order we gave at the spectra: 1st in black, 2nd in red, 3rd in green, 4th in cyan, 5th in blue. When available, *NuSTAR* FPMA and FPMB are the 1st and 2nd spectra, respectively; then we included one observation either from *XMM-Newton* (EPIC pn, MOS1 and MOS2), *Chandra* or *Swift*.

Given the complexity of the model, as well as the range of column density included in the libraries ($10^{22} < N_H < 10^{25} \text{ cm}^{-2}$), we tested the MyTorus code for most of the sources in our sample, but we avoid the targets with spectra with low-counts statistics (for NGC 1056 we measure $\lesssim 200$ counts with FPMA, while no detection at all with FPMB) or those not observed with *NuSTAR* (CGCG381-051, Mrk 897, NGC 5953). In Table 2.4 we present the results of our spectral analysis for the 28 Seyfert 2 galaxies for which we performed the modelling with MyTorus. Six of the best-fit spectra obtained with MyTorus are shown in Fig. 2.2, while the remaining are shown in Section A.

| Source | χ^2 | d.o.f. | $N_H 10^{24} \text{ cm}^{-2}$ | inc | A_L | A_S |
|------------------|----------|--------|-------------------------------|-----------------------|------------------------|---------------------------|
| ESO 033-G002 | 521.77 | 458 | $0.02^{+0.01}_{-0.01}$ | 85 | 1 | 1 |
| IC5063 | 402.762 | 363 | $1.38^{+0.26}_{-0.52}$ | $60.7^{+0.5}_{-0.3}$ | 1 | 1 |
| IRAS F01475-0740 | 104.63 | 122 | $0.0102^{+0.003}_{-0.001}$ | 85 | 30^{+110}_{-15} | 220^{+80}_{-70} |
| IRAS F05189-2524 | 610.445 | 510 | $0.073^{+0.001}_{-0.001}$ | 85 | 1 | 1 |
| IRAS F15480-0344 | 59.64 | 60 | $1.753^{+0.001}_{-0.001}$ | 85 | 157^{+120}_{-71} | 390^{+290}_{-180} |
| MCG-03-34-064 | 1007.1 | 763 | $0.617^{+0.004}_{-0.009}$ | 85 | $14.0^{+1.2}_{-1.4}$ | $6.0^{+1.7}_{-1.9}$ |
| MCG-03-58-007 | 751.707 | 470 | $0.109^{+0.003}_{-0.001}$ | 85 | $3.8^{+0.8}_{-0.1}$ | $4.4^{+0.5}_{-0.7}$ |
| Mrk 0273 | 184.56 | 168 | $0.61^{+0.04}_{-0.04}$ | 83^{+7}_{-4} | $1^{+0.2}_{-0.110}$ | $0.87^{+0.08}_{-0.11}$ |
| Mrk 0463 | 193 | 128 | $0.83^{+0.28}_{-0.06}$ | 85^{+4}_{-2} | $6.3^{+1.8}_{-1.4}$ | $3.3^{+0.4}_{-1.0}$ |
| NGC 0034 | 55.7 | 39 | $0.62^{+0.22}_{-0.12}$ | 72^{+7}_{-2} | 1 | 1 |
| NGC 0262 | 1834.7 | 1025 | $0.20^{+0.00}_{-0.12}$ | $90^{+0}_{-6.8}$ | $0.11^{+0.1}_{-0.050}$ | $1.5^{+0.02}_{-1.3}$ |
| NGC 0424 | 187.1 | 138 | $2.18^{+0.08}_{-0.14}$ | 87^{+3}_{-5} | $1.05^{+0.15}_{-0.09}$ | $0.97^{+0.09}_{-0.05}$ |
| NGC 0513 | 232.5 | 205 | $0.05^{+0.00}_{-0.00}$ | 90 | $1.05^{+0.08}_{-0.18}$ | $0.47^{+0.18}_{-0.12}$ |
| NGC 1125 | 137.4 | 95 | $1.46^{+0.01}_{-0.01}$ | 82^{+2}_{-1} | $4.4^{+1.0}_{-1.4}$ | $10.1^{+2.4}_{-3.4}$ |
| NGC 1320 | 123.4 | 87 | $2.17^{+0.13}_{-0.12}$ | $89^{+0.6}_{-2}$ | $43^{+1.0}_{-5}$ | $7.8^{+0.5}_{-0.7}$ |
| NGC 2992 | 993.351 | 894 | $0.0116^{+0.0002}_{-0.0001}$ | 85 | 1 | $12.2^{+3.2}_{-1.8}$ |
| NGC 3079 | 88.5552 | 83 | $2.3237^{+0.0040}_{-0.0004}$ | 90 | 1 | 1 |
| NGC 4388 | 850.19 | 647 | $0.248^{+0.002}_{-0.003}$ | 90 | $2.45^{+0.10}_{-0.16}$ | $2.74^{+0.02}_{-0.19}$ |
| NGC 5135 | 133.87 | 90 | $2.51^{+0.28}_{-0.59}$ | 88^{+3}_{-6} | $3.20^{+2.9}_{-1.5}$ | $1.0^{+0.3}_{-0.1}$ |
| NGC 5256 | 145.84 | 95 | $0.16^{+0.04}_{-0.06}$ | 90 | 1 | $0.8^{+0.5}_{-0.4}$ |
| NGC 5347 | 47.8919 | 67 | $3.3^{+0.3}_{-0.4}$ | 77^{+5}_{-4} | $5.9^{+1.6}_{-1.2}$ | $2.0^{+0.6}_{-0.3}$ |
| NGC 5506 | 2721.28 | 1674 | $0.03^{+0.01}_{-0.01}$ | 85 | $0.35^{+0.43}_{-0.23}$ | $0.76^{+0.13}_{-0.31}$ |
| NGC 5995 | 539.506 | 525 | $0.01^{+0.00}_{-0.00}$ | 90 | $1.35^{+0.22}_{-0.28}$ | $0.88^{+0.1}_{-0.32}$ |
| NGC 6890 | 243.825 | 229 | $0.25^{+0.02}_{-0.02}$ | 90 | $11^{+2}_{-2.478}$ | $0.002^{+0.001}_{-0.001}$ |
| NGC 7130 | 134.975 | 114 | $3.15^{+1.05}_{-2.02}$ | $89.3^{+0.7}_{-84.3}$ | $1.12^{+0.1}_{-0.09}$ | $1.04^{+0.09}_{-0.17}$ |
| NGC 7674 | 176 | 129 | $0.34^{+0.04}_{-0.02}$ | 90 | $0.68^{+0.02}_{-0.04}$ | 1 |
| TOLOLO 1238-364 | 98.1556 | 80 | $9.24^{+0.70}_{-2.68}$ | 71^{+6}_{-8} | 1 | 1 |
| UGC 05101 | 52.5084 | 41 | $1.57^{+0.10}_{-0.29}$ | 85 | 1 | 1 |

Table 2.4: (1): Source name; (2) χ^2 of the best-fit model (3): Degree of freedom; (4): Column density of the obscuring material in units of 10^{24} cm^{-2} ; (5): Inclination angle of the torus, in degree; (6) Cross-calibration factor of the emission line component; (7) Cross-calibration factor of the scattered component. Quantities which are provided without errors were left fixed during the fitting procedure.

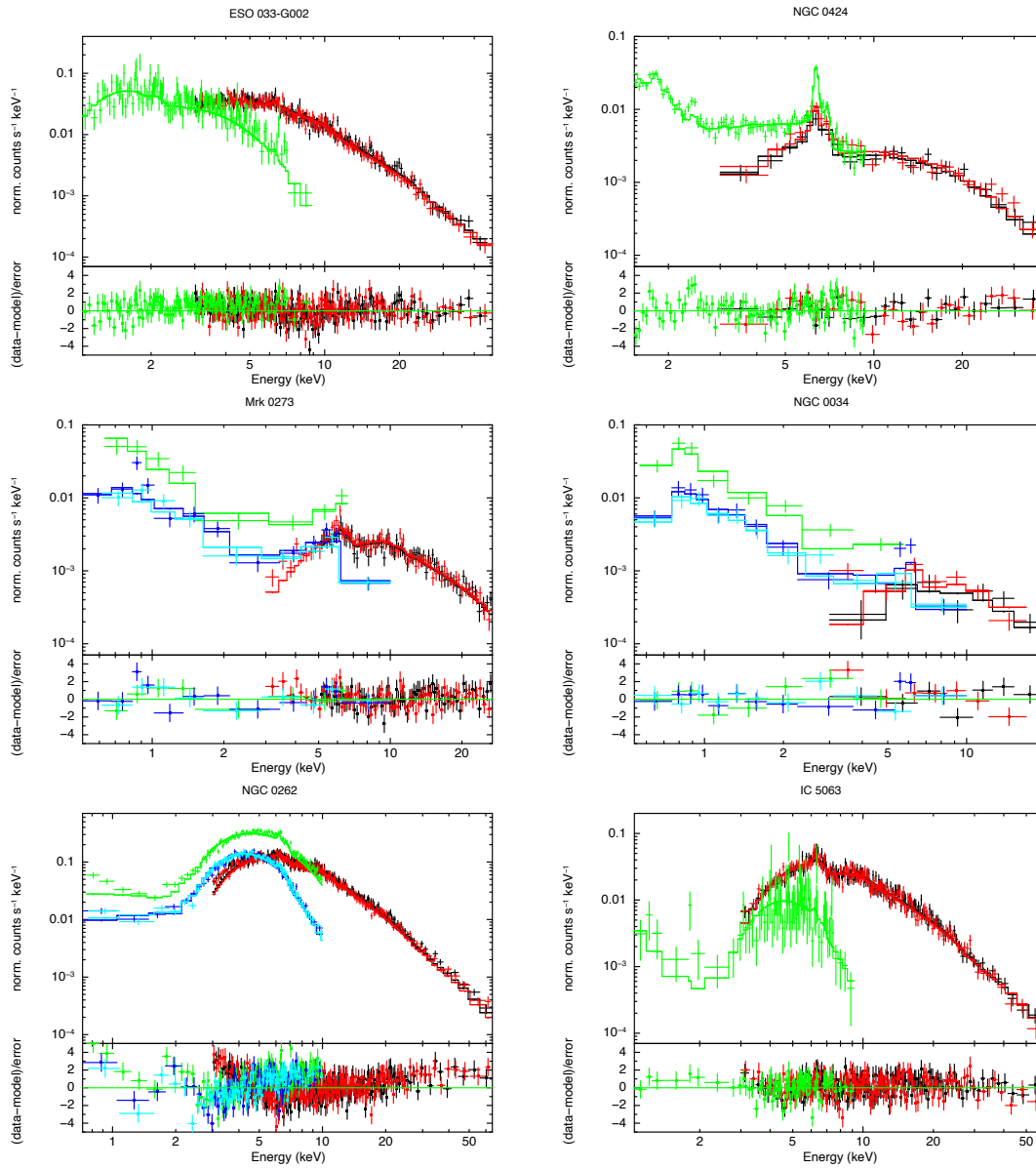


Figure 2.2: X-ray spectra of the objects in our sample, analysed using MyTorus model. In the upper panel, the spectrum and best-fit model, expressed in normalised counts s^{-1} ; in the bottom panels, the residuals (data minus model) are expressed in units of σ . The dataset included in each plot are listed in Table 2.2. The color code is the same as in Fig. 2.1.

2.1.4 Decomposed SED

As already quoted in Section 2.1, our group dedicated a paper (G16) to the analysis of the broad-band spectral energy distribution decomposition (SED) of a sample of 76 mid-IR selected galaxies out of the 12 μm galaxy sample (12MGS; Rush et al. 1993). Given the wealth of multi-wavelength data, from the X-rays to the sub-millimetre, G16 were able to constrain the relative contribution of the stellar, AGN and SF components to the global output of the source. In the case of obscured (narrow-line) Seyfert galaxies, the UV-optical band is dominated by the stellar emission, and the cold diffuse dust is mainly responsible for the far-IR bump. The mid-IR band ($\sim 2.5\text{-}35 \mu\text{m}$) of an active galaxy presents a combination of different components: the thermal radiation from a dusty, compact medium (i.e., the dusty torus); the thermal dust continuum associated with SF; a plethora of spectral features (e.g., polycyclic aromatic hydrocarbon, PAH; the silicate feature at $9.7 \mu\text{m}$) and emission lines (arising from molecular, atomic, and ionic species). G16 included (rebinned) *Spitzer*/IRS spectra, increasing the information in the mid-IR regime. This is crucial to place solid constrain on the relative contribution from the AGN and SF. In addition to the *Spitzer*/IRS spectra, G16 collected wide-band aperture corrected photometry, from the UV to the far-IR wavelengths, from the NASA/IPAC Extragalactic Database (NED)⁸ (see their Table A1 and A2). Here we briefly summarize the approach adopted in G16, while we refer to the relevant paper for details about the SED fitting procedure and the selection of the archival data. The SED-fitting code adopted is SED3FIT (Berta et al. 2013⁹) that reproduces simultaneously the stellar emission and the reprocessed emission from the dust – heated by both stars and the AGN. The code relies on a collection of libraries, in particular the library by Bruzual and Charlot [2003] for the stellar contribution, the one by da Cunha et al. [2008] for the IR dust-emission, and the library of AGN tori by Fritz et al. [2006], updated by Feltre et al. [2012]. An example of decomposed SED for one of our object (NGC 2992) is presented in Fig. 2.3. In Table 3 of G16, the author reported the results of the SED decomposition for their entire sample, among which the 28 objects of our current sample (see Table 2.1). The SED fitting analysis by G16 provided the main host-galaxy properties, namely the SFR (obtained through the Kennicutt 1998 relation), stellar and dust masses (measured as prescribed by da Cunha et al. 2008), IR luminosity (integrated over the 8-1000 μm spectral range), as well as the measurements of the contribution from the AGN, i.e. the bolometric luminosity (L_{bol}) and the fraction of the emission in the 5-40 μm regime (f_{AGN}). To compare the level of extinction in the X-rays and mid-IR, we collect the measurements of the depth ($\tau_{9.7\mu\text{m}}$) of the 9.7 μm silicate feature, as modelled by the dusty torus

⁸<https://ned.ipac.caltech.edu/>

⁹<http://steatreb.altervista.org/alterpages/sed3fit.html>

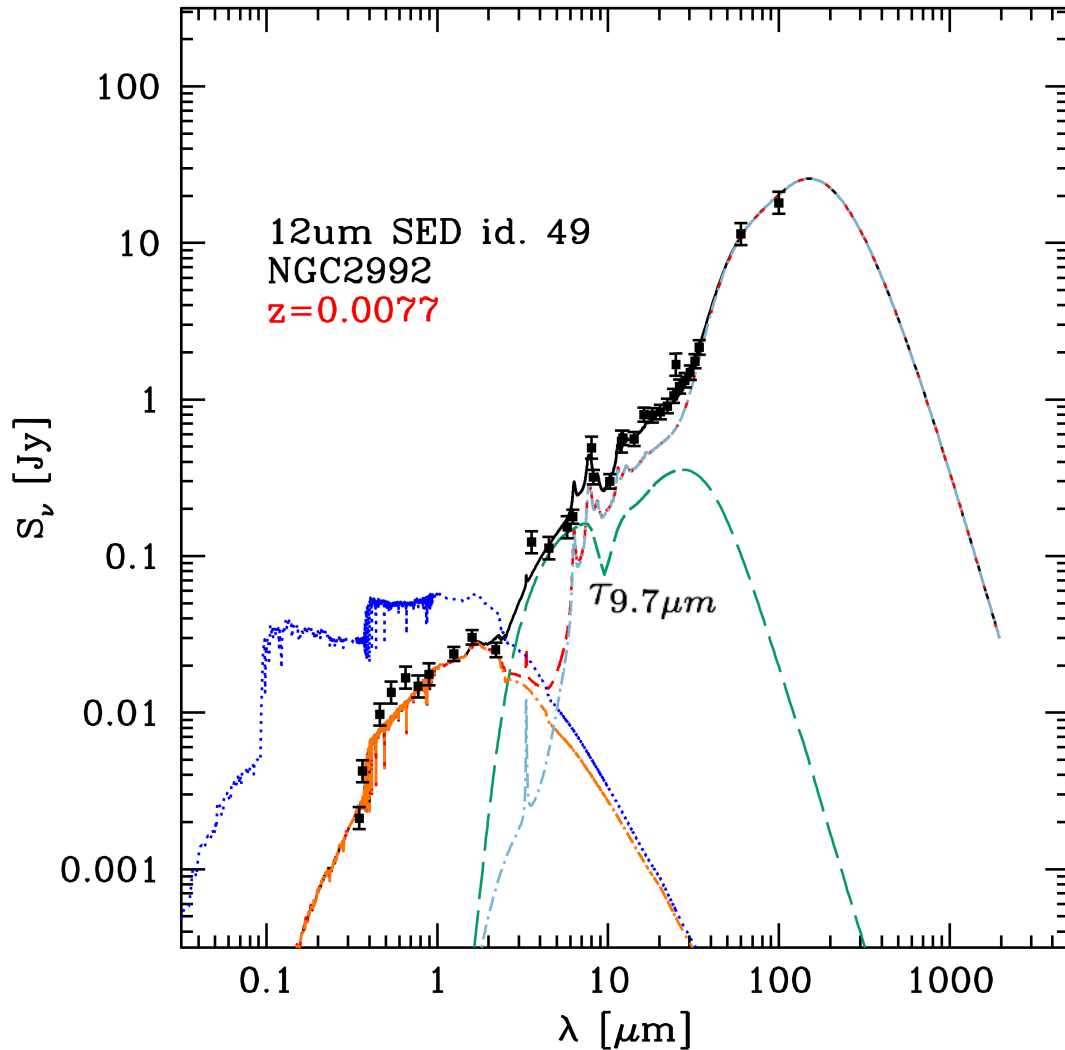


Figure 2.3: Example of decomposed SED for NGC 2992 by G16: un-absorbed and absorbed stellar components are in blue and orange, respectively; the dashed green line is for the dusty torus component, red dashed lines show the combination of extinguished stars and dust IR emission, while pale-blue dot-dashed lines show the dust re-emission. The total emission is in black. The 9.7 μm silicate feature is clearly visible as an absorption feature in the torus model.

component in the SED fitting analysis by G16, to infer the column density of the obscuring material in the mid-IR. Given the relation between the line-of-sight optical depth at 9.7 μm and the corresponding extinction:

$$\frac{A_{9.7\mu\text{m}}}{\text{mag}} = 1.086\tau_{9.7\mu\text{m}}, \quad (2.1)$$

we assumed the V-band extinction to be $A_V = A_{9.7\mu\text{m}} = 19$ [Roche and Aitken, 1985]. Then, we derived the corresponding line-of-sight column density by assuming a dust-to-gas ratio dust-to-gas ratio of $N_{H,9.7\mu\text{m}} = 1.63 \times 10^{21} A_V \text{cm}^{-2} \text{mag}^{-1}$ [Savage and Mathis,

1979].

2.1.5 Mid-IR features

As presented in Chapter 1 and discussed in Section 2.1.4, the mid-IR spectra of the central region of local sources offer a wealth of spectral features which are fundamental diagnostics of the SF vs. AGN interplay. The 2.5-35 μm spectral range is characterised by the concurrent contributions from the thermal continuum emission from the dust associated with SF, as well as spectral features and lines arising from the different gas component (molecular, atomic and ionised), and, if present, the bump due to the AGN radiation reprocessed by the dust. Many of these spectral features have been widely used to determine the impinging mechanism responsible for the observed emission, among which the PAH features, which are associated with SF activity, but can be affected by the presence of strong radiation fields from the AGN (e.g., Armus et al. 2007; Valiante et al. 2007; Sajina et al. 2008). To our purpose, here we are interested in the silicate feature at 9.7 μm , which can be either in absorption and emission. Usually, in the case of obscured AGN as the Seyfert 2 galaxies in our sample, this feature is in absorption, hence it can be used as a proxy of the column density of the obscuring material (e.g., Shi et al. 2006; Xu et al. 2020), which we compare to the one derived from the X-ray spectral analysis.

To this goal, we collected measurements of mid-IR features from the work by Hernan-Caballero and Hatziminaoglou [2011] (HC11, hereafter) for 30 objects out of 32 with X-ray spectral analysis. In HC11, the authors analysed *Spitzer*/IRS spectra of 739 sources, both active and SFGs with redshift up to ~ 3.7 , gathered from a large number of observational campaigns (see Table 1 in HC11 for more details and references). HC11 provided the mid-IR measurements such as the PAH, the strength of the silicates (either in emission or absorption) around 9.7 μm , rest-frame monochromatic luminosities or colours, used as diagnostics to classify the sources in terms of their mid-IR properties. In the case of local objects from HC11 – including the 30 in common with our sample – the *Spitzer*/IRS spectra sample the emission from the nuclear region, where the contribution from the AGN is quite relevant. The actual extraction area depends on the slit mode and the distance of the source ¹⁰, but the central few kpc region was sampled even in the closest objects in our sample.

Since a significant fraction of the *Spitzer*/IRS spectra included in the work by HC11 presented a low signal-to-noise ratio, this made difficult a proper modelling of the mid-IR features. For this reason, the authors defined a homogeneous and concise method providing solid estimates for each source, by combining the linear interpolation of the

¹⁰See also https://irsa.ipac.caltech.edu/data/SPITZER/docs/files/spitzer/irs_pocketguide.pdf for further details on the *Spitzer*/IRS specifications.

continuum with the integration of the emission from the features. In particular, in the case of the $9.7 \mu\text{m}$ silicate features we are interested in, the authors selected two narrow, continuum bands at both sides of each feature, performed a linear interpolation to estimate the continuum around the feature. They then subtracted from the spectrum the interpolated continuum, and integrate the residual (silicate feature) in the $9\text{--}11 \mu\text{m}$ range. The sign of this quantity allows us to determine whether the feature is in emission (integral > 0) or in absorption (integral < 0). For further details about the procedure, we refer to Section 4 in HC11.

2.2 Results and discussion

In this section we present the results of the X-ray spectral analysis, with the aim to provide a complete characterisation of the X-ray properties of our sample of Seyfert 2 galaxies. We compared the results obtained with the “phenomenological” and “physical” (MyTorus) modelling strategy, to test for the consistency of the two approaches. Moreover, we compare the properties of our targets in the X-rays and in the mid-IR. In particular, we investigate if the level of extinction estimated in the X-ray correlate with the obscuration derived from the silicate feature in the mid-IR.

2.2.1 X-ray properties

The results of the X-ray spectral analysis using “phenomenological” models are presented in Table 2.3, while the results obtained with MyTorus are presented in Table 2.4. In Fig. 2.4 we show the $L_X\text{--}N_H$ diagram, where L_X is the intrinsic 2–10 keV luminosity of the AGN primary emission, and N_H is the column density of the obscuring material which is responsible for the extinction of the primary power-law component, both resulting from the “phenomenological” modelling. As it is shown in Fig. 2.4, our sample covers more than 3 orders of magnitude in terms of both intrinsic rest-frame 2–10 keV luminosity ($L_X \sim 10^{40\text{--}44} \text{ erg s}^{-1}$) and column density ($N_H \sim 10^{21\text{--}25} \text{ cm}^{-2}$) of the obscuring material. The mean spectral index $\Gamma_X = 1.96 \pm 0.17$ (where $\sigma = 0.17$ is the dispersion) in our sample is in agreement with that found obscured AGN in the local Universe (e.g., Laha et al. 2020).

The bulk of the sample show X-ray luminosities which are characteristic of the population of local obscured AGN (e.g., Ricci et al. 2017). Few objects (NGC 1056, NGC 5953, CGCG 381-051) show a relatively weak intrinsic X-ray luminosity (lower than $10^{41} \text{ erg s}^{-1}$): this could be due to the presence of a low-luminosity AGN at their centre, or an inactive nucleus. Indeed, on the base of the optical classification reported in the

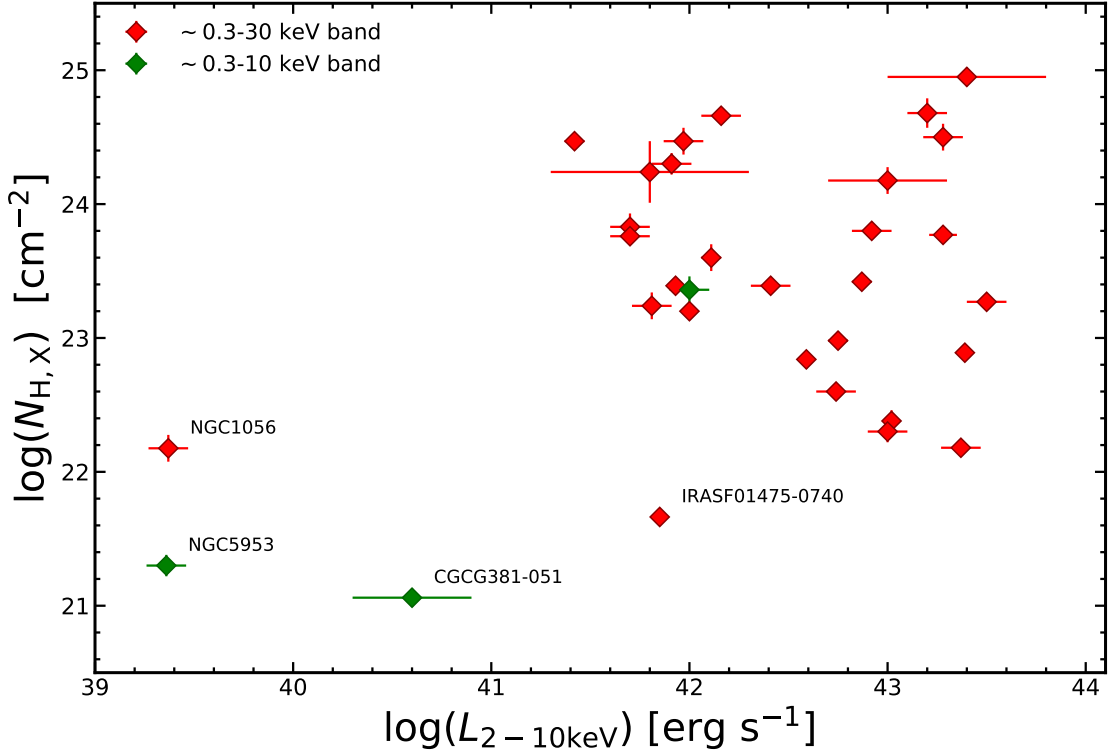


Figure 2.4: Logarithm of the intrinsic 2-10 keV luminosity of the AGN, in units of erg s^{-1} , against the logarithm of the column density of the obscuring material (N_H , in units of cm^{-2}), as derived from the X-ray spectral analysis. Red diamonds represent the object with *NuSTAR* observation (coupled with other X-ray datasets at lower energies), while green diamonds are the sources with were observed only in the band below 10 keV (see Table 2.2). The name of the objects showing either relatively low luminosities or low absorption in the X-rays with respect to the bulk of the sample are reported.

NED catalogue, NGC 5953 is a Seyfert 2 galaxies hosting a low-luminosity AGN, CGCG 381-051 is an HII region galaxy, while NGC 1056 is more likely a star forming galaxy, as confirmed by the new *NuSTAR* observation presented here, where the source is barely detected (signal-to-noise ratio ~ 1 and ~ 5 in FPMA and FPMB, respectively). NGC 1056, for which we obtained a new *NuSTAR*-XMM-*Newton* observation, resulted a relatively weak source ($L_X = 39.28^{+0.13}_{-0.15} \text{ erg s}^{-1}$) also when observed with *NuSTAR* which confirmed the luminosity measured by XMM-*Newton* in 2011 (ID:655381201). Nonetheless, the observation was designed to clearly detect the source (with the net expected counts four times larger than those detected) even in the case of extreme obscuration ($N_H \sim 5 \times 10^{24} \text{ cm}^{-2}$). Given the faint emission mostly observed in the band below 10 keV, we cannot exclude that this galaxy does not host an AGN at all, as suggested by the classification of its nuclear activity from NED. Indeed, the expected contribution from host-galaxy X-ray binaries to the X-ray luminosity ($L_{2-10\text{keV}}^{XRB} = 1.7 \pm 0.2 \text{ erg/s}$, assuming the recipe by Mineo et al. 2012b) is consistent with the one we measured. Further investigation on the nature

of this object will be carried out in the next future, also including multi-wavelength data (e.g. new optical spectra). For NGC 5953 we are waiting for a new *NuSTAR* observation (ID:06158, PI: Salvestrini) which will allow us to reveal the emission at $E > 10$ keV, where the extinction is less efficient. We will also apply in the future for the observation of CGCG 381-051 with *NuSTAR*.

From both the “phenomenological” and “physical” modelling of the X-ray emission from IRAS F01475-0740 we measured a low column density. This Seyfert galaxy is likely an intermediate object between type 1 and type 2 AGN, as suggested by its optical classification [Véron-Cetty and Véron, 2006].

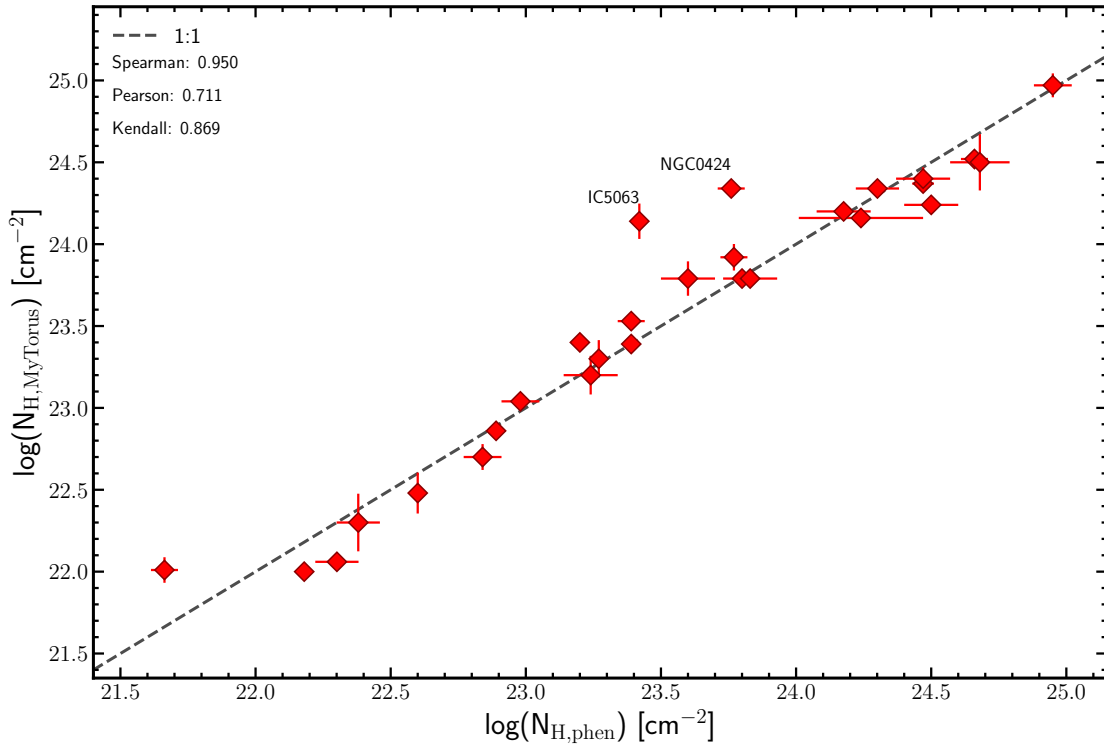


Figure 2.5: Logarithm of the column density of the obscuring material (N_H , in units of cm^{-2}), as derived from the X-ray spectral analysis with the “phenomenological” model (x-axis) and MyTorus (y-axis). In the both models, the N_H considered is the one associated with the attenuation of the primary power-law emission. In the top left corner, the Spearman, Pearson and Kendal correlation coefficients are shown: all of them suggest that the the column density measured with the two modelling approaches correlate. The grey dashed line is the 1:1 relation. Two objects (IC5063 and NGC 0424) deviates significantly from the 1:1 relation.

As quoted in Section 2.1.3.2 regarding the modelling with MyTorus, the best-fit models have been obtained using as prior the information from “phenomenological” model (e.g., the spectral index) to limit the degeneracy among the available parameters. The results we present here have been obtained by assuming the spectral slope to be

the one obtained from the “phenomenological” modelling, while the column density, along with the inclination angle, was left free to vary in MyTorus. In Fig. 2.5 we compared the column density of the obscuring material as estimated with MyTorus (y-axis) and with the “phenomenological” model (x-axis). A general agreement between the estimates derived with the two models is evident, as shown by the correlation coefficients (Spearman, Pearson, Kendall) in the top left corner of Fig. 2.5. Only a couple of objects (and NGC 0424) deviate significantly from the 1:1 relation. In the case of IC5063, the “phenomenological” model is likely underestimating the column density of the obscuring material, which is not coherently modelled to reproduce both the transmitted and the reflected components. Looking at the best-fit parameters from the modelling with MyTorus in Table 2.4, the cross-calibration constant between the reflected component and the transmitted one is large ($A_S = 60.7^{+0.5}_{-0.3}$). For NGC 0424, both the reflected and the emission lines components are strong, hence produced by a dense medium. Even in this case, in the “phenomenological” model, the reflected, transmitted and emission line components are reproduced separately, hence they do not provide a coherent estimate of the column density of the obscuring torus.

A possible future development of this work could be the use of the MyTorus model leaving the column densities of the different components (namely, transmitted, reflected and emission line) free to vary. This approach is usually referred to as “decoupled” mode, when each component is characterised by a single column density of the obscuring material. The interpretation of different column density cannot be always straightforward, but it is a simple way to test the potential clumpy nature of the torus, as observed in several literature work (see Sect. 1.1.2). Indeed, the different component (i.e., attenuated, reflected and the emission line terms) originate when the primary emission interact with different part of the surrounding medium, whose density profile may differ locally. Of course this approach require high-photon counts data to properly model the spectra, otherwise the larger number of free parameters would lead to degeneration between different models in the case of low quality spectra.

2.2.2 Mid-IR and X-ray properties

As discussed in Sect. 1.1, to investigate the intrinsic emission of heavy obscured AGN we need to rely on information from bands that are less affected by extinction, with respect of the optical/UV band, namely the mid-IR and X-ray bands. For this reason, here we compare the X-ray and mid-IR properties of our sample of Seyfert 2 galaxies. First, we compare the intrinsic X-ray luminosity obtained from the primary continuum emission, obtained with the “phenomenological” modelling of the X-ray spectra, with the

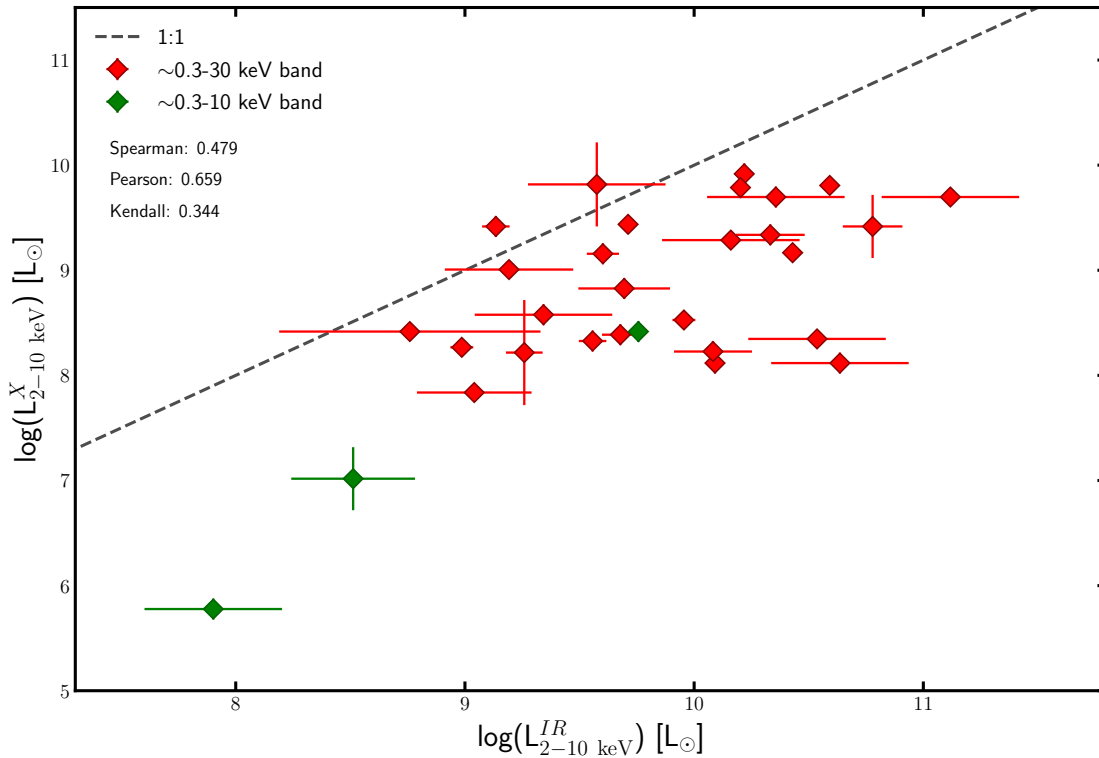


Figure 2.6: Logarithm of the intrinsic 2-10 keV luminosity of the AGN, in units of L_{\odot} , as derived from the X-ray spectral analysis (y-axis) and derived from L_{bol} , by assuming a bolometric correction (x-axis). The correlation coefficients are shown in the top left corner. The grey dashed line is the 1:1 relation. Red diamonds represent the object with *NuSTAR* observation, while green diamonds are the sources with were observed only in the band below 10 keV (see Table 2.2). Here are plotted only 30 Seyfert 2 galaxies out of the 32 with X-ray spectral analysis, since Gruppioni et al. [2016] did not provide the bolometric luminosity for NGC 1056 and NGC 7130.

expected one from the bolometric luminosity of the AGN, as estimated by G16 with the SED fitting analysis. To this end, we assumed for each source, a bolometric correction factor ($k_{bol} = L_{bol}/L_{2-10 keV}$) depends on the bolometric luminosity of the source (we assumed the L_{bol} provided by G16). The k_{bol} values are taken from Lusso et al. [2012] and for our Seyfert 2 galaxies they range between 10 and 25 (see also the recent work by Duras et al. 2020). To account for the wide range of possible k_{bol} for a given L_{bol} , we added in quadrature a ~ 0.3 dex contribution to the uncertainty on the error on 2-10 keV luminosity derived from the L_{bol} . As shown in Fig. 2.6, a correlation between the two quantity is present. Nevertheless, the X-ray luminosity as inferred from the AGN bolometric luminosity provided by G16 are significantly brighter (~ 0.6 dex) than the corresponding values measured from the X-ray spectral analysis. This can be due to a potential contamination from the host-galaxy in the determination of L_{bol} derived from the SED fitting. Alternatively, since our Seyfert 2 galaxies came from a mid-IR selected sample of Luminous Infrared Galaxies (LIRGs; $L_{IR} > 10^{11} L_{\odot}$), our AGN sample

intrinsically emit a larger fraction of its emission in the IR, where the AGN primary continuum is reprocessed by the dusty torus.

In Section 1.1, we stressed the potentiality of combining the information in the mid-IR and X-rays, allowing us to put constrain on the level of obscuration that affect the AGN, which is mainly due to a dusty molecular torus. In Section 2.1.3, we presented how by modelling of the attenuated spectral shape in the X-rays, we are able to derive the intrinsic slope and the column density of the obscuring material which affect the primary AGN emission.

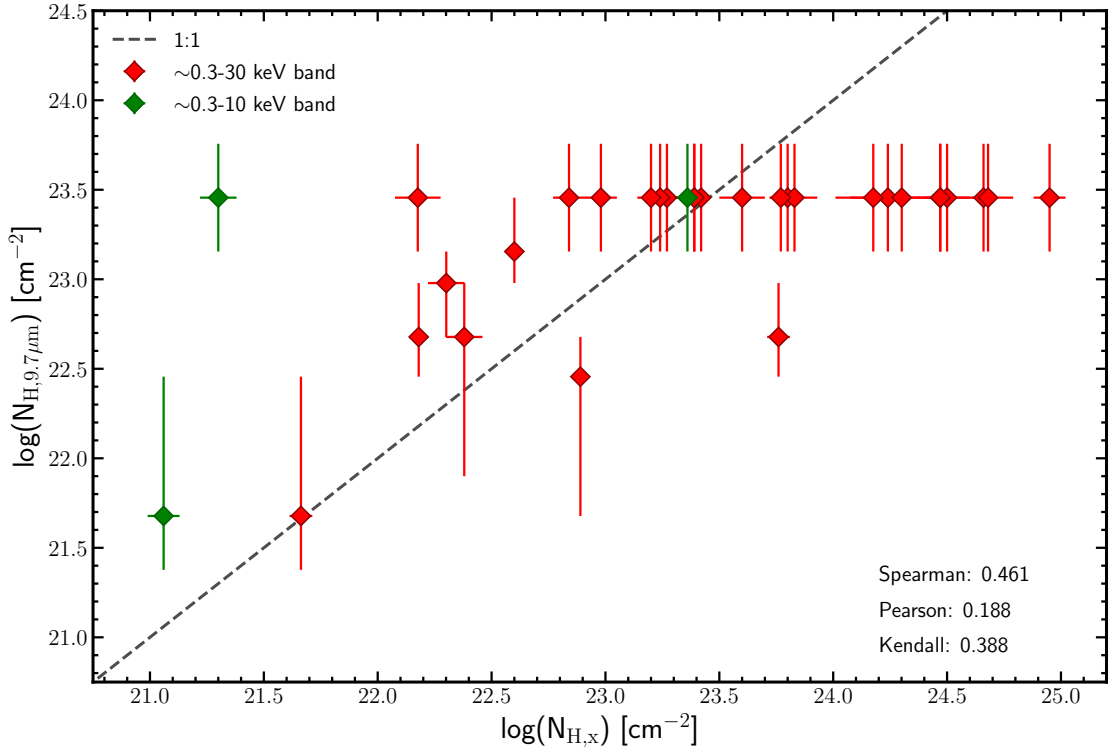


Figure 2.7: The comparison of the neutral gas column density estimated from the $9.7 \mu\text{m}$ silicate absorption feature (y-axis) versus the one obtained from the X-ray obscuring material, both in units of cm^{-2} . The objects observed with both *NuSTAR* and a telescope in the band below 10 keV are in red, while those observed only in the band $E < 10$ keV are in green. The black solid line is the bisector (1:1) and was included only for illustrative purpose. The correlation coefficients are shown on the top left corner.

The silicate feature at rest-frame $9.7 \mu\text{m}$ can be used as a proxy of the obscuration in the mid-IR. Indeed, the silicate feature, which have been observed being mostly in emission in Seyfert 1 objects, and in absorption in Seyfert 2 galaxies, is thought to correlate with the extinction level in the X-rays [Shi et al., 2006]. Several studies have investigated this topic, suggesting also a potential contribution to the feature depth coming

from the galaxy, especially in the case of the deepest strengths [Goulding et al., 2012]. Here, we study this correlation in our sample of mid-IR Seyfert 2 galaxies.

In Fig. 2.7, we compare the column density of the obscuring material measured from the “phenomenological” X-ray spectral analysis ($N_{H,X}$), with the one derived from the strength of the $9.7 \mu\text{m}$ silicate feature as modelled in the SED fitting analysis by G16. We used the results of the “phenomenological” modelling, being available for a larger number of objects. The fact that the library of torii used in the SED decomposition analysis included only a limited number of discrete values, is evident by looking at the possible values of the column density on the y-axis, and on the associated uncertainties, which account for the distance between these discrete values. A weak correlation is present, even if there is a large scatter of $N_{H,X}$ values for the highest $N_{H,9.7\mu\text{m}}$. Indeed, the sources with $\log(N_{H,9.7\mu\text{m}}) > 24$ are likely lower limit, because the torii library used in the SED fitting analysis did not include the highest levels of obscuration. Using an extended torus libraries, i.e. including a wider and denser range of values for the parameter which characterise the torus model may increase the correlation between $N_{H,X}$ and $N_{H,9.7\mu\text{m}}$. Furthermore, four objects in our sample were observed only in the band below 10 keV, hence the limited energy band available to model the X-ray spectrum may affect the estimate of the columns density in the X-rays.

To avoid the problem associated with the discrete values of the silicate features depth as measured from the SED fitting, we further tested the correlation between the extinction level in the mid-IR and X-rays using the direct measurement of the silicate feature, derived by HC11 and here presented in Sect. 2.1.5. HC11 measured the silicate strength as:

$$S_{sil} = \ln[F(\lambda_p)/F_C(\lambda_p)], \quad (2.2)$$

where the feature (F) and continuum flux densities (F_C), respectively, both measured at the feature’s peak (λ_p). In Fig. 2.8 we presented the results, where we also reported on the right y-axis the column density of the obscuring material as derived from the $9.7 \mu\text{m}$ feature. For the large part of the objects (22 out of 32) in our sample with both measurements of the silicate feature strength in the mid-IR and the N_H from the X-rays, there is quite a good correlation between the two quantity (with correlation coefficient by Spearman: 0.620, Pearson: 0.62, Kendall: 0.36, respectively). The Seyfert 2 galaxies in our sample show a trend which is fully consistent with the relation presented by Shi et al. [2006] ($y = -(0.12 \pm 0.03)X + (2.6 \pm 0.7)$). The objects which lie way below the relation (the names are reported in the table) are likely accounting for a contribution from the host galaxy to the strength of the feature, as suggested by Goulding et al. [2012] for edge-on

and merger sources¹¹.

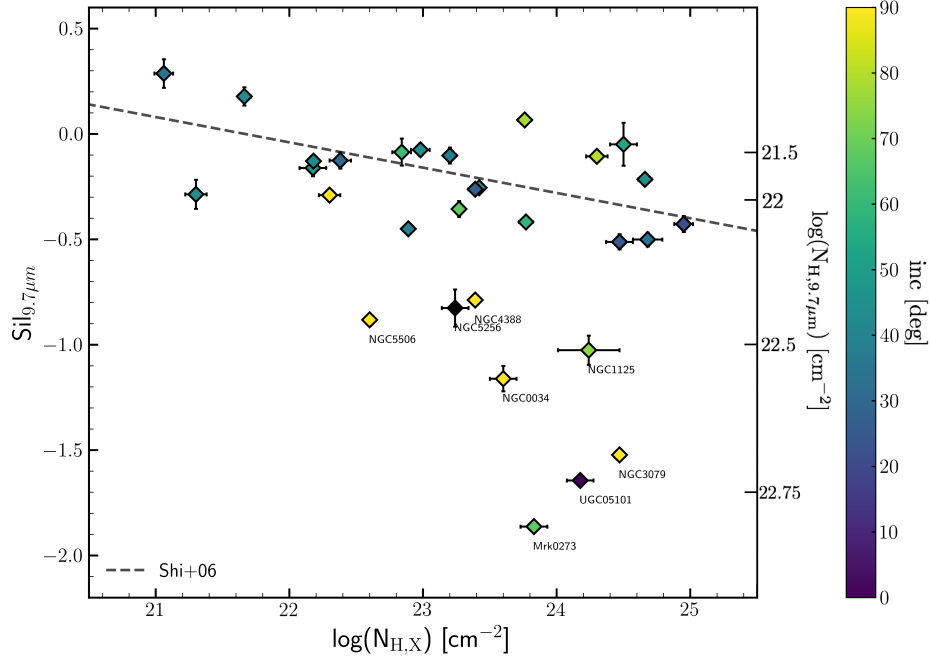


Figure 2.8: The comparison of the neutral gas column density estimated from the $9.7 \mu\text{m}$ silicate absorption feature ($\text{Sil}_{9.7\mu\text{m}}$; y-axis) versus the one obtained from the X-ray obscuring material ($N_{H,X}$; x-axis), both in units of cm^{-2} . $N_{H,X}$ were measured using “phenomenological” models (see Section 2.1.3.1). On the right y-axis we reported the conversion to the column density of the neutral gas (N_H) by assuming the same recipe presented in Section 2.1.4. Our objects are shown as diamonds, colour coded on the base of their inclination angles, which was retrieved from the Hyperleda catalogue [Makarov et al., 2014].

We then conclude that the level of obscuration in the X-rays correlates with the one measured in the mid-IR. Nonetheless, the column density measured in the X-rays are systematically larger, as shown in both Fig. 2.7 and 2.8, which means that some of the material responsible for the extinction at X-ray energies do not contribute at mid-IR wavelength. Furthermore, in Fig. 2.8 we highlights that a contribution from the host-galaxy to the deepest silicate absorption features cannot be excluded.

¹¹Mrk 0273 and NGC5256 are a well know merger, UGC 05101 is a likely merger remnants, while the remaining are all nearly edge-on galaxies ($i \gtrsim 75^\circ$; Makarov et al. 2014). Inclination angles for our sample are also reported in Table 3.1.

2.3 Conclusions

In this Chapter we presented the result of a systematic X-ray spectral analysis for a sample of local Seyfert 2 galaxies taken from G16. By exploiting the wide energy band obtained by combining *NuSTAR* with telescopes sensitive to the band below 10 keV, we were able to model the X-ray emission from the AGN, hence to place constrain of the level of obscuration and measure the intrinsic power of the AGN. We adopt two types of modelling, namely a “phenomenological” and a “physical” modelling, with the latter able to provide a coherent interpretation of the complex X-ray spectral component observed in obscured AGN (see also Sect. 1.1.2). Furthermore, we compared the X-ray and mid-IR properties of our sample of AGN, to obtain a complete characterisation of the targets, as well to test different approaches in different bands to put constrains on the AGN intrinsic power and level of obscuration.

Our main results are:

- We characterised the Seyfert 2 galaxies in our sample in terms of their emission in the X-rays, namely their spectral shape (Γ_X), intrinsic luminosity (L_X) and extinction (N_H). Most of our objects show X-ray properties similar to what observed in nearby AGN ($L_X \sim 10^{42-44}$ erg s⁻¹), while few objects are likely either intrinsically weak ($L_X \sim 10^{40-41}$ erg s⁻¹) or heavily obscured ($N_H > 10^{24}$ cm⁻²).
- The consistency of the two models was tested, finding a relatively good agreement between the measurements obtained with the two, in particular regarding the column density of the obscuring material.
- By comparing the intrinsic X-ray luminosities, as derived in this work, with the one derived from the bolometric luminosity by assuming a k_{bol} factor, we found that our objects are relatively brighter in the IR than in the X-rays. This is likely due to either a potential contamination from the host-galaxy in the IR measurements, as well as an intrinsic properties of this mid-IR selected sample of objects.
- Finally, we compared the level of obscuration in the mid-IR and in the X-rays, finding a general agreement between the two. In particular, a good agreement is evident when comparing the strength of the 9.7 μ m silicate feature with the N_X measured in the X-rays, consistently with previous results in the literature (e.g., Shi et al. 2006; Xu et al. 2020).

3

The effect of AGN activity on the host depletion time

This Chapter is mainly based on “The molecular gas properties in Seyfert 2 galaxies”, F. Salvestrini, C. Gruppioni, E. Hatziminaoglou, F. Pozzi, C. Vignali, V. Casasola, R. Paladino, P. Andreani, A. Giannetti, T. Stanke; to be submitted A&A soon.

The SF activity in galaxies can be affected by the presence of an accreting SMBH. As presented in Section 1.2, AGN are able to inject large amount of energy in the circumnuclear region, preventing the gravitational collapse of molecular clouds, hence the formation of new stars, in processes referred to as “negative” feedback. Indeed, it is widely debated if the feedback from the AGN can reduce the cold molecular gas reservoirs in its host galaxy. By comparing the amount of molecular gas reservoirs, for similar SFR regimes among active and inactive galaxies, significantly shorter depletion times of the molecular components ($t_{depl} = M_{gas}/SFR$) have been observed at high-redshift (e.g., Kakkad et al. 2017; Brusa et al. 2018; Talia et al. 2018), while local Seyfert hosts showed similar properties to normal star-forming galaxies (SFGs; e.g., Rosario et al. 2018; Koss et al. 2020).

To study the effect of nuclear activity on the properties of the host-galaxy ISM our approach is twofold: on the one hand, comparing the molecular gas content and consumption time scales in a sample of active galaxies and a control sample of SF sources; on the other hand, studying the emission in the mid-IR ($\sim 3\text{-}25\ \mu\text{m}$) to disentangle AGN-vs-SF in the nuclear regions. Several comparative studies of the molecular gas content and SF efficiency between local active galaxies and SFGs have been presented over the years (e.g., Maiolino et al. 1997; Bertram et al. 2007; Rosario et al. 2018), suggesting that local AGN hosts cannot be distinguished from inactive sources, in contrast with the results of high-redshift quasars (e.g., Brusa et al. 2018; Talia et al. 2018). Regarding the second approach, among the wealth of diagnostics present in the mid-IR band (e.g., emission line ratios, both emission and absorption spectral features), we focused on the PAH features. PAH features are usually associated with the presence of on-going SF activity, with the nuclear activity supposed to suppress them [Diamond-Stanic and Rieke, 2010], especially the features at the shortest wavelength (i.e., at 6.2 and $7.7\ \mu\text{m}$). However, strong PAH emission were detected in local Seyfert galaxies (e.g., Hönlig et al. 2010, Alonso-Herrero et al. 2014), with recent works suggesting that AGN may enhance PAH features (in sample of nearby AGN, with $L_X \sim 10^{42-44}\ \text{erg s}^{-1}$; e.g. Jensen et al. 2017). The Chapter is structured as follows: the sample is presented in Section 3.1; the data included in the analysis are presented in Section 3.2 and in the subsection therein. We introduce the control sample of inactive galaxies used during the analysis in Section 3.3. In Section 3.4 we analysed the effect of AGN activity on the molecular gas masses and properties of the host galaxy, as well as the effect on the emission from mid-IR features. The conclusions are drawn in Section 3.5.

Throughout the Chapter, distance-dependent quantities are calculated for a standard flat Λ CDM cosmology with the matter density parameter $\Omega_M = 0.30$, the dark energy density parameter $\Omega_\Lambda = 0.70$, and the Hubble constant $H_0 = 70\ \text{km s}^{-1}\ \text{Mpc}^{-1}$ [Komatsu et al., 2009]. Errors are given at 68 per cent confidence level.

3.1 The sample

In the present work we present a detailed analysis of the ISM properties for a sample of Seyfert 2 galaxies drawn from the sample of 76 Seyfert galaxies studied in G16, to complement the characterisation of the AGN through X-ray spectroscopy, presented in Chapter 2. Among the 76 mid-IR-selected active galaxies, we selected the optically-classified obscured source with available CO spectroscopy (both from new and existing observations). The bulk of the sample consists of 23 objects for which we were granted 18h of observing time for CO(2-1) spectroscopy with the Atacama Pathfinder Experiment (APEX) telescope¹ [Güsten et al., 2006]. Ten more sources with low-J CO archival observations were added to the sample (reference to the literature are reported in Table 3.2).

3.2 Data

Here we present the collection of multi-wavelength information used in our study, namely the mm spectroscopy obtained with single-dish facilities (both from proprietary observations and from literature), the results from the SED decomposition performed by G16, and the measurements of PAH features derived from the literature (both were already presented in Section 2.1.4 and 2.1.5, respectively).

3.2.1 Single-dish observations in the sub-mm/mm band

3.2.1.1 APEX data reduction

The observations of the CO(2-1) emission line (at 230.5 GHz rest-frame frequency) for 23 (out of 33) galaxies of our sample were carried out with the PI230 receiver (project 0103.F-9311, PI: F. Salvestrini), mounted on the APEX 12 m antenna. The CO spectra were obtained with single-beam observations pointed on the centre of the galaxy. The requested spectral resolution was 50 km s^{-1} , aimed to resolve the emission line profile with at least 6 channels, assuming a Gaussian line profile with full width half maximum $\text{FWHM} \sim 300 \text{ km s}^{-1}$, as typically observed in the case of low-J transition in local active galaxies (e.g. Papadopoulos et al. 2012). The observations were designed to obtain at least a signal-to-noise ratio $S/N \sim 6$ at the peak of the line, corresponding to $S/N \sim 15$ for the integrated line emission. The resulting integration times ranged between few minutes up to a couple of hours, depending on the brightness of the source. Given the frequency of the CO(2-1) transition, the average main beam (mb) size is $\theta_{mb} \sim 27''$, which corresponds

¹APEX is a single-dish telescope with an antenna diameter of 12 metres, located on the Llano de Chajnantor, in the North of Chile. It was designed as a pathfinder instrument for the ALMA antennas, operating at millimetre and sub-millimetre wavelengths, with both bolometers and heterodyne receivers.

to a physical scale of ~ 10 kpc at the median redshift of the sample $z \sim 0.017$. Data reduction was performed using the CLASS program, which is part of the GILDAS² software. Calibrators were chosen using the standard guideline for APEX observations³. The CO(2-1) emission line profiles for the 23 sources observed with APEX are presented in Fig. 3.1. We first fit the CO line emission with a single Gaussian profile, allowing us to preliminary assess the central velocity (v_0), strength and width (W_{CO}) of the line. The single Gaussian component does not allow us to properly model the CO emission in case of complex profile (as a double-peaked profile, i.e. middle panel, Fig. 3.1). This, along with the low spectral resolution of our observations (i.e., $\delta v_C = 50 \text{ km s}^{-1}$), motivated our decision to estimate the total line fluxes by integrating the emission in a fixed velocity range $[-1100, 1100] \text{ km s}^{-1}$ centred on the systemic velocity of each source, once the baseline was subtracted. This approach secured uniform and solid estimates of the line intensity, even in those cases where the observed line profile differs significantly from that of a single – or double – Gaussian function, and as already been applied in literature works (e.g., Maiolino et al. 1997; Papadopoulos et al. 2012; Rosario et al. 2018). The error on the CO line fluxes were calculated as:

$$\delta I_{CO} = \sigma_{rms}(W_{CO}\delta v_C)^{1/2}, \quad (3.1)$$

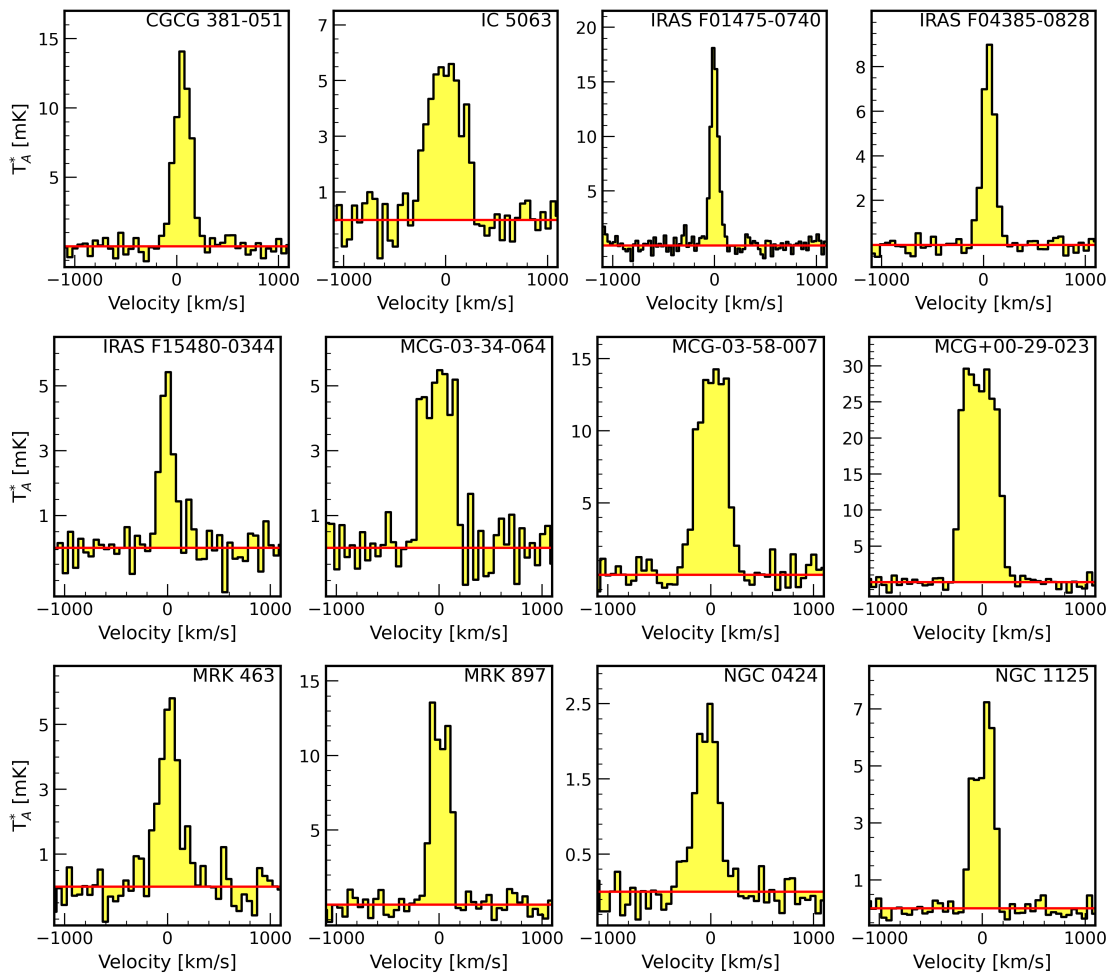
where σ_{rms} is the rms in K (reported in Table 3.2), W_{CO} is the CO line full width half maximum (FWHM) in km s^{-1} , and δv_C is the spectral resolution ($\delta v_C = 50 \text{ km s}^{-1}$). Calibration uncertainties affect significantly the estimates of the CO line intensities, being larger than the spectral noise. We conservatively assume them to be 10% of the intensity, as usually done for similar observations (e.g. Csengeri et al. 2016, Giannetti et al. 2017). The uncertainties reported in Table 3.2 are the quadratic sum of the calibration uncertainties and the spectral noise integrated over the line profile.

To convert the line integrated intensities to fluxes in units of Jy km s^{-1} , we adopted a constant Jy/K conversion factor of 35 ± 3 , suitable for the PI230 receiver⁴. In Table 3.2, we present the new CO fluxes, obtained with APEX.

²<http://www.iram.fr/IRAMFR/GILDAS/>

³<http://www.apex-telescope.org/ns/apex-data/>

⁴<http://www.apex-telescope.org/telescope/efficiency/>



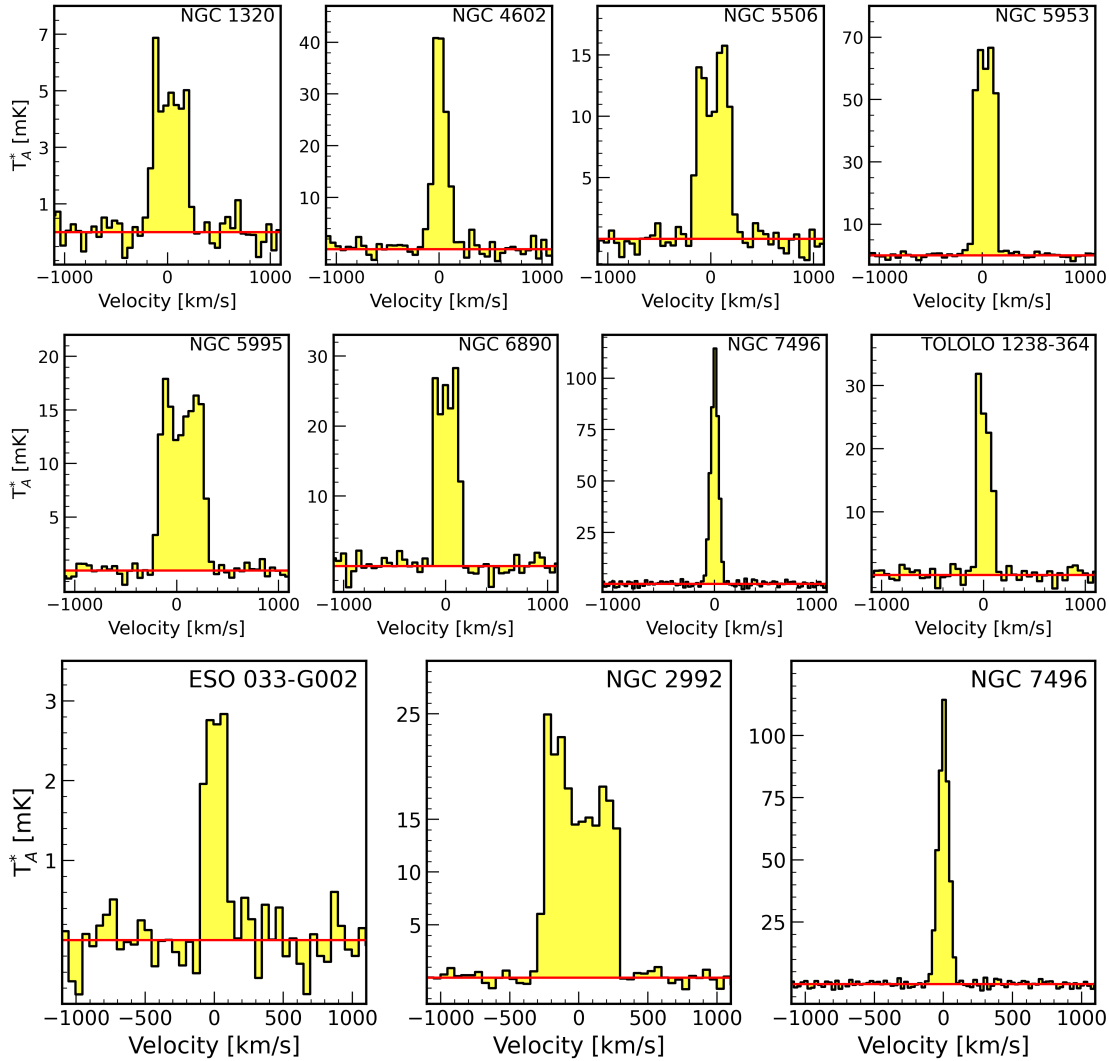


Figure 3.1: CO(2-1) emission line profiles obtained with the APEX telescope. Fluxes are expressed as antenna temperatures [mK] as a function of the velocity [km s^{-1}]. Each panel spans a fixed range of 2000 km s^{-1} of velocity around the systemic velocity of the galaxy to allow a simple visual comparison of the kinematics of the lines. The emission is clearly detected in all the cases, with at least $S/N=4$ in the channel corresponding to the peak of the line profile. On the x-axis, the velocities are calculated with respect to the CO(2-1) expected sky-frequency given the redshift of each source (from NED), assuming the radio conversion for the velocity.

| Name (1) | RA (2) | DEC (3) | z (4) | D (5) | $\log(D_{25}/0.1 \text{ arcmin})$ (6) | $\log(M_{\star}/M_{\odot})$ (7) | $\log(M_{\text{dust}}/M_{\odot})$ (8) |
|------------------|--------------|---------------|----------|----------|--|------------------------------------|--|
| CGCG 381-051 | 23h48m41.29s | +02d14m21.01s | 0.0307 | 135 | 0.848 | 10.43±0.08 | 8.11±0.09 |
| ESO 033-G002 | 04h55m59.59s | -75d32m26.99s | 0.0181 | 79 | 0.971 | 10.60±0.08 | 8.36±0.08 |
| IC 5063 | 20h52m1.99s | -57d4m9.01s | 0.0113 | 49 | 1.429 | 10.69±0.09 | 7.09±0.07 |
| IRAS F01475-0740 | 01h50m2.69s | -07d25m48.0s | 0.0177 | 77 | 0.595 | 9.05±0.06 | 6.62±0.08 |
| IRAS F04385-0828 | 04h40m54.91s | -08d22m22.01s | 0.0151 | 65 | 0.838 | 10.27±0.10 | 8.03±0.08 |
| IRAS F15480-0344 | 15h50m41.50s | -03d53m17.99s | 0.0303 | 133 | 0.647 | 10.75±0.09 | 7.78±0.07 |
| MCG-03-34-064 | 13h22m24.38s | -16d43m43.0s | 0.0165 | 72 | 1.129 | 10.65±0.09 | 7.25±0.08 |
| MCG-03-58-007 | 22h49m36.91s | -19d16m23.99s | 0.0315 | 138 | 0.914 | 10.95±0.11 | 8.82±0.10 |
| MCG+00-29-023 | 11h21m12.20s | -02d59m3.01s | 0.0249 | 109 | 0.92 | 10.95±0.11 | 8.82±0.09 |
| Mrk 0273 | 13h44m42.11s | +55d53m12.65s | 0.0378 | 167 | 0.822 | 11.04±0.08 | 8.03±0.10 |
| Mrk 0463 | 13h56m2.90s | +18d22m18.98s | 0.0504 | 224 | 1.035 | 11.22±0.07 | 7.45±0.11 |
| Mrk 0897 | 21h7m45.80s | +03d52m40.01s | 0.0263 | 115 | 0.838 | 10.91±0.10 | 9.39±0.07 |
| NGC 0034 | 00h11m06.55s | -12d06m26.33s | 0.0196 | 85 | 1.062 | 10.58±0.08 | 7.66±0.08 |
| NGC 0424 | 01h11m27.49s | -38d5m1.0s | 0.0118 | 51 | 1.219 | 10.49±0.08 | 6.65±0.06 |
| NGC 0513 | 01h24m26.85s | +33d47m58.01s | 0.0195 | 85 | 0.791 | 10.78±0.09 | 8.35±0.09 |
| NGC 1125 | 02h51m40.39s | -16d39m1.98s | 0.0109 | 47 | 1.178 | 9.52±0.08 | 6.98±0.08 |
| NGC 1320 | 03h24m48.71s | -03d2m33.0s | 0.0089 | 38 | 1.27 | 10.43±0.08 | 6.56±0.07 |
| NGC 2992 | 09h45m42.01s | -14d19m35.0s | 0.0077 | 33 | 1.465 | 9.19±0.07 | 7.98±0.09 |
| NGC 3079 | 10h01m57.80s | +55d40m47.24s | 0.0037 | 16 | 1.913 | 9.76±0.07 | 7.15±0.10 |
| NGC 4388 | 12h25m46.75s | +12d39m43.51s | 0.0084 | 36 | 1.731 | 9.31±0.09 | 6.97±0.09 |
| NGC 4602 | 12h40m36.52s | -5d7m54.98s | 0.0085 | 37 | 1.11 | 9.42±0.10 | 8.08±0.07 |
| NGC 5135 | 13h25m44.06s | -29d50m01.2s | 0.0137 | 59 | 1.379 | 10.71±0.10 | 7.91±0.10 |
| NGC 5256 | 13h38m17.50s | +48d16m37.0s | 0.0279 | 122 | 1.08 ^a | 10.42±0.08 | 8.26±0.07 |
| NGC 5347 | 13h53m17.83s | +33d29m26.98s | 0.0078 | 34 | 1.21 | 10.11±0.11 | 7.52±0.11 |
| NGC 5506 | 14h13m14.81s | -03d12m27.0s | 0.0062 | 27 | 1.457 | 10.41±0.10 | 8.05±0.08 |
| NGC 5953 | 15h34m32.30s | +15d11m42.0s | 0.0066 | 28 | 1.168 | 9.99±0.06 | 7.40±0.09 |

Continued on next page

Table 3.1 – Continued from previous page

| Name (1) | RA (2) | DEC (3) | z (4) | D (5) | $\log(D_{25}/0.1\text{arcmin})$ (6) | $\log(M_{\star}/M_{\odot})$ (7) | $\log(M_{\text{dust}}/M_{\odot})$ (8) |
|-----------------|--------------|---------------|----------|----------|--|------------------------------------|--|
| NGC 5995 | 15h48m24.91s | -13d45m28.01s | 0.0252 | 110 | 1.008 | 10.87±0.08 | 8.98±0.07 |
| NGC 6890 | 20h18m18.11s | -44d48m23.0s | 0.0081 | 35 | 1.201 | 9.86±0.08 | 6.85±0.12 |
| NGC 7130 | 21h48m19.52s | -34d57m04.48s | 0.0162 | 70 | 1.194 | 10.49±0.09 | 7.74±0.05 |
| NGC 7496 | 23h9m47.20s | -43d25m40.01s | 0.0055 | 24 | 1.525 | 9.46±0.10 | 7.03±0.06 |
| NGC 7674 | 23h27m56.70s | +08d46m45.01s | 0.0289 | 127 | 1.049 | 11.11±0.10 | 8.00±0.07 |
| TOLOLO 1238-364 | 12h40m52.90s | -36d45m22.0s | 0.0109 | 47 | 1.095 | 9.66±0.09 | 7.53±0.11 |
| UGC 05101 | 09h35m51.60s | +61d21m11.45s | 0.0394 | 174 | 1.08 | 10.92±0.08 | 8.25±0.09 |

Table 3.1: Columns: (1) Source name; (2) Right Ascension; (3) Declination; (4) Redshift; (5) Distance, in units of Mpc; (6) Logarithm of the $25 \text{ mag arcsec}^{-2}$ isophotal diameter from the Hyperleda catalogue [Makarov et al., 2014]; (7) Logarithm of the stellar mass from G16; (8) Logarithm of the dust mass from G16. ^a for NGC 5256 we used the D_{25} measurement from the 3RC catalogue [de Vaucouleurs et al., 1991]. Since this object is a major merger, the authors did not provide any estimate for the inclination. To provide the aperture correction factor for NGC 5256 consistently with the remaining part of the sample, we estimated the aperture correction assuming ten evenly spaced inclination angles between face-on ($i = 0^\circ$) and edge-on ($i = 90^\circ$) configurations. We then adopted a mass correction factor $f_{ap} = 1.9 \pm 0.2$, which is the mean of the estimated values and the standard deviation as uncertainty.

3.2.1.2 Literature single-dish data

To extend the sample coverage, we included in the analysis a set of low-J CO emission line fluxes retrieved from the literature (references are reported in Table 3.2). In particular, we searched for CO(2-1) and CO(1-0) spectroscopy obtained with single-dish telescopes, to avoid the filtering out of the flux due to the longer baselines, inherent to the interferometric observations⁵. More precisely, from Papadopoulos et al. [2012] we retrieved the CO(1-0) emission line intensities of four objects (Mrk 0273, NGC 5135, NGC 5256, UGC 05101), obtained with the IRAM 30m antenna ($\theta_{mb} \sim 23''$). The CO(2-1) line intensities for NGC 0034 and NGC 7130 were measured by Albrecht et al. [2007] with the 15m antenna of the Swedish-ESO Submillimeter Telescope (SEST; $\theta_{mb} \sim 45''$). In the work by Maiolino et al. [1997], the author exploited the 12m single-dish facility of the National Radio Astronomy Observatory (NRAO) to study the molecular gas properties of a large sample of local galaxies, among which we retrieved the CO (1-0) flux measurements for NGC 0513, NGC 3079 and NGC 5347. Finally, Rosario et al. [2018] provided the flux of the CO(2-1) transition for NGC 4388, observed with the 15m dish of the James Clerk Maxwell Telescope (JCMT; $\theta_{mb} \sim 22''$). In the end, we retrieved single-dish observations for 33 Seyfert galaxies, out of which 29 were benefit from the X-ray spectral analysis presented in Chapter 2.

3.2.1.3 Aperture correction for the CO flux

Proprietary data from APEX as well as literature data are sub-mm single-dish observations pointed at the centre of the galaxy (i.e. at the optical position), with a typical FOV smaller than the size of the optical emission. To account for potential CO flux loss, we applied aperture correction to the CO line flux based on the relation between the galactic extension determined with optical observations and CO maps. The spatial distribution of the molecular gas, traced by the CO emission, is well described by an exponentially decreasing disk, both perpendicularly to the galactic plane and in the radial direction. The CO scale radius has been shown to be proportional to the optical size of the sources, parametrised by the diameter at the isophotal level $B=25$ mag arcsec⁻² (D_{25} ; e.g., Lisenfeld et al. 2011, Casasola et al. 2017). Following Boselli et al. [2014] we assumed:

$$S_{CO}(r, z) = S_{CO}(0)e^{-r/r_{CO}}e^{-|z|/z_{CO}}, \quad (3.2)$$

where $S_{CO}(0)$ is the central emission, r_{CO} and z_{CO} are the CO scale radius and height, respectively. This method is the 3D extension of the 2D approach proposed by Lisenfeld

⁵An interferometer is limited by the minimum spacing of its antennas. Two antennas cannot be placed closer than some minimum distance (D_{min}) and signals on spatial scales larger than some size ($\propto \lambda/D_{min}$) will be attenuated.

et al. [2011], valid for low-inclination galaxies. Here we assumed $r_{CO}/r_{25} = 0.2^6$, following Lisenfeld et al. [2011], and $z_{CO}/z_{25} = 0.01$, as suggested Boselli et al. [2014]. This assumption have been tested in nearby galaxies with similar morphological classification to our Seyfert 2 galaxies (mostly spirals and S0 objects; see also Boselli et al. 2014, Casasola et al. 2020). The resulting aperture correction factor is:

$$f_{ap} = S_{CO,tot}/S_{CO,mb}, \quad (3.3)$$

where $S_{CO,tot}$ is the total CO flux integrated over the entire galaxy, while $S_{CO,mb}$ is the CO flux measured in the center of the galaxy, convolved with the main beam profile.

The estimated values for the aperture correction have a mean of $f_{ap} = 2.8$ and standard deviation $\sigma_{f_{ap}} = 1.5$, i.e. increasing the CO flux by a factor of a few. The only exception is NGC 4388, whose large optical dimension ($D_{25} \sim 5'$) led to $f_{ap} \sim 15$. We applied the aperture correction to the CO(1-0) luminosity presented in Table 3.2, based on the relation in Eq. 3.3. The contribution of the uncertainty on the aperture correction was added in quadrature to the uncertainty on $L'_{CO(1-0)}$.

3.2.1.4 The molecular gas content

As introduced in Section 1.2.2.1, the molecular gas reservoir can be estimated by measuring the total luminosity of the CO(1-0) emission line ($L'_{CO(1-0)}$). Here, we derived the CO(1-0) luminosity from the aperture-corrected CO flux measurements presented Table 3.2. For the 25 sources with the CO(2-1) flux, we assumed a line flux ratio CO(2-1)/CO(1-0)=3, to extrapolate the flux of the lowest-J transition, as observed for similar objects in the local Universe (e.g. Papadopoulos et al. 2012). Given the CO(1-0) flux, we derived the CO(1-0) luminosity ($L'_{CO(1-0)}$) following Eq. 1.3, as suggested in Carilli and Walter [2013]. The resulting $L'_{CO(1-0)}$ are reported in Table 3.2, while in Fig. 3.2 they are plotted as a function of the IR luminosity, associated with the SF (L_{IR}^{SF} , one of the outcomes of the SED decomposition performed by G16). In our sample, $L'_{CO(1-0)}$ and L_{IR} are tightly correlated (with slope 0.93 ± 0.13 and normalisation 0.90 ± 0.07), consistently with what observed in local objects (e.g., Sargent et al. 2014; Genzel et al. 2010).

The cold molecular gas mass (M_{gas}) is usually derived from the luminosity of the CO(1-0), assuming a CO-to-H₂ conversion factor as following Eq. 1.4, as presented in Solomon and Vanden Bout [2005], and Bolatto et al. [2013]. As shown in Section 1.2.2.1, the CO-to-H₂ conversion factor depends on several sources parameters (e.g., metallicity, starburstness). Our goal is to measure the entire molecular gas mass, we account on the CO emission from region far away form the galactic nucleus, where the AGN dominates the energetics,

⁶ $r_{25}=D_{25}$

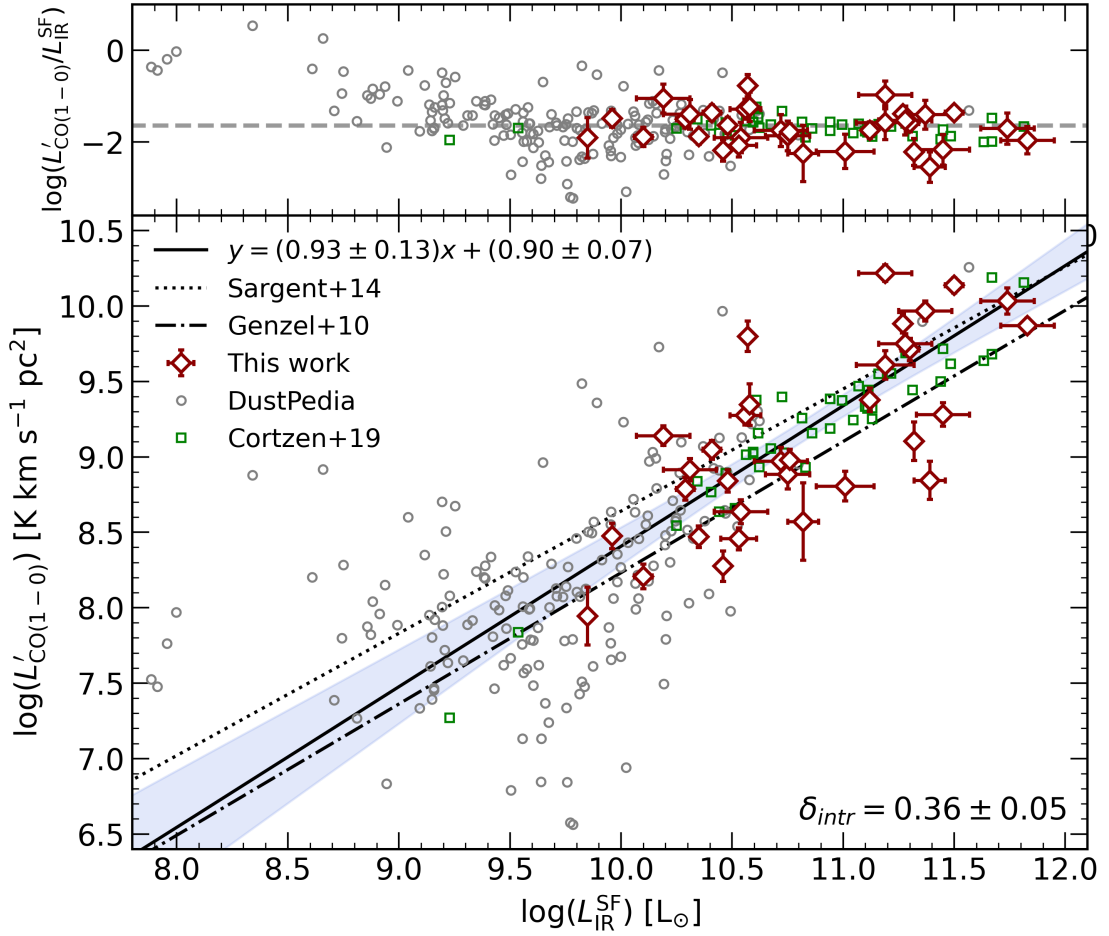


Figure 3.2: Bottom: aperture-corrected CO(1-0) luminosity ($L'_{\text{CO}(1-0)}$) vs IR luminosity (L_{IR}) in logarithmic scales, for the Seyfert 2 galaxies (red diamonds). The best-fit parameters ($\alpha = 0.93 \pm 0.13, \beta = 0.90 \pm 0.07$) were obtained with a MCMC regression analysis, and are represented by the black solid line, while the light-blue area covers the parameters space between the 16th and 84th percentile. The intrinsic dispersion is $\delta_{\text{intr}} = 0.36 \pm 0.05$. $L'_{\text{CO}(1-0)} - L_{\text{IR}}$ relation for SFGs from literature are reported as dotted [Sargent et al., 2014] and dot-dashed [Genzel et al., 2010] lines. The control samples are shown with grey circles (DustPedia) and green squares [Cortzen et al., 2019]. Top: $L'_{\text{CO}(1-0)}/L_{\text{IR}}$ ratio as a function of L_{IR} ; the horizontal grey dashed line is the median value.

thus suggesting Milky-Way like values. However, lower values ($\alpha_{\text{CO}} \sim 3 M_{\odot} \text{pc}^{-2} (\text{K km s}^{-1})^{-1}$) were observed in turbulent region also in absence of AGN-powered outflows [Cicone et al., 2018]. Since the choice of an appropriate α_{CO} factor for each source is a challenging task, which goes beyond the goal of this work, we adopted $\alpha_{\text{CO}} = 1.1 M_{\odot} \text{pc}^{-2} (\text{K km s}^{-1})^{-1}$ for the entire sample of Seyfert 2 galaxies. This value is relatively lower than the one used for since it has been used for local SFGs ($\alpha_{\text{CO}} = 4.3 M_{\odot} \text{pc}^{-2} (\text{K km s}^{-1})^{-1}$), nevertheless it was adopted by other authors (e.g., Rosario et al. 2018, Pozzi et al. 2017) in local active galaxies with similar properties (e.g., M_{\star} , SFR). In the conclusion

we discuss the results on the basis of the adopted α_{CO} value. To account for the uncertain determination of a proper CO-to-H₂ conversion factor, a 30% contribution from the α_{CO} (according to Bolatto et al. 2013) was added in quadrature to the uncertainty on M_{H_2} .

| Name (1) | Spectral line (2) | $I_{CO}[2-1]$ [K km s ⁻¹] (3) | $S_{CO}[2-1]$ [Jy km s ⁻¹] (4) | rms [mK] (5) | W_{CO} [km s ⁻¹] (6) | $\log(L'_{CO(1-0)}/(L_{\odot}))$ (7) | $\log(M_{H_2}/(M_{\odot}))$ (8) | Reference (9) |
|------------------|----------------------|--|---|-----------------|---------------------------------------|---|------------------------------------|------------------|
| CGCG 381-051 | CO(2-1) | 3.4±0.3 | 127±15 | 0.54 | 187±3 | 9.38±0.08 | 9.42±0.15 | (a) |
| ESO 033-G002 | CO(2-1) | 0.67±0.07 | 25±3 | 0.32 | 161±6 | 8.28±0.10 | 8.32±0.16 | (a) |
| IC 5063 | CO(2-1) | 3±0.29 | 111±13.96 | 0.63 | 385±5 | 8.97±0.09 | 9.01±0.15 | (a) |
| IRAS F01475-0740 | CO(2-1) | 2.23±0.18 | 82.65±9.49 | 0.58 | 87.8±1.1 | 8.64±0.08 | 8.68±0.20 | (a) |
| IRAS F04385-0828 | CO(2-1) | 1.77±0.14 | 65.35±7.49 | 0.25 | 142.0±1.6 | 8.46±0.07 | 8.50±0.15 | (a) |
| IRAS F15480-0344 | CO(2-1) | 1.1±0.12 | 40.7±5.41 | 0.5 | 150±5 | 8.81±0.10 | 8.85±0.21 | (a) |
| MCG-03-34-064 | CO(2-1) | 2.56±0.26 | 94.66±12.34 | 0.75 | 334±11 | 8.88±0.10 | 8.93±0.16 | (a) |
| MCG-03-58-007 | CO(2-1) | 6.57±0.54 | 243.14±28.16 | 0.73 | 319±4 | 9.71±0.07 | 9.75±0.18 | (a) |
| MCG+00-29-023 | CO(2-1) | 15.45±1.21 | 571.82±64.42 | 0.5 | 361.2±1.1 | 9.88±0.06 | 9.92±0.15 | (a) |
| Mrk 0273 | CO(1-0) | | | | | 9.87±0.05 | 9.91±0.15 | (b) |
| Mrk 0463 | CO(2-1) | 1.74±0.18 | 64.39±8.43 | 0.53 | 228±7 | 9.61±0.09 | 9.65±0.16 | (a) |
| Mrk 0897 | CO(2-1) | 3.75±0.31 | 138.87±16.2 | 0.6 | 216±3 | 9.28±0.08 | 9.32±0.28 | (a) |
| NGC 0034 | CO(2-1) | | | | | 8.84±0.13 | 8.89±0.18 | (c) |
| NGC 0424 | CO(2-1) | | | | | 8.21±0.08 | 8.25±0.15 | (a) |
| NGC 0513 | CO(1-0) | 0.9±0.08 | 33.4±4.02 | 0.17 | 258±6 | 8.6±0.3 | 8.6±0.3 | (d) |
| NGC 1125 | CO(2-1) | 2.1±0.17 | 77.84±8.87 | 0.21 | 228±2 | 8.47±0.07 | 8.51±0.14 | (a) |
| NGC 1320 | CO(2-1) | 2.61±0.23 | 96.58±11.69 | 0.43 | 338±8 | 8.48±0.08 | 8.52±0.15 | (a) |
| NGC 2992 | CO(2-1) | 12.99±1.02 | 480.52±54.25 | 0.52 | 492±3 | 9.28±0.06 | 9.32±0.14 | (a) |
| NGC 3079 | CO(1-0) | | | | | 9.35±0.14 | 9.39±0.19 | (d) |
| NGC 4388 | CO(2-1) | | | | | 9.80±0.10 | 9.84±0.16 | (e) |
| NGC 4602 | CO(2-1) | 8.96±0.74 | 331.56±38.28 | 1.38 | 148.1±1.9 | 8.84±0.07 | 8.88±0.15 | (a) |
| NGC 5135 | CO(1-0) | | | | | 10.22±0.05 | 10.26±0.13 | (b) |
| NGC 5256 | CO(1-0) | | | | | 10.14±0.05 | 10.18±0.14 | (b) |
| NGC 5347 | CO(1-0) | | | | | 7.94±0.19 | 8.0±0.2 | (d) |
| NGC 5506 | CO(2-1) | 6.68±0.54 | 246.99±28.37 | 0.7 | 327±4 | 8.79±0.08 | 8.83±0.14 | (a) |
| NGC 5953 | CO(2-1) | 20.88±1.63 | 772.68±87.02 | 0.72 | 204.3±0.7 | 9.05±0.06 | 9.09±0.14 | (a) |
| NGC 5995 | CO(2-1) | 9.82±0.78 | 363.27±41.13 | 0.5 | 420±3 | 9.75±0.07 | 9.79±0.14 | (a) |
| NGC 6890 | CO(2-1) | 9.45±0.78 | 349.82±40.38 | 1.21 | 237±3 | 8.91±0.07 | 8.96±0.14 | (a) |
| NGC 7130 | CO(2-1) | | | | | 9.10±0.13 | 9.15±0.18 | (c) |
| NGC 7496 | CO(2-1) | 13.52±1.06 | 500.22±56.42 | 1.23 | 89.4±0.4 | 9.14±0.07 | 9.18±0.14 | (a) |
| NGC 7674 | CO(2-1) | 11.44±0.9 | 423.34±47.9 | 0.79 | 194.8±1.2 | 9.97±0.07 | 10.01±0.14 | (a) |
| TOLOLO 1238-364 | CO(2-1) | 7.58±0.61 | 280.62±32.08 | 0.93 | 151.5±1.9 | 8.98±0.07 | 9.02±0.15 | (a) |

Continued on next page

Table 3.2 – Continued from previous page

| Name | Spectral line | $I_{CO}[2-1]$ [K km s ⁻¹] | $S_{CO}[2-1]$ [Jy km s ⁻¹] | rms [mK] | W_{CO} [km s ⁻¹] | $\log(L'_{CO(1-0)}/L_{\odot})$ | $\log(M_{H_2}/M_{\odot})$ | Reference |
|-----------|---------------|---------------------------------------|--|----------|--------------------------------|--------------------------------|---------------------------|-----------|
| (1) | (2) | (3) | (4) | (5) | (6) | (7) | (8) | (9) |
| UGC 05101 | CO(1-0) | | | | | 10.03±0.09 | 10.08±0.17 | (b) |

Table 3.2: Columns: (1) Source name; (2) Used CO transition; (3) CO brightness in units of K km s⁻¹ from the new APEX observations; (4) CO flux in units of Jy km s⁻¹; (5) RMS of the CO line in units of mK; (6) CO line width in units of km s⁻¹; (7) Logarithm of the $L'_{CO(1-0)}$ in K km s⁻¹ pc², corrected for the aperture (see Section 3.2.1.3); (8) Logarithm of the molecular gas mass (M_{H_2}) in units of M_{\odot} , corrected for the aperture. (9) References to the CO spectroscopy: (a) This work; (b) Papadopoulos et al. [2012]; (c) Albrecht et al. [1997]; (d) Maiolino et al. [2018]; (e) Rosario et al. [2018].

3.2.2 Decomposed SED

The sources in our sample benefit from the detailed SED decomposition analysis performed by G16, which provides a complete description of each source in terms of the different component (e.g., stars, dust, AGN) and the on-going processes (e.g., SF, nuclear accretion). We introduced the approach adopted in G16 in Section 2.1.4, as well as the main results of the SED fitting analysis. Here, to our purposes, we considered the characterisation of host galaxy in terms of SFR, stellar and dust masses, IR luminosity (integrated over the 8-1000 μ m spectral range), and the estimates of the contribution of the AGN (i.e., L_{bol}^{IR} , f_{AGN}). The derived physical properties of both the AGN and the host galaxy are reported in Table 2.1.

3.2.3 Mid-IR features

We collected measurements of mid-IR features from the work by HC11 for 32 out of the 33 objects in our sample. Besides the strength of the silicates around 9.7 μ m considered in Chapter 2, HC11 also provided the mid-IR measurements of the PAH features. The actual extraction area depends on the slit mode and the distance of the source ⁷, but the central few kpc region was sampled even in the closest objects in our sample.

The method used by the authors consists of a combination of the linear interpolation of the continuum with the integration of the emission from the features. By linearly interpolate two narrow, continuum bands at both sides of each feature, the authors estimate the continuum underlying the feature, which is then subtracted from the spectrum. The residual were integrated in a band centred at the expected wavelength of the peak of the PAH feature to obtain the integrated PAH flux. The uncertainties on the PAH intensities and the continuum were estimated by performing Monte Carlo simulations. The authors also provided the equivalent widths (EWs) of the PAH features dividing the integrated PAH flux by the interpolated continuum at the centre of the feature. For further details about the procedure, we refer to Section 4 in HC11.

We collected the luminosities and EWs for the 6.2 and 11.3 μ m PAH features for 28 and 32 out of the 33 objects in our sample, respectively.

⁷See also https://irsa.ipac.caltech.edu/data/SPITZER/docs/files/spitzer/irs_pocketguide.pdf for further details on the *Spitzer*/IRS specifications.

3.3 Control sample

To assess the effect of AGN on the properties of the host galaxy (e.g., in terms of either the molecular gas content or SF activity) we need to compare our sample with local star-forming galaxies that do not harbour an active nucleus. Among the plethora of samples of local objects that have been studied in the literature, we focused on those samples which benefit from a complete characterisation of the sources in terms of their molecular gas, dust and stellar content, as well as the SF activity. The sample of local objects in the DustPedia⁸ project, is ideal for this purpose, given the multi-wavelength imaging and photometry database of the 875 nearby galaxies of this project (Davies et al. 2017; Clark et al. 2018). The DustPedia sample consists of all the galaxies observed by *Herschel*, with optical diameter $> 1'$, recessional velocity $> 3000 \text{ km s}^{-1}$ and with a *WISE* $3.4 \mu\text{m}$ detection with at least a $S/N > 5$ [Davies et al., 2017]. Each galaxy benefits from the results of a CIGALE⁹ SED fitting decomposition, providing the description of the sources in terms of the on-going SF and stellar content [Nersesian et al., 2019]. In particular, we selected our control sample from a recent work of the DustPedia collaboration [Casasola et al., 2020], focused on the molecular gas properties of a sub-sample of 255 spirals. Using single-dish archival observations, the authors derived the molecular gas masses from aperture-corrected low-J CO spectroscopy, with a procedure similar to the one described in Section 3.2.1.4 and assuming a α_{CO} factor suited for inactive galaxies ($\alpha_{\text{CO}} = 4.3 M_{\odot} \text{ pc}^{-2} (\text{K km s}^{-1})^{-1}$; see Casasola et al. 2020 for further details). To build a control sample of inactive galaxies which matches the host-galaxy properties of our Seyfert 2 galaxies, in particular in terms of stellar mass and SFR, we excluded the dwarf galaxies by removing the objects with $M_{\star} < 10^9 M_{\odot}$ (25 objects). Nevertheless, the remaining 230 SFGs from the sample by Casasola et al. [2020] still do not perfectly match our sample in terms of SFR and stellar masses, as shown in Table 3.3. Then, to pair the high-SFR and stellar mass tails of our sample of Seyfert 2 galaxies, we included the sample by Cortzen et al. [2019], where the authors investigated the use of mid-IR features, in particular the PAH features, as tracers of the molecular gas content in local and intermediate-redshift galaxies. The target sample presented by Cortzen et al. [2019] consists of 283 mid-IR selected objects, drawn from the 5 mJy Unbiased Spitzer Extragalactic Survey (5MUSES; Wu et al. 2010) upon the availability of low-J CO spectroscopy, mid-IR PAH features detection, and IR photometry. We further selected those objects (144/283) with estimates of stellar mass, SFR, molecular gas, dust and measurement of the $6.2 \mu\text{m}$ PAH feature. They chose the PAH feature at $6.2 \mu\text{m}$ because it is less affected by the contribution from

⁸<http://dustpedia.astro.noa.gr/>

⁹<https://cigale.lam.fr/>

the warm dust, which is stronger at longer wavelengths. Stellar and dust parameters were obtained through a SED decomposition [Shi et al., 2011], while the SFR is derived assuming the L_{IR} -SFR relation by Kennicutt [1998]. Cortzen et al. [2019] also provided aperture-corrected $L'_{CO(1-0)}$ measurements for 33 (out of 144) 5MUSES objects, derived from CO(1-0) spectroscopy with the IRAM 30m antenna. The measurements of the PAH features were obtained using the PAHFIT code (see Magdis et al. 2013). Cortzen et al. [2019] provided the molecular gas masses derived from the dust content, assuming a well calibrated metallicity-dependent gas-to-dust ratio. This way, the author avoided the dependency on the α_{CO} conversion factor, although in this case the molecular gas masses are affected by the uncertainties related to the assumed dust-to-gas ratio. Nevertheless, we tested the consistency of the method to measure the M_{H_2} adopted by Cortzen et al. [2019] with the procedure presented in Section 3.2.1.4 and in Casasola et al. [2020] for the objects from Cortzen et al. [2019] with $L'_{CO(1-0)}$ measurements. Then, by assuming a $\alpha_{CO}=4.3 M_{\odot} \text{ pc}^{-2} (\text{K km s}^{-1})^{-1}$ in Eq. 1.4, we derived the molecular gas mass and we compared these values with the ones provided by Cortzen et al. [2019], i.e. obtained assuming a dust-to-gas ratio. We found that the two methods provide consistent estimates (within 1σ) for M_{H_2} but given the larger statistics, we used the M_{H_2} derived from the dust content. We refer to Cortzen et al. [2019] for the details on the measurements of the galaxy properties. Among the 144 galaxies with a full set of PAH measurements, we conservatively excluded the sources with an EW of the $6.2 \mu\text{m}$ PAH feature smaller than $0.4 \mu\text{m}$, which is usually adopted as an indicator for AGN or composite objects (i.e. where AGN and SF coexist; e.g., Spoon et al. 2007; Magdis et al. 2013; Cortzen et al. 2019). The remaining 95 objects are putative SFGs.

Since we were interested in collecting SFGs free from any AGN contamination, we further check the potential presence of nuclear activity by cross-matching the SFGs from the DustPedia (230 objects) and 5MUSES (95 objects) samples with the most recent catalogues of X-ray observations: 4XMM-DR9¹⁰ [Webb et al., 2020] and the *Swift*-BAT 105-Month Hard X-ray Survey¹¹ [Oh et al., 2018]. Starting with the 230 from DustePedia cross-matched with the 4XMM-DR9 catalogue, we found 60 targets detected by XMM-*Newton*, which potentially host a relatively luminous AGN (i.e. with an observed X-ray luminosity of $L_{0.2-12\text{keV}} > 10^{41} \text{ ergs}^{-1}$, typical of either intrinsically weak or extremely obscured objects). We used the hardness ratio (HR) as selection criteria to infer the presence of nuclear activity. It is calculated as $HR = (H - S)/(H + S)$, i.e. the normalised difference of the fluxes in the hard 2-12 keV (H) and soft 0.2-2 keV (S) energy bands. The signature of nuclear activity in low and intermediate-redshift AGN is the peak of

¹⁰http://xmmssc.irap.omp.eu/Catalogue/4XMM-DR9/4XMM_DR9.html

¹¹<https://swift.gsfc.nasa.gov/results/bs105mon/>

the X-ray emission in the hard band ($E > 2$ keV), i.e. resulting in positive HR , while the diffuse emission associated with the host-galaxy SF peaks in the soft band, which means negative HR . Sixty potential AGN with $HR > 0$ were excluded in the end. We also searched for objects from the DustPedia sample in the *Swift*-BAT catalogue. Since the emission in the hard X-ray band ($E > 10$ keV) is almost exclusively associated with nuclear activity, we further excluded one source which was detected in the 14-195 keV band within the *Swift*-BAT monitoring. In the end, we retrieved the properties for the 169 local inactive galaxies from the official DustPedia web-page, namely the molecular gas and dust masses, SFR, and stellar mass.

As previously done for the DustPedia objects, we further check for the evidence of nuclear activity, by searching for detection in the X-rays for the 5MUSES galaxies. Then, we cross-matched the 95 5MUSES objects with the 4XMM-DR9 and the *Swift*-BAT 105-Month Hard X-ray Survey. We found that none of the 95 5MUSE was detected within the *Swift*-BAT catalogue, while 41 were detected with XMM-*Newton*, but all of them showed $HR < 0$. Since there were no common sources between the two sets of objects, we set as control sample for our study the 94 objects from Cortzen et al. [2019], combined with the 169 SFGs from Casasola et al. [2020]. The main properties of the two control samples and our Seyfert 2 galaxies are shown in Table 3.3.

In Fig. 3.3 we show the distribution of our sample and the two control samples in the stellar mass-SFR plane, and in the comparison of their dust and stellar masses. For $M_{\star} > 10^{9.5} M_{\odot}$, the Seyfert 2 galaxies have a similar distribution to the SFGs in both dust mass and SFR. In the low stellar mass tail of the sample ($M_{\star} < 10^{9.5} M_{\odot}$) our AGN show a significant larger SFR with respect to the SFGs. This can be done by either the LIRGs nature of our objects, or a potential contribution from the AGN in the measurement of the SFR (which is derived from the IR luminosity of the host galaxy, disentangled from the AGN one during the SED fitting analysis).

3.4 Results and discussion

In what follows we will discuss scaling relations between the molecular gas content, traced by the CO emission, and physical properties such as L_{IR} , stars and dust content.

| | Seyfert 2 | DustPedia | 5MUSES |
|-------------------------------------|----------------|---------------|----------------|
| Number | 33 | 169 | 95 |
| D [Mpc] | 15-224 | 0.3-38.3 | 109-2090 |
| SFR [$M_{\odot} \text{ yr}^{-1}$] | 0.7 - 66.8 | 0.008 - 39.8 | 0.18 - 114.5 |
| $\log(M_{\star}/M_{\odot})$ | 10.3 ± 0.6 | 9.9 ± 0.5 | 10.6 ± 0.5 |
| $\log(M_{dust}/M_{\odot})$ | 7.7 ± 0.7 | 7.0 ± 0.4 | 7.8 ± 0.5 |

Table 3.3: Properties for the studied AGN sample and the control samples by Casasola et al. 2020 (DustPedia) and Cortzen et al. 2019(5MUSES), after accurate cleaning of AGN contaminants. From top to bottom, rows contain the size of sample; the intervals of distances (in units of Mpc) and SFR (in units of $M_{\odot} \text{ yr}^{-1}$); the mean and standard deviation of the logarithm of the stellar and dust masses (both in units of M_{\odot}).

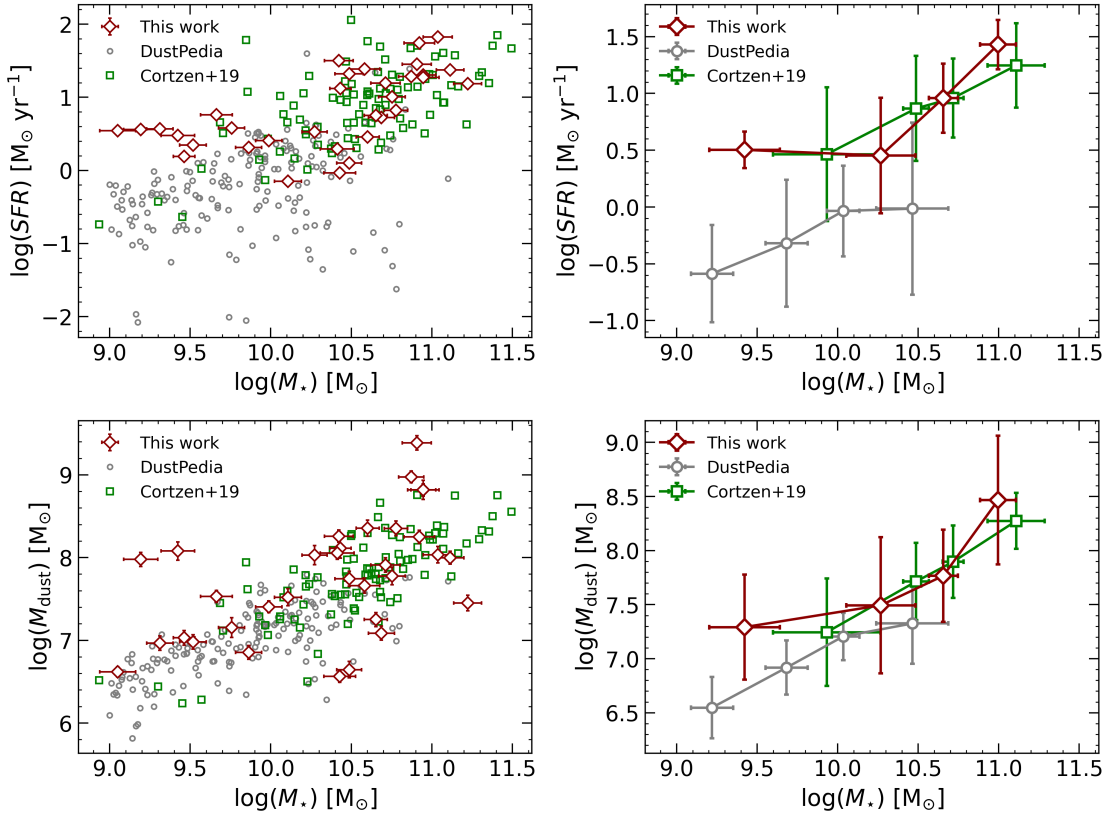


Figure 3.3: Left panels: The SFR (top row) and dust mass (bottom row) as a function of the stellar mass (M_{\star}) for our sample (red diamonds) and the two control samples (grey circles for DustPedia galaxies and green squares for the 5MUSES ones). Right panels: same SFR- M_{\star} and M_{dust} - M_{\star} planes as in the left panels, but with binned data to underline the average trend of active and inactive galaxies. The bins were chosen to include the same number of sources. The mean value and the error bars (standard deviations) in each bin were determined with a bootstrap procedure with 10000 iterations.

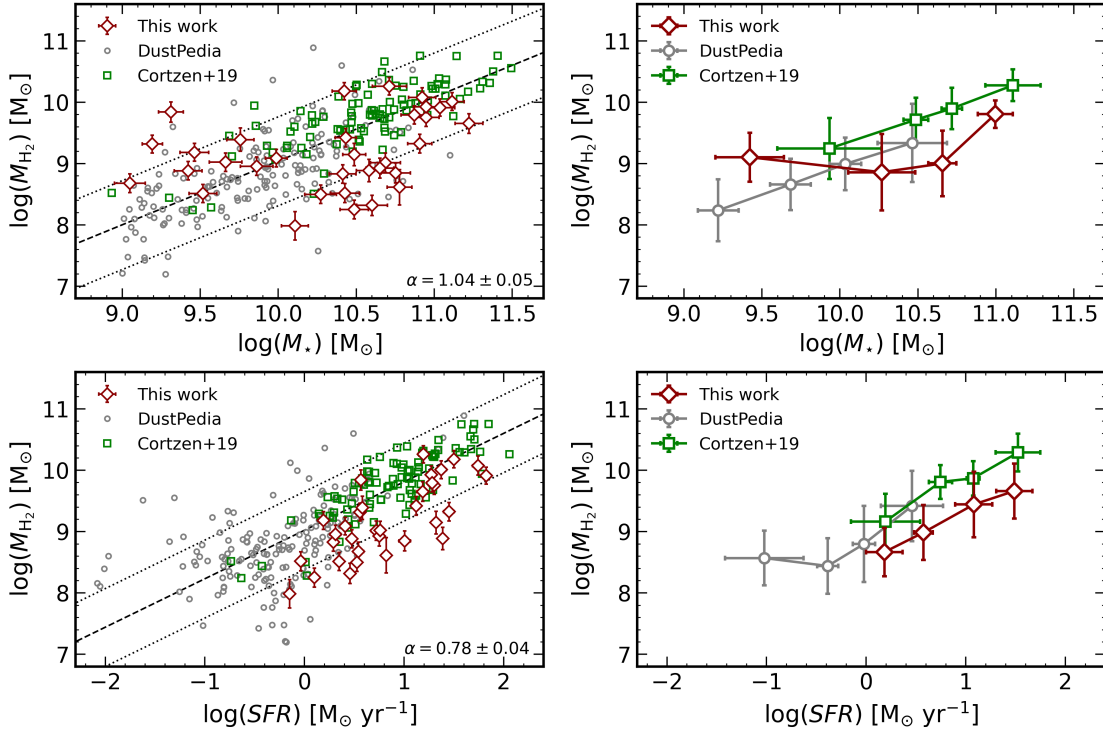


Figure 3.4: Left panels: scaling relations of the molecular gas mass (M_{H_2}) as a function of the host-galaxy stellar mass (M_* ; top row), and SFR (bottom row). Our galaxies are shown as red diamonds, while the control samples are represented by grey circles (DustPedia) and green squares (5MUSES). For pure illustrative purposes, the best-fit trend (grey dashed line) for the samples of inactive galaxies is shown, while the two dotted lines are the same trend shifted by a factor of 0.5 dex. The best-fit slope is reported in the lower right corner. Right panels: same scaling relations as in the left panels, but with binned data to underline the average trend of active and inactive galaxies. The bins were chosen to include the same number of sources. The mean value and the error bars (standard deviations) in each bin were determined with a bootstrap procedure with 10000 iterations.

3.4.1 $L_{IR}-L'_{CO(1-0)}$ relation

Normal star-forming galaxies, for which a relation has been found between stellar mass and star formation (the so-called Main Sequence, MS; e.g. Renzini and Peng 2015), are thought to follow a unique $L_{IR}-L'_{CO(1-0)}$ relation at all redshifts (e.g., Daddi et al. 2010; Genzel et al. 2010; Sargent et al. 2014), suggesting a ubiquitous relation between SF activity and molecular gas reservoir in normal SFGs. Conversely, objects with higher SF efficiency as local ULIRGs and high- z starburst sources exhibit higher $L_{IR}/L'_{CO(1-0)}$ ratios, implying a possible bimodal SF scenario. Here we investigate how our sample of local AGN populates the SF-molecular gas parameter space. Since a direct comparison of SF and molecular gas content could introduce systematic uncertainties, due to the estimate of SFR and M_{H_2} , including the assumption of a CO-to- H_2 conversion factor

which strictly depends on the nature (i.e., Milky-Way like or AGN) of each source, we first study the $L_{IR}-L'_{CO(1-0)}$ relation. In Fig. 3.2 we presented the aperture-corrected CO(1-0) luminosity ($L'_{CO(1-0)}$) as a function of the IR luminosity associated with SF (L_{IR}^{SF}) for the 33 Seyfert 2 galaxies. We fit a line to the data, using the “emcee” package, a pure-Python implementation of Goodman & Weare’s Affine Invariant Markov Chain Monte Carlo (MCMC) Ensemble sampler [Foreman-Mackey et al., 2013]. The best-fit parameters of the linear relation are shown as the black solid line, while the inferred intrinsic dispersion – included in the maximum likelihood as a squared summed contribution to the uncertainties on both luminosity – is $\delta_{intr} = 0.36 \pm 0.05$. The best-fit parameters of the $L_{IR}-L'_{CO(1-0)}$ relation for our sample of Seyfert 2 galaxies are consistent with the results obtained in the literature for local and intermediate-redshift normal SFGs (e.g., Daddi et al. 2010; Genzel et al. 2010; Sargent et al. 2014). Furthermore, our Seyfert 2 galaxies populate common regions of the $L_{IR}-L'_{CO(1-0)}$ diagram as our control sample of SFGs, as clearly shown in Fig. 3.2. This is in agreement with what observed in the upper row of Fig. 3.3, where the AGN populate a common SFR- M_{\star} plane, at least for the $M_{\star} > 10^{9.5} M_{\odot}$.

3.4.2 Molecular gas mass scaling relations

In Table 3.2 we provided the molecular gas masses for our 33 galaxies, which were derived from $L'_{CO(1-0)}$ with the procedure described in Sec. 3.2.1.4. To assess if, and to what extent, AGN can affect the host-galaxy molecular gas content and SF activity, we compare the molecular gas masses (M_{H_2}) as a function of different host-galaxy properties – namely the stellar mass (M_{\star}), and the SFR, dust mass (M_{dust}) and offset from the MS (δ_{MS}) – in our AGN sample, and the control samples (Figs. 3.4 and 3.5, respectively). Looking at the upper left panel of Fig. 3.4, AGN and SFGs samples (DustPedia by Casasola et al. 2020 and 5MUSES by Cortzen et al. 2019) populate the same regime of stellar mass (M_{\star}). Hence, matched in (M_{\star}), AGN have a molecular gas content comparable to that of normal galaxies, following a similar trend over two orders of magnitude. To highlight any hidden trend of the M_{H_2} distribution estimates between AGN and SFGs, in the upper right corner of Fig. 3.4 the binned values of M_{H_2} versus M_{\star} are presented. Each bin contains the same number of entries; the mean and the error bars shown were obtained with a bootstrap procedures with 10000 iterations. We note that the averaged values for the AGN have similar molecular gas content as inactive galaxies.

In the bottom row of Fig. 3.4, the molecular gas masses are presented as a function of SFR. The two quantities show a tighter correlation with respect to the $M_{\star}-M_{H_2}$ distribution, and in agreement with the $L_{IR}-L'_{CO(1-0)}$ relation discussed in Sec. 3.4.1. Nevertheless, when matched in SFR (i.e., $\log(SFR) > 0$) AGN show smaller M_{H_2} with respect to SFGs: almost the entire sample of AGN lies below the M_{H_2} -SFR relation observed for

the DustPedia and 5MUSES SFGs (dashed line). This is confirmed also in the lower right corner, where the binned values of M_{H_2} and SFR are shown. We further checked for any correlation between indicators of the AGN power (AGN bolometric luminosity, L_{AGN}^{bol} ; the ratio of the AGN contribution with respect the entire emission of the galaxy, in the 5-40 μm band, f_{AGN}) and the lower molecular gas content relative to the sequence of SFGs, but we found no significant evidence for such a correlation. This suggest that these result may be due to the assumption of the α_{CO} value, since our sample show similar SFR- M_\star distribution to SFGs.

In the upper left corner of Fig. 3.5, the molecular gas content as a function of the offset from the MS (δ_{MS}) is shown. The excess (or deficiency) of specific SFR (sSFR=SFR/ M_\star) with respect to that expected for MS galaxies can be expressed as $\delta_{MS} = sSFR/sSFR_{MS}$. The normalisation of the MS was derived from the relation by Sargent et al. [2014], which provides the sSFR for MS galaxies, assuming the stellar mass (M_\star) and redshift of our sample. AGN show larger offsets from the MS with respect to the normal galaxies in our control sample, as also visible in top right panel of Fig. 3.5. This happens irrespective to the M_{H_2} with AGN showing larger δ_{MS} over the two orders of magnitude of molecular gas masses. This is consistent with what observed in high-redshift AGN and obscured quasars (e.g., Kakkad et al. 2017; Brusa et al. 2018), which share similar offset from the MS to our local Seyfert 2 galaxies. In the bottom panels of Fig. 3.5, a significant fraction of our sample of AGN show larger dust content (M_{dust}) if paired in M_{H_2} with the control samples. In this case, we do not include the entire sample by Cortzen et al. [2019], since in that work the authors derive the molecular gas mass from M_{dust} by assuming a gas-to-dust ratio, therefore making the two quantities proportional by definition. Nevertheless, we derived the molecular gas mass for 33 objects by Cortzen et al. [2019] with $L'_{CO(1-0)}$ measurements, assuming a $\alpha_{CO}=4.3 M_\odot \text{ pc}^{-2} (\text{K km s}^{-1})^{-1}$ consistently with the α_{CO} value assumed by Casasola et al. [2020] for their inactive galaxies. The AGN which deviate more from the SFGs sequence do not show any peculiarity in terms of AGN power with respect to the remaining objects that follow the trend of the inactive galaxies. Indeed, when matched in M_{dust} , AGN do not significantly differs from the DustPedia SFGs in terms of M_{H_2} .

To conclude, AGN show similar molecular gas content to SFGs over a wide and common range of stellar masses (over two orders of magnitude in M_\star). Nonetheless, when matched in SFR, AGN have systematically smaller molecular gas content, or, conversely, larger SFR if paired in M_{H_2} with the control sample. These higher SFR and ‘normal’ molecular gas content in local AGN could be linked to the nuclear activity. AGN may have had higher H_2 content than SFGs but this molecular gas may have been used both as main ingredient for star formation (resulting in higher SFR) and as AGN fueling (loosing

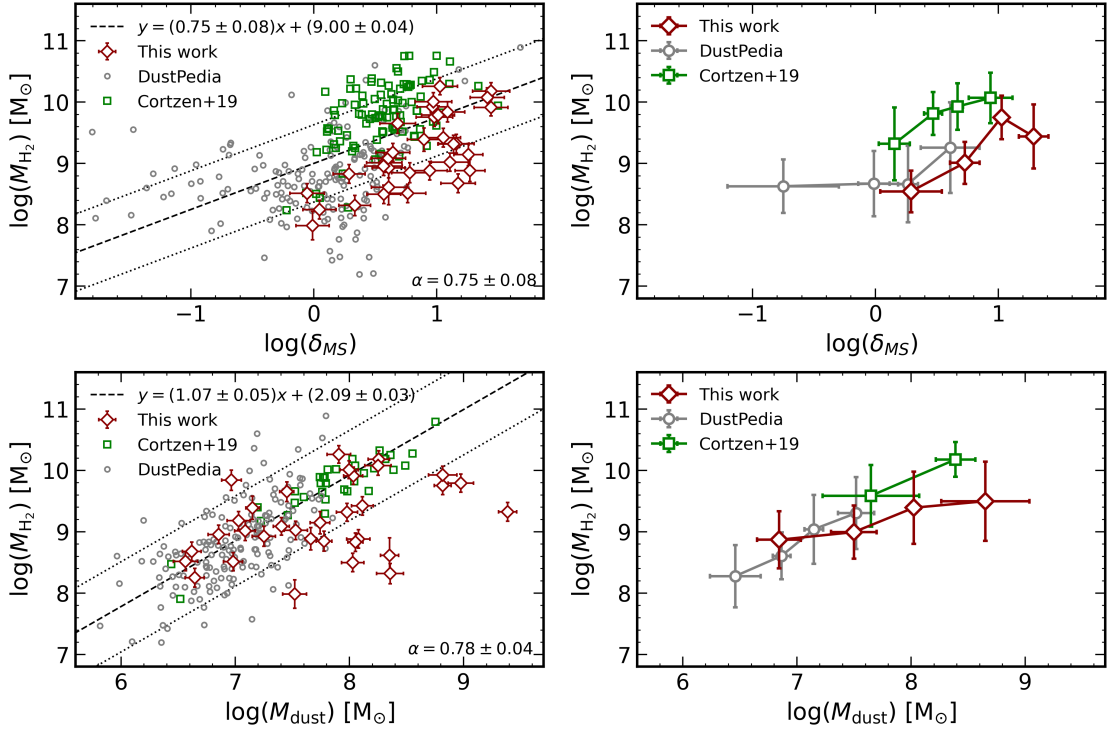


Figure 3.5: Left panels: molecular gas mass (M_{H_2}) versus the offset from the MS (derived assuming the relation by Sargent et al. 2014; top panel), and host-galaxy dust mass (M_{dust} ; top panel). Our sample is plotted as red diamonds, while the control samples are represented by grey circles (DustPedia). In the bottom panel, the M_{H_2} - M_{dust} diagram, where the M_{H_2} of the 33 5MUSES SFGs presented were derived from the CO luminosity [Cortzen et al., 2019], assuming a $\alpha_{CO}=1.1 M_{\odot} \text{ pc}^{-2} (\text{K km s}^{-1})^{-1}$. We do not represent the entire 5MUSES SFGs since their M_{H_2} are derived from the M_{dust} assuming a dust-to-gas ratio. For pure illustrative purposes, the best-fit trend (grey dashed line) for the sample of inactive galaxies is shown, while the two dotted lines are the trend shifted by a factor of 0.5 dex. The best-fit slope is reported in the lower right corner. Right column: same scaling relations presented on the left, but with binned values (using the same method as in Fig. 3.4).

H_2). In addition, molecular gas outflows driven by AGN are frequently detected in local galaxies (e.g., García-Burillo et al. 2014; Audibert et al. 2019), and they are able to drive the gas outwards from the host galaxy. In the Seyfert 2 NGC 1433 Combes et al. [2013] it was revealed the smallest molecular gas outflow ever observed in an external galaxy so far (involving a molecular mass of $3.6 \times 10^6 M_{\odot}$ and with a flow rate $\sim 7 M_{\odot}/\text{yr}$), showing how also relatively low intense outflows are able to influence the balance between gas and SF in galaxies.

Owing to the higher SFRs, the Seyfert 2 galaxies show larger offset from the MS, since δ_{MS} depends on the SFR by definition. Finally, active and inactive galaxies spanning a common range of M_{dust} show similar molecular gas contents.

3.4.3 Molecular gas depletion times

Given the gas mass computed in Section 3.2.1.4 and the SFR provided by G16 we estimate the depletion time for each galaxy. We found depletion times in the range $0.06 < t_{depl} < 1.8$ Gyr (with mean value 0.36 Gyr and $\sigma = 0.36$ Gyr; see the right panel of Fig. 3.6), consistent with what has been reported in previous literature works in local AGN ($L_{bol} \sim 10^{43-46}$ erg s⁻¹) with similar host-galaxy properties in terms of M_* and SFR ($0.1 < t_{depl} < \text{few Gyr}$; e.g., Casasola et al. 2015; Rosario et al. 2018, Koss et al. 2020). Conversely, shorter time scales ($0.01 < t_{depl} < 0.1$ Gyrs) for the gas consumption have been observed in the case of high-redshift AGN or quasars ($z \sim 1-3$; e.g., Brusa et al. 2018; Kakkad et al. 2017; Talia et al. 2018), likely due to the combined enhancement of both SF and AGN activity at the cosmic noon [Madau and Dickinson, 2014].

In the central panel of Fig. 3.6, we plot the depletion times as a function of the offset from the MS of SFGs. In the top and right panels the distributions of δ_{MS} and t_{depl} are shown, respectively.

The Seyfert 2 galaxies show, on average, short t_{depl} and large distances from the MS, with respect to the distribution of SFGs. Looking at the depletion time distribution for the Seyfert 2 galaxies and the control samples (Fig. 3.6, right panel) it is clear that t_{depl} for the AGN peaks at lower values ($t_{depl} \sim 0.3$ Gyr), while the control samples (DustPedia and 5MUSES) peak at $t_{depl} \sim 1$ Gyr. Indeed, our sample occupies a region of the $t_{depl}-\delta_{MS}$ diagram which lies below the trend observed in MS galaxies, represented by the relation by Tacconi et al. [2018] (see the main panel of Fig. 3.6), which describes the expected t_{dep} for MS galaxies, with a given M_* and redshift (here shown at the redshift and M_* of our galaxies).

Since this results depends on the assumption of the α_{CO} in Fig. 3.7 we present the same plot as in Fig. 3.6, but here we assumed a Milky-Way value ($\alpha_{CO}=4.3 M_{\odot} \text{ pc}^{-2} (\text{K km s}^{-1})^{-1}$). It is clear that our sample show a completely consistent distribution of t_{depl} as our control samples of SFGs. Anyway, the deviation of the Seyfert 2 galaxies from the MS, expressed in terms of δ_{MS} , is still clear. We concluded that local AGN are hosted in galaxies where the molecular gas reservoir is similar to that in nearby SFGs. Then, our Seyfert 2 galaxies show longer depletion times with respect to the quasars at higher redshift ($0.01 < t_{depl} < 0.1$ Gyrs at $z \sim 1-3$; e.g., Brusa et al. 2018; Talia et al. 2018).

3.4.4 PAH as tracer of the molecular gas

The $L_{IR}-L_{PAH}$ relation has been widely used as a diagnostic to distinguish between different galaxy population (e.g., Cortzen et al. 2019; Minsley et al. 2020), since different galaxies (e.g., MS galaxies, starbursts, AGN-composite) occupy different parts of the

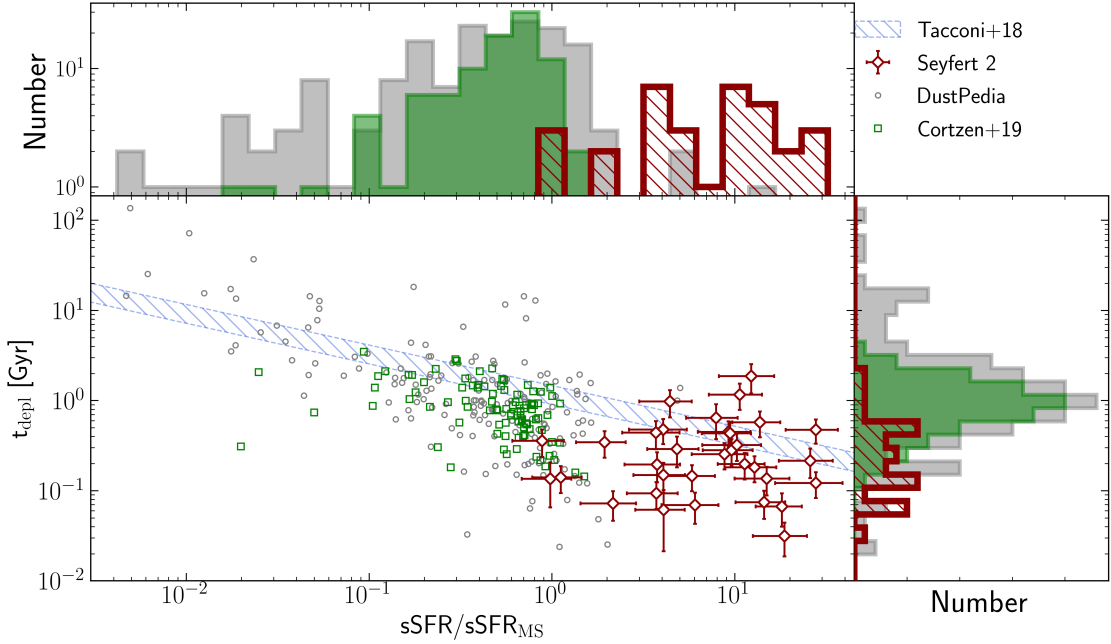


Figure 3.6: Main panel: Depletion time (in units of Gyr) vs, the distance from the MS (δ_{MS}) in terms of the sSFR. The sources in our sample are the red diamond, while the control samples are the grey circles (DustPedia) and green squares [Cortzen et al., 2019]. The dashed region represents the $t_{depl}-\delta_{MS}$ relation by Tacconi et al. [2018], within the interval of stellar masses and redshift in our sample. Upper and right panels: projected histograms of the distance from the MS and the depletion times, respectively, for our sample and the control samples, following the same colour coding.

diagram. This relation can also be used to assess the effect of the AGN on the SF activity of its host galaxy, if any. In the upper panels of Fig. 3.8, we compare the $L_{IR}-L_{PAH}$ distribution for our sample, compared with the control sample by Cortzen et al. [2019], the one with available PAH measurements. The mid-IR features analysed by HC11 (i.e., the PAH at 6.2 and 11.3 μm) seem to correlate with the IR luminosity, as observed in many local objects (e.g., Alonso-Herrero et al. 2016; Jensen et al. 2017; Kirkpatrick et al. 2017), even in presence of nuclear activity. We performed a linear fit of the $L_{IR}-L_{PAH}$ relation, $\log(L_{PAH}) = \alpha \log(L_{IR}) + \beta$, considering both the PAH at 6.2 and 11.3 μm luminosity. The results of this fit are presented in Fig. 3.8. We found a slope ($\alpha = 1.05 \pm 0.02$) slightly steeper than that of Cortzen et al. [2019], and a significantly lower normalisation ($\delta_\beta \sim 0.6$ dex), larger than the intrinsic dispersion of our relation ($\delta = 0.15$ dex). Our sample of active galaxies shows lower 6.2 μm PAH luminosities for a given L_{IR} , suggesting a potential effect of the nuclear activity on the emission of this mid-IR feature. This is supported by the similar trend observed in the sub-sample of active objects (i.e., AGN, or composite, with $\text{EW}_{6.2\mu\text{m}} > 0.4\mu\text{m}$; see also Sargsyan et al. 2012; Stierwalt et al. 2014), by Cortzen et al. [2019], which we represent as blue triangles. Indeed, lower $L_{PAH}-L_{IR}$

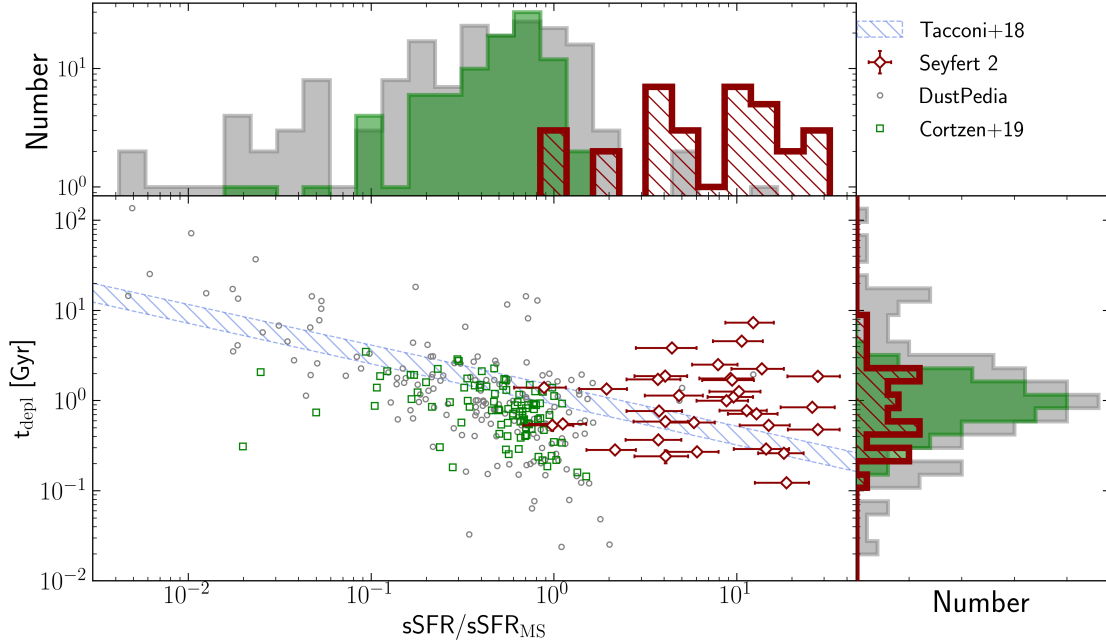


Figure 3.7: Main panel: Depletion time (in units of Gyr) vs, the distance from the MS (δ_{MS}) in terms of the sSFR. Same as Fig. 3.6, but in this case we assumed $\alpha_{CO}=4.3 M_{\odot} \text{ pc}^{-2} (\text{K km s}^{-1})^{-1}$ for the Seyfert 2 galaxies. Upper and right panels: projected histograms of the distance from the MS and the depletion times, respectively, for our sample and the control samples, following the same colour coding.

ratios have been reported in active galaxies compared to SFGs (e.g., Armus et al. 2007; Valiante et al. 2007; Sajina et al. 2008; Diamond-Stanic and Rieke 2010), suggesting that AGN can, at least in part, suppress the PAH luminosity.

We then found similar results for the fit of $L_{PAH,11.3\mu m} - L_{IR}$ ($\alpha = 1.03 \pm 0.03$, but with larger intrinsic dispersion of $\delta = 0.18$ dex; see the right panel of Fig. 3.8). This is in agreement with the literature, since $6 \mu m$ feature is likely excited by SF-related emission, while the one at longer wavelength could be more affected by the presence of AGN impinging radiation, hence resulting in a larger scatter. Our result – i.e. the depleted PAH luminosity in the presence of an nuclear activity – suggests that extrapolating the molecular gas mass from the PAH feature luminosity (as suggested by Cortzen et al. [2019]) can induce a significant underestimation of M_{H_2} if the presence of nuclear activity has not been properly identified, as it happens in the case of heavy extinction of weak nuclear emission, as in some of the sources among our Seyfert 2 galaxies.

In the lower panels of Fig. 3.8, we plot the $6.2 \mu m$ and $11.3 \mu m$ PAH luminosities, respectively, versus the bolometric luminosity of the AGN ($L_{bol,IR}^{AGN}$), provided by G16. Following the results by G16 (see Fig. 10 in G16), we divided the sample in two subsamples on the basis of the f_{AGN} and we fitted separately the two subsamples. We

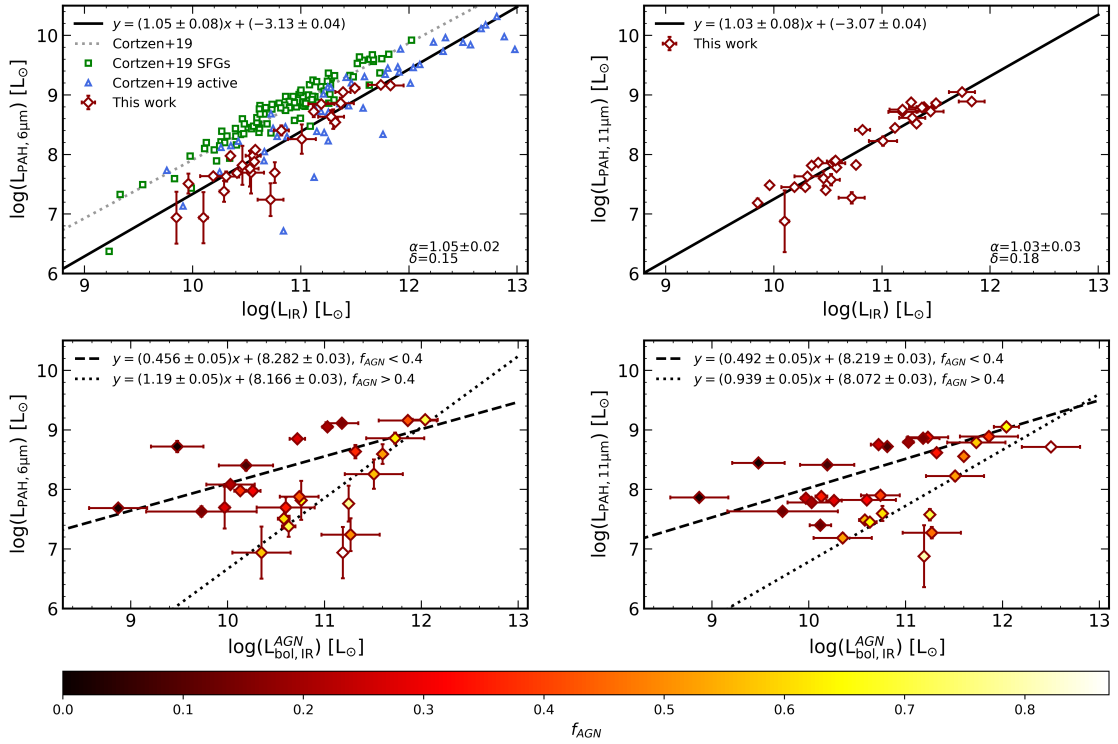


Figure 3.8: Top left panel: The $6.2 \mu\text{m}$ PAH feature luminosity versus the IR luminosity. Our sample is shown as red diamonds, while green squares and blue triangles indicate the inactive and active galaxies in the sample by Cortzen et al. [2019], respectively. Our best fit relation (best fit slope α and dispersion δ are reported in the lower-right corner) is the black solid line, while the grey dotted line is the result of the best fit by the Cortzen et al. [2019]. The best fit relation on the entire parent of our parent Seyfert 2 galaxies by G16 is shown with the dot-dashed line. Top right panel: The $11.3 \mu\text{m}$ PAH feature luminosity versus the IR luminosity for our sample. Points and lines are coded as in the left panel. Bottom panels, from left to right: $6.2 \mu\text{m}$ and $11.3 \mu\text{m}$ PAH luminosities, respectively, versus the bolometric luminosity of the AGN, derived from the broad band SED decomposition performed by G16. Data are colour mapped as a function of the fraction of the AGN emission with respect to the galaxy global outcome in the $5\text{-}40 \mu\text{m}$ band. Dashed (dotted) lines are the best fit relation for the subsample of AGN with $f_{AGN} < 0.4$ (> 0.4).

found that AGN with a relatively larger contribution of the AGN to the mid-IR outcome of the galaxy $f_{AGN} > 0.4$ show fainter PAH emission (both the $6.2 \mu\text{m}$ and $11.3 \mu\text{m}$ features) for a given AGN bolometric luminosity. To summarise, by comparing the PAH emission in our sample of active galaxies with that observed in SFGs by Cortzen et al. [2019], we concluded that the emission from PAH features can be affected, i.e. depleted, by the presence of nuclear activity. Furthermore, by dividing our sample of Seyfert 2 galaxies on the basis of their relative contribution of the AGN to the global emission from the galaxy in the mid-IR, we found that larger f_{AGN} for a given AGN bolometric luminosity corresponds to fainter PAH emission.

3.5 Conclusions

In this Chapter we have studied the properties of a sample of 33 local Seyfert 2 galaxies with the aim of understanding the impact of the nuclear activity on the host-galaxy molecular gas content and SF activity. By considering new and archival CO spectroscopic data, we estimated the mass of the cold molecular component of the ISM – the key ingredient to form new stars. We exploited the results of the detailed SED decomposition by G16, providing the characterisation of each galaxy, e.g. in terms of M_\star , SFR, L_{IR} , and emission from the AGN. By comparing the molecular gas content (M_{H_2}) and the relative depletion time in our sample of local Seyfert 2 galaxies matched in different host-galaxy properties (M_\star , SFR, M_{dust}) to a control sample of SFGs, we investigated the effect of the nuclear activity on the host-galaxy molecular gas reservoir. Furthermore, we investigated the effect of the nuclear activity onto the PAH features, which are widely used as tracers of SF activity, while the presence of the AGN can actually affect their luminosity – in the literature AGN have been observed both suppressing and enhancing the PAH emission (e.g., Sajina et al. 2008) and Jensen et al. 2017, respectively)

The main results of our work are:

- aperture-corrected molecular gas masses were derived for 33 objects ($M_{H_2} \sim 10^{8-10} M_\odot$), estimated by converting the low-J CO luminosity.
- Over a wide range in stellar masses, our AGN show similar molecular gas content, and larger SFR than SFGs. Hence, when matched in molecular gas content, AGN are characterised by larger offset from the MS of normal galaxies with respect to our control samples.
- When comparing the depletion times for the Seyfert 2 galaxies and SFGs, the AGN distribution peaks at similar depletion times to that of SFGs if we assumed the same α_{CO} for both active and inactive galaxies, consistently with the time scales observed in nearby Universe. The choice of a good α_{CO} factor for AGN remain still an issue which need to be properly investigated, especially when we are interested in measuring the molecular gas content in the central of galaxies, while when we consider the CO emission over the entire galaxy we would expect that the effect of AGN activity is diluted. The even shorter depletion times observed in high-redshift AGN and quasars ($z \sim 1-3$; e.g., Brusa et al. 2018, Kakkad et al. 2017, Talia et al. 2018), are likely due to the enhancement of both SF and AGN activity at cosmic noon.

- By studying the L_{PAH} - L_{IR} scaling relations with the PAH features at 6.2 and 11.3 μm , we found that our sample of local Seyfert 2 galaxies shows lower L_{PAH}/L_{IR} ratios with respect to SFGs, as previously observed in AGN-dominated sample. Furthermore, when studying the PAH emission as a function of the AGN bolometric luminosity in our Seyfert 2 galaxies, we found that the objects with a relatively larger contribution from the AGN in the mid-IR f_{AGN} show fainter PAH emission. This suggests that AGN activity is able to suppress the emission of PAH features, being more efficient when the AGN emission dominate the mid-IR regime.

4

A test case: NGC 7213

This Chapter is mainly based on “Molecular gas in the central region of NGC 7213”, F. Salvestrini, C. Gruppioni, F. Pozzi, C. Vignali, A. Giannetti, R. Paladino, E. Hatziminaoglou, 2020, A&A, 641, A151.

In the previous Chapters we emphasise the importance of a multi-wavelength strategy to properly understand the role of AGN in regulating the host galaxy’s SF. As introduced in Section 1.2.2.2, accreting SMBHs are responsible for injecting energy in the circum-nuclear region, providing feedback to its host galaxy and the ISM (see, e.g. Fabian 2012; Somerville and Davé 2015, and references therein). AGN are held responsible for both suppressing the SFR, which constitutes ‘negative feedback’, or enhancing it through the compression of molecular clouds, which constitutes ‘positive feedback’.

For this reason, the SF activity and SMBH properties are believed to be connected, both in high-redshift quasars and in local Seyfert nuclei (see also Fig. 1.1). In this scenario, the molecular gas plays a fundamental role, because it is the main fuel for SF and the more abundant phase of the ISM in the nuclear region. In Chapter 3, we emphasise that studying the properties of the molecular gas in galaxies and the rate at which it is converted into stars (i.e., the depletion time) can be used to assess the effect of the feedback from nuclear activity. This study can be complemented by spatially resolved observations tracing the cold phase of the ISM, to directly probe the physical state of the molecular gas in the nuclear regions, where the emission from the AGN prevails, while at increasing distances from the centre, stellar processes such as supernovae, stellar winds or shocks start dominating.

Given this context, in this Chapter we present a test study to show the potential of the multi-waveband method, focusing our attention on one object out of the 76 by G16. The

target of this study is NGC 7213, a nearby spiral galaxy showing intermediate properties between a low-luminosity AGN (LLAGN) and a LINER. The intermediate nature makes this object interesting to our purpose, allowing us to test our approach in an objects with not extreme properties (as a quasar or a starburst galaxy), where the SF and accretion activity coexist. The multi-wavelength strategy allows us to clarify the intrinsic nature (AGN vs SF) of the source. Finally, we chose NGC 7213 also for the quality and variety of available archival observations in different bands, in particular in the X-rays (e.g. *NuSTAR* and *XMM-Newton*) to characterise the AGN power, and at mm wavelengths (ALMA and APEX) to trace the molecular gas content and kinematics.

This Chapter is organised as follows: in Section 4.1, we summarise the multi-waveband properties of the NGC 7213. In Section 4.2, we introduce the data sets that we reduced and analysed in this work. The interpretation of the CO and the continuum mm emission is presented in Section 4.3. Our conclusions and the results are summarised in Section 4.4.

Throughout the Chapter, distance-dependent quantities are calculated for a standard flat Λ CDM cosmology with the matter density parameter $\Omega_M = 0.30$, the dark energy density parameter $\Omega_\Lambda = 0.70$, and the Hubble constant $H_0 = 70 \text{ km s}^{-1} \text{ Mpc}^{-1}$ [Komatsu et al., 2009]. Errors are given at 68 per cent confidence level.

4.1 NGC 7213

The galaxy NGC 7213 is a nearby ($D=23 \text{ Mpc}$, $z=0.0058$) S0 one, which hosts an active nucleus, and was first discovered with the *HEAO A-2* satellite (e.g. Marshall et al. 1979). The classification of this source was long debated (e.g. Halpern and Filippenko 1984), and nowadays it is known as an intermediate object — between a LLAGN (with $L_{\text{bol}} = 1.7 \times 10^{43} \text{ ergs s}^{-1}$, Emmanoulopoulos et al. 2012) and a LINER (e.g. Starling et al. 2005). The first published optical spectrum by Phillips [1979] suggested the Seyfert 1 classification on the basis of the observed broad $H\alpha$ emission-line component (with full width at zero intensity $\sim 13000 \text{ km s}^{-1}$). They also found that the flux of the $H\alpha$ was relatively low with respect to what was usually measured in typical Seyfert 1 galaxies, and broad components were very weak or absent in the other observed optical emission lines. Later, Halpern and Filippenko [1984] confirmed the presence of the broad $H\alpha$ emission line, but the evidence for a low-excitation narrow-line spectrum led to the inclusion of the source in the LINER class.

The X-ray observations confirmed the ambiguous nature of NGC 7213. Archival observations with different X-ray telescopes over several years showed some spectral features in agreement with the Seyfert 1 classification (e.g. an X-ray spectral slope

$\Gamma_X \sim 1.8$ and no evidence for neutral or ionised absorption features: Bianchi et al. 2008; Lobban et al. 2010; Emmanoulopoulos et al. 2013), while others did not (e.g. the absence of a Compton reflection component, usually observed in local Seyfert 1 galaxies: e.g. Dadina 2008; Ursini et al. 2015).

To complete the multi-band picture of NGC 7213, at radio frequencies the galaxy appears point-like at 3 cm (half power beam width $\text{HPBW} \lesssim 1$ arcsec), which was interpreted by Bransford et al. [1998] as either nuclear synchrotron emission or free-free emission. The radio power is $P_{1.4\text{GHz}} = 3 \times 10^{29} \text{ erg s}^{-1} \text{ Hz}^{-1}$, at least an order of magnitude higher than that of a typical Seyfert, although too low for a radio-loud classification (e.g. Blank et al. 2005). The compactness of the radio emission was also later confirmed by Murphy et al. [2010], who observed NGC 7213 with ATCA at higher frequencies (5, 8, and 20 GHz; see also Bell et al. 2011).

4.2 Multi-waveband data

Here we provide the multi-band picture of NGC 7213 through a new and coherent modelling of the most relevant data to describe the overall emission of the source in the X-rays over a broad energy range (including the hard-X data from *NuSTAR*) and the analysis of sub-mm/mm single-dish (APEX) and interferometric (ALMA) observations. The X-ray data analysis aims at providing an accurate estimate of the accretion power, while the study of the high spatial resolution of the ALMA data is used to characterise the morphology and kinematics of the molecular gas. Finally, the single-dish APEX observation is used to provide reliable estimates of the integrated CO emission, needed to derive the molecular gas mass content.

4.2.1 X-ray data

The NGC 7213 galaxy has been observed extensively over the last 20 years in the X-rays using a number of facilities, in both soft and hard bands. We are interested in characterising the nuclear activity of the source in terms of the emitting power of the AGN, meaning the luminosity in the 2-10 keV band produced by the primary emission. For this reason, we decided to use the largest band available, combining the information from *NuSTAR* (nominally, 3-79 keV) with an instrument in the 0.3-10 keV band (i.e. *XMM-Newton*). We analysed the *NuSTAR* observation and the one from *XMM-Newton* with the longer exposure time separately (130 ks: e.g. Emmanoulopoulos et al. 2013) to obtain a global picture of the properties of the source in terms of the spectral features and continuum emission. We did not combine the *NuSTAR* and *XMM-Newton* observations since they were not taken simultaneously, and previous works revealed evidence for minor

variability in terms of flux and spectral features in NGC 7213 (e.g. Ursini et al. 2015). Nevertheless, the observed variabilities do not significantly affect the X-ray properties of the source (e.g. Bianchi et al. 2003; Lobban et al. 2010; Emmanoulopoulos et al. 2013).

4.2.1.1 X-ray data reduction

We re-analysed and combined the following archival observations from *XMM-Newton* (ID: 605800301; starting on Nov. 11 2009; $t_{\text{exp}} = 132.5$ ks) and *NuSTAR* (ID: 60001031002; starting on Oct. 05 2014; $t_{\text{exp}} = 101.6$ ks). We performed a standard data reduction for each data set similarly to the procedure adopted in 2, and extensively described in Section 2.1.2. Once the spectra were calibrated, we excluded the energy channels where either calibration issues are known to affect the cameras response, or a high background was present (i.e. signal-to-noise ratio ~ 1). In particular, for the *XMM-Newton* pn and MOS cameras, we excluded the channels corresponding to energies below 0.5 keV due to calibration issues, while above 10 keV the background dominates. Regarding *NuSTAR*, as high background affected all the channels above 27 keV and calibration issues affected the channels below 3 keV, these energy intervals were also removed. Both *NuSTAR* and *XMM-Newton* data were grouped with a minimum number of 30 counts in each channel bin.

4.2.1.2 X-ray data analysis

The spectral analysis was performed using the X-Ray Spectral Fitting Package (XSPEC) v. 12.10.0c [Arnaud, 1996]. All the models presented below include the Galactic absorption ($N_{\text{H}} = 1.06 \times 10^{20} \text{ cm}^{-2}$; Kalberla et al. 2005). We also included cross-calibration constants to account for different responses between EPIC pn and both MOS cameras in *XMM-Newton*, and between FPM A and B in *NuSTAR*. We analysed each data set separately and compared our best-fit models with the literature (e.g. Bianchi et al. 2003 for *XMM-Newton*, and Ursini et al. 2015 for *NuSTAR*). This also allowed us to check for any potential variability both in flux and in spectral shape as a function of time, since the observations were taken with a separation of five years.

Starting from the *XMM-Newton* observation, the simplest model we used was a single power-law, with best-fit spectral index $\Gamma_{\text{X}} \sim 1.65$. This represents the primary X-ray emission from the nuclear activity, produced by the inverse Compton of the hot electrons from the corona on the seeds of UV photons produced in the accretion disc. It is the emission we are interested in, since it is strictly associated with the accretion processes onto the SMBH. Clear excesses (up to 5σ) were evident in the ~ 6 -7 keV energy band. Then, we included, one at a time, three Gaussian lines, with a fixed width of 10 eV. Given their best fit energies (see Table 4.1), they can be associated with the Fe $K\alpha$

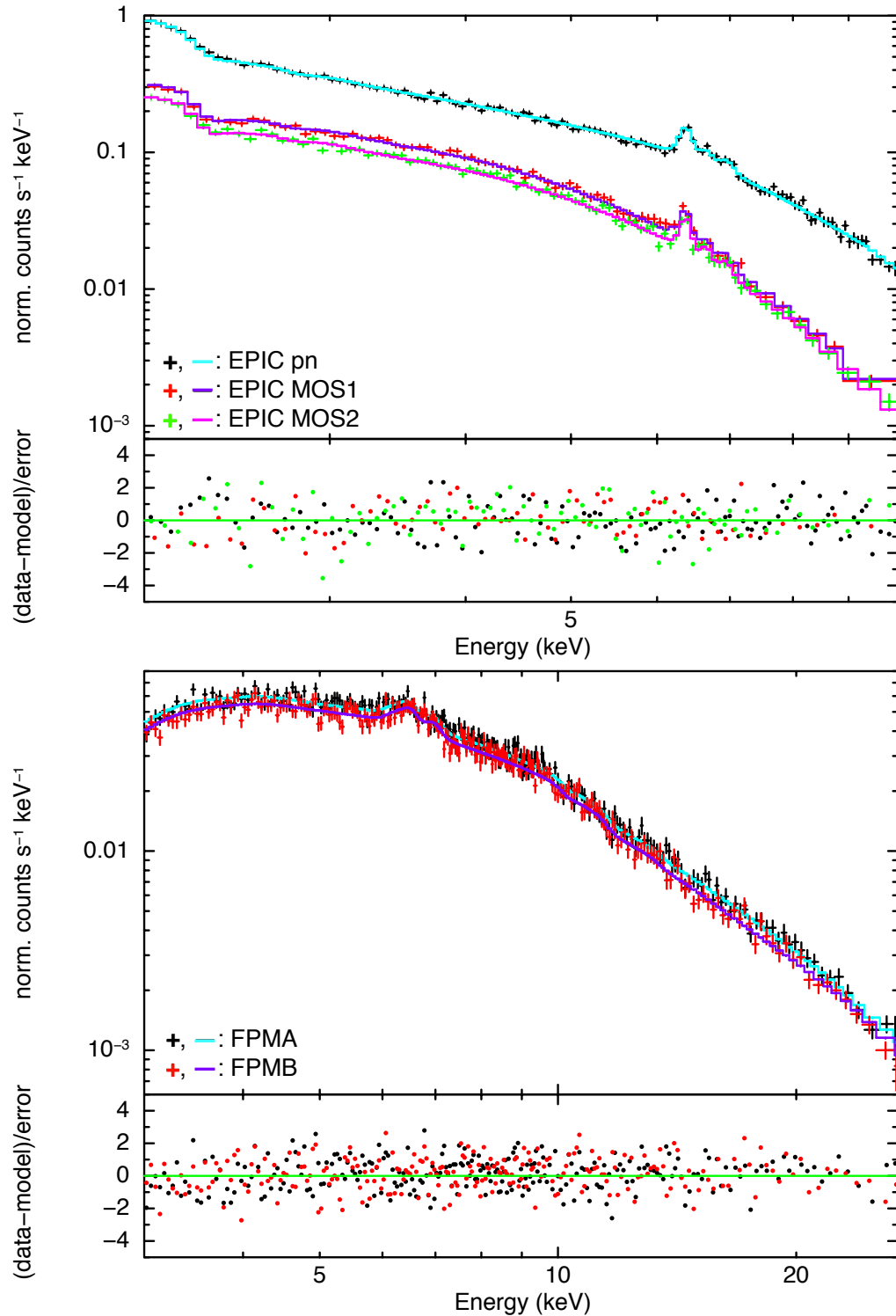


Figure 4.1: From top to bottom: X-ray spectrum of NGC 7213 obtained with XMM-Newton (EPIC pn, MOS1 and MOS2) and NuSTAR (FPMA and FPMB), as a function of the observed-frame energies. Data and the best fit models for each camera are represented in different colours. In both lower panels, we present the residuals (data minus model) in units of σ .

fluorescence emission line at the rest-frame 6.39 keV, and the ionised Fe XXV and Fe XXVI fluorescence emission lines at the rest-frames 6.7 and 6.97 keV, respectively. We found no evidence for absorption of the primary continuum emission ($N_H < 10^{21} \text{ cm}^{-2}$). Since some residuals were present in the soft part of the analysed band (i.e. at ~ 2 keV), we included a ‘mekal’ component, which is needed to model the excess likely produced by the diffuse emission from the high-energy tail of SF. In the end, our best fit model consists of a power law, three Gaussian emission lines, and a thermal component. The best fit model ($\chi^2 = 388.4$ for 321 degrees of freedom) is shown in the top panel of Fig. 4.1, and the best fit parameters are presented in Table 4.1 and are consistent with results in the literature (e.g. Emmanoulopoulos et al. 2013). The flux obtained integrating the primary AGN emission (i.e. the power law) in the rest-frame 2-10 keV is $F_{2-10\text{keV}} = (1.22_{-0.01}^{+0.01}) \times 10^{-11} \text{ ergs s}^{-1} \text{ cm}^{-2}$.

Considering the wide energy band (3-27 keV) offered by *NuSTAR*, we first fit the continuum emission with a single power law. In this case, we obtained a poor fit, with significant residual excess in the $\sim 6-7$ keV band. Given the lower spectral resolution provided by *NuSTAR* (~ 400 eV at 6 keV with respect to ~ 150 eV from *XMM-Newton*), we were not able to constrain both the centroid and the normalisation of the Gaussian lines needed to model the excess in the $\sim 6-7$ keV band. For this reason, we included the Gaussian functions one at a time, setting the energy in correspondence of the best fit obtained with *XMM-Newton*, then we left the normalisation free to vary (as in Ursini et al. 2015). The primary emission spectral index is significantly higher ($\Gamma_X = 1.81 \pm 0.02$) than the one observed with *XMM-Newton*, consistently with the literature [Ursini et al., 2015]. This is likely due to the wider energy band available to model the primary emission where there are no significant contributions from other components (e.g. the thermal component below 3 keV). Part of the primary emission is usually reflected by the surrounding material around the SMBH, resulting in an excess above 10 keV with respect to the continuum. This reflected component is usually observed in Seyfert 1 galaxies (e.g. Perola et al. 2002), but has never been observed in NGC 7213. We checked for the presence of a reflection component, but the fit was not significantly improved by such inclusion. The best fit is presented in the bottom panel of Fig. 4.1 ($\chi^2 = 344.2$ for 342 degrees of freedom), while the best-fit parameters are shown in Table 4.1. Integrating the power law over the rest-frame of the 2-10 keV energy band, we estimated a flux of $F_{2-10\text{keV}} = (1.62_{-0.02}^{+0.02}) \times 10^{-11} \text{ ergs s}^{-1} \text{ cm}^{-2}$.

Comparing the best fit results between the two observations, variability in both flux and spectral shape is present. The observed variability in terms of flux (the flux measured by *XMM-Newton* is $\sim 25\%$ fainter than the that derived by *NuSTAR* data) is consistent with what is usually observed in AGN, while the different spectral slope ($\Gamma_X = 1.64$ and

1.81, see Table 4.1) may be due to the different energy band used for the analysis. In the end, in the X-rays NGC 7213 shows spectral features of a typical low-luminosity Seyfert 1 (i.e. $\Gamma_X \sim 1.8$) with no evidence for obscuration, and $L_{2-10\text{keV}} = (1.25 \pm 0.02) \times 10^{42}$ ergs s^{-1} , using the results from the analysis of the *NuSTAR* observation. Assuming a bolometric conversion factor of $k_{bol} = 9 \pm 5$ as from Lusso et al. [2012], appropriate for the 2-10 keV luminosity of NGC 7213, we estimate the bolometric luminosity to be $L_{bol} = (1.1 \pm 0.6) \times 10^{43}$ ergs s^{-1} , consistent with previous results from literature (e.g. Starling et al. 2005; Emmanoulopoulos et al. 2013). This means that NGC 7213 is accreting at a very low rate, resulting in a rather low fraction of the Eddington luminosity ($\sim 9 \times 10^{-4}$, assuming a black hole mass $M_{BH} \sim 10^8 M_\odot$, as measured from the observed stellar velocity dispersion; Woo and Urry 2002). This value is relatively low with respect to typical Seyfert 1 galaxies (a few per cent), again stressing the intermediate nature of NGC 7213 between a Seyfert galaxy and a LINER.

| Parameter | Value | Value |
|-----------------------|------------------------|------------------------|
| Parameter | XMM-Newton | NuSTAR |
| Γ_X | 1.64 ± 0.02 | 1.81 ± 0.02 |
| $F_{2-10\text{keV}}$ | $1.22^{+0.01}_{-0.01}$ | $1.62^{+0.02}_{-0.02}$ |
| E_1 | $6.40^{+0.01}_{-0.01}$ | |
| norm ₁ | $18.7^{+1.8}_{-1.4}$ | 16^{+3}_{-3} |
| E_2 | $6.69^{+0.02}_{-0.03}$ | |
| norm ₂ | $5.8^{+1.1}_{-1.4}$ | 5^{+3}_{-3} |
| E_3 | $6.95^{+0.06}_{-0.05}$ | 6.95 |
| norm ₃ | $3.1^{+1.7}_{-1.8}$ | 8^{+3}_{-3} |
| kT | $0.4^{+0.1}_{-0.2}$ | |
| norm _{mekal} | 4^{+2}_{-1} | |

Table 4.1: Best fit parameters from the X-ray spectral analysis using XMM-Newton and NuSTAR observations, respectively. From top to bottom: the spectral index (Γ_X), the rest-frame 2-10 keV flux (in units of 10^{-11} ergs $\text{s}^{-1} \text{cm}^{-2}$), the energy of the Gaussian emission lines (in units of keV), with their normalisation (in units of 10^{-6} photons $\text{cm}^{-2} \text{s}^{-1}$). In the XMM-Newton observation it was necessary to include a thermal component ‘mekal’, accounting for the excess in the soft band at ~ 2 keV, likely produced by hot diffuse gas. The plasma temperature of the ‘mekal’ component is in units of keV, while the normalisation is in units of 10^{-3} photons $\text{cm}^2 \text{s}^{-1}$.

4.2.2 ALMA data

The ALMA observations of NGC 7213 were taken in May 2014 (early science project: 2012.1.00474.S, PI: N. Nagar) at 230 GHz (band 6), in configuration C32-5, including 31 12m antennas. These observations cover the angular scales in the range of $0.5''$ - $25''$, corresponding to 60 pc - 3 kpc at the redshift of the source, where $0.5''$ is the spatial

resolution, while $25''$ is the field of view (FoV). However, the largest angular scale that was recovered with the adopted antenna configuration is $6.2''$, or 750 pc. The spectral setup consisted of three high-resolution spectral windows with 1920 channels of 976.562 kHz in width each, and a low-resolution spectral window of 128 channels of 15.626 MHz in width. Two of the high-resolution spectral windows were centred on the observed frame frequency of the $^{12}\text{CO}(2-1)$ and $\text{CS}(5-4)$ emission lines at 229.2 GHz and 243.5 GHz, respectively. The remaining two windows were centred on the sky frequencies at 240.4 GHz and 227.8 GHz, respectively, in order to measure the sub-mm continuum emission.

The data were calibrated using the ALMA calibration scripts, with CASA version 4.5.3. J2056-4714 was observed as bandpass calibrator, J2235-4835 as phase calibrator, while Neptune was used as an amplitude calibrator, assuming the Butler-JPL-Horizons 2012 model. From the calibrated data, continuum and line images were obtained using the CASA task, ‘clean’. We adopted the natural weighting to get the best signal-to-noise ratio.

4.2.2.1 The continuum emission

In Fig. 4.2, the contour levels of the continuum emission (at 235.1 GHz, or 1.28 mm), obtained from the line-free channels in all the four spectral windows, are presented in red. The beam size is $0.48'' \times 0.44''$ (with a beam position angle of ~ 81.1 deg) and a 1σ RMS level of 8.9×10^{-5} Jy beam $^{-1}$. The emission is clearly produced by a $\lesssim 60$ pc-sized point-like source. Using the ‘imfit’ task from the CASA software, we fitted the map with an elliptical Gaussian profile. The best fit centroid is consistent (within the uncertainties) with the NGC 7213 radio position provided by the NASA-IPAC Extragalactic Database (NED)¹. The ‘imfit’ task provided the continuum flux density, integrating the Gaussian profile, with the corresponding uncertainty: $F_{\nu, \text{cont}} = 40.1 \pm 0.1$ mJy.

4.2.2.2 The CO(2-1) emission line

The CO(2-1) emission line was extracted from the continuum-subtracted cube of the first spectral window. We used the CO(2-1) frequency at the redshift of $z = 0.0058$ (NED) as a reference frequency. We used the ‘clean’ task to iteratively clean the dirty image, selecting a natural weighting scheme of the visibilities. We binned the cube to increase the signal-to-noise ratio, requiring a spectral resolution of 10 km s^{-1} . The cleaned image of the CO(2-1) emission line has a synthesised beam of $0.50'' \times 0.47''$, with a position angle of 73.4 deg and an average 1σ RMS of $0.1 \text{ mJy beam}^{-1}$ per channel.

¹<https://ned.ipac.caltech.edu/>

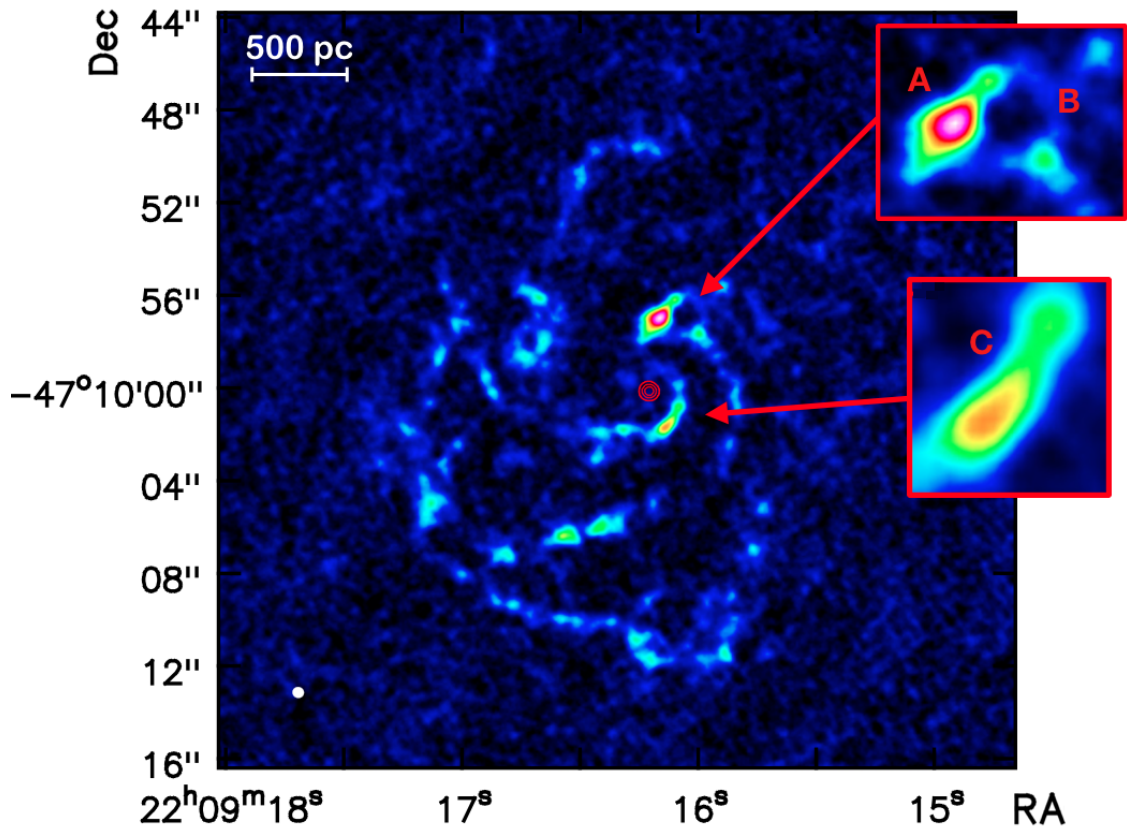


Figure 4.2: ALMA CO(2-1) integrated intensity image with the continuum emission overlaid in red contours (at 5σ , 10σ , and 50σ levels). The white ellipse in the bottom-left corner represents the synthesised beam of $0.50'' \times 0.47''$ with a position angle of 73.4 deg. The three interesting regions are magnified in the two boxes: a possible outflow (A) located at the edge of a super bubble (B) and a second potential outflow observed from the PV diagram analysis (C; see Fig. 4.7).

As presented in the integrated intensity map (see Fig. 4.2), the spatial distribution of the CO line flux follows a spiral-like pattern, which is characterised by a clumpy emission. This can be explained by the combination of the intrinsic clumpy nature of the emitting medium, with the lack of a more diffuse component, which has most likely been resolved because of the extended antenna configuration adopted for the interferometric observation. Using a circular region with a diameter of $25''$ (or ~ 3 kpc, roughly corresponding to the FoV of the instrument), we measured $f_{\text{CO,ALMA}} = 112 \pm 5 \text{ Jy km s}^{-1}$ as the flux of the CO(2-1) emission line. The uncertainty on the flux density is the quadratic sum of the two main contributions: the RMS within the same aperture, and the flux calibration uncertainty ($\sim 5\%$, as suggested when using Neptune as flux calibrator).

Regarding the morphology, the CO(2-1) emission traces the spiral arms of the galaxy, as can be observed in Fig. 4.3, where the contours of the CO emission line

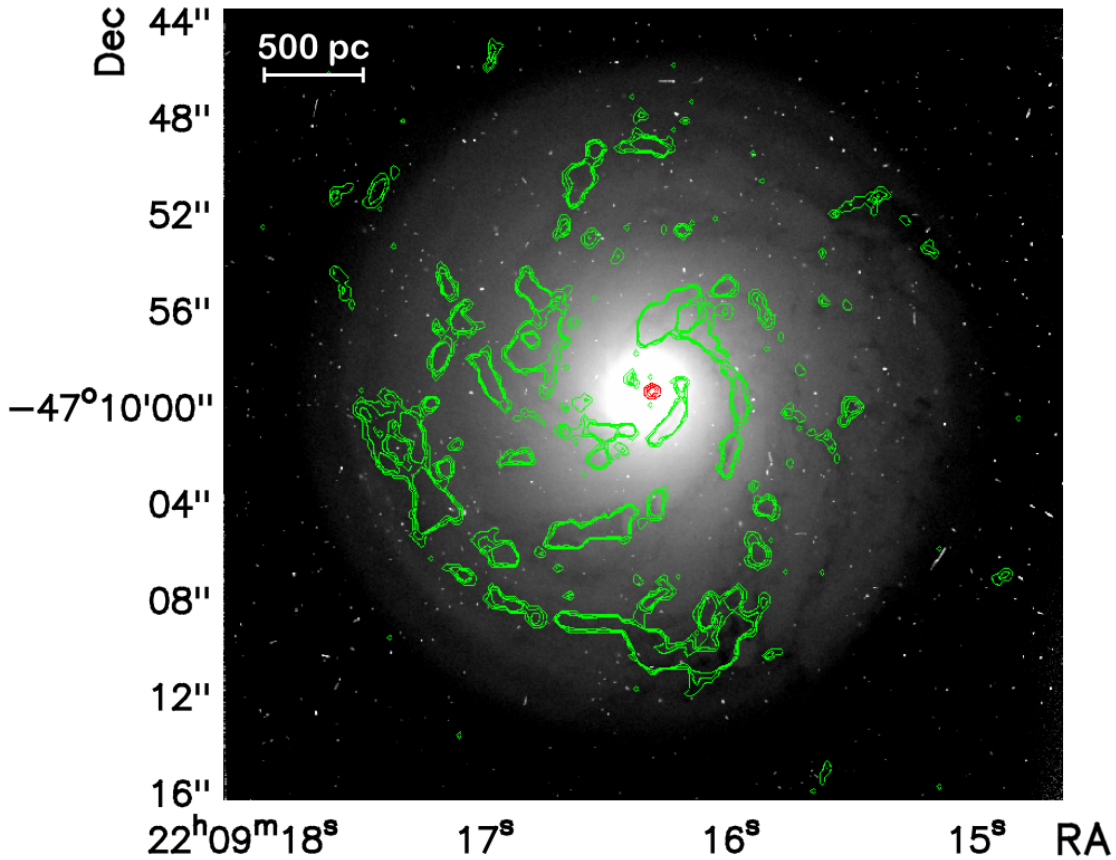


Figure 4.3: Contour levels of continuum (red) and CO(2-1) line emission (green, at 2σ , 4σ , and 6σ levels) are superimposed on an optical image from the Hubble Space Telescope (*HST*; F606W filter). The molecular gas follows the same spiral-like pattern as the optical emission. The continuum is produced by a point-like source.

are superimposed onto an archival *HST* optical observation (taken with the F606W filter on the WFPC2; Malkan et al. 1998). The molecular gas is clearly co-spatial with the spiral arms, while the size of the narrow-line region, estimated from the [O III] line observed with the FR533N filter on the *HST*/WFPC2 [Schmitt et al., 2003], is less than 100 pc. This suggests that the CO(2-1) is most likely heated by the stellar activity within the arms rather than the low-luminosity AGN hosted in the centre. This is in agreement with theoretical models (e.g. Obreschkow and Rawlings 2009; Meijerink et al. 2007; Vallini et al. 2019), where the impinging radiation for the low-J transitions like the CO(2-1) mainly comes from the photodissociation regions (PDRs; e.g. Pozzi et al. 2017; Mingozi et al. 2018) rather than from the X-ray dissociation region (XDR) heated by the central AGN. Indeed, looking at both Fig. 4.2 and Fig. 4.3, CO emission is not present correspondingly with the location of both the ALMA continuum emission and the peak of the optical emission, both indicative of the location of the nucleus.

4.2.3 APEX data

The APEX observation of the CO(2-1) emission line (at 229.2 GHz sky frequency) was carried out with the PI230 receiver at the Atacama Pathfinder Experiment (APEX; project 0103.F-9311, PI: F. Salvestrini). The need for the single-dish observation was motivated by the potential filtering of the CO emission at intermediate and large scales in the interferometric observations. Indeed, the archival ALMA data were limited by the maximum recoverable scale (MRS; $\sim 6.2''$, or ~ 750 pc) of the antenna configuration adopted. This could result in a significant underestimation of the molecular gas content traced by the CO emission. As reported in Section 4.2.2.2, the clumpy morphology observed in the interferometric observation, along with the lack of a fainter diffuse component, supported this hypothesis.

We adopted a standard data reduction, using the CLASS program, as described in 3.2.1.1. The CO(2-1) emission-line profile is presented in Fig. 4.4. The spectral resolution requested for the APEX observation (50 km s^{-1}) is sufficient to observe the double-peak structure of the line profile. This profile is generally associated with rotation-dominated motion, in agreement with the results from the kinematical study of the ALMA data that is presented in Section 4.3.2. The integrated CO(2-1) surface brightness was obtained performing a fit using a double Gaussian function to the line profile. The resulting value is $\Sigma_{\text{CO}} = 9.6 \pm 1.4 \text{ K km s}^{-1}$. As for the APEX CO spectroscopy presented in 3.2.1.1, we conservatively assumed the uncertainty on the surface brightness to be 10%, due to the large calibration uncertainties. To compare this value with the one that we obtained from the ALMA observation, we used the Jy/K conversion factor, which depends on the aperture efficiency of the telescope. In the configuration adopted for our observation (PI230 detector), with Jupiter as a calibrator, the conversion factor is 35 ± 3^2 . Then, $f_{\text{CO,APEX}} = 340 \pm 60 \text{ Jy km s}^{-1}$, meaning ~ 3 times the $f_{\text{CO,ALMA}}$ reported in Section 4.2.2.2. This implies that the ALMA interferometric observations only recovered about 30% of the CO(2-1) flux density measured with APEX.

4.2.4 SED decomposition

The galaxy NGC 7213 benefits from a detailed SED decomposition performed by G16, which allowed us to disentangle the relative contributions of AGN and SF activity to the global IR outcome of the source, providing a characterisation of the host galaxy in terms of stellar and dust content (M_{\star} and M_{dust} , respectively), and ongoing SF (SFR). Here, we briefly introduce the photometric data collected from the archive and the SED decomposition procedure adopted by G16 was already presented in Section 2.1.4. The

²<http://www.apex-telescope.org/telescope/efficiency/>

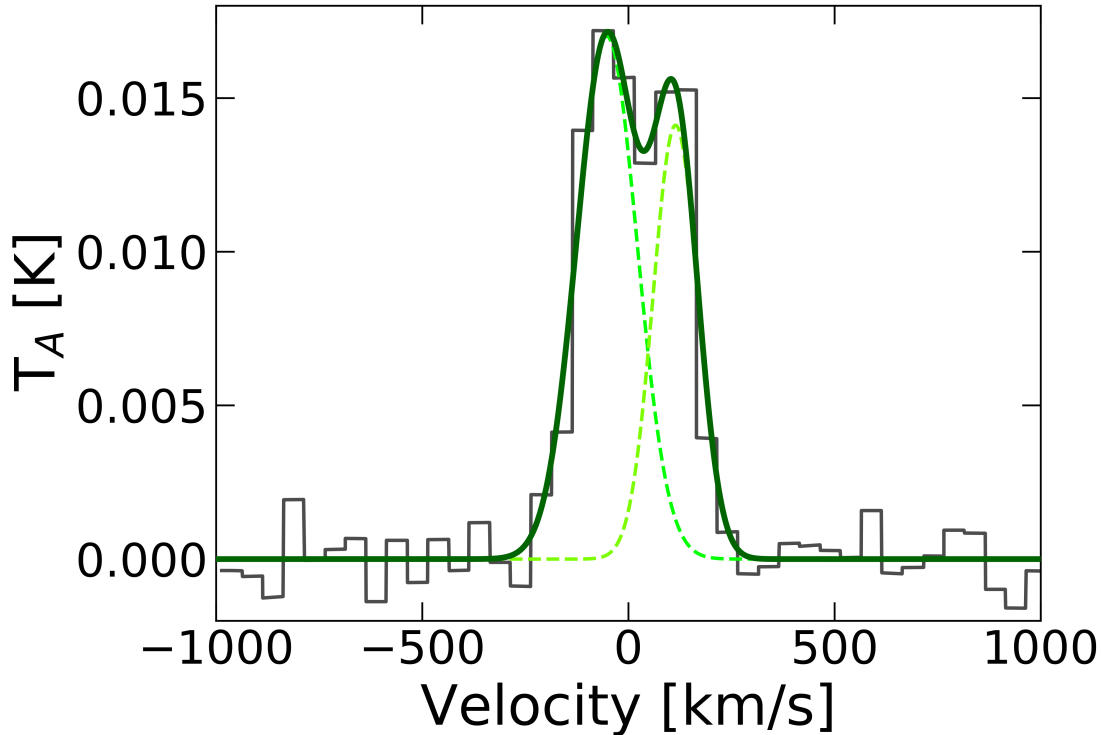


Figure 4.4: CO(2-1) emission line observed with the PI230 receiver at APEX. On the x-axis, the velocity in km s^{-1} , on the y-axis the antenna temperature in K; the channel width is $\Delta v=50 \text{ km s}^{-1}$. Two Gaussian functions (in dashed light green lines, while the sum of the two is in dark green) are needed to reproduce the double-peak spectrum profile (in black). A rotation-dominated kinematics is suggested by the double-peaked line profile.

homogenised catalogue of total fluxes, from the UV to the far-IR, is presented by G16 (see also their Table A.1: the flux densities are corrected for the aperture and magnitude zero point). In the case of NGC 7213, the photometric data included in the analysis are: the U, B, V, and R bands from de Vaucouleurs et al. [1991]; the near-infrared measurements from the catalogue by Jarrett et al. [2000]; the IRS spectrum re-binned by Gruppioni et al. [2016] and the photometry by Gallimore et al. [2010b] and Moshir and et al. [1990] in the mid-IR; and the far-IR photometry by Spinoglio et al. [2002]. In order to limit the degeneracy among the torus parameters, in G16 the AGN configurations of obscured sources were excluded for NGC 7213 (as supported by optical observations of the source and by the X-ray spectral properties presented in Section 4.2.1.2). The best fit model and the decomposition in the different components is presented in Fig. 4.5. The host-stellar contribution and the dusty SF dominate over the AGN in the optical bands and in the entire IR band, respectively. While this could appear to be in contrast with the type 1/broad-line nature of the AGN, it is in agreement with the relatively weak nuclear activity observed in NGC 7213 (revealed also through the X-ray spectral analysis reported Section 4.2.1.2).

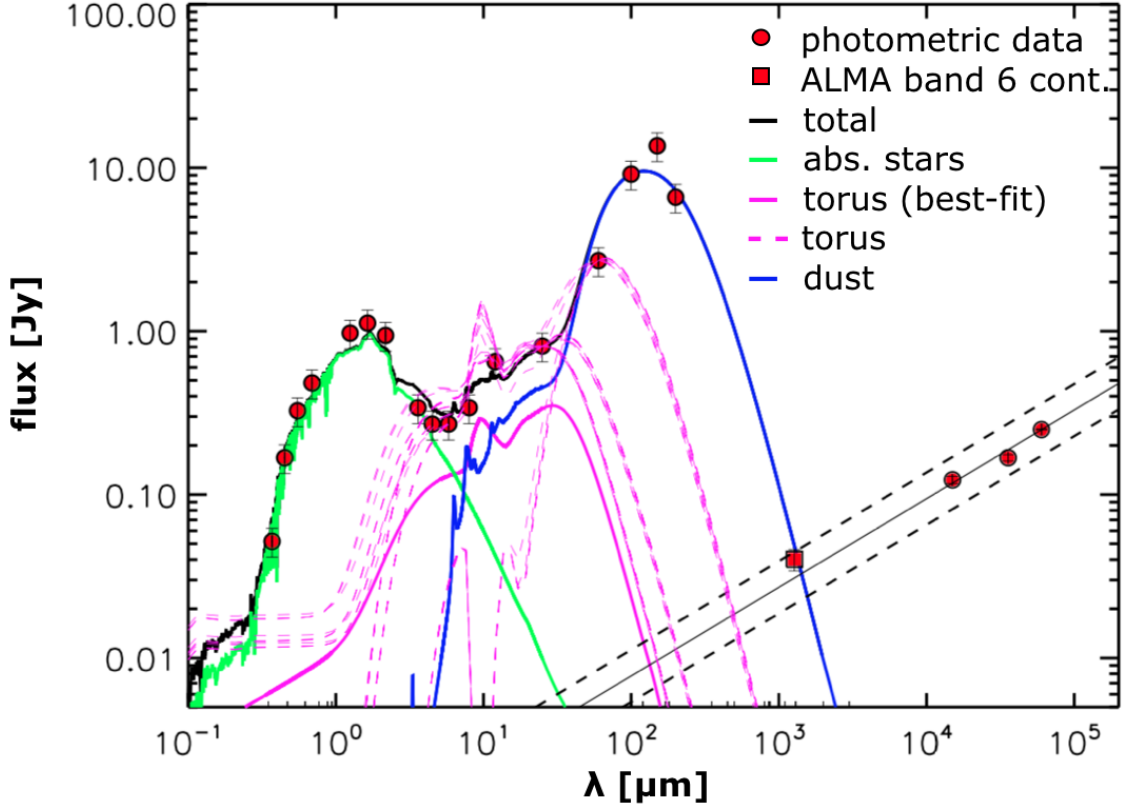


Figure 4.5: Decomposed SED of NGC 7213, obtained with the SED3FIT code [Berta et al., 2013]. Green, pink (continuous line), and blue lines represent the contribution from the extinguished stars, the dusty torus, and the emission reprocessed by dust, respectively, while the black solid curve is the sum of all components (total emission). The red circles are the photometric measurements, from the optical to the radio frequencies (i.e. the ATCA observations at 5, 8, and 20 GHz, not included in the SED decomposition). As explained in Section 4.2.4, the nature of this emission (represented by the red square) is compatible with non-thermal emission produced in the nuclear region, i.e. synchrotron emission. Even considering extreme models (the pink dashed lines), the dusty torus cannot be responsible for the observed emission (red square), since it would be too faint at mm wavelengths (at least two orders of magnitudes fainter). Then, we fitted the three radio-frequency observations by ATCA with a power law, obtaining the best-fit slope represented by the black solid line (the dashed lines correspond to the $1-\sigma$ levels).

4.3 Interpreting the CO and continuum mm emission

4.3.1 The point-like continuum

The continuum map at 235.1 GHz (or 1.28 mm) is shown in Fig. 4.2. Two interpretations are consistent with the point-like nature of the observed continuum: a) nuclear synchrotron emission, b) thermal dust emission. The interpretation in point a), which is the non-thermal emission produced in the very nuclear region, is supported by the compact morphology and the result of the fit presented in Fig. 4.5. Indeed, the ALMA continuum emission (represented by a red square, Fig. 4.5) is consistent with the extrapolation of the

relation derived from the radio points including uncertainties. This relation was obtained by fitting a power-law relation ($S_\nu \propto \lambda^\alpha$) to the radio flux densities at 5, 8, and 20 GHz (obtained simultaneously at the Australia Telescope Compact Array, ATCA; Murphy et al. 2010). Indeed, the source appears to be point like (i.e. there is no evidence for jets or large-scale structures) at these frequencies. We obtained a slope of $\alpha = 0.54 \pm 0.03$, which is consistent with the slope observed in the case of synchrotron emission. With the current data, we are not able to exclude the contribution from other mechanisms (e.g. free-free emission; see discussion in Ruffa et al. 2018).

Regarding point b), which is the contribution from thermal emission, we refer to the results of the SED de-composition analysis presented in G16 and briefly introduced in Section 4.2.4. Given the point-like nature of the continuum emission observed with ALMA (shown as a red square in Fig. 4.5), we conclude that it cannot be associated with the tail of the far-IR bump. This possibility is rejected since the far-IR bump is expected to be produced by a diffuse dust component, which was not detected in the ALMA observation. Alternatively, it could be associated with the thermal emission from the dusty torus, even if the predicted torus emission at 1.3 mm is significantly lower than the observed flux for the best fit torus template (see the thick pink line in Fig. 4.5). To test this hypothesis, we also considered extreme torus configurations (pink dashed lines) to maximise the torus contribution to the far-IR emission. In particular, we considered torus models with high optical depth ($\tau = 10$) and with the highest outer-to-inner radius ratio ($R_{max}/R_{min} = 300$). Since the dust sublimation radius is usually assumed as the inner radius, with a size of \sim pc for a typical AGN luminosity as in the case of NGC 7213 (e.g. Fritz et al. 2006), this corresponds to an outer radius of \sim 300 pc. It is important to notice that the ‘extension’ of a typical torus in an intermediate-luminous AGN is below 10 pc, as was observed with ALMA in local active galaxies (e.g. García-Burillo et al. 2014). Having said this, when we also considered these extremely extended torus models, we were not able to reproduce a significant fraction of the continuum emission observed with ALMA. We thus excluded the thermal emission from dust as a major contribution to the observed continuum emission at 1.3 mm.

4.3.2 Molecular gas kinematics

The spatial resolution provided by ALMA observations allowed us to perform a detailed study of the kinematics of the molecular gas, tracing it from the large scales (e.g. the rotating galactic disc) to the very central regions, where the accretion onto the central SMBH takes place. This kind of study has been successfully performed on large numbers of local Seyfert galaxies (e.g. García-Burillo et al. 2014), and also in galaxies from the same parent sample (e.g. Sabatini et al. 2018). Following a similar approach to

that adopted by Sabatini et al. [2018], we used the ^{3D}BAROLO (3D-Based Analysis of Rotating Object via Line Observations) software [Di Teodoro and Fraternali, 2015] to model the kinematics of the molecular gas, as traced by the CO(2-1) emission line. The ^{3D}BAROLO code was specifically developed to fit 3D tilted-ring models based on two main assumptions: i) the material that is responsible for the observed emission has to be contained in a thin disc, and ii) the kinematic has to be dominated by rotation. The first assumption is generally accepted for local S0 galaxies. Regarding assumption ii), the ALMA observation of NGC 7213 revealed a rotation-dominated pattern, clearly visible from the velocity map (moment-1 map) of the CO(2-1) emission line (see the central panel of Fig. 4.6). We fixed the kinematic centre to the centroid of the continuum emission, whose profiles have been fitted (using the 'imfit' task from CASA) using an elliptical Gaussian. This is based on the assumption that the nucleus is the centre of the rotation and is responsible for the continuum emission (see Section 4.3.1). To reduce the model degeneracies, we set the disc geometry by fixing some parameters. From the data, we set the position angle of the major axis to $PA^{\text{major}} = 330^\circ$ from north to west. We also fixed the inclination of the disc with respect to the line of sight to $i = 30^\circ$, as estimated in the literature (e.g. Storchi-Bergmann et al. 1996; Lin et al. 2018). The central velocity of the ALMA data cube has been chosen to be that of the CO(2-1) sky frequency, meaning 229.2 GHz, but we left the systemic velocity (v_{sys}) free to vary in order to account for potential inaccuracies relative to the adopted sky frequency. Given the tradeoff of 'holes' and clumpy emission, we preferred the pixel-by-pixel (i.e. 'local') normalisation over the 'azimuthal' one (i.e. the azimuthally averaged flux in each ring) in order to account for the non-axial symmetry of the emission, meaning regions with anomalous gas distribution, which could affect the global fit. For the same reason, we allowed ^{3D}BAROLO to perform a smoothing of the input data cube by a factor of 2 of the original beam of the observation (i.e. the data were convolved with an elliptical Gaussian that was twice the size of the original beam), and to cut the smoothed cube at a signal-to-noise ratio of 4. We set the maximum number of radii to eight, separated by 1.5'' or ~ 180 pc, excluding the outermost part of the field of view, where ^{3D}BAROLO was not able to fit the model to the faint clumpy emission. To summarise, the free parameters are: the circular velocity, the systemic velocity, and the velocity dispersion.

At first, we did not include any potential radial velocity components in order to reduce the number of free parameters. Once the best fit model was obtained, meaning the residuals (data minus model) showed no significant evidence for rotational motion, we tested for the presence of a radial velocity component (v_{rad}). We ran the code with this additional free parameter, but its best fit value was consistent with zero. By assuming different values of the PA ($PA = 320^\circ - 340^\circ$) and inclination ($i = 20^\circ - 40^\circ$) one at a time, we tested

the goodness of the fiducial values of the PA and inclination angle. Since the residual clumps proved to be not sensitive to the choices of the assumptions, we preferred the best fit model with $\text{PA}^{\text{major}} = 330^\circ$ and $i = 30^\circ$. The results from the kinematical analysis are presented in Fig. 4.6, where the comparison between the model and the data in terms of intensity, velocity, and velocity dispersion maps (zeroth, first, and second moments, respectively) is shown. The model and data (smoothed by a factor of 2) are in excellent agreement. The kinematics of the molecular gas, traced by the CO(2-1) emission line, are clearly dominated by purely circular rotational motions around the nucleus. This is the first successful attempt to model the kinematics of the molecular gas in NGC 7213, thanks to the software ^{3D}BAROLO, which is able to handle the available data, despite the sparse information that limited previous attempts to model the kinematics (e.g. Ramakrishnan et al. 2019). As is clearly visible in Fig. 4.7, we found that the data cube central velocity was offset by an additional $\delta V_{\text{sys}} = 36 \pm 10 \text{ km s}^{-1}$. This means that the systemic velocity of the source with respect to our rest frame has to be $V_{\text{sys}} = 1716 \pm 10 \text{ km s}^{-1}$, which is a mean value between the systemic velocity obtained from the study of the stellar kinematics by Schnorr-Müller et al. [2014], and the results by Ramakrishnan et al. [2019]. Looking at the lower panels of Fig. 4.6, the velocity dispersion in the best-fit model is $\sim 10 - 15 \text{ km s}^{-1}$: values that are expected from a rotation-dominated disc. The highest values of the velocity dispersion ($\sigma_{\text{disp}} \sim 70 \text{ km s}^{-1}$) are not reproduced by the best fit model. The high-dispersion residual clumps proved to be insensitive to our assumptions (e.g. PA, i , v_{rad}), therefore we suggest that the residuals are associated with non-rotational motion, as we discuss in Section 4.3.3.

4.3.3 Complex structures in the CO emission

The results of the modelling of the gas kinematics presented in Section 4.3.2 pointed out the presence of a few regions where the kinematics are not strictly associated with rotational motion. To investigate the nature of these regions, we used both the position-velocity (PV) diagrams, shown in Fig. 4.7, and the moment maps (intensity, velocity, and velocity dispersion maps) from Fig. 4.6. In particular, we focused on three regions, which we named A, B, and C (see Fig. 4.2) and interpreted as follows:

Region A is an extended emission (of the order of $1.5'' \times 2.5''$), showing an asymmetric line profile (see Fig. 4.8). Region B is a possible super bubble, meaning it is a nearly circular void of $0.7''$ or 90 pc in diameter, surrounded by likely shocked material. It is located $3.3''$ (400 pc) NE of the nucleus. Region C is a likely outflow located $1.4''$ (150 pc) SE of the nucleus along the minor axis.

Since Region A is located at the edge of the circular void identified as Region B, the former can be interpreted as the emission produced by the shock front impacting on the

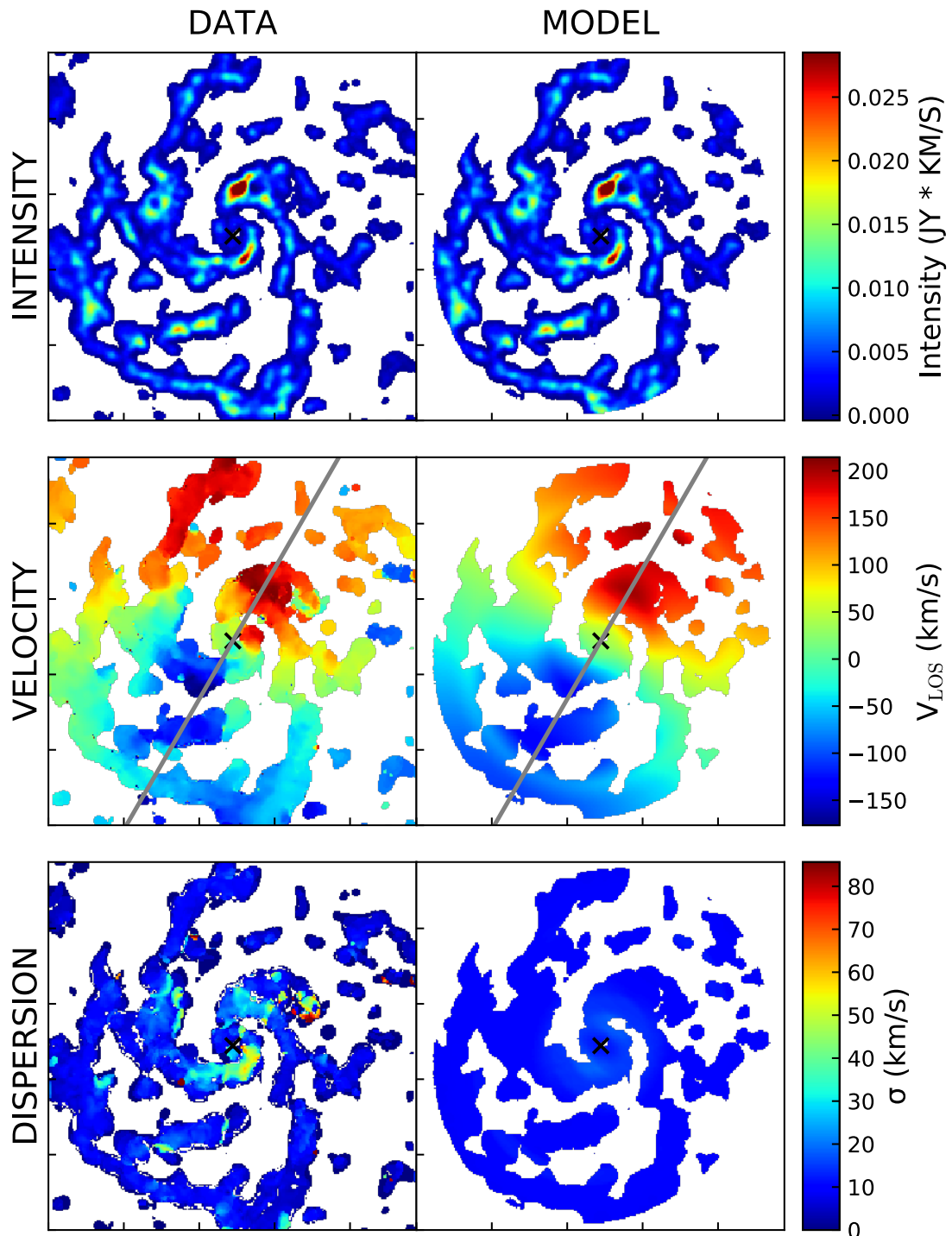


Figure 4.6: From top to bottom: comparison between the flux, velocity, and velocity dispersion maps obtained from the data (left column) and the best fit model produced by the 3^{D} BAROLO code (right column). Both the data and model have been convolved with an elliptical Gaussian twice the size of the beam of the observation. This smoothing procedure helps the 3^{D} BAROLO in the fitting procedure, especially in the case of clumpy emission as the one analysed here. The grey lines in the central panels represent the direction of the position angle; the same slit was used to extract the position-velocity (PV) diagram on the major axis, as presented in the top panel of Fig. 4.7.

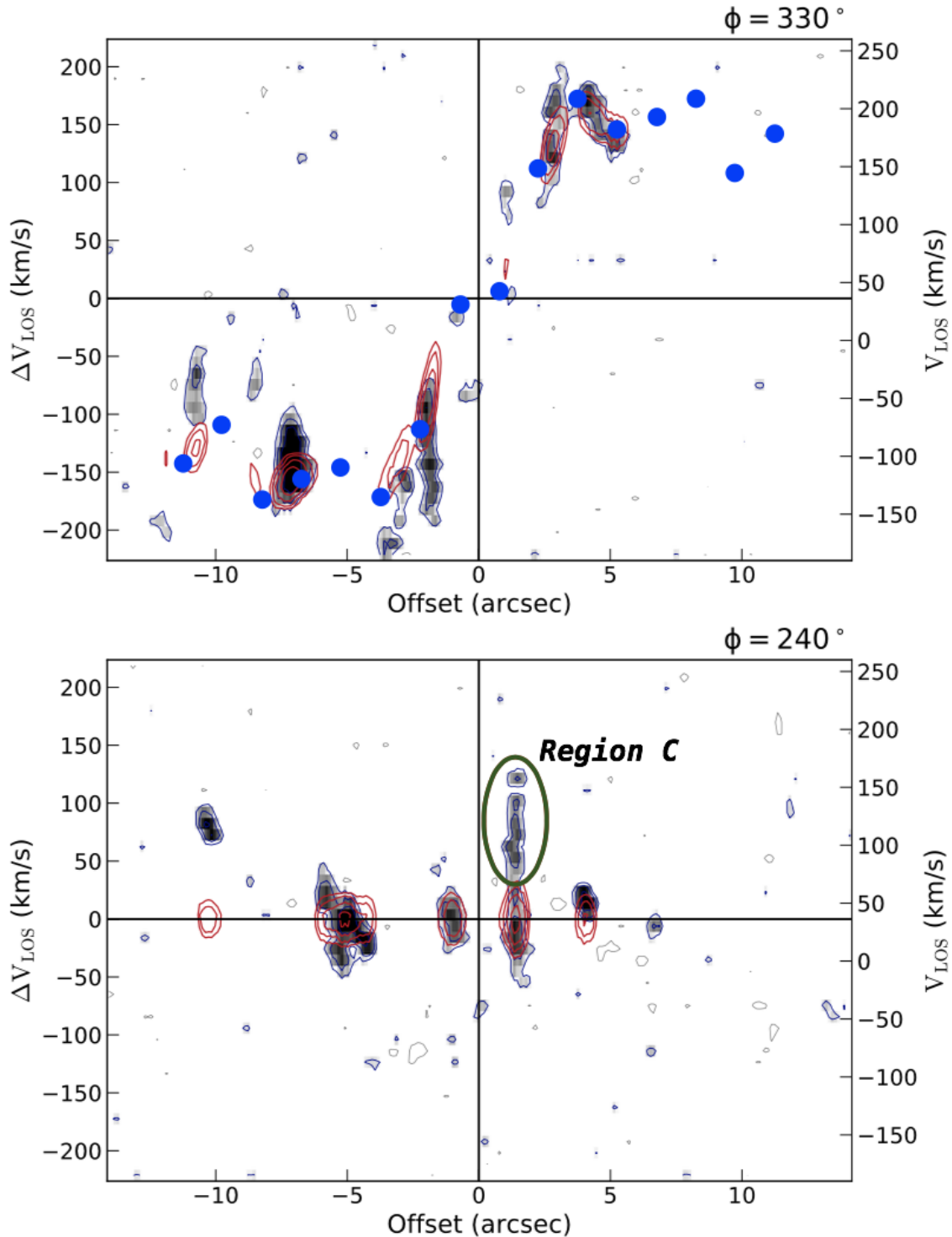


Figure 4.7: PV diagrams on the major (top panel) and minor (bottom panel) axis, respectively. On the x-axis, the angular distance from the centre of the source along the direction fixed by the angle ϕ is reported. On the right y-axis, the velocity along the line of sight (in km s^{-1}) is shown as it appears in the input data cube. On the left, the velocity along the line of sight (in km s^{-1}) is shown, once the systemic velocity ($v_{\text{sys}} = 36 \pm 10 \text{ km s}^{-1}$) has been subtracted. The data are represented in grey scales with blue contours, while the the best fit model is identified by red contours. In the upper panel, the blue circles represent the projected best fit rotational velocity at different radial distances from the centre, associated with each ring of the disc. In the bottom panel, the signature of the potential outflow associated with Region C (bordered in green; see Section 4.3.3) is clearly visible as an excess of CO emission over 100 km s^{-1} with an offset of $\sim 1''$ from the centre of the rotation.

surrounding medium. However, further observations that successfully recover the CO emission at all scales with good spatial resolutions are needed to validate this hypothesis. The potential outflow in Region C was identified from the PV diagram along the minor axis, presented in the bottom panel of Fig. 4.7. This emission (Region C), located along one of the spiral arms and observed over 100 km/s (corresponding to at least 10 channels), is clearly not consistent with what is expected from a rotation-dominated disc. The interpretation as emission from outflowing gas is supported by the presence, at the same location, of a peak in velocity dispersion associated with a $1.5'' \times 1''$, or $180 \text{ pc} \times 120 \text{ pc}$ region (see the dispersion map in Fig. 4.6). From the residual of the kinematical modelling, we measured the peak velocity (v_{max}), the size (R_{OF}), and the flux of the emission associated with the outflow. The flux was used to derive the outflow mass (M_{OF}), following the procedure extensively described in Section 4.3.4. The molecular gas outflow mass was calculated by assuming an $\alpha_{CO} = 1.1 M_{\odot} \text{ pc}^{-2} (\text{K km s}^{-1})^{-1}$, as for the gas mass from the APEX observation, which is a value similar to the one used in literature (e.g. Cicone et al. 2014; Fiore et al. 2017). Then, we computed the mass-outflow rate (\dot{M}_{OF}) of Region C, assuming a spherical geometry (i.e. $\dot{M}_{OF} = 3v_{max}M_{OF}/R_{OF}$; Cicone et al. 2014). We compared this value ($\dot{M}_{OF} \sim 0.03 \pm 0.02 M_{\odot} \text{ yr}^{-1}$) with the one we expected from the $\dot{M}_{OF} - L_{AGN}$ relation (e.g. Cicone et al. 2014; Fiore et al. 2017), predicting, for Region C, a mass loss $\dot{M}_{OF} \sim 7-15 M_{\odot} \text{ yr}^{-1}$. This prediction is at least two orders of magnitude larger than what we measured, thus suggesting that it is unlikely to be purely AGN driven. Furthermore, the outflow is located relatively far from the low-luminous nucleus of NGC 7213, thus suggesting a dominant contribution from a stellar-like driven mechanism. The same calculation was performed in the case of the potential outflow in Region A, suggesting a stellar-related mechanism powering the molecular wind, given the measured $\dot{M}_{OF} \sim 0.05 \pm 0.03 M_{\odot} \text{ yr}^{-1}$.

4.3.4 The molecular gas mass

Here we describe briefly the method adopted to measure the cold molecular gas mass (M_{gas}) from the luminosity of the CO(1-0), already reported extensively in Chapter 1. To measure M_{gas} using Eq. 1.4, we need to, a) extrapolate the CO(1-0) luminosity from our measurements of the CO(2-1) line, and b) assume an appropriate value for the α_{CO} . Regarding point a), we adopted a typical CO(2-1)-to-CO(1-0) flux ratio ~ 3 (e.g. Papadopoulos et al. 2012), similarly to what done in Sect. 3.2.1.4, which we used to extrapolate the CO(1-0) emission-line flux from the APEX data. We did not take into account the CO(2-1) line flux observed with ALMA, because, as explained in Section 4.2.3, it represents only a fraction of the flux observed with APEX. This difference is likely due to the filtering out of the large-scale emission in the interferometric observation,

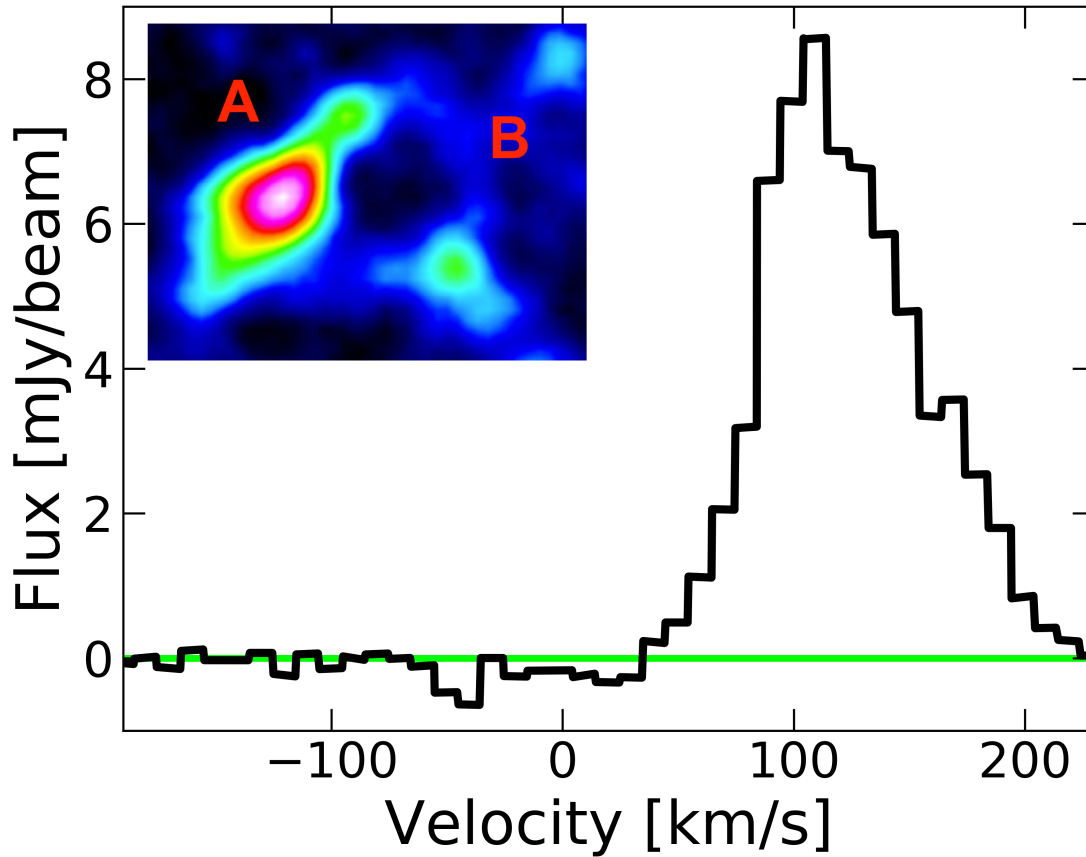


Figure 4.8: Asymmetric line profile observed in correspondence with the potential outflow in Region A. This emission is likely produced by shocked material.

hence considering that the CO flux measured with ALMA could result in a significant underestimate of M_{gas} .

Then, we calculated $L'_{\text{CO}(1-0)}$ following Carilli and Walter [2013], assuming Eq. 1.3. We obtained $L'_{\text{CO}(1-0),\text{APEX}} = (1.8 \pm 0.3) \times 10^8 \text{K km s}^{-1} \text{pc}^2$. To check whether the CO emission recovered by APEX observation is representative of the expected molecular gas emission from NGC 7213, we used the relation $\log(L'_{\text{CO}(1-0)}) = (0.73 \pm 0.03) \log(L_{\text{IR}}) + (1.24 \pm 0.04)$ (e.g. Carilli and Walter 2013), which relates the CO and the IR luminosity (L_{IR}). A negligible contribution from the AGN in the far-IR was accurately assumed (see also Fig. 4.5). Using the SF-related IR luminosity provided by G16 ($L_{\text{IR}} = (1.0 \pm 0.3) \times 10^{10} L_{\odot}$), we obtained $L'_{\text{CO}(1-0)} = (4 \pm 2) \times 10^8 \text{K km s}^{-1} \text{pc}^2$. The CO luminosity obtained with APEX is roughly a factor of ~ 2 smaller than the one extrapolated from the IR emission; however, the two values are consistent within the uncertainties. This suggests that the CO luminosity collected within the APEX aperture ($25''$, or $\sim 3 \text{kpc}$) is almost representative of the CO emission from the entire galaxy, hence of the entire molecular gas content. Therefore, for the estimate of M_{gas} presented in this section, we used the CO(1-0) luminosity from

APEX.

The choice of an appropriate α_{CO} factor (point b) depends on the ISM conditions, particularly on the metallicity (see Fig. 1.13), as shown in Section 1.2.2.1. Since we cannot derive the metallicity for NGC 7213 from the optical spectrum, we assume it to be solar like. For active and luminous IR galaxies, the generally adopted α_{CO} values are in the range $\sim 0.3\text{-}2.5 M_{\odot} \text{ pc}^{-2} (\text{K km s}^{-1})^{-1}$ (see also Downes and Solomon 1998; Papadopoulos et al. 2012). For NGC 7213, we assumed $\alpha_{\text{CO}} = 1.1 M_{\odot} \text{ pc}^{-2} (\text{K km s}^{-1})^{-1}$, which is used for the nuclear regions of local AGN host-galaxies (e.g. Sandstrom et al. 2013; Rosario et al. 2018). Thus, we compared our result with literature works on local active galaxies showing similar properties to NGC 7213 (e.g. Pozzi et al. 2017; Rosario et al. 2018). Based on the above assumptions, the molecular gas mass derived from the flux estimate obtained with APEX is $M_{\text{gas}} = (2.0 \pm 0.3) \times 10^8 M_{\odot}$.

Given M_{gas} , we estimated the depletion time, as $t_{\text{depl}} = M_{\text{gas}}/\text{SFR}$. Since the SFR provided by G16 ($\text{SFR} = 1.0 \pm 0.1 M_{\odot} \text{ yr}^{-1}$) is referred to the entire galaxy, while the APEX aperture covers $\sim 25''$ (or ~ 3 kpc), we needed to scale down the SFR. This is necessary since the two measurements were obtained with different apertures and because the SF surface brightness in NGC 7213 appeared to be extended beyond the central region [Diamond-Stanic and Rieke, 2012]. We considered the PACS observation at $70 \mu\text{m}$ from the *Herschel* telescope (PSF FWHM $\sim 5.6''$), where the contribution from the central AGN should be less important to the global IR outcome with respect to the relative nuclear contribution at shorter wavelengths, as suggested by the result of the SED decomposition analysis presented in Fig. 4.5 and from the low-luminosity nature of NGC 7213 presented in this work. The extended IR emission at $70 \mu\text{m}$ is almost entirely produced by the SF activity, hence it can be used as a proxy of the SFR surface brightness. We found the flux ratio within the entire galaxy (F_{tot}) and the APEX aperture ($25''$; $F_{25''}$) to be $F_{\text{tot}}/F_{25''} = 2.0 \pm 0.3$. Eventually, assuming the scaled SFR, we measured a depletion time of $t_{\text{depl}} = 0.4 \pm 0.1$ Gyr. The depletion time of NGC 7213 is consistent with the distribution of values we observed in the Seyfert 2 galaxies analysed in Chapter 3, accordingly to the common nature of these objects (mid-IR Seyfert galaxies). Furthermore, this value is also consistent with what is observed in the local Universe ($0.1 < t_{\text{depl}} < \text{few Gyr}$; e.g. Rosario et al. 2018) in objects with both similar host-galaxy properties in terms of M_{\star} , SFR and AGN luminosity ($L_{\text{bol}} \sim 10^{43\text{-}46} \text{ erg s}^{-1}$), but larger than what is observed at high redshift ($0.01 < t_{\text{depl}} < 0.1$ Gyrs; e.g. Brusa et al. 2018; Kakkad et al. 2017; Talia et al. 2018). The observed difference in t_{depl} between high- and low-redshift samples is most likely due to the stronger SF and AGN activity at the cosmic noon (e.g. Madau and Dickinson 2014), resulting in shorter timescales for the gas consumption. It is worth recalling that the derived t_{depl} depends on the assumption of the α_{CO} . If we had chosen $\alpha_{\text{CO}} \sim 4.4 M_{\odot} \text{ pc}^{-2} (\text{K km s}^{-1})^{-1}$ as in the case of Milky-Way like galaxies, it would have turned out t_{depl} about four time larger, which is a value still consistent with observed in the local Universe.

4.4 Discussion and conclusions

In the analysis of NGC7213, which was chosen as a 'test case' from the sample of G16 because of its intriguing intermediate nature between a LINER and a LLAGN, we present a multi-wavelength approach to the study of local active galaxies. The multi-band information helps us to draw a more complete picture of the physical processes in this object, the different phases of the ISM in the host galaxy, and the role of the AGN. The source was selected from the sample presented by G16, on the basis of the quality of the available archival observations in the X-rays and at mm wavelengths. To this aim, we performed a spectral analysis of X-ray archival observations to study the accretion-related emission in terms of power and spectral shape. We also combined the high-sensitivity and high-spectral resolution from ALMA, which is crucial to tracing the molecular gas kinematics down to sub-kpc scales, with the spatially integrated information provided by APEX, to estimate the molecular gas content. The main results of this work can be summarised as follows:

- Our re-analysis of archival XMM-Newton and NuSTAR observations allowed us to properly characterise the central engine in terms of spectral shape and power over the 2–27 keV energy band. The results of the X-ray spectral analysis (i.e. $\Gamma_X = 1.81 \pm 0.02$ and $F_{2-10\text{keV}} = 1.62^{+0.02}_{-0.02} \text{ ergs s}^{-1} \text{ cm}^{-2}$, derived from NuSTAR observations due to the wide energy band covered: see Table 4.1) support the presence of an unobscured AGN in the centre of NGC 7213, which is in agreement with its classification as a un-obscured AGN, based on the optical broad-line features. However, the relatively low luminosity of the source in the X-rays ($L_{2-10\text{keV}} \sim 1 \times 10^{42} \text{ ergs s}^{-1}$) suggests a low accretion rate that is far below the Eddington limit. The energetics related to the nuclear activity of NGC 7213 place the source in an intermediate stage between a typical un-obscured Seyfert and a LINER.
- Using ^{3D}BAROLO on the ALMA data of the CO(2-1) emission, we obtained the first model of the molecular gas kinematics in the central regions of NGC 7213. The best-fit model well reproduces the velocity fields, which are dominated by a rotational pattern. From the residuals we found no evidence for non-rotationally dominated motion in the central region (i.e. $\lesssim 60 \text{ pc}$ from the nucleus). This means that the SMBH hosted in NGC 7213 cannot significantly affect the motion of the molecular gas traced by the CO(2-1) at the scales recovered in the available observation, since there is no evidence for nuclear inflows or molecular gas streaming feeding the AGN.

- The study of the CO emission-line data cube showed some evidence for two potential outflows, located within 500 pc of the nucleus. Region A is located at the edge of a circular void, and it is likely a super-bubble. The evidence for Region C came from the PV-diagram analysis and is located along one of the spiral arms. Given the sizes and the location of both, they are more likely powered by stellar activity, rather than by the AGN, but better data are needed to confirm this hypothesis.
- The continuum emission at 235.1 GHz (1.28 mm) is produced by a point-like source. Based on an SED analysis, we concluded that the most reasonable interpretation is the continuum being produced through synchrotron radiation in the nuclear region, in agreement with the extrapolation of the ATCA observations at longer wavelengths.
- The molecular gas mass of NGC 7213 is $M_{\text{gas}} = (2.0 \pm 0.3) \times 10^8 M_{\odot}$, which was obtained by converting the CO luminosity observed with APEX. We underline how the ALMA observation would have underestimated the gas mass by a factor of ~ 3 , given the filtering out of the large-scale emission in interferometric observations. We estimate a depletion time of $t_{\text{depl}} = 0.4 \pm 0.1$ Gyr, which is consistent with what is observed in local moderately luminous Seyfert galaxies (e.g. Rosario et al. 2018). This suggests a negligible, if any, AGN impact on the host galaxy's SF activity.

The proposed approach allowed us to combine the available multi-wavelength information to obtain a coherent picture of the source in terms of both AGN activity and host galaxy ISM properties. In the case of NGC 7213, the accretion-related emission from the AGN is rather weak, and thus unable to significantly impact the molecular gas content and distribution of the galaxy, and hence to influence the SF activity, as suggested by the depletion time. Given the results of our study, NGC 7213 can be classified as a LLAGN.

5

Conclusions and future perspectives

In this Thesis I presented the importance of a multi-wavelength strategy to assess the role of AGN activity in regulating the host-galaxy ISM properties, in particular concerning the molecular components. A complete picture of the processes that regulate the formation of new stars and the accretion of matter onto SMBH can be obtained by combining the information from different wave bands. Here I emphasise the potentiality of this approach a two-fold strategy, combining a detailed study of the AGN emission, to unveil its intrinsic power, with the characterisation of the molecular gas component of the ISM, which is necessary to the host SF and, potentially, involved in the accretion process. Here I draw the conclusions of the work I did during my PhD and which I extensively presented in the previous Chapters.

Unveiling the intrinsic power in local Seyfert 2 galaxies

In Chapter 1 I stressed how the characterisation of the AGN intrinsic emission is necessary to properly constrain its contribution to the excitation of the different ISM components. For this reason, I dedicated a large fraction of my work to the determination of the intrinsic power of local AGN, focusing on obscured objects. To this goal, in Chapter 2 I presented a systematic spectral analysis on a collection of both proprietary and archival X-ray observations of a sample of 32 local Seyfert 2 galaxies. I exploited the broad energy band obtained by combining *NuSTAR* with telescopes sensitive below 10 keV, to determine the level of obscuration in the X-rays ($N_{H,X}$) and, then, measuring the AGN accretion related emission (L_X). Two modelling approaches were tested: a “phenomenological” and a “physical” (MyTorus) model. By comparing the results from the two modelling approached, I found consistent measurements of $N_{H,X}$.

In Chapter 1.1 I showed that a multi-wavelength study of the AGN emission is crucial to determine its intrinsic power, especially in the case of heavy obscuration or weak emission. For this reason, I compared the X-ray and mid-IR properties of my sample of objects, using the IR measurements from a detailed SED analysis performed by Gruppioni et al. [2016] and mid-IR spectral decomposition by Hernán-Caballero and Hatziminaoglou [2011]. By comparing the IR and X-ray luminosities, the Seyfert 2 galaxies in my sample appeared brighter in the IR than in the X-rays. This can be partially due to a potential contamination from the host-galaxy to the determination of the AGN bolometric output in the IR regime, although it may be an intrinsic properties of this mid-IR selected sample of objects.

As presented in Section 1.1.2, many recent works aimed at studying the properties of the dusty torus, which is responsible for the obscuration and re-emission of the AGN primary radiation. Several approaches are applied, focusing on single band (e.g., in the X-rays; Marchesi et al. 2019 and reference therein), or with a combination of multi-wavelength data (e.g., fitting with a torus model the mid-IR and the X-ray data; e.g., Esparza-Arredondo et al. 2019). In this context, I compared the level of obscuration in the mid-IR and in the X-rays. In particular, I compared the strength of the $9.7 \mu\text{m}$ silicate feature (which is in absorption in Seyfert 2 galaxies) with the N_H measured in the X-rays: there is a good correlation between the two quantities, consistently with previous results in the literature (e.g., Shi et al. 2006; Xu et al. 2020). To conclude, I measured relatively larger column densities in the X-rays with respect to those measured in the IR, suggesting that part of the material that is responsible for the extinction in the X-rays does not contribute in the IR.

A coherent modelling of the torus on the base of the mid-IR and X-ray observations will be one of the future development of this work, even though it requires high quality data, especially in the X-ray, where long integration time are required for the weakest and heavily obscured objects. Meanwhile, the next step will be the inclusion of different torus models in the analysis, to better characterise the X-ray properties (e.g. intrinsic power, spectral shape) of my objects, as well as to test the consistency of the results from the different models (e.g., `borus02` by Baloković et al. 2018).

The effect of AGN activity on the host depletion time

In Section 1.2.2.1 I show that the molecular gas play a fundamental role in the context of the galaxy evolution, being necessary to the formation of new stars, as well as potentially involved in the accretion onto the SMBH. It is then important to investigate the amount of molecular gas which is available in each galaxy, along with the timescale at which this gas is converted into new stars, to distinguish AGN hosts from SFGs. To this

goal, in Chapter 3 I studied the host-galaxy molecular gas properties of 33 local Seyfert 2 galaxies, among which 29 benefit from the analysis presented in Chapter 2. First, using new and archival low-J CO line observations I measured the CO luminosity and, by correcting for the aperture, I extrapolate the galaxy-integrated CO luminosity. Then I converted the luminosity of the CO into molecular gas mass by assuming a constant conversion factor. By comparing my sample with a finely selected control sample of SFGs, I found that over a wide range in stellar masses, AGN cannot be distinguished from SFGs in terms of their molecular gas content, even if they show a larger deviation from the MS of SFGs (in particular, in terms of SFR). The distribution of Seyfert 2 galaxies in terms of depletion times is consistent with that of local inactive galaxies, although this conclusion strongly rely on the assumed conversion factor from CO to molecular gas mass.

In the second part of Chapter 3, I included in my analysis the measurements of PAH features, which are mid-IR diagnostics usually associated with on-going SF activity in galaxies. When comparing the PAH emission in AGN and SFGs, I found fainter PAH luminosity in the sample of obscured Seyfert galaxies. Finally, I confirmed the negative effect of nuclear activity on the emission of the PAH feature by showing that among the objects in my sample, the Seyfert nuclei which dominate their host emission in the mid-IR regime (5-40 μm), are those showing a increased suppression of the PAH emission.

A test case: NGC 7213

The synthesis of my approach is presented in Chapter 4, where the methodologies developed in the previous chapters are applied to a test case objects, providing a complete and coherent picture of the role of the AGN and its effect on the host-galaxy properties across the (almost) entire electromagnetic spectrum (from the X-rays to the radio frequencies). Among the sources from the parent sample by G16, I selected an interesting objects, with an intermediate nature between a LINER and a Seyfert, which benefit from an extensive observational coverage at all wavelength.

By following the strategy designed in Chapter 2, I performed a spectral analysis of X-ray archival observations to study the accretion-related emission, necessary to determine the intrinsic emission radiated by the central accreting SMBH. In Section 1.2 I showed that the AGN can affect the ISM by injecting large amount of energy (both particles and photons) in the surrounding medium, hence affecting the physical properties of the ISM, in particular of the molecular gas. I then analysed an archival ALMA observation, looking for the signatures of AGN feedback, in the form of molecular outflow, traced by the CO(2-1) emission line. Interestingly, using the ^{3D}BAROLO code on the ALMA

data, I obtained a detailed modelling of the molecular rotating disk, showing off some evidence for two potential outflows, located within 500 pc of the nucleus. In this case, the characterisation of the AGN power I derived in the first part of this work, helped us in ruling out the contribution from the nuclear activity as a driving mechanism for the two outflows. Furthermore, following the prescription described in Chapter 3, I derived the molecular gas content of the galaxy using single-dish CO observation as well as its depletion time scale. NGC 7213 place itself in the intermediate regime between Seyfert galaxies and local SFGs, anyway far from the quasar at higher redshift ($z \sim 1-3$; e.g., Brusa et al. 2018).

The application of my methodology on the test case NGC 7213, as presented in Chapter 4 and in the relative publication [Salvestrini et al., 2020], allowed us to combine the available multi-wavelength information to obtain a coherent picture of the source in terms of both AGN activity and host galaxy ISM properties. In NGC 7213, the accretion-related emission from the AGN is rather weak, and thus unable to significantly impact the content and distribution of the molecular gas, and hence to influence the SF activity, as suggested by the depletion time.

The multi-wavelength strategy I designed in Chapter 4 can be easily extended to the large part of the parent sample by G16, since most of the objects benefit from an excellent observational coverage from the X-rays to the sub-mm/mm band. I plan to use sub-mm/mm interferometric ALMA observations, available for the majority of the sample, to search for evidences of the AGN feedback. To this purpose, during my visiting period at the European Southern Observatory (ESO; as reported in the attached research activity statement) I had the opportunity to join the TWelve micron WInd STatistics (TWIST) project, which is devoted at unveiling the feeding and feedback processes in active galaxies in the local Universe. The sample used in the TWIST project is a collection of 41 nearby AGN from the 12MGS (14 Seyfert I, 20 Seyfert 2, and 7 Low-ionization Nuclear Emission-line Regions, LINERs; $20 < D \text{ [Mpc]} < 55$), which have been observed with ALMA (project 2018.1.00366.S and 2017.1.00236.S, PI Malkan, Co-I Hatziminaoglou) in band 6, to trace the CO(2-1) emission line. The goal of the project is to systematically study the “feeding” and “feedback” processes in the local Universe. While early results from the study on single object (ESO 420-G13) have already been published [Fernández-Ontiveros et al., 2020], the results from the extensive analysis of the sample (to which I collaborated) will be published in the next future.

Moreover, I plan to use interferometric facilities to investigate the ISM physical conditions at GMC scales (some tens of pc) by tracing molecular gas lines (e.g., HCN and HCO⁺ for the high-density molecular phase, CS, SiO and HNCO for the shock-excited material) in

the central region of nearby AGN.

To summarise, this Thesis highlights the crucial role that multi-wavelength studies play in exploring in detail the interplay between the AGN and its host-galaxy SF, tracing the driving physical processes (e.g., shocks, SMBH accretion, SF) which takes place in the nuclear region of composite objects like IR-selected local Seyfert presented in this work, involving different ISM components. The full sample of 36 Seyfert 2 galaxies (32 presented in Chapter 2 and 3 in Chapter 3) represent a reference sample of obscured AGN at low redshift ($z \sim 0.003 - 0.05$) for this kind of study, thanks to the wealth of multi-wavelength information. Indeed, the systematic characterisation of the nuclear emission in local obscured Seyfert galaxies is a starting point to study the distribution of this elusive population of AGN at higher redshift. This challenging task requires a multi-wavelength approach, as I showed in Chapter 2 to accurately determine the level of obscuration and, hence, of the intrinsic power of local AGN. Then, in Chapters 3 I showed that the signature of the impact of nuclear activity in local obscured Seyfert galaxies is clearly visible in the mid-IR (with fainter PAH emission), while AGN do not distinguish significantly themselves from SFGs in terms of molecular gas content.

The results presented in Chapters 2 and 3, suggest that the population of relatively luminous (with $L_{bol} \sim 10^{11-12} L_{\odot}$) Seyfert galaxies are intermediate objects where AGN and SF activity coexist.

To conclude, the methods described in Chapters 2 and 3, along with the test-case application presented in Chapter 4, represent a starting point to investigate the connection between the growth of BHs and their host galaxies, first, in the local Universe, to be then extended to AGN at higher redshift.

Appendices

A

X-ray spectra

A.1 Phenomenological model

Here we show the remaining X-ray spectra analysed with the adoption of “phenomenological” models, as presented in Chapter 2.

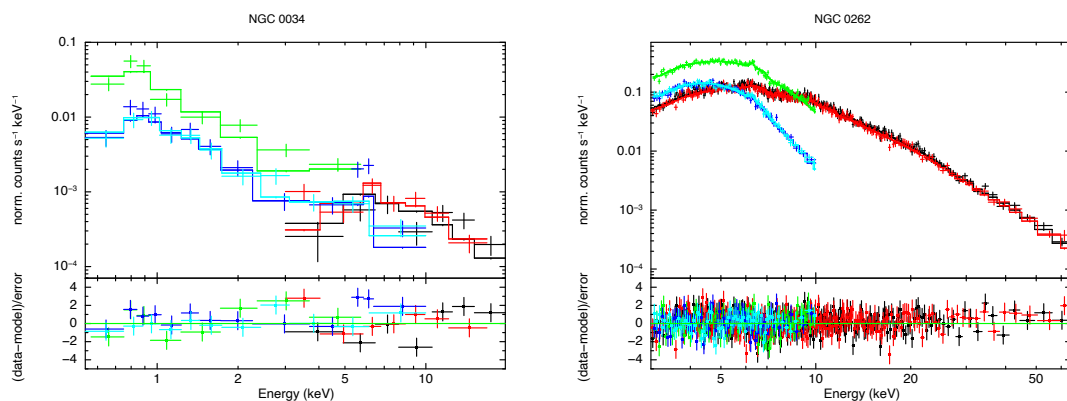


Figure A.1: X-ray spectra of the objects in our sample, analysed using the phenomenological model. In the upper panel, the spectrum and best-fit model, expressed in normalised counts s^{-1} ; in the bottom panels, the residuals (data minus model) are expressed in units of σ . The dataset included in each plot are listed in Table 2.2 and are color coded depending on the order we gave at the spectra: 1st in black, 2nd in red, 3rd in green, 4th in cyan, 5th in blue. When available, *NuSTAR* FPMA and FPMB are the 1st and 2nd spectra, respectively; then we included one observation either from *XMM-Newton* (EPIC pn, MOS1 and MOS2), *Chandra* or *Swift*.

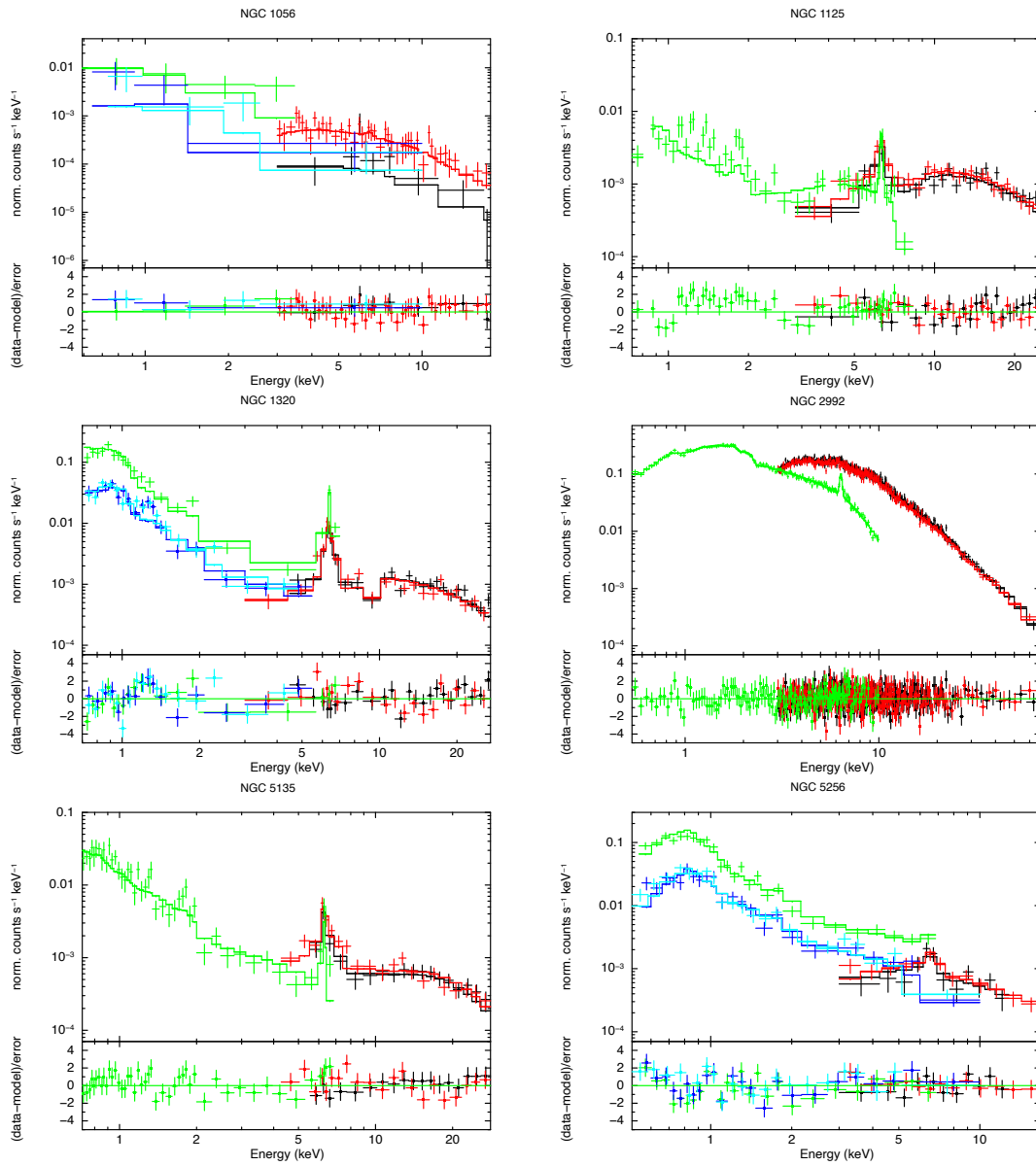


Figure A.2: Same caption as in Fig. A.1.

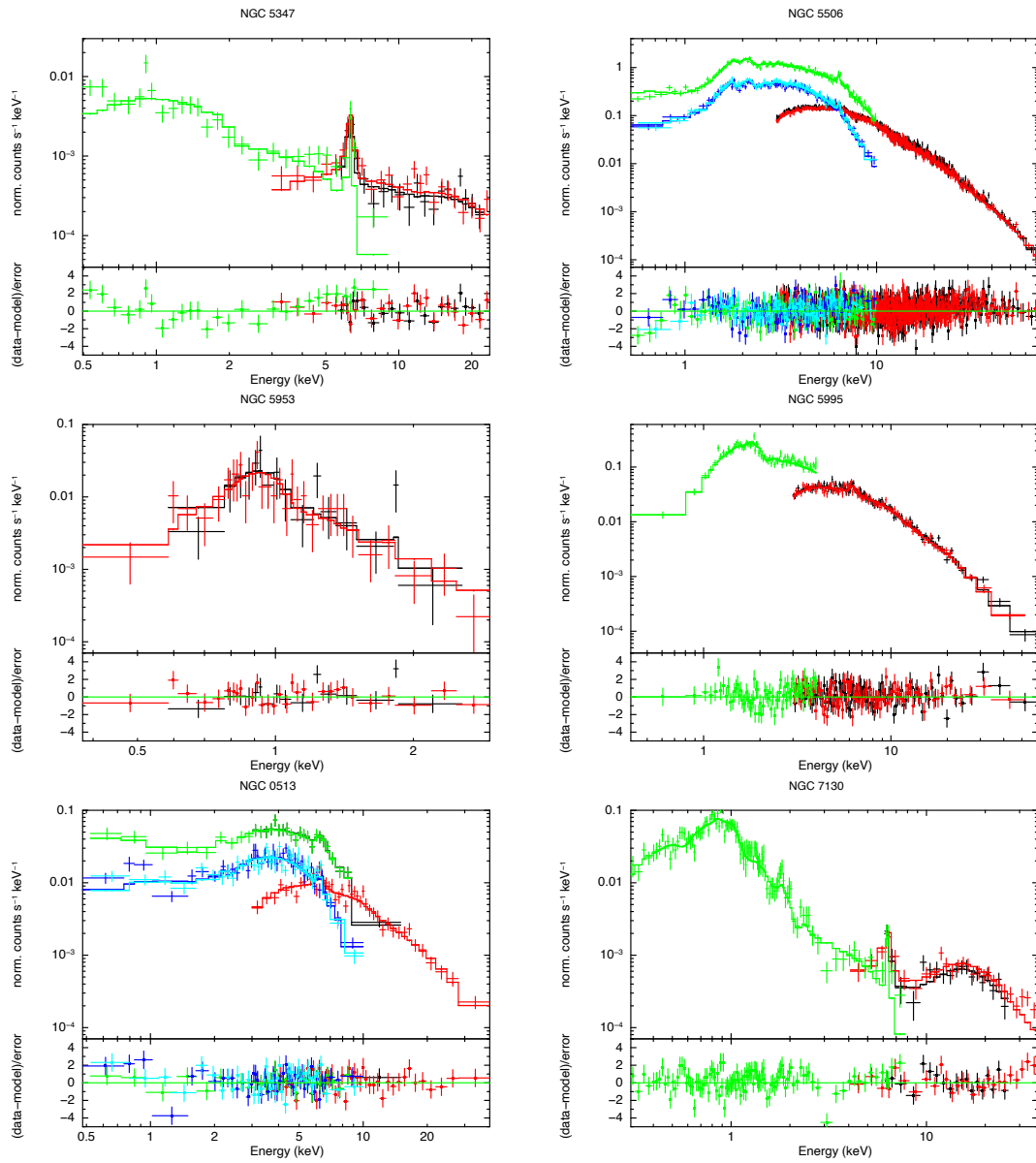


Figure A.3: Same caption as in Fig. A.1.

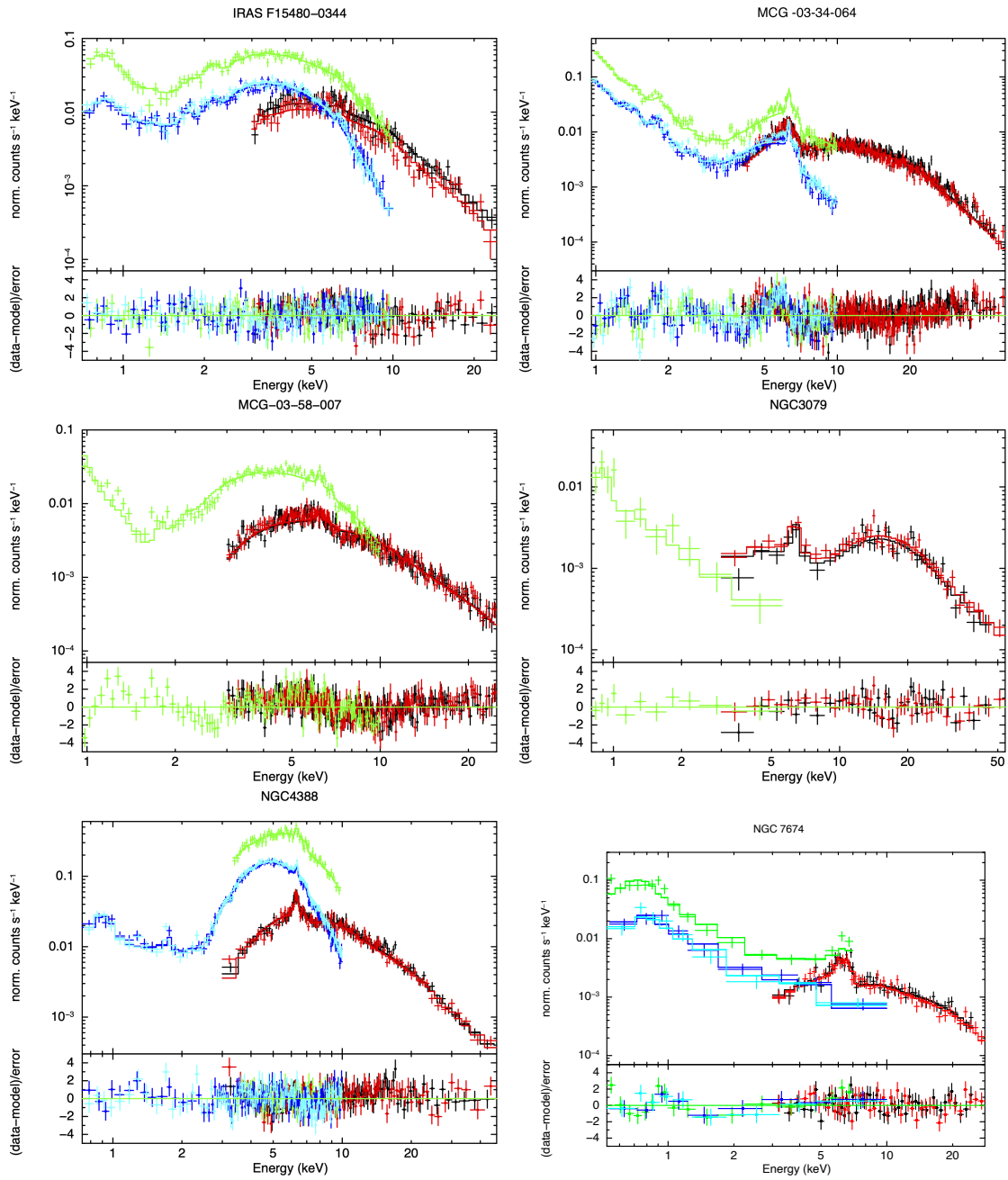


Figure A.4: Same caption as in Fig. A.1.

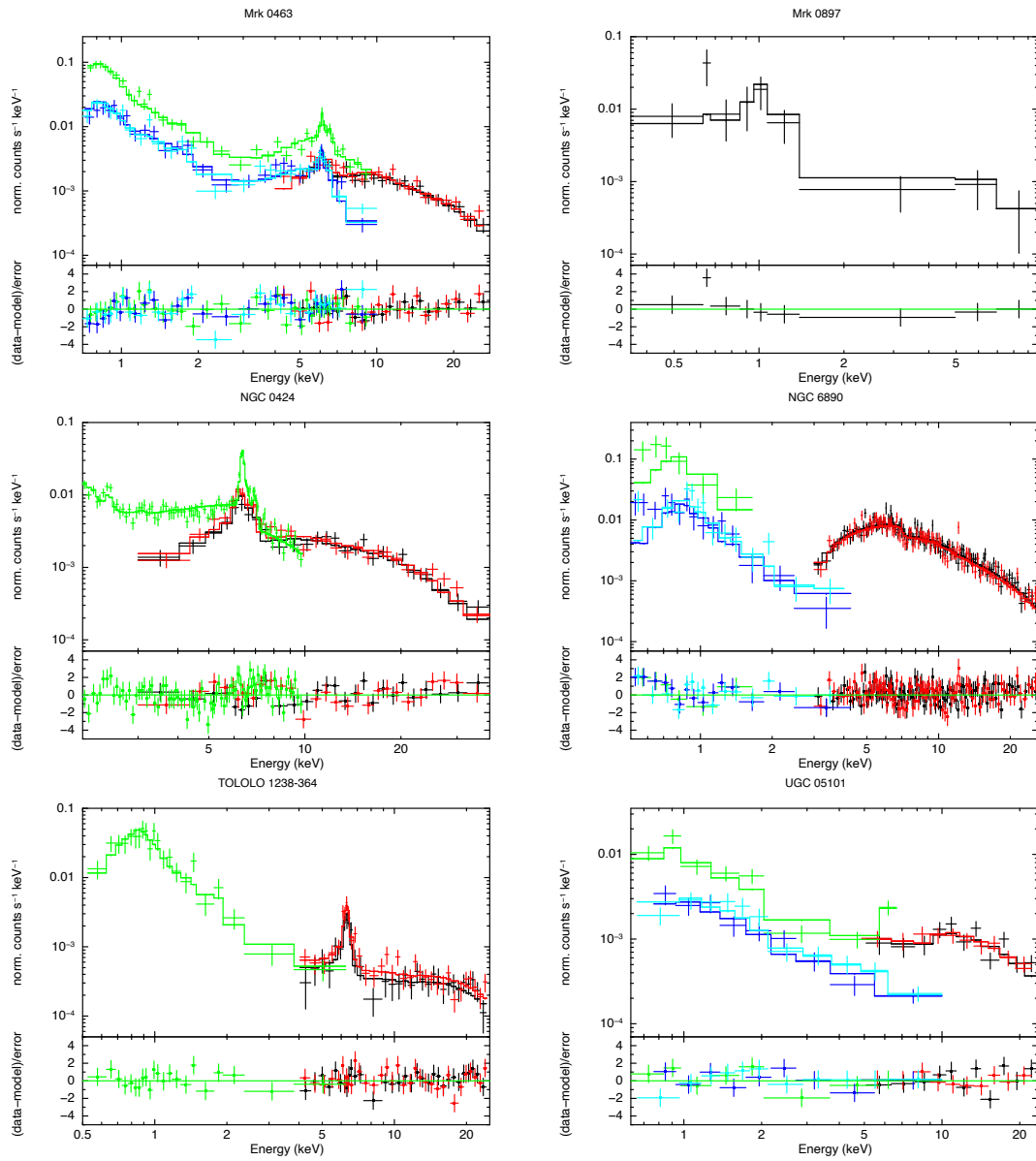


Figure A.5: Same caption as in Fig. A.1.

A.2 MyTorus model

The remaining X-ray spectra obtained from the X-ray spectral analysis using MyTorus are presented in this Section.

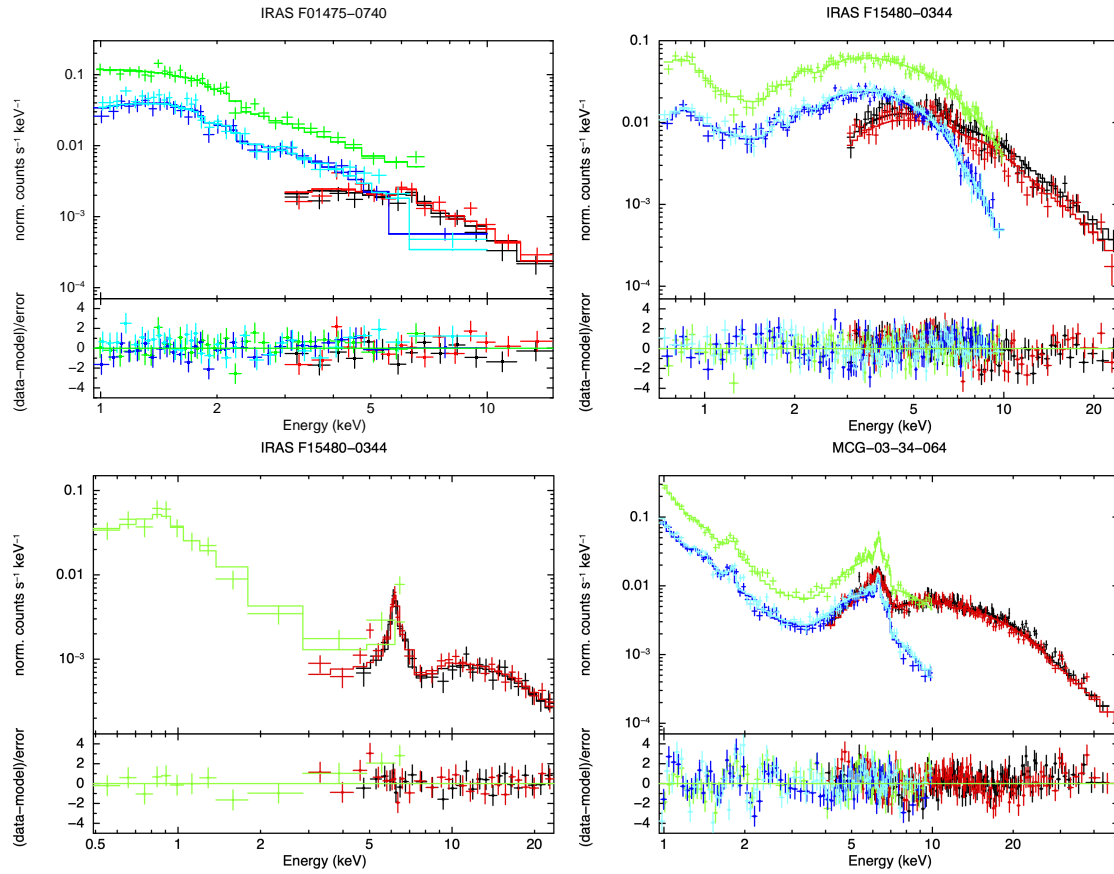


Figure A.6: X-ray spectra of the objects in our sample, analysed using MyTorus model. In the upper panel, the spectrum and best-fit model, expressed in normalised counts s^{-1} ; in the bottom panels, the residuals (data minus model) are expressed in units of σ . The dataset included in each plot are listed in Table 2.2. The color code is the same as in Fig. 2.1.

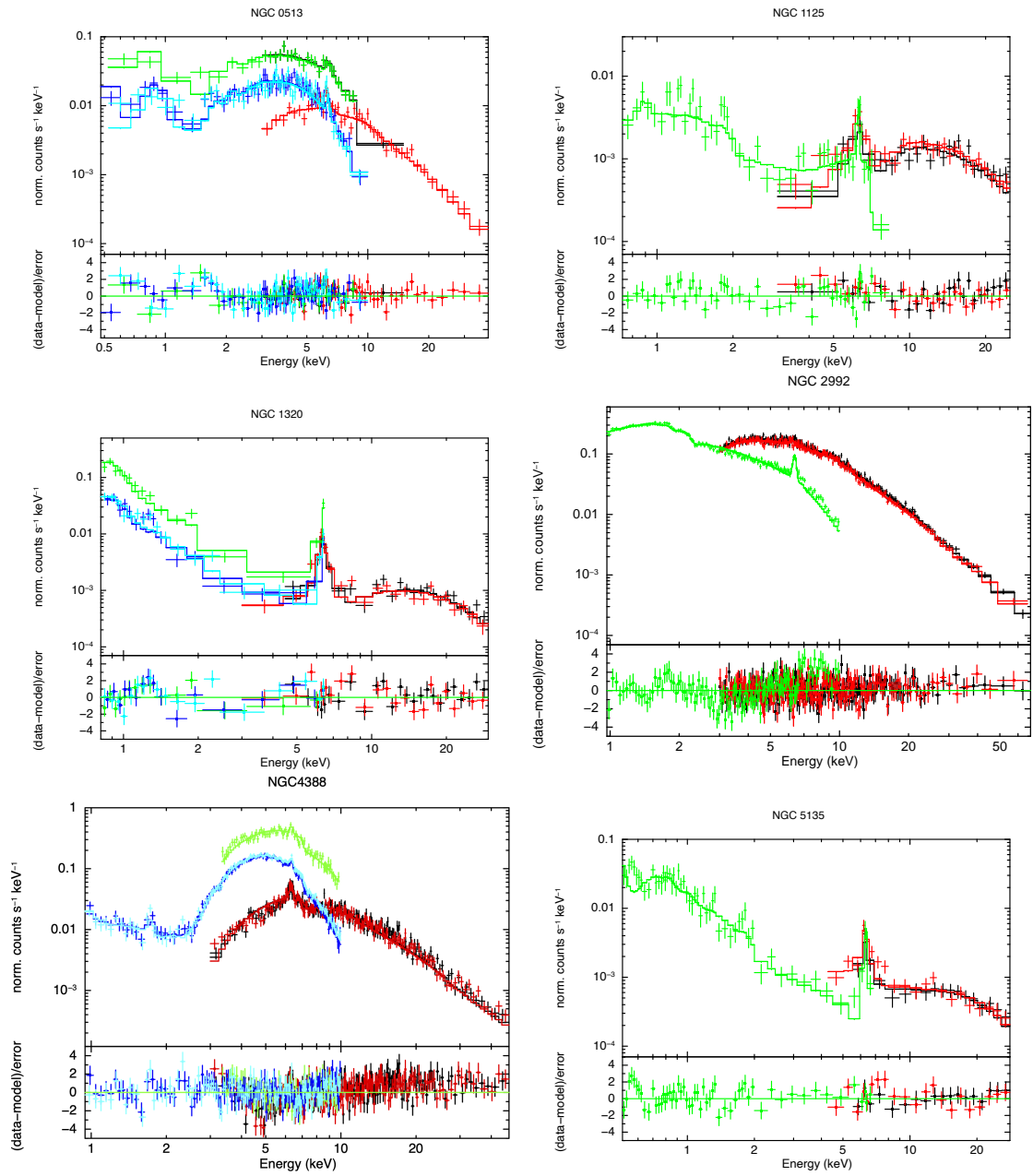


Figure A.7: Same caption as in Fig. A.6.

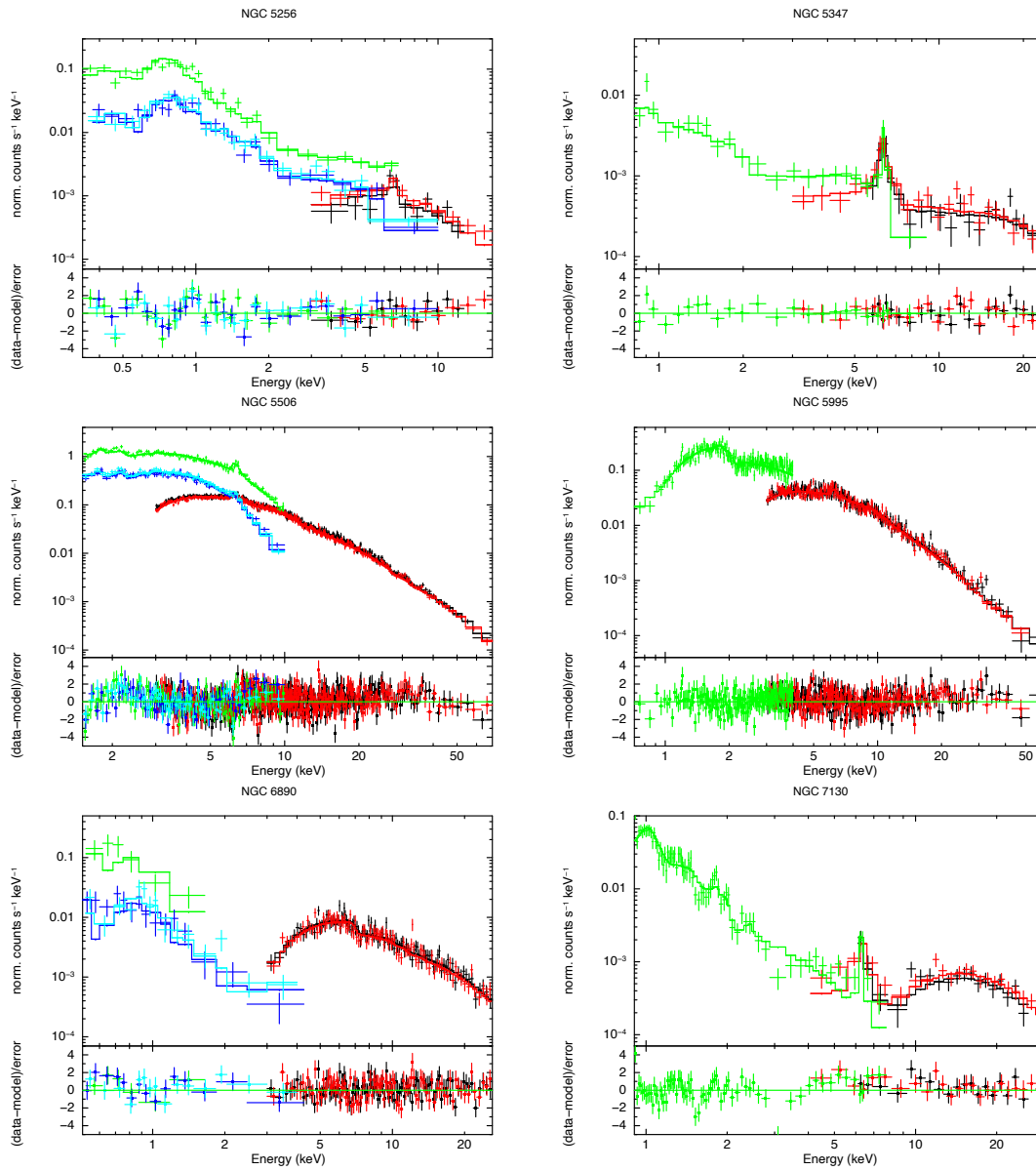


Figure A.8: Same caption as in Fig. A.6.

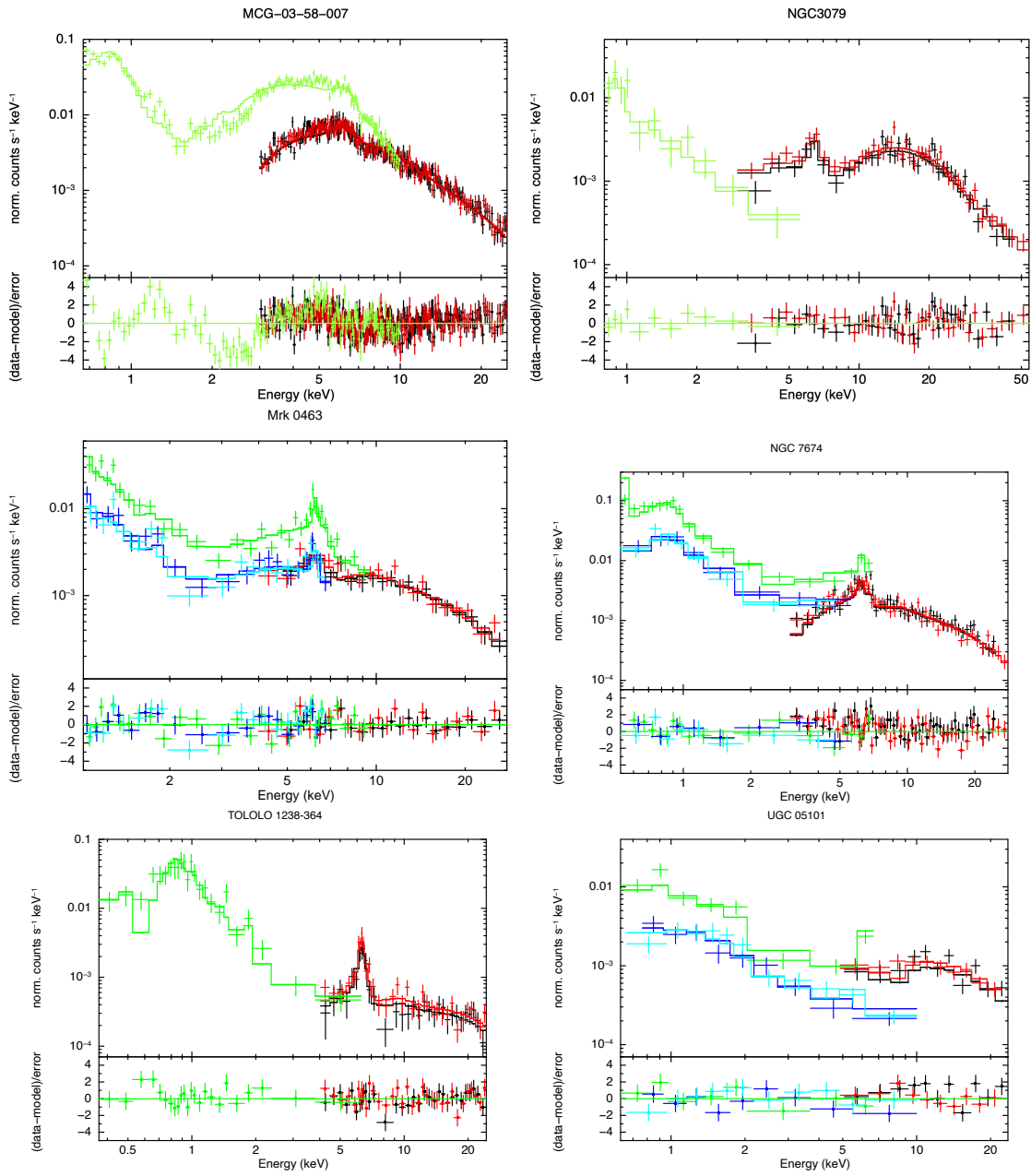


Figure A.9: Same caption as in Fig. A.6.

Bibliography

- S. Aalto. Galaxies and Galaxy Nuclei: From Hot Cores to Cold Outflows. In D. Iono, K. Tatematsu, A. Wootten, and L. Testi, editors, *Revolution in Astronomy with ALMA: The Third Year*, volume 499 of *Astronomical Society of the Pacific Conference Series*, page 85, December 2015.
- S. Aalto, S. Garcia-Burillo, S. Muller, J. M. Winters, P. van der Werf, C. Henkel, F. Costagliola, and R. Neri. Detection of HCN, HCO⁺, and HNC in the Mrk 231 molecular outflow. Dense molecular gas in the AGN wind. *A&A*, 537:A44, January 2012. doi: 10.1051/0004-6361/201117919.
- S. Aalto, S. Martín, F. Costagliola, E. González-Alfonso, S. Muller, K. Sakamoto, G. A. Fuller, S. García-Burillo, P. van der Werf, R. Neri, M. Spaans, F. Combes, S. Viti, S. Mühle, L. Armus, A. Evans, E. Sturm, J. Cernicharo, C. Henkel, and T. R. Greve. Probing highly obscured, self-absorbed galaxy nuclei with vibrationally excited HCN. *A&A*, 584:A42, December 2015. doi: 10.1051/0004-6361/201526410.
- S. Aalto, S. Muller, F. Costagliola, K. Sakamoto, J. S. Gallagher, N. Falstad, S. König, K. Dasyra, K. Wada, F. Combes, S. García-Burillo, L. E. Kristensen, S. Martín, P. van der Werf, A. S. Evans, and J. Kotilainen. Luminous, pc-scale CO 6-5 emission in the obscured nucleus of NGC 1377. *A&A*, 608:A22, December 2017. doi: 10.1051/0004-6361/201730650.
- J. Aird, K. Nandra, E. S. Laird, A. Georgakakis, M. L. N. Ashby, P. Barmby, A. L. Coil, J. S. Huang, A. M. Koekemoer, C. C. Steidel, and C. N. A. Willmer. The evolution of the hard X-ray luminosity function of AGN. *MNRAS*, 401(4):2531–2551, February 2010. doi: 10.1111/j.1365-2966.2009.15829.x.
- J. Aird, A. L. Coil, A. Georgakakis, K. Nandra, G. Barro, and P. G. Pérez-González. The evolution of the X-ray luminosity functions of unabsorbed and absorbed AGNs out to $z \sim 5$. *MNRAS*, 451(2):1892–1927, August 2015. doi: 10.1093/mnras/stv1062.
- M. Albrecht, E. Krügel, and R. Chini. Dust and CO emission towards the centers of normal galaxies, starburst galaxies and active galactic nuclei. I. New data and updated catalogue. *A&A*, 462(2):575–579, February 2007. doi: 10.1051/0004-6361:20047017.
- D. M. Alexander and R. C. Hickox. What drives the growth of black holes? *New A Rev.*, 56(4):93–121, June 2012. doi: 10.1016/j.newar.2011.11.003.
- A. Alonso-Herrero, C. Ramos Almeida, P. Esquej, P. F. Roche, A. Hernán-Caballero, S. F. Hönl, O. González-Martín, I. Aretxaga, R. E. Mason, C. Packham, N. A. Levenson, J. M. Rodríguez Espinosa, R. Siebenmorgen, M. Pereira-Santaella, T. Díaz-Santos, L. Colina, C. Alvarez, and C. M. Telesco. Nuclear 11.3 μm PAH emission in local active galactic nuclei. *MNRAS*, 443(3):2766–2782, September 2014. doi: 10.1093/mnras/stu1293.
- A. Alonso-Herrero, P. Esquej, P. F. Roche, C. Ramos Almeida, O. González-Martín, C. Packham, N. A. Levenson, R. E. Mason, A. Hernán-Caballero, M. Pereira-Santaella, C. Alvarez, I. Aretxaga, E. López-Rodríguez, L. Colina, T. Díaz-Santos, M. Imanishi,

- J. M. Rodríguez Espinosa, and E. Perlman. A mid-infrared spectroscopic atlas of local active galactic nuclei on sub-arcsecond resolution using GTC/CanariCam. *MNRAS*, 455(1):563–583, January 2016. doi: 10.1093/mnras/stv2342.
- Almudena Alonso-Herrero, Miguel Pereira-Santaella, George H. Rieke, and Dimitra Rigopoulou. Local Luminous Infrared Galaxies. II. Active Galactic Nucleus Activity from Spitzer/Infrared Spectrograph Spectra. *ApJ*, 744(1):2, January 2012. doi: 10.1088/0004-637X/744/1/2.
- Hongjun An, Kristin K. Madsen, Niels J. Westergaard, Steven E. Boggs, Finn E. Christensen, William W. Craig, Charles J. Hailey, Fiona A. Harrison, Daniel K. Stern, and William W. Zhang. In-flight PSF calibration of the NuSTAR hard X-ray optics. In Tadayuki Takahashi, Jan-Willem A. den Herder, and Mark Bautz, editors, *Space Telescopes and Instrumentation 2014: Ultraviolet to Gamma Ray*, volume 9144 of *Society of Photo-Optical Instrumentation Engineers (SPIE) Conference Series*, page 91441Q, July 2014. doi: 10.1117/12.2055481.
- Robert Antonucci. Unified models for active galactic nuclei and quasars. *ARA&A*, 31: 473–521, January 1993. doi: 10.1146/annurev.aa.31.090193.002353.
- L. Armus, V. Charmandaris, J. Bernard-Salas, H. W. W. Spoon, J. A. Marshall, S. J. U. Higdon, V. Desai, H. I. Teplitz, L. Hao, D. Devost, B. R. Brandl, Y. Wu, G. C. Sloan, B. T. Soifer, J. R. Houck, and T. L. Herter. Observations of Ultraluminous Infrared Galaxies with the Infrared Spectrograph on the Spitzer Space Telescope. II. The IRAS Bright Galaxy Sample. *ApJ*, 656(1):148–167, February 2007. doi: 10.1086/510107.
- K. A. Arnaud. XSPEC: The First Ten Years. In G. H. Jacoby and J. Barnes, editors, *Astronomical Data Analysis Software and Systems V*, volume 101 of *Astronomical Society of the Pacific Conference Series*, page 17, 1996.
- D. Asmus, P. Gandhi, A. Smette, S. F. Hönic, and W. J. Duschl. Mid-infrared properties of nearby low-luminosity AGN at high angular resolution. *A&A*, 536:A36, December 2011. doi: 10.1051/0004-6361/201116693.
- D. Asmus, S. F. Hönic, P. Gandhi, A. Smette, and W. J. Duschl. The subarcsecond mid-infrared view of local active galactic nuclei - I. The N- and Q-band imaging atlas. *MNRAS*, 439(2):1648–1679, April 2014. doi: 10.1093/mnras/stu041.
- D. Asmus, P. Gandhi, S. F. Hönic, A. Smette, and W. J. Duschl. The subarcsecond mid-infrared view of local active galactic nuclei - II. The mid-infrared-X-ray correlation. *MNRAS*, 454(1):766–803, November 2015. doi: 10.1093/mnras/stv1950.
- A. Audibert, F. Combes, S. García-Burillo, L. Hunt, A. Eckart, S. Aalto, V. Casasola, F. Boone, M. Krips, S. Viti, S. Müller, K. Dasyra, P. van der Werf, and S. Martín. ALMA captures feeding and feedback from the active galactic nucleus in NGC 613. *A&A*, 632:A33, December 2019. doi: 10.1051/0004-6361/201935845.
- Y. Avni and H. Tananbaum. X-ray properties of optically selected QSOs. *ApJ*, 305:83–99, June 1986. doi: 10.1086/164230.
- E. Bañados, T. Connor, D. Stern, J. Mulchaey, X. Fan, R. Decarli, E. P. Farina, C. Mazzucchelli, B. P. Venemans, F. Walter, F. Wang, and J. Yang. Chandra X-Rays from the Redshift 7.54 Quasar ULAS J1342+0928. *ApJ*, 856:L25, April 2018. doi: 10.3847/2041-8213/aab61e.
- M. Baloković, M. Brightman, F. A. Harrison, A. Comastri, C. Ricci, J. Buchner, P. Gandhi, D. Farrah, and D. Stern. New Spectral Model for Constraining Torus Covering Factors from Broadband X-Ray Spectra of Active Galactic Nuclei. *ApJ*, 854(1):42, February 2018. doi: 10.3847/1538-4357/aaa7eb.

- Volker Beckmann and Chris R. Shrader. *Active Galactic Nuclei*. 2012.
- M. E. Bell, T. Tzioumis, P. Uttley, R. P. Fender, P. Arévalo, E. Breedt, I. McHardy, D. E. Calvelo, O. Jamil, and E. Körding. X-ray and radio variability in the low-luminosity active galactic nucleus NGC 7213. *MNRAS*, 411(1):402–410, Feb 2011. doi: 10.1111/j.1365-2966.2010.17692.x.
- S. Berta, D. Lutz, P. Santini, S. Wuyts, D. Rosario, D. Brisbin, A. Cooray, A. Franceschini, C. Gruppioni, E. Hatziminaoglou, H. S. Hwang, E. Le Floch, B. Magnelli, R. Nordon, S. Oliver, M. J. Page, P. Popesso, L. Pozzetti, F. Pozzi, L. Riguccini, G. Rodighiero, I. Roseboom, D. Scott, M. Symeonidis, I. Valtchanov, M. Viero, and L. Wang. Panchromatic spectral energy distributions of Herschel sources. *A&A*, 551:A100, Mar 2013. doi: 10.1051/0004-6361/201220859.
- T. Bertram, A. Eckart, S. Fischer, J. Zuther, C. Straubmeier, L. Wisotzki, and M. Krips. Molecular gas in nearby low-luminosity QSO host galaxies. *A&A*, 470(2):571–583, August 2007. doi: 10.1051/0004-6361:20077578.
- S. Bianchi, G. Matt, I. Balestra, and G. C. Perola. The origin of the iron lines in NGC 7213. *A&A*, 407:L21–L24, Aug 2003. doi: 10.1051/0004-6361:20031054.
- Stefano Bianchi, Fabio La Franca, Giorgio Matt, Matteo Guainazzi, Elena Jimenez Bailón, Anna Lia Longinotti, Fabrizio Nicastro, and Laura Pentericci. A broad-line region origin for the iron ka line in ngc 7213. *Monthly Notices of the Royal Astronomical Society: Letters*, 389(1):L52–L56, 2008. doi: 10.1111/j.1745-3933.2008.00521.x. URL <http://dx.doi.org/10.1111/j.1745-3933.2008.00521.x>.
- D. L. Blank, J. I. Harnett, and P. A. Jones. An 8.4-GHz Long Baseline Array observation of the unusual Seyfert galaxy NGC 7213. *MNRAS*, 356(2):734–736, Jan 2005. doi: 10.1111/j.1365-2966.2004.08506.x.
- Alberto D. Bolatto, Adam K. Leroy, Katherine Jameson, Eve Ostriker, Karl Gordon, Brandon Lawton, Snežana Stanimirović, Frank P. Israel, Suzanne C. Madden, Sacha Hony, Karin M. Sandstrom, Caroline Bot, Mónica Rubio, P. Frank Winkler, Julia Roman-Duval, Jacco Th. van Loon, Joana M. Oliveira, and Rémy Indebetouw. The State of the Gas and the Relation between Gas and Star Formation at Low Metallicity: The Small Magellanic Cloud. *ApJ*, 741(1):12, November 2011. doi: 10.1088/0004-637X/741/1/12.
- Alberto D. Bolatto, Mark Wolfire, and Adam K. Leroy. The CO-to-H₂ Conversion Factor. *ARA&A*, 51(1):207–268, Aug 2013. doi: 10.1146/annurev-astro-082812-140944.
- A. Boselli, L. Cortese, and M. Boquien. Cold gas properties of the Herschel Reference Survey. I. ¹²CO(1-0) and HI data. *A&A*, 564:A65, April 2014. doi: 10.1051/0004-6361/201322311.
- W. N. Brandt and D. M. Alexander. Cosmic X-ray surveys of distant active galaxies. The demographics, physics, and ecology of growing supermassive black holes. *A&A Rev.*, 23:1, January 2015. doi: 10.1007/s00159-014-0081-z.
- M. A. Bransford, P. N. Appleton, C. A. Heisler, R. P. Norris, and A. P. Marston. Radio-luminous Southern Seyfert Galaxies. I. Radio Images and Selected Optical/Near-Infrared Spectroscopy. *ApJ*, 497(1):133–162, Apr 1998. doi: 10.1086/305438.
- Murray Brightman, Kirpal Nandra, Mara Salvato, Li-Ting Hsu, James Aird, and Cyprian Rangel. Compton thick active galactic nuclei in Chandra surveys. *MNRAS*, 443(3): 1999–2017, September 2014. doi: 10.1093/mnras/stu1175.

- M. Brusa, G. Cresci, E. Daddi, R. Paladino, M. Perna, A. Bongiorno, E. Lusso, M. T. Sargent, V. Casasola, C. Feruglio, F. Fraternali, I. Georgiev, V. Mainieri, S. Carniani, A. Comastri, F. Duras, F. Fiore, F. Mannucci, A. Marconi, E. Piconcelli, G. Zamorani, R. Gilli, F. La Franca, G. Lanzuisi, D. Lutz, P. Santini, N. Z. Scoville, C. Vignali, F. Vito, S. Rabien, L. Busoni, and M. Bonaglia. Molecular outflow and feedback in the obscured quasar XID2028 revealed by ALMA. *A&A*, 612:A29, Apr 2018. doi: 10.1051/0004-6361/201731641.
- G. Bruzual and S. Charlot. Stellar population synthesis at the resolution of 2003. *MNRAS*, 344(4):1000–1028, Oct 2003. doi: 10.1046/j.1365-8711.2003.06897.x.
- Catherine L. Buchanan, Jack F. Gallimore, Christopher P. O’Dea, Stefi A. Baum, David J. Axon, Andrew Robinson, Moshe Elitzur, and Martin Elvis. Spitzer IRS Spectra of a Large Sample of Seyfert Galaxies: A Variety of Infrared Spectral Energy Distributions in the Local Active Galactic Nucleus Population. *AJ*, 132(1):401–419, July 2006. doi: 10.1086/505022.
- Johannes Buchner, Murray Brightman, Kirpal Nandra, Robert Nikutta, and Franz E. Bauer. X-ray spectral and eclipsing model of the clumpy obscurer in active galactic nuclei. *A&A*, 629:A16, September 2019. doi: 10.1051/0004-6361/201834771.
- C. L. Carilli and F. Walter. Cool Gas in High-Redshift Galaxies. *ARA&A*, 51(1):105–161, Aug 2013. doi: 10.1146/annurev-astro-082812-140953.
- V. Casasola, L. P. Cassarà, S. Bianchi, S. Verstocken, E. Xilouris, L. Magrini, M. W. L. Smith, I. De Looze, M. Galametz, S. C. Madden, M. Baes, C. Clark, J. Davies, P. De Vis, R. Evans, J. Fritz, F. Galliano, A. P. Jones, A. V. Mosenkov, S. Viaene, and N. Ysard. Radial distribution of dust, stars, gas, and star-formation rate in DustPedia face-on galaxies. *A&A*, 605:A18, September 2017. doi: 10.1051/0004-6361/201731020.
- V. Casasola, S. Bianchi, P. De Vis, L. Magrini, E. Corbelli, C. J. R. Clark, J. Fritz, A. Nersesian, S. Viaene, M. Baes, L. P. Cassarà, J. Davies, I. De Looze, W. Dobbels, M. Galametz, F. Galliano, A. P. Jones, S. C. Madden, A. V. Mosenkov, A. Trčka, and E. Xilouris. The ISM scaling relations in DustPedia late-type galaxies: A benchmark study for the Local Universe. *A&A*, 633:A100, January 2020. doi: 10.1051/0004-6361/201936665.
- Viviana Casasola, Leslie Hunt, Françoise Combes, and Santiago García-Burillo. The resolved star-formation relation in nearby active galactic nuclei. *A&A*, 577:A135, May 2015. doi: 10.1051/0004-6361/201425313.
- G. Chartas, M. Cappi, F. Hamann, M. Eracleous, S. Strickland, M. Giustini, and T. Misawa. The Wide-angle Outflow of the Lensed $z = 1.51$ AGN HS 0810+2554. *ApJ*, 824(1):53, June 2016. doi: 10.3847/0004-637X/824/1/53.
- G. Chartas, H. Krawczynski, L. Zalesky, C. S. Kochanek, X. Dai, C. W. Morgan, and A. Mosquera. Measuring the Innermost Stable Circular Orbits of Supermassive Black Holes. *ApJ*, 837(1):26, March 2017. doi: 10.3847/1538-4357/aa5d50.
- C. Cicone, R. Maiolino, E. Sturm, J. Graciá-Carpio, C. Feruglio, R. Neri, S. Aalto, R. Davies, F. Fiore, J. Fischer, S. García-Burillo, E. González-Alfonso, S. Hailey-Dunsheath, E. Piconcelli, and S. Veilleux. Massive molecular outflows and evidence for AGN feedback from CO observations. *A&A*, 562:A21, February 2014. doi: 10.1051/0004-6361/201322464.
- Claudia Cicone, Marcella Brusa, Cristina Ramos Almeida, Giovanni Cresci, Bernd Husemann, and Vincenzo Mainieri. The largely unconstrained multiphase nature of outflows in AGN host galaxies. *Nature Astronomy*, 2:176–178, February 2018. doi: 10.1038/s41550-018-0406-3.

- C. J. R. Clark, S. Verstocken, S. Bianchi, J. Fritz, S. Viaene, M. W. L. Smith, M. Baes, V. Casasola, L. P. Cassara, J. I. Davies, I. De Looze, P. De Vis, R. Evans, M. Galametz, A. P. Jones, S. Lianou, S. Madden, A. V. Mosenkov, and M. Xilouris. DustPedia: Multiwavelength photometry and imagery of 875 nearby galaxies in 42 ultraviolet-microwave bands. *A&A*, 609:A37, January 2018. doi: 10.1051/0004-6361/201731419.
- F. Combes, S. García-Burillo, V. Casasola, L. Hunt, M. Krips, A. J. Baker, F. Boone, A. Eckart, I. Marquez, R. Neri, E. Schinnerer, and L. J. Tacconi. ALMA observations of feeding and feedback in nearby Seyfert galaxies: an AGN-driven outflow in NGC 1433. *A&A*, 558:A124, October 2013. doi: 10.1051/0004-6361/201322288.
- Françoise Combes. Molecular gas in distant galaxies from ALMA studies. *A&A Rev.*, 26(1):5, August 2018. doi: 10.1007/s00159-018-0110-4.
- I. Cortzen, J. Garrett, G. Magdis, D. Rigopoulou, F. Valentino, M. Pereira-Santaella, F. Combes, A. Alonso-Herrero, S. Toft, E. Daddi, D. Elbaz, C. Gómez-Guijarro, M. Stockmann, J. Huang, and C. Kramer. PAHs as tracers of the molecular gas in star-forming galaxies. *MNRAS*, 482(2):1618–1633, January 2019. doi: 10.1093/mnras/sty2777.
- Giovanni Cresci and Roberto Maiolino. Observing positive and negative AGN feedback. *Nature Astronomy*, 2:179–180, February 2018. doi: 10.1038/s41550-018-0404-5.
- T. Csengeri, A. Weiss, F. Wyrowski, K. M. Menten, J. S. Urquhart, S. Leurini, F. Schuller, H. Beuther, S. Bontemps, L. Bronfman, Th. Henning, and N. Schneider. The ATLASGAL survey: distribution of cold dust in the Galactic plane. Combination with Planck data. *A&A*, 585:A104, Jan 2016. doi: 10.1051/0004-6361/201526639.
- Richard H. Cyburt, Brian D. Fields, Keith A. Olive, and Tsung-Han Yeh. Big bang nucleosynthesis: Present status. *Rev. Mod. Phys.*, 88:015004, Feb 2016. doi: 10.1103/RevModPhys.88.015004. URL <https://link.aps.org/doi/10.1103/RevModPhys.88.015004>.
- Elisabete da Cunha, Stéphane Charlot, and David Elbaz. A simple model to interpret the ultraviolet, optical and infrared emission from galaxies. *MNRAS*, 388(4):1595–1617, Aug 2008. doi: 10.1111/j.1365-2966.2008.13535.x.
- E. Daddi, D. Elbaz, F. Walter, F. Bournaud, F. Salmi, C. Carilli, H. Dannerbauer, M. Dickinson, P. Monaco, and D. Riechers. Different Star Formation Laws for Disks Versus Starbursts at Low and High Redshifts. *ApJ*, 714(1):L118–L122, May 2010. doi: 10.1088/2041-8205/714/1/L118.
- M. Dadina. Seyfert galaxies in the local Universe ($z \leq 0.1$): the average X-ray spectrum as seen by BeppoSAX. *A&A*, 485(2):417–424, Jul 2008. doi: 10.1051/0004-6361:20077569.
- J. I. Davies, M. Baes, S. Bianchi, A. Jones, S. Madden, M. Xilouris, M. Bocchio, V. Casasola, L. Cassara, C. Clark, I. De Looze, R. Evans, J. Fritz, M. Galametz, F. Galliano, S. Lianou, A. V. Mosenkov, M. Smith, S. Verstocken, S. Viaene, M. Vika, G. Wagle, and N. Ysard. DustPedia: A Definitive Study of Cosmic Dust in the Local Universe. *PASP*, 129(974):044102, April 2017. doi: 10.1088/1538-3873/129/974/044102.
- Gerard de Vaucouleurs, Antoinette de Vaucouleurs, Jr. Corwin, Herold G., Ronald J. Buta, Georges Paturel, and Pascal Fouque. *Third Reference Catalogue of Bright Galaxies*. 1991.

- I. Delvecchio, C. Gruppioni, F. Pozzi, S. Berta, G. Zamorani, A. Cimatti, D. Lutz, D. Scott, C. Vignali, G. Cresci, A. Feltre, A. Cooray, M. Vaccari, J. Fritz, E. Le Floc'h, B. Magnelli, P. Popesso, S. Oliver, J. Bock, M. Carollo, T. Contini, O. Le Fèvre, S. Lilly, V. Mainieri, A. Renzini, and M. Scodreggio. Tracing the cosmic growth of supermassive black holes to $z \sim 3$ with Herschel. *MNRAS*, 439(3):2736–2754, April 2014. doi: 10.1093/mnras/stu130.
- E. M. Di Teodoro and F. Fraternali. ^{3D} BAROLO: a new 3D algorithm to derive rotation curves of galaxies. *MNRAS*, 451:3021–3033, August 2015. doi: 10.1093/mnras/stv1213.
- Aleksandar M. Diamond-Stanic and George H. Rieke. The Effect of Active Galactic Nuclei on the Mid-infrared Aromatic Features. *ApJ*, 724(1):140–153, November 2010. doi: 10.1088/0004-637X/724/1/140.
- Aleksandar M. Diamond-Stanic and George H. Rieke. The Relationship between Black Hole Growth and Star Formation in Seyfert Galaxies. *ApJ*, 746(2):168, February 2012. doi: 10.1088/0004-637X/746/2/168.
- R. L. Dickman, Ronald L. Snell, and F. Peter Schloerb. Carbon Monoxide as an Extragalactic Mass Tracer. *ApJ*, 309:326, October 1986. doi: 10.1086/164604.
- C. Done, P. T. Życki, and D. A. Smith. The X-ray spectrum of Cyg X-2. *MNRAS*, 331(2):453–462, March 2002. doi: 10.1046/j.1365-8711.2002.05195.x.
- D. Downes and P. M. Solomon. Rotating Nuclear Rings and Extreme Starbursts in Ultraluminous Galaxies. *ApJ*, 507(2):615–654, Nov 1998. doi: 10.1086/306339.
- B. T. Draine. Interstellar Dust Grains. *ARA&A*, 41:241–289, January 2003. doi: 10.1146/annurev.astro.41.011802.094840.
- B.T. Draine. *Physics of the Interstellar and Intergalactic Medium*. Princeton Series in Astrophysics. Princeton University Press, 2010. ISBN 9781400839087. URL <https://books.google.it/books?id=FycJvKHyiwsC>.
- F. Duras, A. Bongiorno, F. Ricci, E. Piconcelli, F. Shankar, E. Lusso, S. Bianchi, F. Fiore, R. Maiolino, A. Marconi, F. Onori, E. Sani, R. Schneider, C. Vignali, and F. La Franca. Universal bolometric corrections for active galactic nuclei over seven luminosity decades. *A&A*, 636:A73, April 2020. doi: 10.1051/0004-6361/201936817.
- Martin Elvis, Belinda J. Wilkes, Jonathan C. McDowell, Richard F. Green, Jill Bechtold, S. P. Willner, M. S. Oey, Elisha Polomski, and Roc Cutri. Atlas of Quasar Energy Distributions. *ApJS*, 95:1, November 1994. doi: 10.1086/192093.
- D. Emmanoulopoulos, I. E. Papadakis, I. M. McHardy, P. Arévalo, D. E. Calvelo, and P. Uttley. The 'harder when brighter' X-ray behaviour of the low-luminosity active galactic nucleus NGC 7213. *MNRAS*, 424(2):1327–1334, Aug 2012. doi: 10.1111/j.1365-2966.2012.21316.x.
- D. Emmanoulopoulos, I. E. Papadakis, F. Nicastro, and I. M. McHardy. X-ray spectral analysis of the low-luminosity active galactic nucleus NGC 7213 using long XMM-Newton observations. *MNRAS*, 429(4):3439–3448, Mar 2013. doi: 10.1093/mnras/sts610.
- Donaji Esparza-Arredondo, Omaira González-Martín, Deborah Dultzin, Cristina Ramos Almeida, Jacopo Fritz, Josefa Masegosa, Alice Pasetto, Mariela Martínez-Paredes, Natalia Osorio-Clavijo, and Cesar Victoria-Ceballos. Physical Parameters of the Torus for the Type 2 Seyfert IC 5063 from Mid-IR and X-Ray Simultaneous Spectral Fitting. *ApJ*, 886(2):125, December 2019. doi: 10.3847/1538-4357/ab4ced.

- P. A. Evans, A. P. Beardmore, K. L. Page, J. P. Osborne, P. T. O'Brien, R. Willingale, R. L. C. Starling, D. N. Burrows, O. Godet, L. Vetere, J. Racusin, M. R. Goad, K. Wiersema, L. Angelini, M. Capalbi, G. Chincarini, N. Gehrels, J. A. Kennea, R. Margutti, D. C. Morris, C. J. Mountford, C. Pagani, M. Perri, P. Romano, and N. Tanvir. Methods and results of an automatic analysis of a complete sample of Swift-XRT observations of GRBs. *MNRAS*, 397(3):1177–1201, August 2009. doi: 10.1111/j.1365-2966.2009.14913.x.
- A. C. Fabian. Observational Evidence of Active Galactic Nuclei Feedback. *ARA&A*, 50: 455–489, Sep 2012. doi: 10.1146/annurev-astro-081811-125521.
- A. C. Fabian, J. S. Sanders, S. Ettori, G. B. Taylor, S. W. Allen, C. S. Crawford, K. Iwasawa, R. M. Johnstone, and P. M. Ogle. Chandra imaging of the complex X-ray core of the Perseus cluster. *MNRAS*, 318(4):L65–L68, November 2000. doi: 10.1046/j.1365-8711.2000.03904.x.
- A. Feltre, E. Hatziminaoglou, J. Fritz, and A. Franceschini. Smooth and clumpy dust distributions in AGN: a direct comparison of two commonly explored infrared emission models. *MNRAS*, 426(1):120–127, Oct 2012. doi: 10.1111/j.1365-2966.2012.21695.x.
- Roberto Cid Fernandes, Rosa M. Gonzalez Delgado, Henrique Schmitt, Thaisa Storchi-Bergmann, Lucimara P. Martins, Enrique Perez, Timothy Heckman, Claus Leitherer, and Daniel Schaerer. The stellar populations of low-luminosity active galactic nuclei. i. ground-based observations. *The Astrophysical Journal*, 605(1):105–126, apr 2004. doi: 10.1086/382217. URL <https://doi.org/10.1086/382217>.
- J. A. Fernández-Ontiveros, K. M. Dasyra, E. Hatziminaoglou, M. A. Malkan, M. Pereira-Santaella, M. Papachristou, L. Spinoglio, F. Combes, S. Aalto, N. Nagar, M. Imanishi, P. Andreani, C. Ricci, and R. Slater. A CO molecular gas wind 340 pc away from the Seyfert 2 nucleus in ESO 420-G13 probes an elusive radio jet. *A&A*, 633:A127, January 2020. doi: 10.1051/0004-6361/201936552.
- F. Fiore, C. Feruglio, F. Shankar, M. Bischetti, A. Bongiorno, M. Brusa, S. Carniani, C. Cicone, F. Duras, A. Lamastra, V. Mainieri, A. Marconi, N. Menci, R. Maiolino, E. Piconcelli, G. Vietri, and L. Zappacosta. AGN wind scaling relations and the co-evolution of black holes and galaxies. *A&A*, 601:A143, May 2017. doi: 10.1051/0004-6361/201629478.
- A. Fluetsch, R. Maiolino, S. Carniani, A. Marconi, C. Cicone, M. A. Bourne, T. Costa, A. C. Fabian, W. Ishibashi, and G. Venturi. Cold molecular outflows in the local Universe and their feedback effect on galaxies. *MNRAS*, 483(4):4586–4614, March 2019. doi: 10.1093/mnras/sty3449.
- Daniel Foreman-Mackey, David W. Hogg, Dustin Lang, and Jonathan Goodman. emcee: The MCMC Hammer. *PASP*, 125(925):306, March 2013. doi: 10.1086/670067.
- J. Fritz, A. Franceschini, and E. Hatziminaoglou. Revisiting the infrared spectra of active galactic nuclei with a new torus emission model. *MNRAS*, 366:767–786, March 2006. doi: 10.1111/j.1365-2966.2006.09866.x.
- Antonella Fruscione, Jonathan C. McDowell, Glenn E. Allen, Nancy S. Brickhouse, Douglas J. Burke, John E. Davis, Nick Durham, Martin Elvis, Elizabeth C. Galle, Daniel E. Harris, David P. Huenemoerder, John C. Houck, Bish Ishibashi, Margarita Karovska, Fabrizio Nicastro, Michael S. Noble, Michael A. Nowak, Frank A. Primini, Aneta Siemiginowska, Randall K. Smith, and Michael Wise. CIAO: Chandra's data analysis system. In David R. Silva and Rodger E. Doxsey, editors, *Society of Photo-Optical Instrumentation Engineers (SPIE) Conference Series*, volume 6270 of *Society of Photo-Optical Instrumentation Engineers (SPIE) Conference Series*, page 62701V, June 2006. doi: 10.1117/12.671760.

- Frédéric Galliano. Some insights on the dust properties of nearby galaxies, as seen with Herschel. *Planet. Space Sci.*, 149:38–44, December 2017. doi: 10.1016/j.pss.2017.09.006.
- Frédéric Galliano, Maud Galametz, and Anthony P. Jones. The interstellar dust properties of nearby galaxies. *Annual Review of Astronomy and Astrophysics*, 56(1):673–713, 2018. doi: 10.1146/annurev-astro-081817-051900. URL <https://doi.org/10.1146/annurev-astro-081817-051900>.
- J. F. Gallimore, A. Yzaguirre, J. Jakoboski, M. J. Stevenosky, D. J. Axon, S. A. Baum, C. L. Buchanan, M. Elitzur, M. Elvis, C. P. O’Dea, and A. Robinson. Infrared Spectral Energy Distributions of Seyfert Galaxies: Spitzer Space Telescope Observations of the 12 μm Sample of Active Galaxies. *ApJS*, 187(1):172–211, March 2010a. doi: 10.1088/0067-0049/187/1/172.
- J. F. Gallimore, A. Yzaguirre, J. Jakoboski, M. J. Stevenosky, D. J. Axon, S. A. Baum, C. L. Buchanan, M. Elitzur, M. Elvis, C. P. O’Dea, and A. Robinson. Infrared Spectral Energy Distributions of Seyfert Galaxies: Spitzer Space Telescope Observations of the 12 μm Sample of Active Galaxies. *ApJS*, 187(1):172–211, March 2010b. doi: 10.1088/0067-0049/187/1/172.
- P. Gandhi, H. Horst, A. Smette, S. Hönig, A. Comastri, R. Gilli, C. Vignali, and W. Duschl. Resolving the mid-infrared cores of local Seyferts. *A&A*, 502(2):457–472, August 2009. doi: 10.1051/0004-6361/200811368.
- S. García-Burillo, F. Combes, A. Usero, S. Aalto, M. Krips, S. Viti, A. Alonso-Herrero, L. K. Hunt, E. Schinnerer, A. J. Baker, F. Boone, V. Casasola, L. Colina, F. Costagliola, A. Eckart, A. Fuente, C. Henkel, A. Labiano, S. Martín, I. Márquez, S. Müller, P. Planesas, C. Ramos Almeida, M. Spaans, L. J. Tacconi, and P. P. van der Werf. Molecular line emission in NGC 1068 imaged with ALMA. I. An AGN-driven outflow in the dense molecular gas. *A&A*, 567:A125, Jul 2014. doi: 10.1051/0004-6361/201423843.
- R. Genzel, L. J. Tacconi, J. Gracia-Carpio, A. Sternberg, M. C. Cooper, K. Shapiro, A. Bolatto, N. Bouché, F. Bournaud, A. Burkert, F. Combes, J. Comerford, P. Cox, M. Davis, N. M. Förster Schreiber, S. García-Burillo, D. Lutz, T. Naab, R. Neri, A. Omont, A. Shapley, and B. Weiner. A study of the gas-star formation relation over cosmic time. *MNRAS*, 407(4):2091–2108, Oct 2010. doi: 10.1111/j.1365-2966.2010.16969.x.
- A. Giannetti, S. Leurini, F. Wyrowski, J. Urquhart, T. Csengeri, K. M. Menten, C. König, and R. Güsten. ATLASGAL-selected massive clumps in the inner Galaxy. V. Temperature structure and evolution. *A&A*, 603:A33, Jul 2017. doi: 10.1051/0004-6361/201630048.
- R. Gilli, C. A. Norman, and C. Vignali. ALMA Reveals a Compact Starburst Around a Hidden QSO at $z\sim 5$. In D. Iono, K. Tatematsu, A. Wootten, and L. Testi, editors, *Revolution in Astronomy with ALMA: The Third Year*, volume 499 of *Astronomical Society of the Pacific Conference Series*, page 17, December 2015.
- Roberto Gilli, Andrea Comastri, and Gunther Hasinger. The synthesis of the cosmic x-ray background in the chandra and xmm-newton era. *Astronomy and Astrophysics*, 463, 10 2006. doi: 10.1051/0004-6361:20066334.
- B. Godard, G. Pineau des Forêts, P. Lesaffre, A. Lehmann, A. Gusdorf, and E. Falgarone. Models of irradiated molecular shocks. *A&A*, 622:A100, February 2019. doi: 10.1051/0004-6361/201834248.

- A. D. Goulding and D. M. Alexander. Towards a complete census of AGN in nearby Galaxies: a large population of optically unidentified AGN. *MNRAS*, 398(3):1165–1193, September 2009. doi: 10.1111/j.1365-2966.2009.15194.x.
- A. D. Goulding, D. M. Alexander, F. E. Bauer, W. R. Forman, R. C. Hickox, C. Jones, J. R. Mullaney, and M. Trichas. Deep Silicate Absorption Features in Compton-thick Active Galactic Nuclei Predominantly Arise due to Dust in the Host Galaxy. *ApJ*, 755(1):5, August 2012. doi: 10.1088/0004-637X/755/1/5.
- P. Gratier, J. Braine, N. J. Rodríguez-Fernández, F. P. Israel, K. F. Schuster, N. Brouillet, and E. Gardan. The molecular interstellar medium of the Local Group dwarf NGC 6822. The molecular ISM of NGC 6822. *A&A*, 512:A68, March 2010. doi: 10.1051/0004-6361/200911722.
- C. Gruppioni, S. Berta, L. Spinoglio, M. Pereira-Santaella, F. Pozzi, P. Andreani, M. Bonato, G. De Zotti, M. Malkan, M. Negrello, L. Vallini, and C. Vignali. Tracing black hole accretion with SED decomposition and IR lines: from local galaxies to the high-*z* Universe. *MNRAS*, 458:4297–4320, June 2016. doi: 10.1093/mnras/stw577.
- R. Güsten, L. Å. Nyman, P. Schilke, K. Menten, C. Cesarsky, and R. Booth. The Atacama Pathfinder EXperiment (APEX) - a new submillimeter facility for southern skies -. *A&A*, 454(2):L13–L16, Aug 2006. doi: 10.1051/0004-6361:20065420.
- J. P. Halpern and A. V. Filippenko. The nonstellar continuum of the Seyfert galaxy NGC 7213. *ApJ*, 285:475–482, October 1984. doi: 10.1086/162522.
- C. M. Harrison. Impact of supermassive black hole growth on star formation. *Nature Astronomy*, 1:0165, July 2017. doi: 10.1038/s41550-017-0165.
- C. M. Harrison, S. J. Molyneux, J. Scholtz, and M. E. Jarvis. Establishing the impact of powerful AGN on their host galaxies. *arXiv e-prints*, art. arXiv:2006.01196, June 2020.
- Christopher Harrison. *Observational constraints on the influence of active galactic nuclei on the evolution of galaxies*. PhD thesis, Durham University, September 2014.
- Fiona A. Harrison, William W. Craig, Finn E. Christensen, Charles J. Hailey, William W. Zhang, Steven E. Boggs, Daniel Stern, W. Rick Cook, Karl Forster, Paolo Giommi, Brian W. Grefenstette, Yunjin Kim, Takao Kitaguchi, Jason E. Koglin, Kristin K. Madsen, Peter H. Mao, Hiromasa Miyasaka, Kaya Mori, Matteo Perri, Michael J. Pivovarov, Simonetta Puccetti, Vikram R. Rana, Niels J. Westergaard, Jason Willis, Andreas Zoglauer, Hongjun An, Matteo Bachetti, Nicolas M. Barrière, Eric C. Bellm, Varun Bhalerao, Nicolai F. Brejnholt, Felix Fuerst, Carl C. Liebe, Craig B. Markwardt, Melania Nynka, Julia K. Vogel, Dominic J. Walton, Daniel R. Wik, David M. Alexander, Lynn R. Cominsky, Ann E. Hornschemeier, Allan Hornstrup, Victoria M. Kaspi, Greg M. Madejski, Giorgio Matt, Silvano Molendi, David M. Smith, John A. Tomsick, Marco Ajello, David R. Ballantyne, Mislav Baloković, Didier Barret, Franz E. Bauer, Roger D. Blandford, W. Niel Brandt, Laura W. Brenneman, James Chiang, Deepto Chakrabarty, Jerome Chenevez, Andrea Comastri, Francois Dufour, Martin Elvis, Andrew C. Fabian, Duncan Farrah, Chris L. Fryer, Eric V. Gotthelf, Jonathan E. Grindlay, David J. Helfand, Roman Krivonos, David L. Meier, Jon M. Miller, Lorenzo Natalucci, Patrick Ogle, Eran O. Ofek, Andrew Ptak, Stephen P. Reynolds, Jane R. Rigby, Gianpiero Tagliaferri, Stephen E. Thorsett, Ezequiel Treister, and C. Megan Urry. The Nuclear Spectroscopic Telescope Array (NuSTAR) High-energy X-Ray Mission. *ApJ*, 770(2):103, June 2013. doi: 10.1088/0004-637X/770/2/103.
- E. Hatziminaoglou, J. Fritz, A. Franceschini, A. Afonso-Luis, A. Hernán-Caballero, I. Pérez-Fourron, S. Serjeant, C. Lonsdale, S. Oliver, M. Rowan-Robinson, D. Shupe, H. E. Smith, and J. Surace. Properties of dusty tori in active galactic nuclei - I.

- The case of SWIRE/SDSS quasars. *MNRAS*, 386(3):1252–1264, May 2008. doi: 10.1111/j.1365-2966.2008.13119.x.
- Timothy M. Heckman and Philip N. Best. The Coevolution of Galaxies and Supermassive Black Holes: Insights from Surveys of the Contemporary Universe. *ARA&A*, 52: 589–660, August 2014. doi: 10.1146/annurev-astro-081913-035722.
- C. Henkel, S. Mühle, G. Bendo, G. I. G. Józsa, Y. Gong, S. Viti, S. Aalto, F. Combes, S. García-Burillo, L. K. Hunt, J. Mangum, S. Martín, S. Müller, J. Ott, P. van der Werf, A. A. Malawi, H. Ismail, E. Alkhuja, H. M. Asiri, R. Aladro, F. Alves, Y. Ao, W. A. Baan, F. Costagliola, G. Fuller, J. Greene, C. M. V. Impellizzeri, F. Kamali, R. S. Klessen, R. Mauersberger, X. D. Tang, K. Tristram, M. Wang, and J. S. Zhang. Molecular line emission in NGC 4945, imaged with ALMA. *A&A*, 615:A155, July 2018. doi: 10.1051/0004-6361/201732174.
- A. Hernán-Caballero and E. Hatziminaoglou. An atlas of mid-infrared spectra of star-forming and active galaxies. *MNRAS*, 414(1):500–511, Jun 2011. doi: 10.1111/j.1365-2966.2011.18413.x.
- Ryan C. Hickox and David M. Alexander. Obscured Active Galactic Nuclei. *ARA&A*, 56: 625–671, September 2018. doi: 10.1146/annurev-astro-081817-051803.
- Alexander Hobbs, Sergei Nayakshin, Chris Power, and Andrew King. Feeding supermassive black holes through supersonic turbulence and ballistic accretion. *MNRAS*, 413(4): 2633–2650, June 2011. doi: 10.1111/j.1365-2966.2011.18333.x.
- D. J. Hollenbach and A. G. G. M. Tielens. Photodissociation regions in the interstellar medium of galaxies. *Reviews of Modern Physics*, 71(1):173–230, Jan 1999. doi: 10.1103/RevModPhys.71.173.
- S. F. Hönic, M. Kishimoto, P. Gandhi, A. Smette, D. Asmus, W. Duschl, M. Polletta, and G. Weigelt. The dusty heart of nearby active galaxies. I. High-spatial resolution mid-IR spectro-photometry of Seyfert galaxies. *A&A*, 515:A23, June 2010. doi: 10.1051/0004-6361/200913742.
- S. F. Hönic, C. Leipski, R. Antonucci, and M. Haas. Quantifying the Anisotropy in the Infrared Emission of Powerful Active Galactic Nuclei. *ApJ*, 736(1):26, July 2011. doi: 10.1088/0004-637X/736/1/26.
- Sebastian F. Hönic. Redefining the Torus: A Unifying View of AGNs in the Infrared and Submillimeter. *ApJ*, 884(2):171, October 2019. doi: 10.3847/1538-4357/ab4591.
- H. Horst, P. Gandhi, A. Smette, and W. J. Duschl. The mid IR - hard X-ray correlation in AGN and its implications for dusty torus models. *A&A*, 479(2):389–396, February 2008. doi: 10.1051/0004-6361:20078548.
- Kohei Ichikawa, Masatoshi Imanishi, Yoshihiro Ueda, Takao Nakagawa, Mai Shirahata, Hidehiro Kaneda, and Shinki Oyabu. AKARI IRC 2.5-5 μm Spectroscopy of Infrared Galaxies over a Wide Luminosity Range. *ApJ*, 794(2):139, October 2014. doi: 10.1088/0004-637X/794/2/139.
- Kohei Ichikawa, Claudio Ricci, Yoshihiro Ueda, Kenta Matsuoka, Yoshiki Toba, Taiki Kawamuro, Benny Trakhtenbrot, and Michael J. Koss. The Complete Infrared View of Active Galactic Nuclei from the 70 Month Swift/BAT Catalog. *ApJ*, 835(1):74, January 2017. doi: 10.3847/1538-4357/835/1/74.
- Masatoshi Imanishi and Philip R. Maloney. 3.1 Micron H₂O Ice Absorption in LINER-Type Ultraluminous Infrared Galaxies with Cool Far-Infrared Colors: The Centrally Concentrated Nature of Their Deeply Buried Energy Sources. *ApJ*, 588(1):165–174, May 2003. doi: 10.1086/368354.

- Masatoshi Imanishi, C. C. Dudley, Roberto Maiolino, Philip R. Maloney, Takao Nakagawa, and Guido Risaliti. A Spitzer IRS Low-Resolution Spectroscopic Search for Buried AGNs in Nearby Ultraluminous Infrared Galaxies: A Constraint on Geometry between Energy Sources and Dust. *ApJS*, 171(1):72–100, July 2007. doi: 10.1086/513715.
- Masatoshi Imanishi, Kouichiro Nakanishi, and Takuma Izumi. ALMA HCN and HCO+ J = 3-2 Observations of Optical Seyfert and Luminous Infrared Galaxies: Confirmation of Elevated HCN-to-HCO+ Flux Ratios in AGNs. *AJ*, 152(6):218, December 2016. doi: 10.3847/0004-6256/152/6/218.
- Masatoshi Imanishi, Kouichiro Nakanishi, and Takuma Izumi. ALMA Multiple-transition Observations of High-density Molecular Tracers in Ultraluminous Infrared Galaxies. *ApJ*, 856(2):143, April 2018. doi: 10.3847/1538-4357/aab42f.
- Masatoshi Imanishi, Kouichiro Nakanishi, and Takuma Izumi. ALMA Spatially Resolved Dense Molecular Gas Survey of Nearby Ultraluminous Infrared Galaxies. *ApJS*, 241(2):19, April 2019. doi: 10.3847/1538-4365/ab05b9.
- Masatoshi Imanishi, Dieu D. Nguyen, Keiichi Wada, Yoshiaki Hagiwara, Satoru Iguchi, Takuma Izumi, Nozomu Kawakatu, Kouichiro Nakanishi, and Kyoko Onishi. ALMA 0"02 Resolution Observations Reveal HCN-abundance-enhanced Counter-rotating and Outflowing Dense Molecular Gas at the NGC 1068 Nucleus. *ApJ*, 902(2):99, October 2020. doi: 10.3847/1538-4357/abaf50.
- F. P. Israel. Dust and molecules in the Local Group galaxy NGC 6822. II. CO and molecular hydrogen. *A&A*, 317:65–72, January 1997.
- T. H. Jarrett, T. Chester, R. Cutri, S. Schneider, M. Skrutskie, and J. P. Huchra. 2MASS Extended Source Catalog: Overview and Algorithms. *AJ*, 119(5):2498–2531, May 2000. doi: 10.1086/301330.
- J. J. Jensen, S. F. Hönig, S. Rakshit, A. Alonso-Herrero, D. Asmus, P. Gandhi, M. Kishimoto, A. Smette, and K. R. W. Tristram. PAH features within few hundred parsecs of active galactic nuclei. *MNRAS*, 470(3):3071–3094, September 2017. doi: 10.1093/mnras/stx1447.
- A. P. Jones, M. Köhler, N. Ysard, M. Bocchio, and L. Verstraete. The global dust modelling framework THEMIS. *A&A*, 602:A46, June 2017. doi: 10.1051/0004-6361/201630225.
- D. Kakkad, V. Mainieri, M. Brusa, P. Padovani, S. Carniani, C. Feruglio, M. Sargent, B. Husemann, A. Bongiorno, M. Bonzini, E. Piconcelli, J. D. Silverman, and W. Rujopakarn. ALMA observations of cold molecular gas in AGN hosts at $z \sim 1.5$ - evidence of AGN feedback? *MNRAS*, 468(4):4205–4215, Jul 2017. doi: 10.1093/mnras/stx726.
- P. M. W. Kalberla, W. B. Burton, Dap Hartmann, E. M. Arnal, E. Bajaja, R. Morras, and W. G. L. Pöppel. The Leiden/Argentine/Bonn (LAB) Survey of Galactic HI. Final data release of the combined LDS and IAR surveys with improved stray-radiation corrections. *A&A*, 440(2):775–782, Sep 2005. doi: 10.1051/0004-6361:20041864.
- E. S. Kammoun, J. M. Miller, A. Zoghbi, K. Oh, M. Koss, R. F. Mushotzky, L. W. Brenneman, W. N. Brandt, D. Proga, A. M. Lohfink, J. S. Kaastra, D. Barret, E. Behar, and D. Stern. A Hard Look at NGC 5347: Revealing a Nearby Compton-thick AGN. *ApJ*, 877(2):102, June 2019. doi: 10.3847/1538-4357/ab1c5f.
- E. Kara, A. C. Fabian, E. M. Cackett, P. Uttley, D. R. Wilkins, and A. Zoghbi. Discovery of high-frequency iron K lags in Ark 564 and Mrk 335. *MNRAS*, 434(2):1129–1137, September 2013. doi: 10.1093/mnras/stt1055.

- Jr. Kennicutt, Robert C. Star Formation in Galaxies Along the Hubble Sequence. *ARA&A*, 36:189–232, January 1998. doi: 10.1146/annurev.astro.36.1.189.
- Robert C. Kennicutt and Neal J. Evans. Star Formation in the Milky Way and Nearby Galaxies. *ARA&A*, 50:531–608, September 2012. doi: 10.1146/annurev-astro-081811-125610.
- Allison Kirkpatrick, Stacey Alberts, Alexandra Pope, Guillermo Barro, Matteo Bonato, Dale D. Kocevski, Pablo Pérez-González, George H. Rieke, Lucia Rodríguez-Muñoz, Anna Sajina, Norman A. Grogin, Kameswara Bharadwaj Mantha, Viraj Pand ya, Janine Pforr, Mara Salvato, and Paola Santini. The AGN-Star Formation Connection: Future Prospects with JWST. *ApJ*, 849(2):111, November 2017. doi: 10.3847/1538-4357/aa911d.
- M. Kishimoto, S. F. Hönig, R. Antonucci, F. Millour, K. R. W. Tristram, and G. Weigelt. Mapping the radial structure of AGN tori. *A&A*, 536:A78, December 2011. doi: 10.1051/0004-6361/201117367.
- Ralf S. Klessen and Simon C. O. Glover. Physical Processes in the Interstellar Medium. *Saas-Fee Advanced Course*, 43:85, January 2016. doi: 10.1007/978-3-662-47890-5_2.
- Anne Klitsch, Céline Péroux, Martin A. Zwaan, Ian Smail, Dylan Nelson, Gergö Popping, Chian-Chou Chen, Benedikt Diemer, R. J. Ivison, James R. Allison, Sébastien Muller, A. Mark Swinbank, Aleksandra Hamanowicz, Andrew D. Biggs, and Rajeshwari Dutta. ALMACAL - VI. Molecular gas mass density across cosmic time via a blind search for intervening molecular absorbers. *MNRAS*, 490(1):1220–1230, November 2019. doi: 10.1093/mnras/stz2660.
- E. Komatsu, J. Dunkley, M. R. Nolta, C. L. Bennett, B. Gold, G. Hinshaw, N. Jarosik, D. Larson, M. Limon, L. Page, D. N. Spergel, M. Halpern, R. S. Hill, A. Kogut, S. S. Meyer, G. S. Tucker, J. L. Weiland, E. Wollack, and E. L. Wright. Five-Year Wilkinson Microwave Anisotropy Probe Observations: Cosmological Interpretation. *ApJS*, 180:330–376, February 2009. doi: 10.1088/0067-0049/180/2/330.
- John Kormendy and Luis C. Ho. Coevolution (Or Not) of Supermassive Black Holes and Host Galaxies. *ARA&A*, 51(1):511–653, August 2013. doi: 10.1146/annurev-astro-082708-101811.
- Michael J. Koss, Benjamin Strittmatter, Isabella Lamperti, Taro Shimizu, Benny Trakhtenbrot, Amelie Saintonge, Ezequiel Treister, Claudia Cicone, Richard Mushotzky, Kyuseok Oh, Claudio Ricci, Daniel Stern, Tonima T. Ananna, Franz E. Bauer, George C. Privon, Rudolf E. Bar, Carlos De Breuck, Fiona Harrison, Kohei Ichikawa, Meredith C. Powell, David Rosario, David B. Sanders, Kevin Schawinski, Li Shao, C. Megan Urry, and Sylvain Veilleux. BAT AGN Spectroscopic Survey-XX: Molecular Gas in Nearby Hard X-ray Selected AGN Galaxies. *arXiv e-prints*, art. arXiv:2010.15849, October 2020.
- J. H. Krolik and T. R. Kallman. X-ray ionization and the Orion Molecular Cloud. *ApJ*, 267:610–624, April 1983. doi: 10.1086/160897.
- Sibasish Laha, Alex G. Markowitz, Mirko Krumpke, Robert Nikutta, Richard Rothschild, and Tathagata Saha. The Variable and Non-variable X-Ray Absorbers in Compton-thin Type II Active Galactic Nuclei. *ApJ*, 897(1):66, July 2020. doi: 10.3847/1538-4357/ab92ab.
- G. Lanzuisi, R. Gilli, M. Cappi, M. Dadina, S. Bianchi, M. Brusa, G. Chartas, F. Civano, A. Comastri, A. Marinucci, R. Middei, E. Piconcelli, C. Vignali, W. N. Brandt, F. Tombesi, and M. Gaspari. NuSTAR Measurement of Coronal Temperature in Two Luminous, High-redshift Quasars. *ApJ*, 875(2):L20, April 2019. doi: 10.3847/2041-8213/ab15dc.

- Andy Lawrence and Martin Elvis. Misaligned Disks as Obscurers in Active Galaxies. *ApJ*, 714(1):561–570, May 2010. doi: 10.1088/0004-637X/714/1/561.
- S. Lepp and A. Dalgarno. X-ray-induced chemistry of interstellar clouds. *A&A*, 306: L21–L24, February 1996.
- Adam Leroy, Alberto Bolatto, Snezana Stanimirovic, Norikazu Mizuno, Frank Israel, and Caroline Bot. The Spitzer Survey of the Small Magellanic Cloud: Far-Infrared Emission and Cold Gas in the Small Magellanic Cloud. *ApJ*, 658(2):1027–1046, April 2007. doi: 10.1086/511150.
- Adam K. Leroy, Alberto Bolatto, Karl Gordon, Karin Sandstrom, Pierre Gratier, Erik Rosolowsky, Charles W. Engelbracht, Norikazu Mizuno, Edvige Corbelli, Yasuo Fukui, and Akiko Kawamura. The CO-to-H₂ Conversion Factor from Infrared Dust Emission across the Local Group. *ApJ*, 737(1):12, August 2011. doi: 10.1088/0004-637X/737/1/12.
- N. A. Levenson, K. A. Weaver, T. M. Heckman, H. Awaki, and Y. Terashima. Accretion and Outflow in the Active Galactic Nucleus and Starburst of NGC 5135. *ApJ*, 602(1): 135–147, February 2004. doi: 10.1086/380836.
- Lichen Liang, Robert Feldmann, Dušan Kereš, Nick Z. Scoville, Christopher C. Hayward, Claude-André Faucher-Giguère, Corentin Schreiber, Xiangcheng Ma, Philip F. Hopkins, and Eliot Quataert. On the dust temperatures of high-redshift galaxies. *MNRAS*, 489 (1):1397–1422, October 2019. doi: 10.1093/mnras/stz2134.
- M.-Y. Lin, R. I. Davies, E. K. S. Hicks, L. Burtscher, A. Contursi, R. Genzel, M. Koss, D. Lutz, W. Maciejewski, F. Müller-Sánchez, G. Orban de Xivry, C. Ricci, R. Riffel, R. A. Riffel, D. Rosario, M. Schartmann, A. Schnorr-Müller, T. Shimizu, A. Sternberg, E. Sturm, T. Storchi-Bergmann, L. Tacconi, and S. Veilleux. LLAMA: nuclear stellar properties of Swift-BAT AGN and matched inactive galaxies. *MNRAS*, 473:4582–4611, February 2018. doi: 10.1093/mnras/stx2618.
- U. Lisenfeld, D. Espada, L. Verdes-Montenegro, N. Kuno, S. Leon, J. Sabater, N. Sato, J. Sulentic, S. Verley, and M. S. Yun. The AMIGA sample of isolated galaxies. IX. Molecular gas properties. *A&A*, 534:A102, October 2011. doi: 10.1051/0004-6361/201117056.
- Daizhong Liu, Yu Gao, Kate Isaak, Emanuele Daddi, Chentao Yang, Nanyao Lu, and Paul van der Werf. High-J CO versus Far-infrared Relations in Normal and Starburst Galaxies. *ApJ*, 810(2):L14, September 2015. doi: 10.1088/2041-8205/810/2/L14.
- Y. Liu and X. Li. A direct comparison of X-ray spectral models for tori in active galactic nuclei. *MNRAS*, 448:L53–L57, March 2015. doi: 10.1093/mnrasl/slu198.
- A. P. Lobban, J. N. Reeves, D. Porquet, V. Braitto, A. Markowitz, L. Miller, and T. J. Turner. Evidence for a truncated accretion disc in the low-luminosity Seyfert galaxy, NGC 7213? *MNRAS*, 408(1):551–564, Oct 2010. doi: 10.1111/j.1365-2966.2010.17143.x.
- E. Lusso and G. Risaliti. The Tight Relation between X-Ray and Ultraviolet Luminosity of Quasars. *The Astrophysical Journal*, 819(2):154, 2016.
- E. Lusso, A. Comastri, C. Vignali, G. Zamorani, M. Brusa, R. Gilli, K. Iwasawa, M. Salvato, F. Civano, M. Elvis, A. Merloni, A. Bongiorno, J. R. Trump, A. M. Koekemoer, E. Schinnerer, E. Le Floc’h, N. Cappelluti, K. Jahnke, M. Sargent, J. Silverman, V. Mainieri, F. Fiore, M. Bolzonella, O. Le Fèvre, B. Garilli, A. Iovino, J. P. Kneib, F. Lamareille, S. Lilly, M. Mignoli, M. Scodreggio, and D. Vergani. The X-ray to optical-UV luminosity ratio of X-ray selected type 1 AGN in XMM-COSMOS. *A&A*, 512:A34, March 2010. doi: 10.1051/0004-6361/200913298.

- E. Lusso, A. Comastri, B. D. Simmons, M. Mignoli, G. Zamorani, C. Vignali, M. Brusa, F. Shankar, D. Lutz, J. R. Trump, R. Maiolino, R. Gilli, M. Bolzonella, S. Puccetti, M. Salvato, C. D. Impey, F. Civano, M. Elvis, V. Mainieri, J. D. Silverman, A. M. Koekemoer, A. Bongiorno, A. Merloni, S. Berta, E. Le Floch, B. Magnelli, F. Pozzi, and L. Riguccini. Bolometric luminosities and Eddington ratios of X-ray selected active galactic nuclei in the XMM-COSMOS survey. *MNRAS*, 425(1):623–640, Sep 2012. doi: 10.1111/j.1365-2966.2012.21513.x.
- D. Lutz, R. Maiolino, H. W. W. Spoon, and A. F. M. Moorwood. The relation between AGN hard X-ray emission and mid-infrared continuum from ISO spectra: Scatter and unification aspects. *A&A*, 418:465–473, May 2004. doi: 10.1051/0004-6361:20035838.
- Jianwei Lyu, G. H. Rieke, and Yong Shi. Dust-deficient Palomar-Green Quasars and the Diversity of AGN Intrinsic IR Emission. *ApJ*, 835(2):257, February 2017. doi: 10.3847/1538-4357/835/2/257.
- Chelsea L. MacLeod, Nicholas P. Ross, Andy Lawrence, Mike Goad, Keith Horne, William Burgett, Ken C. Chambers, Heather Flewelling, Klaus Hodapp, Nick Kaiser, Eugene Magnier, Richard Wainscoat, and Christopher Waters. A systematic search for changing-look quasars in SDSS. *MNRAS*, 457(1):389–404, March 2016. doi: 10.1093/mnras/stv2997.
- Piero Madau and Mark Dickinson. Cosmic Star-Formation History. *ARA&A*, 52:415–486, Aug 2014. doi: 10.1146/annurev-astro-081811-125615.
- S. C. Madden, A. Poglitsch, N. Geis, G. J. Stacey, and C. H. Townes. [C II] 158 Micron Observations of IC 10: Evidence for Hidden Molecular Hydrogen in Irregular Galaxies. *ApJ*, 483(1):200–209, July 1997. doi: 10.1086/304247.
- G. E. Magdis, D. Rigopoulou, G. Helou, D. Farrah, P. Hurley, A. Alonso-Herrero, J. Bock, D. Burgarella, S. Chapman, V. Charmandaris, A. Cooray, Y. Sophia Dai, D. Dale, D. Elbaz, A. Feltre, E. Hatziminaoglou, J. S. Huang, G. Morrison, S. Oliver, M. Page, D. Scott, and Y. Shi. Mid- to far-infrared properties of star-forming galaxies and active galactic nuclei. *A&A*, 558:A136, October 2013. doi: 10.1051/0004-6361/201322226.
- R. Maiolino and F. Mannucci. De re metallica: the cosmic chemical evolution of galaxies. *A&A Rev.*, 27(1):3, February 2019. doi: 10.1007/s00159-018-0112-2.
- R. Maiolino, M. Ruiz, G. H. Rieke, and P. Papadopoulos. Molecular Gas, Morphology, and Seyfert Galaxy Activity. *ApJ*, 485(2):552–569, August 1997. doi: 10.1086/304438.
- R. Maiolino, H. R. Russell, A. C. Fabian, S. Carniani, R. Gallagher, S. Cazzoli, S. Arribas, F. Belfiore, E. Bellocchi, L. Colina, G. Cresci, W. Ishibashi, A. Marconi, F. Mannucci, E. Oliva, and E. Sturm. Star formation inside a galactic outflow. *Nature*, 544(7649):202–206, March 2017. doi: 10.1038/nature21677.
- Dmitry Makarov, Philippe Prugniel, Nataliya Terekhova, H el ene Courtois, and Isabelle Vauglin. HyperLEDA. III. The catalogue of extragalactic distances. *A&A*, 570:A13, October 2014. doi: 10.1051/0004-6361/201423496.
- Matthew A. Malkan, Varoujan Gorjian, and Raymond Tam. A Hubble Space Telescope Imaging Survey of Nearby Active Galactic Nuclei. *ApJS*, 117(1):25–88, Jul 1998. doi: 10.1086/313110.
- Philip R. Maloney, David J. Hollenbach, and A. G. G. M. Tielens. X-Ray-irradiated Molecular Gas. I. Physical Processes and General Results. *ApJ*, 466:561, July 1996. doi: 10.1086/177532.

- S. Marchesi, M. Ajello, A. Comastri, G. Cusumano, V. La Parola, and A. Segreto. X-Ray Spectral Properties of Seven Heavily Obscured Seyfert 2 Galaxies. *ApJ*, 836(1):116, February 2017. doi: 10.3847/1538-4357/836/1/116.
- S. Marchesi, M. Ajello, L. Marcotulli, A. Comastri, G. Lanzuisi, and C. Vignali. Compton-thick AGNs in the NuSTAR Era. *ApJ*, 854(1):49, February 2018. doi: 10.3847/1538-4357/aaa410.
- S. Marchesi, M. Ajello, X. Zhao, L. Marcotulli, M. Baloković, M. Brightman, A. Comastri, G. Cusumano, G. Lanzuisi, V. La Parola, A. Segreto, and C. Vignali. Compton-thick AGNs in the NuSTAR Era. III. A Systematic Study of the Torus Covering Factor. *ApJ*, 872(1):8, February 2019. doi: 10.3847/1538-4357/aafbeb.
- A. Marinucci, S. Bianchi, V. Braitto, G. Matt, E. Nardini, and J. Reeves. Tracking the iron K α line and the ultra fast outflow in NGC 2992 at different accretion states. *MNRAS*, 478(4):5638–5649, August 2018. doi: 10.1093/mnras/sty1436.
- F. E. Marshall, E. A. Boldt, S. S. Holt, R. F. Mushotzky, S. H. Pravdo, R. E. Rothschild, and P. J. Serlemitsos. New hard X-ray sources observed with HEAO A-2. *ApJS*, 40: 657–666, Jul 1979. doi: 10.1086/190600.
- N. Mashian, E. Sturm, A. Sternberg, A. Janssen, S. Hailey-Dunsheath, J. Fischer, A. Conrursi, E. González-Alfonso, J. Graciá-Carpio, A. Poglitsch, S. Veilleux, R. Davies, R. Genzel, D. Lutz, L. Tacconi, A. Verma, A. Weiß, E. Polisensky, and T. Nikola. High-J CO Sleds in Nearby Infrared Bright Galaxies Observed By Herschel/PACS. *ApJ*, 802(2):81, April 2015. doi: 10.1088/0004-637X/802/2/81.
- C. F. McKee and J. P. Ostriker. A theory of the interstellar medium: three components regulated by supernova explosions in an inhomogeneous substrate. *ApJ*, 218:148–169, November 1977. doi: 10.1086/155667.
- Christopher F. McKee and Eve C. Ostriker. Theory of Star Formation. *ARA&A*, 45(1): 565–687, September 2007. doi: 10.1146/annurev.astro.45.051806.110602.
- R. Meijerink and M. Spaans. Diagnostics of irradiated gas in galaxy nuclei. I. A far-ultraviolet and X-ray dominated region code. *A&A*, 436(2):397–409, June 2005. doi: 10.1051/0004-6361:20042398.
- R. Meijerink, M. Spaans, and F. P. Israel. Diagnostics of irradiated dense gas in galaxy nuclei. II. A grid of XDR and PDR models. *A&A*, 461(3):793–811, Jan 2007. doi: 10.1051/0004-6361:20066130.
- S. Mineo, M. Gilfanov, and R. Sunyaev. X-ray emission from star-forming galaxies - I. High-mass X-ray binaries. *MNRAS*, 419(3):2095–2115, January 2012a. doi: 10.1111/j.1365-2966.2011.19862.x.
- S. Mineo, M. Gilfanov, and R. Sunyaev. X-ray emission from star-forming galaxies - II. Hot interstellarmedium. *MNRAS*, 426(3):1870–1883, November 2012b. doi: 10.1111/j.1365-2966.2012.21831.x.
- M. Mingozzi, L. Vallini, F. Pozzi, C. Vignali, A. Mignano, C. Gruppioni, M. Talia, A. Cimatti, G. Cresci, and M. Massardi. CO excitation in the Seyfert galaxy NGC 34: stars, shock or AGN driven? *MNRAS*, 474:3640–3648, March 2018. doi: 10.1093/mnras/stx3011.
- R. Minsley, A. Petric, E. Lambrides, A. Diamond-Stanic, M. Merhi, M. Chiaberge, and N. Flagey. Molecular Gas Heating and Modified Dust Properties in Active Galaxies: Growing Black Holes or Tidal Shocks? In *American Astronomical Society Meeting Abstracts #235*, volume 235 of *American Astronomical Society Meeting Abstracts*, page 304.09, January 2020.

- Yusuke Miyamoto, Naomasa Nakai, Masumichi Seta, Dragan Salak, Makoto Nagai, and Hiroyuki Kaneko. ALMA multiline observations toward the central region of NGC 613. *PASJ*, 69(5):83, October 2017. doi: 10.1093/pasj/psx076.
- Raffaella Morganti. Archaeology of active galaxies across the electromagnetic spectrum. *Nature Astronomy*, 1:596–605, September 2017. doi: 10.1038/s41550-017-0223-0.
- Raffaella Morganti, Tom Oosterloo, J. B. Raymond Oonk, Wilfred Frieswijk, and Clive Tadhunter. The fast molecular outflow in the Seyfert galaxy IC 5063 as seen by ALMA. *A&A*, 580:A1, August 2015. doi: 10.1051/0004-6361/201525860.
- D. J. Mortlock, S. J. Warren, B. P. Venemans, M. Patel, P. C. Hewett, R. G. McMahon, C. Simpson, T. Theuns, E. A. González-Solares, A. Adamson, S. Dye, N. C. Hambly, P. Hirst, M. J. Irwin, E. Kuiper, A. Lawrence, and H. J. A. Röttgering. A luminous quasar at a redshift of $z = 7.085$. *Nature*, 474:616–619, June 2011. doi: 10.1038/nature10159.
- M. Moshir and et al. IRAS Faint Source Catalogue, version 2.0. *IRAS Faint Source Catalogue*, page 0, January 1990.
- Kendrah D. Murphy and Tahir Yaqoob. An X-ray spectral model for Compton-thick toroidal reprocessors. *MNRAS*, 397(3):1549–1562, August 2009. doi: 10.1111/j.1365-2966.2009.15025.x.
- Tara Murphy, Elaine M. Sadler, Ronald D. Ekers, Marcella Massardi, Paul J. Hancock, Elizabeth Mahony, Roberto Ricci, Sarah Burke-Spolaor, Mark Calabretta, Rajan Chhetri, Gianfranco de Zotti, Philip G. Edwards, Jennifer A. Ekers, Carole A. Jackson, Michael J. Kesteven, Emma Lindley, Katherine Newton-McGee, Chris Phillips, Paul Roberts, Robert J. Sault, Lister Staveley-Smith, Ravi Subrahmanyan, Mark A. Walker, and Warwick E. Wilson. The Australia Telescope 20 GHz Survey: the source catalogue. *MNRAS*, 402(4):2403–2423, Mar 2010. doi: 10.1111/j.1365-2966.2009.15961.x.
- R. Nanni, C. Vignali, R. Gilli, A. Moretti, and W. N. Brandt. The X-ray properties of z 6 luminous quasars. *A&A*, 603:A128, July 2017. doi: 10.1051/0004-6361/201730484.
- Desika Narayanan and Mark R. Krumholz. A theory for the excitation of CO in star-forming galaxies. *MNRAS*, 442(2):1411–1428, Aug 2014. doi: 10.1093/mnras/stu834.
- Desika Narayanan, Mark R. Krumholz, Eve C. Ostriker, and Lars Hernquist. A general model for the CO-H₂ conversion factor in galaxies with applications to the star formation law. *MNRAS*, 421(4):3127–3146, April 2012. doi: 10.1111/j.1365-2966.2012.20536.x.
- A. Nersesian, E. M. Xilouris, S. Bianchi, F. Galliano, A. P. Jones, M. Baes, V. Casasola, L. P. Cassarà, C. J. R. Clark, J. I. Davies, M. Declair, W. Dobbels, I. De Looze, P. De Vis, J. Fritz, M. Galametz, S. C. Madden, A. V. Mosenkov, A. Trčka, S. Verstocken, S. Viaene, and S. Lianou. Old and young stellar populations in DustPedia galaxies and their role in dust heating. *A&A*, 624:A80, April 2019. doi: 10.1051/0004-6361/201935118.
- Hagai Netzer. Revisiting the Unified Model of Active Galactic Nuclei. *ARA&A*, 53: 365–408, August 2015. doi: 10.1146/annurev-astro-082214-122302.
- D. Obreschkow and S. Rawlings. Compactness of cold gas in high-redshift galaxies. *MNRAS*, 400(2):665–669, Dec 2009. doi: 10.1111/j.1365-2966.2009.15500.x.
- Kyuseok Oh, Michael Koss, Craig B. Markwardt, Kevin Schawinski, Wayne H. Baumgartner, Scott D. Barthelmy, S. Bradley Cenko, Neil Gehrels, Richard Mushotzky, Abigail Petulante, Claudio Ricci, Amy Lien, and Benny Trakhtenbrot. The 105-Month Swift-BAT All-sky Hard X-Ray Survey. *ApJS*, 235(1):4, March 2018. doi: 10.3847/1538-4365/aaa7fd.

- Eve C. Ostriker and Rahul Shetty. Maximally Star-forming Galactic Disks. I. Starburst Regulation Via Feedback-driven Turbulence. *ApJ*, 731(1):41, April 2011. doi: 10.1088/0004-637X/731/1/41.
- P. Padovani, N. Miller, K. I. Kellermann, V. Mainieri, P. Rosati, and P. Tozzi. The VLA Survey of Chandra Deep Field South. V. Evolution and Luminosity Functions of Sub-millijansky Radio Sources and the Issue of Radio Emission in Radio-quiet Active Galactic Nuclei. *ApJ*, 740(1):20, October 2011. doi: 10.1088/0004-637X/740/1/20.
- P. Padovani, E. Resconi, P. Giommi, B. Arsioli, and Y. L. Chang. Extreme blazars as counterparts of IceCube astrophysical neutrinos. *MNRAS*, 457(4):3582–3592, April 2016. doi: 10.1093/mnras/stw228.
- P. Padovani, D. M. Alexander, R. J. Assef, B. De Marco, P. Giommi, R. C. Hickox, G. T. Richards, V. Smolčić, E. Hatziminaoglou, V. Mainieri, and M. Salvato. Active galactic nuclei: what’s in a name? *A&A Rev.*, 25(1):2, August 2017. doi: 10.1007/s00159-017-0102-9.
- Padelis P. Papadopoulos, Paul P. van der Werf, E. M. Xilouris, K. G. Isaak, Yu Gao, and S. Mühle. The molecular gas in luminous infrared galaxies - I. CO lines, extreme physical conditions and their drivers. *MNRAS*, 426(4):2601–2629, Nov 2012. doi: 10.1111/j.1365-2966.2012.21001.x.
- Miguel Pereira-Santaella, Luigi Spinoglio, Gemma Busquet, Christine D. Wilson, Jason Glenn, Kate G. Isaak, Julia Kamenetzky, Naseem Rangwala, Maximilien R. P. Schirm, Maarten Baes, Michael J. Barlow, Alessandro Boselli, Asantha Cooray, and Diane Cormier. Herschel/SPIRE Submillimeter Spectra of Local Active Galaxies. *ApJ*, 768(1):55, May 2013. doi: 10.1088/0004-637X/768/1/55.
- Miguel Pereira-Santaella, Luigi Spinoglio, Paul P. van der Werf, and Javier Piqueras López. Warm molecular gas temperature distribution in six local infrared bright Seyfert galaxies. *A&A*, 566:A49, June 2014. doi: 10.1051/0004-6361/201423430.
- G. C. Perola, G. Matt, M. Cappi, F. Fiore, M. Guainazzi, L. Maraschi, P. O. Petrucci, and L. Piro. Compton reflection and iron fluorescence in BeppoSAX observations of Seyfert type 1 galaxies. *A&A*, 389:802–811, Jul 2002. doi: 10.1051/0004-6361:20020658.
- P. O. Petrucci, F. Ursini, A. De Rosa, S. Bianchi, M. Cappi, G. Matt, M. Dadina, and J. Malzac. Testing warm Comptonization models for the origin of the soft X-ray excess in AGNs. *A&A*, 611:A59, March 2018. doi: 10.1051/0004-6361/201731580.
- P. O. Petrucci, D. Gronkiewicz, A. Rozanska, R. Belmont, S. Bianchi, B. Czerny, G. Matt, J. Malzac, R. Middei, A. De Rosa, F. Ursini, and M. Cappi. Radiation spectra of warm and optically thick coronae in AGNs. *A&A*, 634:A85, February 2020. doi: 10.1051/0004-6361/201937011.
- M. M. Phillips. Optical Spectrophotometry of the Suspected X-Ray Galaxies NGC 6221 and NGC 7213. *ApJ*, 227:L121, February 1979. doi: 10.1086/182881.
- E. Piconcelli, E. Jimenez-Bailón, M. Guainazzi, N. Schartel, P. M. Rodríguez-Pascual, and M. Santos-Lleó. Evidence for a multizone warm absorber in the XMM-Newton spectrum of Markarian 304. *MNRAS*, 351(1):161–168, June 2004. doi: 10.1111/j.1365-2966.2004.07764.x.
- Gergö Popping, Eelco van Kampen, Roberto Decarli, Marco Spaans, Rachel S. Somerville, and Scott C. Trager. Sub-mm emission line deep fields: CO and [C II] luminosity functions out to $z = 6$. *MNRAS*, 461(1):93–110, September 2016. doi: 10.1093/mnras/stw1323.

- F. Pozzi, L. Vallini, C. Vignali, M. Talia, C. Gruppioni, M. Mingozzi, M. Massardi, and P. Andreani. CO excitation in the Seyfert galaxy NGC 7130. *MNRAS*, 470(1):L64–L68, September 2017. doi: 10.1093/mnrasl/slx077.
- M. A. Prieto, M. Mezcuca, J. A. Fernández-Ontiveros, and M. Schartmann. The central parsecs of active galactic nuclei: challenges to the torus. *MNRAS*, 442(3):2145–2164, August 2014. doi: 10.1093/mnras/stu1006.
- Daniel Proga, Yan-Fei Jiang, Shane W. Davis, James M. Stone, and Daniel Smith. The Effects of Irradiation on Cloud Evolution in Active Galactic Nuclei. *ApJ*, 780(1):51, January 2014. doi: 10.1088/0004-637X/780/1/51.
- Rostislav Protasov, David A. van Dyk, Alanna Connors, Vinay L. Kashyap, and Aneta Siemiginowska. Statistics, Handle with Care: Detecting Multiple Model Components with the Likelihood Ratio Test. *ApJ*, 571(1):545–559, May 2002. doi: 10.1086/339856.
- V. Ramakrishnan, N. M. Nagar, C. Finlez, T. Storchi-Bergmann, R. Slater, A. Schnorr-Müller, R. A. Riffel, C. G. Mundell, and A. Robinson. Nuclear kinematics in nearby AGN - I. An ALMA perspective on the morphology and kinematics of the molecular CO(2-1) emission. *MNRAS*, 487(1):444–455, Jul 2019. doi: 10.1093/mnras/stz1244.
- C. Ramos Almeida, N. A. Levenson, A. Alonso-Herrero, A. Asensio Ramos, J. M. Rodríguez Espinosa, A. M. Pérez García, C. Packham, R. Mason, J. T. Radomski, and T. Díaz-Santos. Testing the Unification Model for Active Galactic Nuclei in the Infrared: Are the Obscuring Tori of Type 1 and 2 Seyferts Different? *ApJ*, 731(2):92, April 2011. doi: 10.1088/0004-637X/731/2/92.
- Alvio Renzini and Ying-jie Peng. An Objective Definition for the Main Sequence of Star-forming Galaxies. *ApJ*, 801(2):L29, March 2015. doi: 10.1088/2041-8205/801/2/L29.
- C. Ricci, B. Trakhtenbrot, M. J. Koss, Y. Ueda, I. Del Vecchio, E. Treister, K. Schawinski, S. Paltani, K. Oh, I. Lamperti, S. Berney, P. Gandhi, K. Ichikawa, F. E. Bauer, L. C. Ho, D. Asmus, V. Beckmann, S. Soldi, M. Baloković, N. Gehrels, and C. B. Markwardt. BAT AGN Spectroscopic Survey. V. X-Ray Properties of the Swift/BAT 70-month AGN Catalog. *ApJS*, 233(2):17, December 2017. doi: 10.3847/1538-4365/aa96ad.
- Gordon T. Richards, Michael A. Strauss, Xiaohui Fan, Patrick B. Hall, Sebastian Jester, Donald P. Schneider, Daniel E. Vanden Berk, Chris Stoughton, Scott F. Anderson, Robert J. Brunner, Jim Gray, James E. Gunn, Željko Ivezić, Margaret K. Kirkland, G. R. Knapp, Jon Loveday, Avery Meiksin, Adrian Pope, Alexander S. Szalay, Anirudda R. Thakar, Brian Yanny, Donald G. York, J. C. Barentine, Howard J. Brewington, J. Brinkmann, Masataka Fukugita, Michael Harvanek, Stephen M. Kent, S. J. Kleinman, Jurek Krzesiński, Daniel C. Long, Robert H. Lupton, Thomas Nash, Jr. Neilsen, Eric H., Atsuko Nitta, David J. Schlegel, and Stephanie A. Snedden. The Sloan Digital Sky Survey Quasar Survey: Quasar Luminosity Function from Data Release 3. *AJ*, 131(6):2766–2787, June 2006. doi: 10.1086/503559.
- G. Risaliti and M. Elvis. *A Panchromatic View of AGN*, volume 308, page 187. 2004. doi: 10.1007/978-1-4020-2471-9_6.
- G. Risaliti, M. Elvis, G. Fabbiano, A. Baldi, A. Zezas, and M. Salvati. Occultation Measurement of the Size of the X-Ray-emitting Region in the Active Galactic Nucleus of NGC 1365. *ApJ*, 659(2):L111–L114, April 2007. doi: 10.1086/517884.
- P. F. Roche and D. K. Aitken. An investigation of the interstellar extinction - II. Towards the mid-infrared sources in the Galactic Centre. *MNRAS*, 215:425–435, August 1985. doi: 10.1093/mnras/215.3.425.

- Julia Roman-Duval, James M. Jackson, Mark Heyer, Jill Rathborne, and Robert Simon. Physical Properties and Galactic Distribution of Molecular Clouds Identified in the Galactic Ring Survey. *ApJ*, 723(1):492–507, November 2010. doi: 10.1088/0004-637X/723/1/492.
- D. J. Rosario, L. Burtscher, R. I. Davies, M. Koss, C. Ricci, D. Lutz, R. Riffel, D. M. Alexander, R. Genzel, E. H. Hicks, M. Y. Lin, W. Maciejewski, F. Müller-Sánchez, G. Orban de Xivry, R. A. Riffel, M. Schartmann, K. Schawinski, A. Schnorr-Müller, A. Saintonge, T. Shimizu, A. Sternberg, T. Storchi-Bergmann, E. Sturm, L. Tacconi, E. Treister, and S. Veilleux. LLAMA: normal star formation efficiencies of molecular gas in the centres of luminous Seyfert galaxies. *MNRAS*, 473(4):5658–5679, Feb 2018. doi: 10.1093/mnras/stx2670.
- M. J. F. Rosenberg, P. P. van der Werf, S. Aalto, L. Armus, V. Charmandaris, T. Díaz-Santos, A. S. Evans, J. Fischer, Y. Gao, E. González-Alfonso, T. R. Greve, A. I. Harris, C. Henkel, F. P. Israel, K. G. Isaak, C. Kramer, R. Meijerink, D. A. Naylor, D. B. Sanders, H. A. Smith, M. Spaans, L. Spinoglio, G. J. Stacey, I. Veenendaal, S. Veilleux, F. Walter, A. Weiß, M. C. Wiedner, M. H. D. van der Wiel, and E. M. Xilouris. The Herschel Comprehensive (U)LIRG Emission Survey (HERCULES): CO Ladders, Fine Structure Lines, and Neutral Gas Cooling. *ApJ*, 801(2):72, March 2015. doi: 10.1088/0004-637X/801/2/72.
- I. Ruffa, C. Vignali, A. Mignano, R. Paladino, and K. Iwasawa. The role of molecular gas in the nuclear regions of IRAS 00183-7111. ALMA and X-ray investigations of an ultraluminous infrared galaxy. *A&A*, 616:A127, Sep 2018. doi: 10.1051/0004-6361/201732268.
- B. Rush, M. A. Malkan, and L. Spinoglio. The extended 12 micron galaxy sample. *ApJS*, 89:1–33, November 1993. doi: 10.1086/191837.
- G. Sabatini, C. Gruppioni, M. Massardi, A. Giannetti, S. Burkutean, A. Cimatti, F. Pozzi, and M. Talia. Unveiling the inner morphology and gas kinematics of NGC 5135 with ALMA. *MNRAS*, 476:5417–5431, June 2018. doi: 10.1093/mnras/sty570.
- Anna Sajina, Lin Yan, Dieter Lutz, Aaron Steffen, George Helou, Minh Huynh, David Frayer, Philip Choi, Linda Tacconi, and Kalliopi Dasyra. Spitzer Mid-Infrared Spectroscopy of Infrared Luminous Galaxies at $z \sim 2$. III. Far-IR to Radio Properties and Optical Spectral Diagnostics. *ApJ*, 683(2):659–682, August 2008. doi: 10.1086/589914.
- F. Salvestrini, G. Risaliti, S. Bisogni, E. Lusso, and C. Vignali. Quasars as standard candles II. The non-linear relation between UV and X-ray emission at high redshifts. *A&A*, 631:A120, November 2019. doi: 10.1051/0004-6361/201935491.
- F. Salvestrini, C. Gruppioni, F. Pozzi, C. Vignali, A. Giannetti, R. Paladino, and E. Hatziminaoglou. Molecular gas in the central region of NGC 7213. *A&A*, 641:A151, September 2020. doi: 10.1051/0004-6361/202037660.
- K. M. Sandstrom, A. K. Leroy, F. Walter, A. D. Bolatto, K. V. Croxall, B. T. Draine, C. D. Wilson, M. Wolfire, D. Calzetti, R. C. Kennicutt, G. Aniano, J. Donovan Meyer, A. Usero, F. Bigiel, E. Brinks, W. J. G. de Blok, A. Crocker, D. Dale, C. W. Engelbracht, M. Galametz, B. Groves, L. K. Hunt, J. Koda, K. Kreckel, H. Linz, S. Meidt, E. Pellegrini, H. W. Rix, H. Roussel, E. Schinnerer, A. Schrubba, K. F. Schuster, R. Skibba, T. van der Laan, P. Appleton, L. Armus, B. Brandl, K. Gordon, J. Hinz, O. Krause, E. Montiel, M. Sauvage, A. Schmiedeke, J. D. T. Smith, and L. Vigroux. The CO-to-H₂ Conversion Factor and Dust-to-gas Ratio on Kiloparsec Scales in Nearby Galaxies. *ApJ*, 777(1):5, November 2013. doi: 10.1088/0004-637X/777/1/5.

- M. T. Sargent, E. Daddi, M. Béthermin, H. Aussel, G. Magdis, H. S. Hwang, S. Juneau, D. Elbaz, and E. da Cunha. Regularity Underlying Complexity: A Redshift-independent Description of the Continuous Variation of Galaxy-scale Molecular Gas Properties in the Mass-star Formation Rate Plane. *ApJ*, 793(1):19, September 2014. doi: 10.1088/0004-637X/793/1/19.
- L. Sargsyan, V. Leboutteiller, D. Weedman, H. Spoon, J. Bernard-Salas, D. Engels, G. Stacey, J. Houck, D. Barry, J. Miles, and A. Samsonyan. [C II] 158 μm Luminosities and Star Formation Rate in Dusty Starbursts and Active Galactic Nuclei. *ApJ*, 755(2):171, August 2012. doi: 10.1088/0004-637X/755/2/171.
- B. D. Savage and J. S. Mathis. Observed properties of interstellar dust. *ARA&A*, 17:73–111, January 1979. doi: 10.1146/annurev.aa.17.090179.000445.
- S. Sazonov, E. Churazov, and R. Krivonos. Does the obscured AGN fraction really depend on luminosity? *MNRAS*, 454(2):1202–1220, December 2015. doi: 10.1093/mnras/stv2069.
- M. Schartmann, K. Meisenheimer, H. Klahr, M. Camenzind, S. Wolf, and Th. Henning. The effect of stellar feedback on the formation and evolution of gas and dust tori in AGN. *MNRAS*, 393(3):759–773, March 2009. doi: 10.1111/j.1365-2966.2008.14220.x.
- H. R. Schmitt, J. L. Donley, R. R. J. Antonucci, J. B. Hutchings, and A. L. Kinney. A Hubble Space Telescope Survey of Extended [O III] $\lambda 5007$ Emission in a Far-Infrared Selected Sample of Seyfert Galaxies: Observations. *ApJS*, 148(2):327–352, October 2003. doi: 10.1086/377440.
- A. Schnorr-Müller, T. Storchi-Bergmann, N. M. Nagar, and F. Ferrari. Gas inflows towards the nucleus of the active galaxy NGC 7213. *MNRAS*, 438:3322–3331, March 2014. doi: 10.1093/mnras/stt2440.
- N. Scoville, K. Sheth, H. Aussel, P. Vanden Bout, P. Capak, A. Bongiorno, C. M. Casey, L. Murchikova, J. Koda, J. Álvarez-Márquez, N. Lee, C. Laigle, H. J. McCracken, O. Ilbert, A. Pope, D. Sanders, J. Chu, S. Toft, R. J. Ivison, and S. Manohar. ISM Masses and the Star formation Law at $Z = 1$ to 6: ALMA Observations of Dust Continuum in 145 Galaxies in the COSMOS Survey Field. *ApJ*, 820(2):83, Apr 2016. doi: 10.3847/0004-637X/820/2/83.
- Francesco Shankar, David H. Weinberg, and Jordi Miralda-Escudé. Self-Consistent Models of the AGN and Black Hole Populations: Duty Cycles, Accretion Rates, and the Mean Radiative Efficiency. *ApJ*, 690(1):20–41, January 2009. doi: 10.1088/0004-637X/690/1/20.
- O. Shemmer, W. N. Brandt, D. P. Schneider, X. Fan, M. A. Strauss, A. M. Diamond-Stanic, G. T. Richards, S. F. Anderson, J. E. Gunn, and J. Brinkmann. Chandra Observations of the Highest Redshift Quasars from the Sloan Digital Sky Survey. *ApJ*, 644:86–99, June 2006. doi: 10.1086/503543.
- O. Shemmer, W. N. Brandt, M. Paolillo, S. Kaspi, C. Vignali, P. Lira, and D. P. Schneider. Exploratory X-Ray Monitoring of Luminous Radio-quiet Quasars at High Redshift: No Evidence for Evolution in X-Ray Variability. *ApJ*, 848:46, October 2017. doi: 10.3847/1538-4357/aa8b78.
- Y. Shi, G. H. Rieke, D. C. Hines, V. Gorjian, M. W. Werner, K. Cleary, F. J. Low, P. S. Smith, and J. Bouwman. 9.7 μm Silicate Features in Active Galactic Nuclei: New Insights into Unification Models. *ApJ*, 653(1):127–136, December 2006. doi: 10.1086/508737.

- Yong Shi, George Helou, Lin Yan, Lee Armus, Yanling Wu, Casey Papovich, and Sabrina Stierwalt. Extended Schmidt Law: Role of Existing Stars in Current Star Formation. *ApJ*, 733(2):87, June 2011. doi: 10.1088/0004-637X/733/2/87.
- T. Taro Shimizu, Richard F. Mushotzky, Marcio Meléndez, Michael J. Koss, Amy J. Barger, and Lennox L. Cowie. Herschel far-infrared photometry of the Swift Burst Alert Telescope active galactic nuclei sample of the local universe - III. Global star-forming properties and the lack of a connection to nuclear activity. *MNRAS*, 466(3): 3161–3183, April 2017. doi: 10.1093/mnras/stw3268.
- R. Siebenmorgen, M. Haas, E. Krügel, and B. Schulz. Discovery of 10 μm silicate emission in quasars. Evidence of the AGN unification scheme. *A&A*, 436(1):L5–L8, June 2005. doi: 10.1051/0004-6361:200500109.
- Kazimierz Sliwa, Christine D. Wilson, Susanne Aalto, and George C. Privon. Extreme CO isotopic abundances in the ULIRG IRAS 13120-5453: An extremely young starburst or top-heavy initial mass function. *The Astrophysical Journal*, 840(2):L11, may 2017. doi: 10.3847/2041-8213/aa6ea4. URL <https://doi.org/10.3847/2041-8213/aa6ea4>.
- M. W. L. Smith, S. A. Eales, H. L. Gomez, J. Roman-Duval, J. Fritz, R. Braun, M. Baes, G. J. Bendo, J. A. D. L. Blommaert, M. Boquien, A. Boselli, D. L. Clements, A. R. Cooray, L. Cortese, I. De Looze, G. P. Ford, W. K. Gear, G. Gentile, K. D. Gordon, J. Kirk, V. Lebouteiller, S. Madden, E. Mentuch, B. O'Halloran, M. J. Page, B. Schulz, L. Spinoglio, J. Verstappen, C. D. Wilson, and D. A. Thilker. The Herschel Exploitation of Local Galaxy Andromeda (HELGA). II. Dust and Gas in Andromeda. *ApJ*, 756(1): 40, September 2012. doi: 10.1088/0004-637X/756/1/40.
- Małgorzata A. Sobolewska, Aneta Siemiginowska, and Piotr T. Życki. High-Redshift Radio-quiet Quasars: Exploring the Parameter Space of Accretion Models. II. Patchy Corona Model. *ApJ*, 617(1):102–112, December 2004. doi: 10.1086/425262.
- P. M. Solomon and P. A. Vanden Bout. Molecular Gas at High Redshift. *ARA&A*, 43(1): 677–725, Sep 2005. doi: 10.1146/annurev.astro.43.051804.102221.
- P. M. Solomon, A. R. Rivolo, J. Barrett, and A. Yahil. Mass, Luminosity, and Line Width Relations of Galactic Molecular Clouds. *ApJ*, 319:730, August 1987. doi: 10.1086/165493.
- Rachel S. Somerville and Romeel Davé. Physical Models of Galaxy Formation in a Cosmological Framework. *ARA&A*, 53:51–113, Aug 2015. doi: 10.1146/annurev-astro-082812-140951.
- Luigi Spinoglio and Matthew A. Malkan. The 12 Micron Galaxy Sample. I. Luminosity Functions and a New Complete Active Galaxy Sample. *ApJ*, 342:83, July 1989. doi: 10.1086/167577.
- Luigi Spinoglio, Paola Andreani, and Matthew A. Malkan. The Far-Infrared Energy Distributions of Seyfert and Starburst Galaxies in the Local Universe: Infrared Space Observatory Photometry of the 12 Micron Active Galaxy Sample. *ApJ*, 572(1):105–123, June 2002. doi: 10.1086/340302.
- H. W. W. Spoon, J. A. Marshall, J. R. Houck, M. Elitzur, L. Hao, L. Armus, B. R. Brandl, and V. Charmandaris. Mid-Infrared Galaxy Classification Based on Silicate Obscuration and PAH Equivalent Width. *ApJ*, 654(1):L49–L52, January 2007. doi: 10.1086/511268.
- Steven Stahler and Francesco Palla. The formation of stars. *The Formation of Stars*, by Steven W. Stahler, Francesco Palla, pp. 865. ISBN 3-527-40559-3. Wiley-VCH, January 2005., 01 2005. doi: 10.1002/9783527618675.

- Snežana Stanimirović, Claire E. Murray, Min-Young Lee, Carl Heiles, and Jesse Miller. Cold and Warm Atomic Gas around the Perseus Molecular Cloud. I. Basic Properties. *ApJ*, 793(2):132, October 2014. doi: 10.1088/0004-637X/793/2/132.
- R. L. C. Starling, M. J. Page, G. Branduardi-Raymont, A. A. Breeveld, R. Soria, and K. Wu. The X-ray spectrum of NGC 7213 and the Seyfert-LINER connection. *MNRAS*, 356(2):727–733, January 2005. doi: 10.1111/j.1365-2966.2004.08493.x.
- A. T. Steffen, I. Strateva, W. N. Brandt, D. M. Alexander, A. M. Koekemoer, B. D. Lehmer, D. P. Schneider, and C. Vignali. The X-Ray-to-Optical Properties of Optically Selected Active Galaxies over Wide Luminosity and Redshift Ranges. *AJ*, 131:2826–2842, June 2006. doi: 10.1086/503627.
- S. Stierwalt, L. Armus, V. Charmandaris, T. Diaz-Santos, J. Marshall, A. S. Evans, S. Haan, J. Howell, K. Iwasawa, D. C. Kim, E. J. Murphy, J. A. Rich, H. W. W. Spoon, H. Inami, A. O. Petric, and V. U. Mid-infrared Properties of Luminous Infrared Galaxies. II. Probing the Dust and Gas Physics of the GOALS Sample. *ApJ*, 790(2):124, August 2014. doi: 10.1088/0004-637X/790/2/124.
- T. Storchi-Bergmann, R. S. Nemmen, P. F. Spinelli, M. Eracleous, A. S. Wilson, A. V. Filippenko, and M. Livio. Evidence of a Starburst within 9 Parsecs of the Active Nucleus of NGC 1097. *ApJ*, 624(1):L13–L16, May 2005. doi: 10.1086/430421.
- Thaisa Storchi-Bergmann, Alberto Rodriguez-Ardila, Henrique R. Schmitt, Andrew S. Wilson, and Jack A. Baldwin. Circumnuclear Star Formation in Active Galaxies. *ApJ*, 472:83, Nov 1996. doi: 10.1086/178043.
- Thaisa Storchi-Bergmann, Rosa M. González Delgado, Henrique R. Schmitt, R. Cid Fernandes, and Timothy Heckman. Circumnuclear Stellar Population, Morphology, and Environment of Seyfert 2 Galaxies: An Evolutionary Scenario. *ApJ*, 559(1):147–156, September 2001. doi: 10.1086/322290.
- E. Sturm, M. Schweitzer, D. Lutz, A. Contursi, R. Genzel, M. D. Lehnert, L. J. Tacconi, S. Veilleux, D. S. Rupke, D. C. Kim, A. Sternberg, D. Maoz, S. Lord, J. Mazzarella, and D. B. Sanders. Silicate Emissions in Active Galaxies: From LINERs to QSOs. *ApJ*, 629(1):L21–L23, August 2005. doi: 10.1086/444359.
- Masahiro Suganuma, Yuzuru Yoshii, Yukiyasu Kobayashi, Takeo Minezaki, Keigo Enya, Hiroyuki Tomita, Tsutomu Aoki, Shintaro Koshida, and Bruce A. Peterson. Reverberation Measurements of the Inner Radius of the Dust Torus in Nearby Seyfert 1 Galaxies. *ApJ*, 639(1):46–63, March 2006. doi: 10.1086/499326.
- M. Symeonidis, B. M. Giblin, M. J. Page, C. Pearson, G. Bendo, N. Seymour, and S. J. Oliver. AGN are cooler than you think: the intrinsic far-IR emission from QSOs. *MNRAS*, 459(1):257–276, June 2016. doi: 10.1093/mnras/stw667.
- L. J. Tacconi, R. Genzel, A. Saintonge, F. Combes, S. García-Burillo, R. Neri, A. Bolatto, T. Contini, N. M. Förster Schreiber, S. Lilly, D. Lutz, S. Wuyts, G. Accurso, J. Boissier, F. Boone, N. Bouché, F. Bournaud, A. Burkert, M. Carollo, M. Cooper, P. Cox, C. Feruglio, J. Freundlich, R. Herrera-Camus, S. Juneau, M. Lippa, T. Naab, A. Renzini, P. Salome, A. Sternberg, K. Tadaki, H. Übler, F. Walter, B. Weiner, and A. Weiss. PHIBSS: Unified Scaling Relations of Gas Depletion Time and Molecular Gas Fractions. *ApJ*, 853(2):179, February 2018. doi: 10.3847/1538-4357/aaa4b4.
- Linda J. Tacconi, Reinhard Genzel, and Amiel Sternberg. The evolution of the star-forming interstellar medium across cosmic time. *Annual Review of Astronomy and Astrophysics*, 58(1):157–203, 2020. doi: 10.1146/annurev-astro-082812-141034. URL <https://doi.org/10.1146/annurev-astro-082812-141034>.

- M. Talia, F. Pozzi, L. Vallini, A. Cimatti, P. Cassata, F. Fraternali, M. Brusa, E. Daddi, I. Delvecchio, E. Ibar, E. Liuzzo, C. Vignali, M. Massardi, G. Zamorani, C. Gruppioni, A. Renzini, M. Mignoli, L. Pozzetti, and G. Rodighiero. ALMA view of a massive spheroid progenitor: a compact rotating core of molecular gas in an AGN host at $z = 2.226$. *MNRAS*, 476(3):3956–3963, May 2018. doi: 10.1093/mnras/sty481.
- Silvia Tommasin, Luigi Spinoglio, Matthew A. Malkan, and Giovanni Fazio. Spitzer-IRS High-Resolution Spectroscopy of the 12 μm Seyfert Galaxies. II. Results for the Complete Data Set. *ApJ*, 709(2):1257–1283, February 2010. doi: 10.1088/0004-637X/709/2/1257.
- Q. D. Tran, D. Lutz, R. Genzel, D. Rigopoulou, H. W. W. Spoon, E. Sturm, M. Gerin, D. C. Hines, A. F. M. Moorwood, D. B. Sanders, N. Scoville, Y. Taniguchi, and M. Ward. Isocam-Cvf 5-12 Micron Spectroscopy of Ultraluminous Infrared Galaxies. *ApJ*, 552(2):527–543, May 2001. doi: 10.1086/320543.
- James Trussler, Roberto Maiolino, Claudia Maraston, Yingjie Peng, Daniel Thomas, Daniel Goddard, and Jianhui Lian. Both starvation and outflows drive galaxy quenching. *MNRAS*, 491(4):5406–5434, February 2020. doi: 10.1093/mnras/stz3286.
- C. Megan Urry and Paolo Padovani. Unified Schemes for Radio-Loud Active Galactic Nuclei. *PASP*, 107:803, September 1995. doi: 10.1086/133630.
- F. Ursini, A. Marinucci, G. Matt, S. Bianchi, A. Tortosa, D. Stern, P. Arévalo, D. R. Ballantyne, F. E. Bauer, A. C. Fabian, F. A. Harrison, A. M. Lohfink, C. S. Reynolds, and D. J. Walton. The NuSTAR X-ray spectrum of the low-luminosity active galactic nucleus in NGC 7213. *MNRAS*, 452:3266–3272, September 2015. doi: 10.1093/mnras/stv1527.
- F. Ursini, P. O. Petrucci, G. Matt, S. Bianchi, M. Cappi, B. De Marco, A. De Rosa, J. Malzac, A. Marinucci, G. Ponti, and A. Tortosa. High-energy monitoring of NGC 4593 with XMM-Newton and NuSTAR. X-ray spectral analysis. *MNRAS*, 463(1):382–392, November 2016. doi: 10.1093/mnras/stw2022.
- F. Ursini, P. O. Petrucci, S. Bianchi, G. Matt, R. Middei, G. Marcel, J. Ferreira, M. Cappi, B. De Marco, A. De Rosa, J. Malzac, A. Marinucci, G. Ponti, and A. Tortosa. NuSTAR/XMM-Newton monitoring of the Seyfert 1 galaxy HE 1143-1810. Testing the two-corona scenario. *A&A*, 634:A92, February 2020. doi: 10.1051/0004-6361/201936486.
- A. Usero, S. García-Burillo, A. Fuente, and J. Martín-Pintado. XDR Chemistry in the Circumnuclear Disk of NGC 1068. In Susanne Aalto, Susanne Huttemeister, and Alan Pedlar, editors, *The Neutral ISM in Starburst Galaxies*, volume 320 of *Astronomical Society of the Pacific Conference Series*, page 273, December 2004.
- E. Valiante, D. Lutz, E. Sturm, R. Genzel, L. J. Tacconi, M. D. Lehnert, and A. J. Baker. A Mid-Infrared Spectroscopic Study of Submillimeter Galaxies: Luminous Starbursts at High Redshift. *ApJ*, 660(2):1060–1071, May 2007. doi: 10.1086/513306.
- L. Vallini, A. G. G. M. Tielens, A. Pallottini, S. Gallerani, C. Gruppioni, S. Carniani, F. Pozzi, and M. Talia. Impact of X-rays on CO emission from high- z galaxies. *MNRAS*, 490(4):4502–4514, Dec 2019. doi: 10.1093/mnras/stz2837.
- P. P. van der Werf, K. G. Isaak, R. Meijerink, M. Spaans, A. Rykala, T. Fulton, A. F. Loenen, F. Walter, A. Weiß, L. Armus, J. Fischer, F. P. Israel, A. I. Harris, S. Veilleux, C. Henkel, G. Savini, S. Lord, H. A. Smith, E. González-Alfonso, D. Naylor, S. Aalto, V. Charmandaris, K. M. Dasyra, A. Evans, Y. Gao, T. R. Greve, R. Güsten, C. Kramer, J. Martín-Pintado, J. Mazzarella, P. P. Papadopoulos, D. B. Sanders, L. Spinoglio, G. Stacey, C. Vlahakis, M. C. Wiedner, and E. M. Xilouris. Black hole accretion and

- star formation as drivers of gas excitation and chemistry in Markarian 231. *A&A*, 518: L42, July 2010. doi: 10.1051/0004-6361/201014682.
- M. P. Véron-Cetty and P. Véron. A catalogue of quasars and active nuclei: 12th edition. *A&A*, 455(2):773–777, August 2006. doi: 10.1051/0004-6361:20065177.
- C. Vignali, W. N. Brandt, X. Fan, J. E. Gunn, S. Kaspi, D. P. Schneider, and M. A. Strauss. Exploratory Chandra Observations of the Highest-Redshift Quasars: X-Rays from the Dawn of the Modern Universe. *AJ*, 122:2143–2155, November 2001. doi: 10.1086/323712.
- C. Vignali, W. N. Brandt, D. P. Schneider, and S. Kaspi. X-Ray Lighthouses of the High-Redshift Universe. II. Further Snapshot Observations of the Most Luminous $z \sim 4$ Quasars with Chandra. *AJ*, 129:2519–2530, June 2005. doi: 10.1086/430217.
- F. Vito, W. N. Brandt, B. D. Lehmer, C. Vignali, F. Zou, F. E. Bauer, M. Bremer, R. Gilli, R. J. Ivison, and C. Spingola. Chandra reveals a luminous Compton-thick QSO powering a Ly α blob in a $z = 4$ starbursting protocluster. *A&A*, 642:A149, October 2020. doi: 10.1051/0004-6361/202038848.
- Keiichi Wada and Colin A. Norman. Obscuring Material around Seyfert Nuclei with Starbursts. *ApJ*, 566(1):L21–L24, February 2002. doi: 10.1086/339438.
- Steven R. Warren, Evan D. Skillman, Adrienne M. Stilp, Julianne J. Dalcanton, Jürgen Ott, Fabian Walter, Eric A. Petersen, Bärbel Koribalski, and Andrew A. West. Tracing Cold H I Gas in nearby, Low-mass Galaxies. *ApJ*, 757(1):84, September 2012. doi: 10.1088/0004-637X/757/1/84.
- N. A. Webb, M. Coriat, I. Traulsen, J. Ballet, C. Motch, F. J. Carrera, F. Koliopoulos, J. Authier, I. de la Calle, M. T. Ceballos, E. Colomo, D. Chuard, M. Freyberg, T. Garcia, M. Kolehmainen, G. Lamer, D. Lin, P. Maggi, L. Michel, C. G. Page, M. J. Page, J. V. Perea-Calderon, F. X. Pineau, P. Rodriguez, S. R. Rosen, M. Santos Lleo, R. D. Saxton, A. Schwöpe, L. Tomás, M. G. Watson, and A. Zakardjian. The XMM-Newton serendipitous survey. IX. The fourth XMM-Newton serendipitous source catalogue. *A&A*, 641:A136, September 2020. doi: 10.1051/0004-6361/201937353.
- D. R. Wilkins, E. Kara, A. C. Fabian, and L. C. Gallo. Caught in the act: measuring the changes in the corona that cause the extreme variability of 1H 0707-495. *MNRAS*, 443(3):2746–2756, September 2014. doi: 10.1093/mnras/stu1273.
- Jong-Hak Woo and C. Megan Urry. Active Galactic Nucleus Black Hole Masses and Bolometric Luminosities. *ApJ*, 579(2):530–544, Nov 2002. doi: 10.1086/342878.
- Yanling Wu, George Helou, Lee Armus, Diane Cormier, Yong Shi, Daniel Dale, Kalliopi Dasyra, J. D. Smith, Casey Papovich, Bruce Draine, Nurur Rahman, Sabrina Stierwalt, Dario Fadda, G. Lagache, and Edward L. Wright. Infrared Luminosities and Aromatic Features in the 24 μ m Flux-limited Sample of 5MUSES. *ApJ*, 723(1):895–914, November 2010. doi: 10.1088/0004-637X/723/1/895.
- Jun Xu, Mou-Yuan Sun, Yong-Quan Xue, Jun-Yao Li, and Zhi-Cheng He. X-ray absorption and 9.7 μ m silicate feature as a probe of AGN torus structure. *Research in Astronomy and Astrophysics*, 20(9):147, September 2020. doi: 10.1088/1674-4527/20/9/147.
- Jinyi Yang, Feige Wang, Xiaohui Fan, Joseph F. Hennawi, Frederick B. Davies, Minghao Yue, Eduardo Banados, Xue-Bing Wu, Bram Venemans, Aaron J. Barth, Fuyan Bian, Konstantina Boutsia, Roberto Decarli, Emanuele Paolo Farina, Richard Green, Linhua Jiang, Jiang-Tao Li, Chiara Mazzucchelli, and Fabian Walter. Pōniuā’ena: A Luminous $z = 7.5$ Quasar Hosting a 1.5 Billion Solar Mass Black Hole. *ApJ*, 897(1):L14, July 2020. doi: 10.3847/2041-8213/ab9c26.

- J. S. Young and N. Z. Scoville. Molecular gas in galaxies. *ARA&A*, 29:581–625, January 1991. doi: 10.1146/annurev.aa.29.090191.003053.
- Judith S. Young, Shuding Xie, Linda Tacconi, Pat Knezek, Paul Viscuso, Lowell Tacconi-Garman, Nick Scoville, Steve Schneider, F. Peter Schloerb, Steve Lord, Amy Lesser, Jeff Kenney, Yi-Long Huang, Nick Devereux, Mark Claussen, James Case, John Carpenter, Mike Berry, and Lori Allen. The FCRAO Extragalactic CO Survey. I. The Data. *ApJS*, 98:219, May 1995. doi: 10.1086/192159.
- A. Zaino, S. Bianchi, A. Marinucci, G. Matt, F. E. Bauer, W. N. Brandt, P. Gandhi, M. Guainazzi, K. Iwasawa, S. Puccetti, C. Ricci, and D. J. Walton. Probing the circumnuclear absorbing medium of the buried AGN in NGC 1068 through NuSTAR observations. *MNRAS*, 492(3):3872–3884, March 2020. doi: 10.1093/mnras/staa107.
- A. A. Zdziarski, A. C. Fabian, K. Nandra, A. Celotti, M. J. Rees, C. Done, P. S. Coppi, and G. M. Madejski. Physical processes in the X-ray/gamma-ray source of IC 4329A. *MNRAS*, 269:L55–L60, August 1994. doi: 10.1093/mnras/269.1.L55.